Analyse et atténuation par shunt piézoélectrique résonant des vibrations induites par l'écoulement subies par des surfaces portants navales

Yann Watine

HESAM UNIVERSITÉ

Arts et Métiers Sciences et Technologies

ÉCOLE DOCTORALE SCIENCES ET MÉTIERS DE L'INGÉNIEUR

Institut de Recherche de l'Ecole Navale (IRENAV)

Laboratoire de Mécanique des Structures et des Systèmes Couplés

THÈSE

présentée par : **Yann WATINE**
soutenue le : **22 Septembre 2023**

pour obtenir le grade de : **Docteur d'HESAM Université**

préparée à : **École Nationale Supérieure d'Arts et Métiers et École Navale**

Discipline : **Sciences pour l'Ingénieur**

Spécialité : **Interaction fluide-structure**

Analysis and mitigation by resonant piezoelectric shunt of flow-induced vibrations sustained by naval lifting surfaces

THÈSE dirigée par :

M. Jacques-André ASTOLFI Professeur des Universités, IRENav, École Navale

M. Jean-François DEÜ Professeur des Universités, LMSSC, Cnam Paris

et co-encadrée par :

Mme. Céline GABILLET Maître de Conferences, IRENav, École Navale

M. Boris LOSSOUARN Maître de Conférences, LMSSC, Cnam Paris

Jury

Mme. Shabnam ARBAB CHIRANI	Professeur, Institut de Recherche Dupuy de Lôme , École Nationale d'Ingénieurs de Brest	Présidente
M. Xavier ESCALER	Professeur, Barcelona Fluids and Energy Laboratory, Universitat Politécnica de Catalunya	Rapporteur
M. Jean-Camille CHASSAING	Professeur, Institut Jean le Rond d'Alembert, Sorbonne Université	Rapporteur
M. Laurent MAXIT	Maître de conférences, Laboratoire Vibrations Acoustique, INSA Lyon	Examinateur

THÈSE

A mes parents

Remerciements

Cette thèse a été financée par l'Ecole Navale et est une collaboration entre l'Institut de Recherche de l'Ecole Navale (IRENav) et le Laboratoire de Mécanique des Structures et des Systèmes Couplés (LMSSC) au sein du projet structurant SmartFoil visant à développer des techniques de Smart Structures pour le domaine naval. Je remercie sincèrement l'Ecole Navale pour avoir financé mes travaux ainsi que les équipes techniques des différents laboratoires pour avoir rendu possible les nombreuses campagnes expérimentales, notamment par la réalisation des prototypes et la préparation des équipements de mesure.

J'exprime mes sincères remerciements à mes directeurs de thèse, le Professeur Jacques-André Astolfi et le Professeur Jean-François Deü, pour m'avoir accordé leur confiance tout au long de ce travail et pour m'avoir confié le dispositif expérimental et les ressources de calcul nécessaires. Je remercie le Professeur Astolfi pour m'avoir incité à donner le meilleur de moi-même et de m'avoir initié au monde passionnant et exigeant qu'est la recherche. Les nombreux échanges avec le Professeur Astolfi, mêmes à des heures tardives, m'ont permis de fortement progresser dans mes réflexions et de mener à bien la résolution de problèmes techniques complexes. Je remercie le Professeur Deü pour sa bienveillance et pour ses précieux conseils ainsi que pour la liberté qu'il m'a accordé pour explorer diverses directions de recherche. Je remercie également mes directeurs de thèse pour m'avoir offert la chance de présenter mes travaux lors de différents congrès. De Orlando à Athènes en passant par Nantes, ces congrès m'ont permis de me confronter à des scientifiques de renom.

Toute ma reconnaissance va également à mes encadrants de thèse, le Docteur Céline Gabillet et le Docteur Boris Lossouarn. Leur implication sans limites et leur soutien tout au long de la thèse et même pendant les confinements du Covid 19 m'ont permis d'avancer rapidement et dans les meilleures conditions possibles. Merci au Docteur Gabillet pour m'avoir enseigné la rigueur scientifique et le gout de se confronter à l'inconnu. Merci pour votre confiance et pour votre bienveillance et pour tous les

conseils que vous m'avez donnés. Merci au Docteur Lossouarn pour m'avoir initié au monde fascinant des matériaux piézoélectriques. Merci pour votre disponibilité permanente malgré la distance entre nos lieux de travail et pour la clarté de vos explications. Nos nombreux échanges ont été pour moi une grande source de motivation.

Je remercie le Professeur Escaler et le Professeur Chassaing, rapporteurs, pour leur lecture attentive de mon manuscrit de thèse. Je remercie également le professeur Arbab Chirani pour avoir présidé le jury et le Docteur Laurent Maxit pour avoir été examinateur de ma soutenance. Merci aux membres du jury pour les échanges constructifs à l'issue de la soutenance.

Merci également à mon collègue de bureau Paul François pour son soutien et pour les discussions enflammées sur l'acquisition de voiliers, le surf en Presqu'ile de Crozon, les foils du futur et bien d'autres sujets passionnants dont la liste est infinie. Merci également à tous mes collègues de travail. Merci aux élèves et étudiants de l'Ecole Navale à qui j'ai eu la chance d'enseigner. Participer à la formation des futurs officiers de la Marine Nationale a été pour moi un grand honneur.

Du fond de mon cœur je remercie mes parents, Anne et Gaetan Watine pour m'avoir soutenu pendant mes très longues études et pour m'avoir réconforté pendant les moments difficiles. Merci maman pour m'avoir transmis le gout du travail intellectuel, merci papa de m'avoir transmis la passion de l'océan et de la technique. Mes pensées et ma reconnaissance vont également à ma grand-mère Lilianne Vandenmeulebrouck qui m'a appris, parmi tant de choses, la détermination et la ténacité. Merci également à mes amis, Carl Louis Larsson, Kenan Autret, Vianney Michelet, Alexis Salkin, Cécile Lhommeau, Anne-Camille Tanguy et Antoine Le Peley. J'espère avoir désormais un peu plus de temps à vous consacrer.

Enfin je tiens à remercier sincèrement mon institutrice à l'Ecole Notre Dame d'Izel Vor, Armelle Guyader et ma professeure de français au Collège Saint Joseph, Mme Bouguyon, pour avoir cru en moi et pour m'avoir donné l'envie d'apprendre. Je suis certain que mon gout pour la connaissance à pris naissance pendant vos cours.

Résumé

Les vibrations induites par l'écoulement subies par des surfaces portantes navales peuvent entraîner un rayonnement acoustique et une fatigue structurelle précoce. Une étude expérimentale de ces vibrations a été menée afin 1) d'étudier le couplage fluide-structure de surfaces portantes allongées sous excitation fluide et 2) de concevoir un dispositif efficace d'atténuation des vibrations consistant en un shunt piézoélectrique résonnant passif. Les structures étudiées consistent en une plaque plane de section rectangulaire en aluminium de rapport corde/épaisseur de 16,7 et en un hydrofoil tronqué en aluminium de type NACA 66-306 d'un rapport corde/épaisseur de 13,9. Différentes vitesses d'écoulement, associées à des nombres de Reynolds basés sur la corde compris entre 250000 et 950000, ont été analysées à zéro degré d'incidence dans le tunnel hydrodynamique de l'Institut de Recherche de l'École Navale (IRENav). La vitesse de vibration des deux structures a été évaluée par vibrométrie laser. Le sillage a été caractérisé par vélocimétrie d'image de particule et analysé par étude statistique de l'écoulement moyen et par décomposition orthogonale propre. La dynamique des tourbillons de Karman a été analysée à l'aide d'un algorithme de détection des tourbillons.

L'analyse de la réponse vibratoire à différentes vitesses d'écoulement a mis en évidence trois régimes de vibration distincts, à savoir l'absence de résonance, la résonance sans accrochage et la résonance avec accrochage avec le premier mode de torsion. Pour la plaque plane, deux sources d'excitation coexistent : 1) l'instabilité de bord de fuite et 2) l'instabilité de cisaillement qui se traduit par deux modes de lâché tourbillonnaire. Le régime de résonance avec accrochage est caractérisé par une augmentation de la contribution à l'énergie cinétique turbulente total du lâché tourbillonnaire primaire de Karman et de sa première harmonique, en accord avec une augmentation de la traînée. Un dispositif innovant consistant en un shunt résonnant passif connecté à un patch piézoélectrique intégré à la surface de l'hydrofoil a été mis en œuvre. Les vibrations de type torsion ont été atténuées à une vitesse d'écoulement nulle dans l'air et dans l'eau et à différentes vitesses d'écoulement dans l'eau. Deux types de shunts

piézoélectriques résonnants passifs ont été testés : le shunt avec inductance bobinée et le shunt à inductance synthétique.

Le shunt avec inductance bobinée a démontré un niveau d'atténuation des vibrations de 18 dB de l'amplitude maximale des vibrations du mode de torsion lorsque l'hydrofoil est immergé dans l'eau à une vitesse d'écoulement nulle. Le shunt à inductance synthétique a été testé à une vitesse d'écoulement nulle et a permis d'atténuer les vibrations de 31 dB dans l'air et de 21 dB dans l'eau. En plus de l'étude expérimentale, un modèle éléments finis de l'hydrofoil équipé d'un transducteur piézoélectrique a été mis en œuvre avec COMSOL Multiphysics. Le shunt à inductance bobinée est adapté aux vibrations de grande amplitude et a été testé sous écoulement. Différents régimes de vibration ont été identifiés : absence de résonance, résonance et accrochage avec le premier mode de torsion. Pour cette configuration, la valeur efficace du signal de vitesse de vibration a été réduite par le shunt de 62 % à l'accrochage. Sous accrochage, le lâché tourbillonnaire de Karman est moins corrélé en phase et un contenu fréquentiel à large bande est introduit lorsque le shunt est activé. En conclusion, les recherches menées dans le cadre de cette étude ont permis de mieux comprendre les mécanismes vibratoires induits par l'écoulement à l'origine de vibrations de forte amplitude et le shunt piézoélectrique résonnant a démontré sa capacité à réduire ces vibrations.

Mots-clés : interaction fluide-structure, vibrations induites par l'écoulement, lâché tourbillonnaire, contrôle de vibration, shunt résonant, couplage piézoélectrique, TR-PIV, POD, SPOD.

Abstract

Flow-induced vibrations (FIV) sustained by naval lifting surfaces may lead to acoustic noise and early structural fatigue. An experimental study of the flow induced vibrations sustained by marine lifting surfaces was conducted in order to 1) investigate the fluid-structure coupling of elongated surfaces under flow excitation which may be subjected to a higher number of freedom degrees than short surfaces and to 2) design an efficient vibration mitigation device consisting of a passive resonant piezoelectric shunt. The studied structures consist of a blunt flat aluminium plate of chord-to-thickness ratio 16.7 and a truncated NACA 66-306 aluminium hydrofoil of chord-to-thickness ratio 13.9. Various flow velocities, associated with chord-based Reynolds numbers ranging between 2.5×10^5 and 9.5×10^5 were analysed at zero degrees of incidence in the hydrodynamic tunnel of the French Naval Academy Research Institute (IRENav). The vibration velocity of both structures was evaluated using laser vibrometry and spectral analysis. The near-wake flow field was characterized by Time-Resolved Particle Image Velocimetry (TR-PIV) and analysed by statistical analysis of the mean flow, Proper Orthogonal Decomposition (POD) of the turbulent flow and its spectral variant (SPOD). The dynamics of the Karman vortices were analysed by using a vortex detection algorithm and different patterns, contributing to the total Turbulent Kinetic Energy (TKE), were identified according to the vibration regime.

The analysis of the vibrational response at various flow velocities has highlighted three distinct vibration regimes consisting of no-resonance, lock-off resonance and lock-in resonance with the first twisting mode. For the blunt plate, two excitation sources coexist: 1) the Trailing Edge Vortex Shedding (TEVS) instability and 2) The Impinging Shear Layer (ISL) instability which results in two Karman vortex shedding modes. Of particular interest is the lock-off resonance regime which occurs when the vortex shedding frequency of the secondary Karman mode synchronizes with the twisting mode natural frequency. For the lock-off and lock-in resonance regimes, the wake bubble flapping

contributes to the total TKE at low frequency. The lock-in resonance regime is characterized by an increase in the contribution to the total TKE of both the primary Karman vortex shedding and its first harmonic in agreement with an increase of the drag.

An innovative setup consisting of a passive resonant shunt connected to a piezoelectric transducer integrated on the truncated hydrofoil surface was implemented. Twisting type vibrations were mitigated at zero flow velocity in air and in water and at various flow velocities in water. Two types of passive resonant piezoelectric shunts were tested: the copper wired inductor shunt and the synthetic inductor shunt. The copper wired inductor shunt has demonstrated a vibration mitigation level of 18 dB of the twisting mode maximal vibration magnitude when the hydrofoil is immersed in water at zero flow velocity. The synthetic inductor shunt is constituted of an electronic circuit based on operational amplifiers. It was tested at zero flow velocity and provided a vibration mitigation of 31 dB in air and of 21 dB in water. In addition to the experimental study, a numerical model of the hydrofoil embedded with piezoelectric transducer was implemented with COMSOL *Multiphysics*. A passive resonant shunt was also simulated in order to predict the frequency response functions proper to various shunt parameters. Numerical and experimental results were compared and appeared to be in agreement.

The copper wired inductor shunt is well adapted for high magnitude vibrations and was tested under flow conditions. Different vibration regimes consisting of no resonance, resonance and lock-in with the first twisting mode and with the second bending mode were identified. For this configuration, the root mean square value of the vibration velocity signal was reduced by the shunt by 62% at the lock-in regime. When the shunt is activated, the vibration magnitude is reduced for Reynolds ranging in $[3.5 \times 10^5; 4.25 \times 10^5]$. The shunt also induces a smoother transition between different lock-in regimes and a narrower range of Reynolds numbers were resonance occurs. At lock-in, the Karman vortex shedding is less phase correlated and broadband frequency content is introduced when the shunt is activated. In the end, the investigations conducted through this study have offered new insights about the flow-induced vibration mechanisms leading to high magnitude vibrations and the resonant piezoelectric shunt has demonstrated its high capability to reduce these vibrations.

Keywords : fluid-structure interaction, flow-induced vibrations, vortex shedding, vibration mitigation, resonant shunt, piezoelectric coupling, TR-PIV, POD, SPOD.

Résumé étendu en Français

Présentation de la problématique

Les interactions fluide-structure (IFS) sont définies comme un transfert d'énergie bidirectionnel dans un domaine composé à la fois d'un fluide et d'un solide. Parmi les nombreuses disciplines de l'ingénierie concernées par les interactions fluide-structure, la thématique des vibrations induites par l'écoulement est cruciale pour la conception de structures marines performantes et résistantes. Tout corps solide, lorsqu'il est placé dans un écoulement à nombre de Reynold élevé, induit des instabilités hydrodynamiques qui peuvent générer un phénomène de lâché tourbillonnaire périodique et alternatif. Le champ de pression dans le sillage de l'objet immergé est directement affecté par la répartition des tourbillons, ce qui entraîne une fluctuation des forces de portance et de traînée. Ce mécanisme induit une excitation structurelle conduisant à des vibrations de forte amplitude. Lorsque la fréquence de lâché des tourbillons coïncide avec une fréquence propre de la structure ou l'une de ses harmoniques, l'amplitude des vibrations augmente considérablement. Le mécanisme d'instabilité à l'origine du lâché tourbillonnaire peut alors se coupler avec les mouvements de la structure ce qui entraîne la synchronisation de la fréquence de lâché tourbillonnaire avec la fréquence de vibration sur une large gamme de vitesses d'écoulement. Ce phénomène, connu sous le nom de "lock-in", peut avoir des conséquences dramatiques pour diverses applications industrielles. Le mécanisme conduisant aux vibrations induites par le lâché tourbillonnaire est particulièrement complexe lorsque le nombre de Reynolds est élevé et dans le cas d'écoulements turbulents séparés et rattachés. Les écoulements turbulents rattachés concernent les corps présentant un rapport corde/épaisseur important, tels que les plaques planes, les hydrofoils ou les pales d'hélice. Pour ces types d'écoulements, le couplage entre le détachement au bord d'attaque et le lâché de tourbillons dans le sillage est beaucoup plus complexe que dans les écoulements fortement séparés. Lorsque le couplage fluide-structure se produit, la compréhension physique et la

modélisation de ces types d'écoulements sont complexes. Ces vibrations d'origine hydrodynamique sont particulièrement impactantes pour le domaine maritime et naval.

La croissance drastique de la flotte militaire mondiale à la lumière des récents événements géopolitiques a remis les questions de discrétion acoustique au premier plan de la recherche et de l'innovation. Les vibrations structurelles sont notamment responsables de la propagation des ondes acoustiques dans le domaine fluide. Ces ondes acoustiques peuvent se propager dans le champ lointain si leur énergie est suffisamment élevée, ce qui entraîne une augmentation considérable de la signature acoustique des navires. La réduction des vibrations subies par les pales d'hélice, les gouvernails et les ailerons constituent un défi majeur pour l'ingénierie navale. Dans le domaine de la préservation de la faune marine, la réduction du bruit induit par les activités humaines en milieu marin, appelé bruit anthropique, est également une préoccupation majeure. Depuis les années 1950, le nombre de navires naviguant sur les océans a fortement augmenté en raison du commerce maritime mondial, ce qui a entraîné une pollution sonore excessive. La survie de nombreux organismes marins dépend de l'interprétation des informations acoustiques de leur environnement. La pollution sonore peut provoquer un masquage auditif et, dans le cas le plus critique, des dommages physiologiques [23, 24]. De nombreux États accordent une importance grandissante à la réduction du bruit acoustique sous-marin et l'intègrent désormais à leur politique environementale. Par exemple, la législation européenne favorise la réduction de la pollution sonore par le biais de la directive-cadre européenne Stratégie pour le milieu marin [25, 26].

Au cours de la dernière décennie, les surfaces portantes marines ont connu un développement considérable dans le domaine des sports nautiques. De nouvelles disciplines telles-que le wing foil, le kite foil, le surf foil et le windsurf foil sont apparues, toutes basées sur l'intégration d'hydrofoils sur différents types de planches de surf. Ces dispositifs ont largement contribué au développement rapide d'hydrofoils à haut rendement, légers et compétitifs visant à battre des records de vitesse mondiaux ou à remporter des championnats internationaux tels que les Jeux Olympiques. Le domaine de la voile de compétition a également été profondément influencé par l'ajout de surfaces portantes sur la coque des voiliers. Aujourd'hui, la plupart des monocoques et multicoques de dernière génération utilisent des hydrofoils pour s'élever au-dessus de la surface de la mer et réduire ainsi la résistance à l'avancement afin de maximiser la vitesse. Les vibrations induites par l'écoulement sont d'une importance primordiale pour ces applications car les vitesses atteintes coïncident avec les nombres de Reynolds où les instabilités hydrodynamiques peuvent se coupler avec les fréquences propres des hydrofoils. En outre,

l'utilisation croissante de matériaux légers tels que les composites à base de fibre de verre ou de carbone peut entraîner une délamination des fibres du matériau sous l'effet des vibrations. La fatigue structurelle, résultant de vibrations de forte amplitude, peut également provoquer une détérioration précoce des hydrofoils et de la structure du navire. En outre, le confort des voiliers de dernière génération a été considérablement réduit en raison du bruit acoustique émis par les hydrofoils. De nos jours, de nombreux marins professionnels utilisent des casques anti-bruit pour éviter les sons perçants induits par les appendices, ce qui entraîne un épuisement précoce et réduit l'attention pendant la veille.

Dans un contexte différent, la demande croissante d'énergie et le besoin de sources respectueuses de l'environnement ont contribué au développement rapide des énergies marines renouvelables. La plupart des centrales hydro-électriques sont composées d'éléments structurels souvent situés dans des zones de forts courants susceptibles de provoquer des vibrations. D'une manière plus générale, les machines hydrauliques composées de turbines et de pompes sont également fortement impactées par les vibrations [11]. Pour ces dispositifs, les modifications ou les réparations après fabrication entraîneront souvent des dépenses prohibitives en raison de la difficulté d'accès et de la complexité globale des systèmes. Par ailleurs, à bord des navires, de nombreux équipements sont composés de pompes rotatives. Leur vitesse de rotation élevée est souvent propice à l'apparition de vibrations et peut conduire à une usure précoce et à un rayonnement acoustique particulièrement gênant pour les applications liées au domaine naval de défense.

Les applications industrielles affectées par les vibrations d'origine hydrodynamique introduites dans la présente section sont multiples et la liste est loin d'être exhaustive. Au fil des ans, de nombreux projets de recherche ont étudié, à la fois expérimentalement et numériquement, les mécanismes à l'origine des vibrations afin de trouver des solutions pour réduire celles-ci. Les techniques d'atténuation des vibrations couramment adoptées consistent à modifier des structures existantes par la suppression ou l'ajout de matière afin de découpler les fréquences propres des sources d'excitation hydrodynamiques. Une approche différente consiste à modifier la géométrie afin d'altérer les instabilités hydrodynamiques. Par exemple, la modification du bord de fuite d'un hydrofoil permet de réduire considérablement l'amplitude des vibrations et la gamme des vitesses d'écoulement où le couplage se produit. Toutefois, ces solutions peuvent également minimiser les performances de la surface portante, ce qui est souvent incompatible avec les applications pour lesquelles l'optimisation des performances est une préoccupation majeure. Des systèmes plus avancés, tels que le contrôle du sillage

par génération d'ondes acoustiques ou le soufflage et l'aspiration de la couche limite, ont également été étudiés et ont fourni des solutions prometteuses, mais nécessitent en contrepartie l'intégration de systèmes complexes souvent inadaptés aux dispositifs marins. Compte tenu du haut niveau d'exigence propre aux applications marines modernes, il est nécessaire de développer des dispositifs d'atténuation des vibrations qui soient hautement adaptables, robustes et faciles à intégrer sur différents types de structures. Les systèmes basés sur les matériaux piézoélectriques répondent à ces exigences.

La piézoélectricité est la capacité de certains matériaux à générer un champ électrique lorsqu'une force mécanique leur est appliquée et, inversement, à générer une déformation s'ils sont exposés à un champ électrique. Depuis la découverte de la piézoélectricité à la fin du 19$^{\text{ème}}$ siècle, les processus de fabrication des matériaux piézoélectriques ont connu une formidable évolution donnant lieu à de multiples applications industrielles telles que les capteurs acoustiques et de pression, les actionneurs mécatroniques, les sonars et, comme présenté dans cette étude, les dispositifs d'atténuation des vibrations. Une étape importante a été franchie avec le développement des céramiques piézoélectriques et, plus récemment, des composites piézoélectriques. Les transducteurs basés sur ces matériaux sont constitués de fines plaques déformables et robustes grâce à une coque protectrice encapsulante. Ces propriétés permettent une intégration aisée sur diverses structures complexes telles-que les pales d'hélice ou les hydrofoils. L'atténuation des vibrations peut être obtenue lorsqu'un transducteur piézoélectrique est connecté à une inductance et à une résistance. Ce circuit électrique simple est appelé shunt résonant passif et est basé sur l'accord d'une fréquence électrique avec une fréquence mécanique pour atteindre un transfert d'énergie optimal. Les shunts ont démontré des niveaux d'atténuation des vibrations conséquents pour les applications dans l'air et sont simples à mettre en œuvre. Cependant, peu d'essais ont été réalisés pour atténuer les vibrations dans l'eau et/ou sous écoulement. L'acquisition de nouvelles connaissances dans cette configuration permettra d'utiliser des shunts piézoélectriques résonants pour les surfaces portantes marines et offrira un système efficace pour réduire les vibrations induites par l'écoulement.

Objectifs de l'étude

L'objectif principal de cette étude est la conception et l'essai d'un dispositif d'atténuation des vibrations de type shunt piézoélectrique résonant passif intégré à une surface portante placée sous écoulement d'eau. Pour atteindre cet objectif, deux axes ont été développés. Le premier axe consiste en une étude expérimentale des phénomènes hydrodynamiques conduisant à des vibrations de grande amplitude subies par des structures de fort allongement placées dans un écoulement à nombre de Reynolds élevé. À cette fin, deux structures différentes ont été immergées dans le tunnel hydrodynamique de l'École Navale. La première structure étudiée consiste en une plaque plane en aluminium de section rectangulaire dont le rapport corde/épaisseur est de 16,7. La seconde structure est un hydrofoil tronqué en aluminium de type NACA 66-306 dont le rapport corde/épaisseur est de 13,9. Les deux structures sont étudiées à incidence nulle avec un nombre de Reynolds basé sur la corde compris entre $2,5 \times 10^5$ et $9,5 \times 10^5$ (correspondant à des vitesses d'écoulement comprises entre 2,5 et 9,5 m.s^{-1}). La dynamique du sillage, le lâché tourbillonnaire et les vibrations structurelles ont été étudiés grâce à la vélocimétrie par images de particules résolue en temps (TR-PIV) et la vibrométrie laser. Bien que ces types de structures ont de nombreuses applications industrielles, il semble que peu d'études aient porté sur les vibrations d'origine hydrodynamiques de corps allongés placés dans un écoulement à haut Reynolds. En effet, la physique propre à ces configurations est complexe en raison de l'interaction de divers phénomènes hydrodynamiques et structurels. Afin d'obtenir de nouveaux résultats, des méthodes d'analyse avancées ont été utilisées, à savoir la décomposition orthogonale propre (POD) et sa variante spectrale (SPOD), ainsi que des algorithmes de détection des tourbillons et des outils d'analyse statistique et spectrale. La compréhension précise de l'interaction fluide-structure conduisant aux vibrations permettra d'améliorer les performances des structures marines et d'accroître l'efficacité des dispositifs d'atténuation des vibrations.

Le deuxième axe est consacré au développement d'un shunt passif résonant basé sur des transducteurs piézoélectriques intégrés à l'hydrofoil tronqué. Ce dispositif est autonome en termes d'énergie et offre une grande simplicité d'intégration pour diverses structures marines. Des essais expérimentaux ont été réalisés dans différentes configurations : en air et en eau sans écoulement puis à différentes vitesses d'écoulement. Une attention particulière a été accordée à l'atténuation du premier mode de torsion en eau. À notre connaissance, ce type de vibration n'a jamais été atténué à l'aide d'un shunt

piézoélectrique résonant passif. Pour atteindre le niveau d'atténuation maximal, un réglage précis des paramètres du shunt est nécessaire. Pour faciliter cette tâche, un modèle numérique de l'hydrofoil équipé de transducteurs piézoélectriques et connecté à un shunt résonant passif a été construit à l'aide du logiciel COMSOL *Multiphysics*. Cette approche basée sur la méthode des éléments finis permet notamment d'éviter des essais expérimentaux longs et coûteux ainsi que de limiter les modifications post-fabrication. Cet outil facilitera grandement la conception de futurs prototypes d'hydrofoils.

Le chapitre 1 du manuscrit consiste en une introduction générale et une revue de la littérature. Le dispositif expérimental et les méthodes d'analyse sont introduits dans le chapitre 2. Les principaux résultats sont ensuite exposés. Le chapitre 3 présente une analyse des interactions fluide-structure subies par des corps de grand allongement. Le chapitre 4 est dédié à l'atténuation des vibrations d'un hydrofoil par shunt piézoélectrique résonant. Le chapitre 5 présente l'impact d'une atténuation de vibration sur le sillage proche d'un hydrofoil. Des conclusions et des perspectives de recherche sont ensuite apportées.

Interactions fluide-structure de corps de grand allongement

La première partie de l'étude porte sur une analyse du détachement tourbillonnaire et des vibrations subies par une plaque plane de section rectangulaire. Des expériences ont été menées à incidence nulle pour des nombres de Reynolds Re_c (basés sur la corde) compris entre 2.5×10^5 et 9.5×10^5 induisant un sillage turbulent. A partir des champs de vecteurs obtenus par vélocimétrie à image de particules, les propriétés hydrodynamiques du sillage ont été évaluées par analyse statistique, décomposition orthogonale propre et identification des tourbillons. La réponse structurelle de la plaque a été mesurée par vibrométrie laser au moyen d'une analyse modale. Les interactions fluide-structure ont été analysées pour trois régimes de vibration différents : hors résonance, résonance sans accrochage et résonance avec accrochage avec le premier mode de torsion. Les caractéristiques des neuf premiers modes POD ont été étudiées en fonction des différents régimes de vibration afin de comprendre la physique propre au sillage proche.

La figure 1 présente une cartographie de la densité spectrale issue des signaux de vitesse de vibration mesurés par vibrométrie laser à différents nombres de Reynolds. Cette cartographie est représentative de la réponse vibratoire de la plaque et permet d'identifier les différents régimes de vibration.

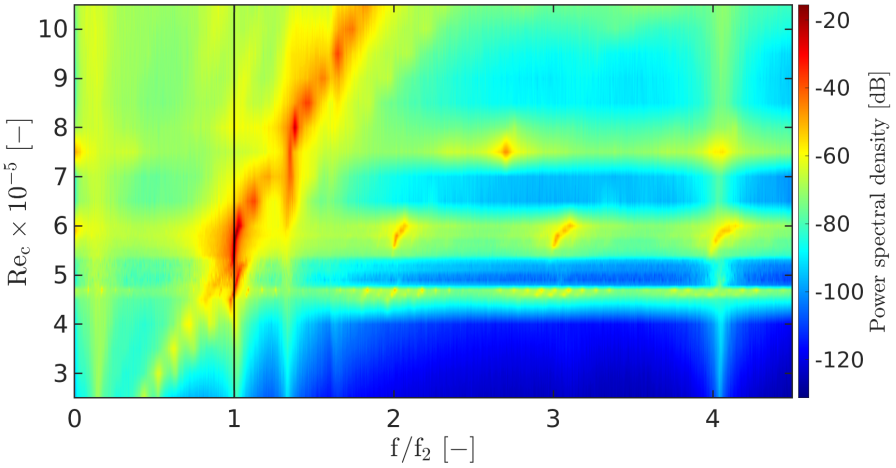

Figure 1: Cartographie spectrale de la vitesse de vibration de la plaque plane de section rectangulaire. Cartographie exprimée dans le plan (f_s/f_2, Re_c). Densité spectrale exprimée en dB. f_2 correspond à la fréquence propre du premier mode de torsion.

Deux sources d'excitation hydrodynamiques dont le nombre de Strouhal est différent sont également présentes. Ces sources d'excitation peuvent être attribuées à la coexistence de deux mécanismes d'excitation, un rapport corde/épaisseur de 16.7 étant à la transition entre deux régimes d'excitation. La source d'excitation primaire, identifiée comme étant l'instabilité de bord de fuite, consiste en un lâché tourbillonnaire primaire de Karman dont le nombre de Strouhal caractéristique est $St_{D1} = 0,195$. La source d'excitation secondaire, identifiée comme l'instabilité de la couche de cisaillement, est attribuée à un bord d'attaque rectangulaire. Celle-ci correspond à un nombre de Strouhal $St_{D2} = 0.227$. Les zones de densité spectrale maximale de la figure 1 sont notamment associées à des régimes de résonance caractéristiques de vibrations de forte amplitude. Trois régimes de vibration ont ainsi été mis en évidence : la non-résonance ($Re_c = 3,0 \times 10^5$), la résonance sans accrochage ($Re_c = 4,8 \times 10^5$) et la résonance avec accrochage ($Re_c = 5,7 \times 10^5$). Lors de la résonance sans accrochage, la source d'excitation secondaire se synchronise avec la fréquence propre du mode de torsion, ce qui entraîne un maximum local de l'amplitude de vibration. Dans le sillage, ce régime est caractérisé par la coexistence de deux modes distincts de lâché tourbillonnaire de Karman de Strouhals respectifs St_{D1} et St_{D2}. À notre connaissance, un tel régime de résonance sans accrochage n'a pas été analysé par le passé. Ce régime est particulièrement important pour la conception de structures soumises à des vibrations d'origine hydrodynamique, car il implique l'apparition précoce d'un régime de résonance. En conséquence, des vibrations de grande amplitude peuvent apparaître pour une gamme de Reynolds

et de vitesses réduites plus large que celle attendue pour la résonance avec accrochage. Les amplitudes de vibration les plus élevées ont été observées pendant le régime de résonance avec accrochage pour lequel la source d'excitation primaire se synchronise avec la fréquence naturelle du mode de torsion, ce qui entraîne un fort couplage fluide-structure. Ce régime se caractérise par un élargissement du sillage et une augmentation de la contribution à l'énergie cinétique turbulente totale des harmoniques du lâché tourbillonnaire primaire de Karman. Un autre point intéressant est l'émergence, dans les modes les plus énergétiques, d'une structure associée à une bulle de recirculation basse fréquence pour tous les régimes de résonance (résonance sans accrochage et résonance avec accrochage). Ceci est cohérent avec les observations de Miyanawala et al. [128]. Les figures 2 et 3 présentent les champs de vorticité associés aux neuf premiers modes POD respectivement pour le régime de résonance sans accrochage et pour le régime de résonance avec accrochage. Pour chaque mode POD, la contribution au niveau d'énergie global est précisée.

Pour le régime de non-résonance, une attention particulière a été accordée à la caractérisation du phénomène de lâché tourbillonnaire de Karman associé au Strouhal St_{D1} à partir des deux premiers modes POD. En particulier, la fréquence de lâché, ainsi que la taille et la circulation des tourbillons ont été évalués en fonction du nombre de Reynolds. Cette caractérisation est utile pour une modélisation d'ordre réduit du sillage permettant de faciliter la compréhension des phénomènes physiques sous-jacents. Il est intéressant de noter que la taille et la circulation des tourbillons de Karman semblent être contrôlés par deux paramètres qui sont les nombres de Strouhal et de Reynolds et cela quelle que soit la géométrie du bord de fuite et le rapport corde/épaisseur. Le nombre de Strouhal mesuré $St_D = 0.195$ est en accord avec le nombre de Strouhal observé dans la littérature pour des plaques de grand allongement.

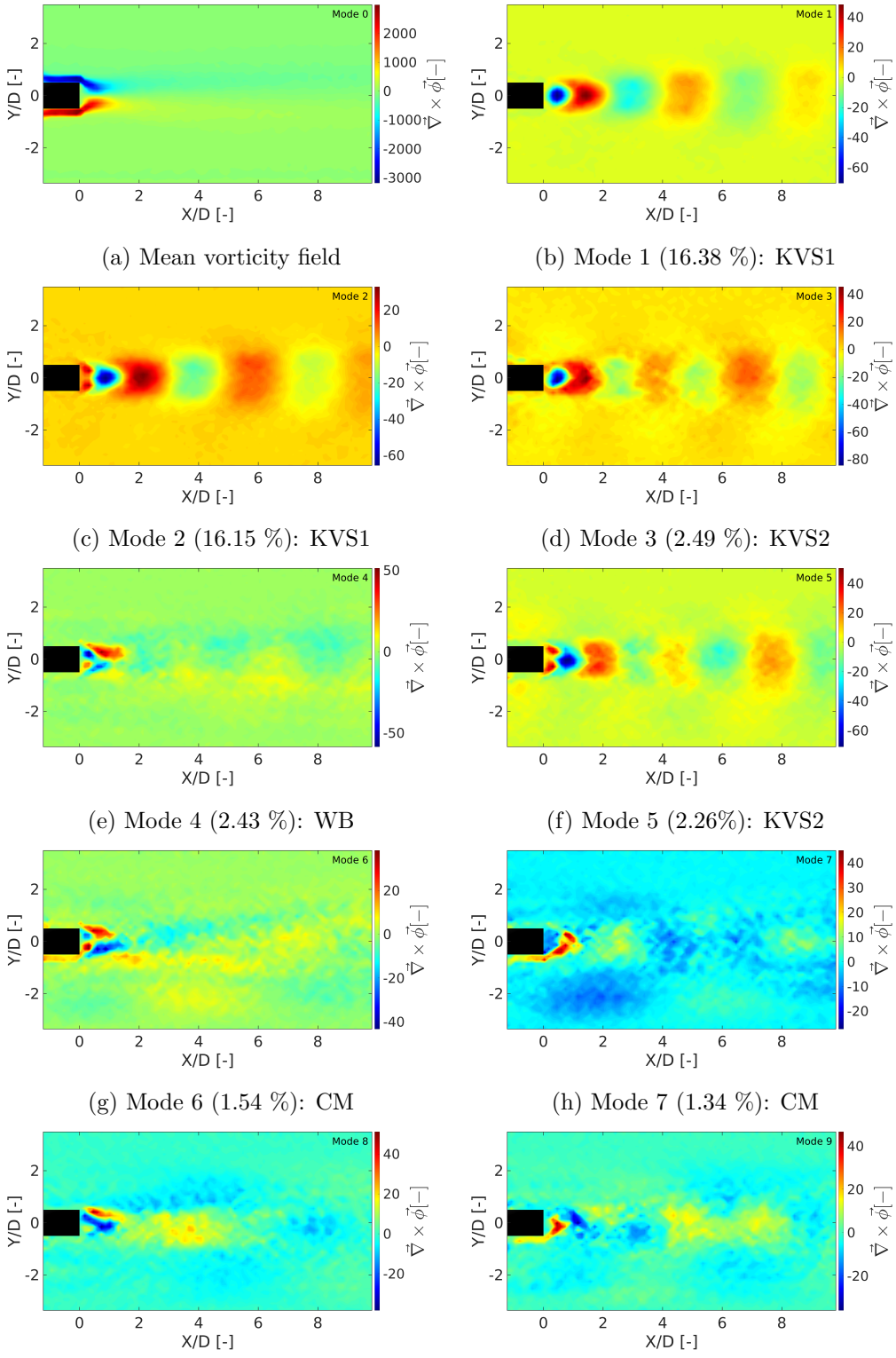

(a) Mean vorticity field

(b) Mode 1 (16.38 %): KVS1

(c) Mode 2 (16.15 %): KVS1

(d) Mode 3 (2.49 %): KVS2

(e) Mode 4 (2.43 %): WB

(f) Mode 5 (2.26%): KVS2

(g) Mode 6 (1.54 %): CM

(h) Mode 7 (1.34 %): CM

(i) Mode 8 (1.23 %): CM

(j) Mode 9 (1.11 %): CM

Figure 2: Cartographies (x, y) du champ de vorticité généré par la plaque rectangulaire. Champ de vorticité moyen et modes POD de 1 à 9 à $U_0 = 4.8$ m.s^{-1} ($Re_c = 4.8 \times 10^5$, régime de résonance sans accrochage).

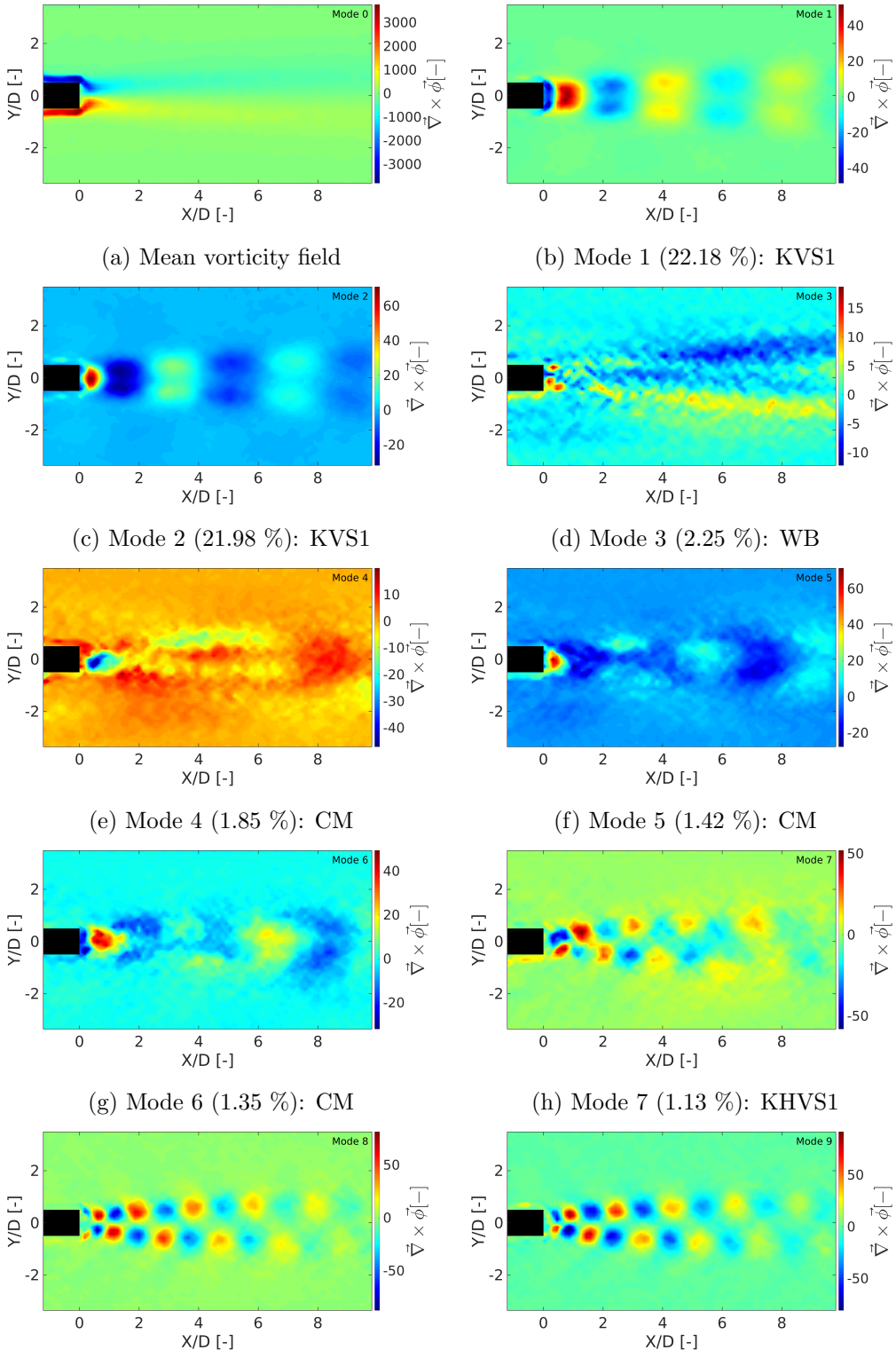

(a) Mean vorticity field

(b) Mode 1 (22.18 %): KVS1

(c) Mode 2 (21.98 %): KVS1

(d) Mode 3 (2.25 %): WB

(e) Mode 4 (1.85 %): CM

(f) Mode 5 (1.42 %): CM

(g) Mode 6 (1.35 %): CM

(h) Mode 7 (1.13 %): KHVS1

(i) Mode 8 (1.09 %): KHVS1

(j) Mode 9 (1.09 %): KHVS1

Figure 3: Cartographies (x, y) du champ de vorticité généré par la plaque rectangulaire. Champ de vorticité moyen et modes POD de 1 à 9 à $U_0 = 5.7$ m.s^{-1} ($Re_c = 5.7 \times 10^5$, régime de résonance avec accrochage).

Atténuation des vibrations d'un hydrofoil par shunt piézoélectrique résonant

La seconde partie de l'étude est consacrée à l'atténuation des vibrations induites par l'écoulement sur l'hydrofoil au moyen d'un shunt piézoélectrique résonant passif. L'hydrofoil est équipé de deux patchs piézoélectriques DuraAct utilisés pour l'excitation du foil en absence d'écoulement et d'un patch piézoélectrique MFC dédié au contrôle et à l'atténuation des vibrations. Un modèle numérique de l'hydrofoil a été réalisé à l'aide du code de calcul par éléments finis COMSOL *Multiphysics*. L'objectif de cette partie de l'étude est d'obtenir un outil de conception précis pour prédire les fréquences propres et les facteurs de couplage de structures équipées de patchs piézoélectriques. Une attention particulière a été accordée à la modélisation des propriétés piézoélectriques de la couche active du patch MFC. Sa modélisation est en effet plus complexe et nécessite un recalage des propriétés piézoélectriques. Le tableau 1 présente les fréquences propres calculées ainsi que les facteurs de couplage calculés et expérimentaux. Les résultats numériques et expérimentaux se sont avérés être en bon accord, ce qui permet de valider le modèle numérique. Un shunt passif résonant a également été simulé avec COMSOL afin de prédire les fonctions de réponse en fréquence des vibrations de l'hydrofoil couplé au shunt. Cela permet d'ajuster simplement les paramètres du shunt afin d'évaluer l'atténuation de vibration maximale atteignable. L'utilisation de cet outil numérique permet d'éviter des investigations expérimentales souvent coûteuses et permet d'anticiper une configuration optimale des shunts résonants. Deux types de shunts résonants ont été testés: un shunt à inductance synthétique et un shunt a inductance bobinée. La capacité des deux circuits à atténuer les vibrations de l'hydrofoil a été caractérisée expérimentalement par vibrométrie laser dans l'air et dans l'eau à une vitesse d'écoulement nulle et à différentes vitesses d'écoulement.

L'étude a montré que le shunt à inductance synthétique permet une variation aisée de l'inductance et de la résistance interne du circuit. Cependant, ce système est limité à de faibles niveaux de vibration car les composants électroniques constitutifs, notamment les amplificateurs opérationnels, ne sont pas en mesure de supporter une tension élevée. Les figures 4a et 4b présentent les foncions de réponse en fréquence obtenues lorsque le patch piézoélectrique MFC intégré à l'hydrofoil est en circuit ouvert, en court-circuit et lorsque celui-ci est connecté au shunt à inductance synthétique. La figure 4a correspond à des mesures en air et la figure 4b à des mesures en eau. Pour ces deux configurations, la vitesse d'écoulement est nulle et des vibrations forcées sont générées par les patchs DuraAct intégrés

	Air			Eau		
	f_n^{num}	kc_n^{num}	kc_n^{exp}	f_n^{num}	kc_n^{num}	kc_n^{exp}
MFC						
	f_1^{cc}=87.688 Hz f_1^{co}=87.718 Hz	3.04%	3.3%	f_1^{cc}=38.416 Hz f_1^{co}=38.434 Hz	3.10%	3.70%
	f_2^{cc}=517.412 Hz f_2^{co}=519.572 Hz	9.15%	9.2%	f_2^{cc}=284.58 Hz f_2^{co}=285.54 Hz	8.20%	8.50%
	f_3^{cc}=629.710 Hz f_3^{co}=629.925 Hz	2.61%	2.6%	f_3^{cc}=301.91 Hz f_3^{co}=302.28 Hz	4.95%	4.70%
DuraAct Flexion						
	f_1^{cc}=87.678 Hz f_1^{co}=88.689 Hz	15.23%	15.0%	f_1^{cc}=38.416 Hz f_1^{co}=38.860 Hz	15.25%	N.C.
	f_2^{cc}=517.411 Hz f_2^{co}=517.412 Hz	0.14%	0.5%	f_2^{cc}=284.583 Hz f_2^{co}=284.586 Hz	0.47%	N.C.
	f_3^{cc}=629.710 Hz f_3^{co}=629.712 Hz	0.19%	1.8%	f_3^{cc}=301.911 Hz f_3^{co}=301.922 Hz	0.88%	N.C.

Table 1: Fréquences propres en circuit-ouvert f_{co} et court-circuit f_{cc} et facteurs de couplage k_c associés obtenus par calcul numérique. Comparaison avec les résultats experimentaux (f_1, f_2, f_3 : fréquences naturelles du 1^{er} mode de flexion, 1^{er} mode de torsion, 2^{eme} mode de flexion respectivement.).

à l'hydrofoil. Le premier mode de torsion est atténué de 31 dB (équivalent à diviser l'amplitude par 36) en air et de 21 dB (équivalent à diviser l'amplitude par 11) en eau.

Afin de s'affranchir des limitations propres au shunt à inductance synthétique, un shunt à inductance bobinée a été investigué. Celui-ci est apte à atténuer des vibrations de forte amplitude telles que celles induites par l'écoulement et entraînant un niveau de tension élevé aux bornes du patch piézoélectrique. Cependant, ce type de shunt nécessite un dimensionnement précis de la bobine car il est complex de modifier l'inductance après la fabrication de la bobine. Un faible ajustement est néanmoins possible grâce à une vis intégrée à la bobine. Ce type de shunt a été testé avec l'hydrofoil placé sous écoulement. La figure 5a présente les signaux de vitesse de vibration en configuration shunt non-activé et activé mesurés par vibrométrie laser (pour $Re_c = 3.74 \times 10^5$) lors du régime résonant avec accrochage au premier mode de torsion qui est caractérisé par des vibrations de très grande am-

plitude. Une réduction de 59% de la valeur RMS du signal de vibration est observée lorsque le shunt est activé. Par la suite, le shunt à inductance bobinée a été testé à différents nombres de Reynolds associés à différents régimes vibratoires non résonants et résonants. D'après la figure 5b, il apparait que ce type de shunt offre un niveau de réduction vibratoire notable pour une gamme de Reynolds comprise entre 2.98×10^5 et 4.68×10^5.

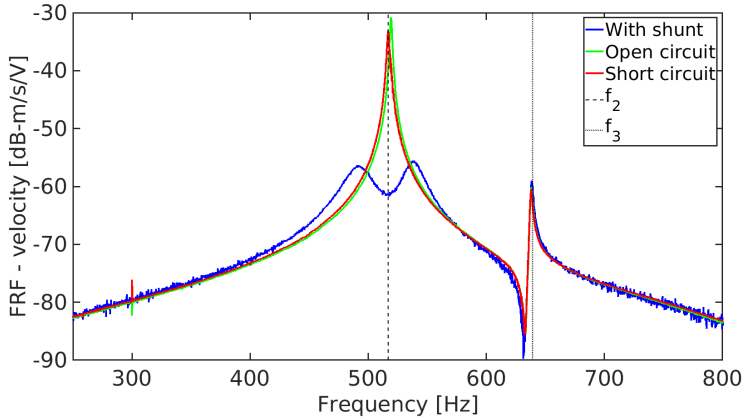

(a) air

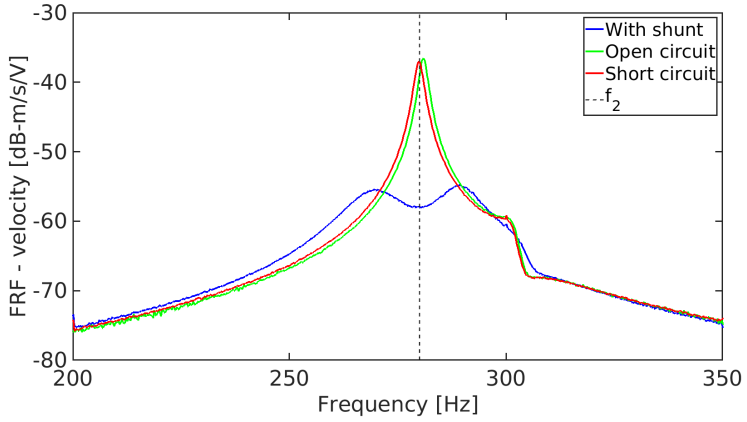

(b) water

Figure 4: Fonctions de réponse en fréquence lorsque le patch MFC est branché en court circuit, circuit ouvert et lorsque le shunt à inductance synthétique est activé. Configuration en air (a) et en eau (b). Zéro vitesse d'écoulement et vibrations forcées par les patch DuraAct intégrés à l'hydrofoil.

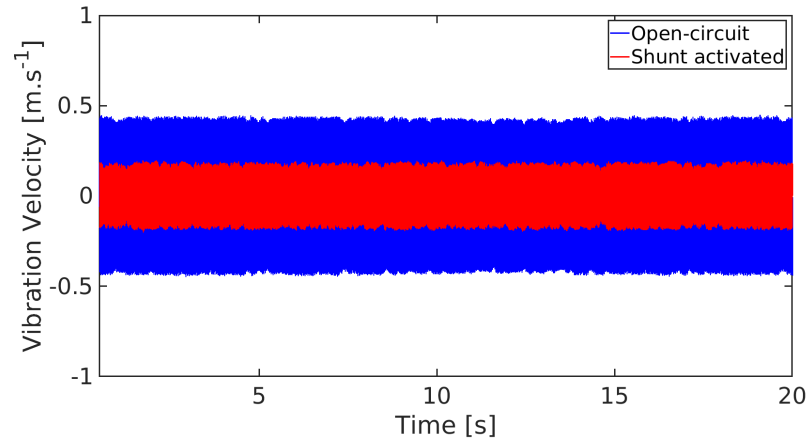

(a)

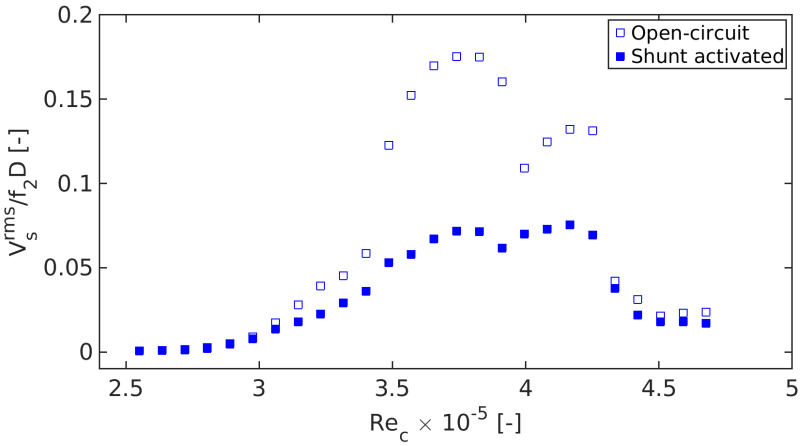

(b)

Figure 5: (a) Évolution temporelle de la vitesse de vibration à $U_0 = 4.4$ m.s^{-1} ($Re_c = 3.74 \times 10^5$, régime d'accrochage) en circuit-ouvert et lorsque le shunt à inductance bobinée est activé. (b) Evolution de l'écart type de la vitesse vibratoire V_s^{rms} de l'hydrofoil avec le nombre de Reynolds.

Impact d'une atténuation de vibration sur le sillage proche d'un hydrofoil

Les méthodes POD et SPOD ont été employées pour étudier l'impact de l'atténuation des vibrations du shunt piézoélectrique sur le mécanisme d'instabilité du sillage. Lorsque l'hydrofoil est placé sous écoulement, différents régimes vibratoires ont été identifiés : régime non-résonant, résonance et accrochage avec le premier mode de torsion f_2, le second mode de flexion f_3. La figure 6 montre la cartographie en Reynolds de la densité spectrale de vitesse vibratoire de l'hydrofoil, avec (figure 6a) et sans (figure 6b) shunt activé. Lors du régime de non-résonance, le lâché tourbillonnaire de Karman

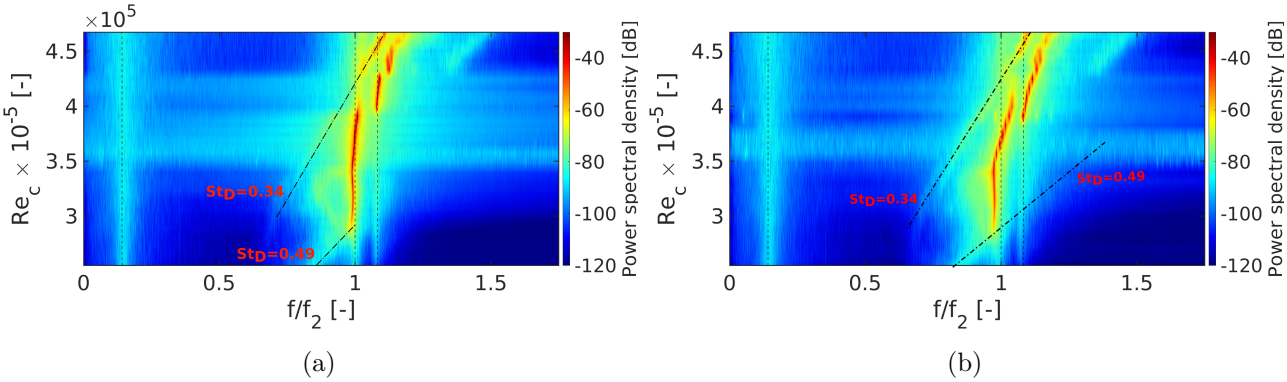

Figure 6: Cartographie spectrale de la vitesse de vibration de l'hydrofoil, avec (a) et sans (b) shunt activé. Cartographie exprimée dans le plan $(f_s/f_2,\ Re_c)$. Densité spectrale exprimée en dB. f_2 correspond à la fréquence propre du premier mode de torsion

est caractérisé par un contenu fréquentiel large bande. Lors de l'accrochage avec le premier mode de torsion, la déformation de la structure consiste principalement en une déformée en torsion qui tend à réorganiser le sillage proche. L'activation du shunt induit une transition plus douce entre les différents régimes d'accrochages et une gamme plus réduite de nombres de Reynolds où la résonance avec accrochage avec le premier mode de torsion se produit. Par la suite, les propriétés hydrodynamiques du sillage proche de l'hydrofoil ont été caractérisées par TR-PIV pour les configurations de shunt activé et non activé. L'analyse statistique en moyenne temporelle montre que la taille de la bulle de recirculation à proximité du bord de fuite est significativement réduite pendant l'accrochage avec le premier mode de torsion. La traînée augmente pour ce régime, ce qui implique que les performances globales de l'hydrofoil sont légèrement réduites lorsque des vibrations de grande amplitude se produisent. Le shunt a tendance à augmenter la taille de la bulle de recirculation tout en réduisant la traînée, ce qui offre des possibilités prometteuses d'amélioration des performances globales des surfaces portantes et ouvre la voie à diverses applications industrielles.

Les méthodes d'analyse SPOD et POD ont été mises en œuvre pour identifier les structures cohérentes dans le sillage proche de l'hydrofoil et caractériser ainsi la dynamique du sillage aux différents régimes vibratoires avec et sans shunt activé. Les figures 7a et 7b présentent les spectres d'énergie des différents modes SPOD aux régimes de non-résonance et d'accrochage sans shunt activé. Le regime de non-résonance est caractérisé par deux pics large bande dont l'amplitude maximale correspond à des nombres de Strouhal $St_D = 0.49$ et $St_D = 0.98$. Les distributions spatiales associées à ces nombres de Strouhal et présentées par les figures 7c et 7d sont représentatives de structures de type lâché

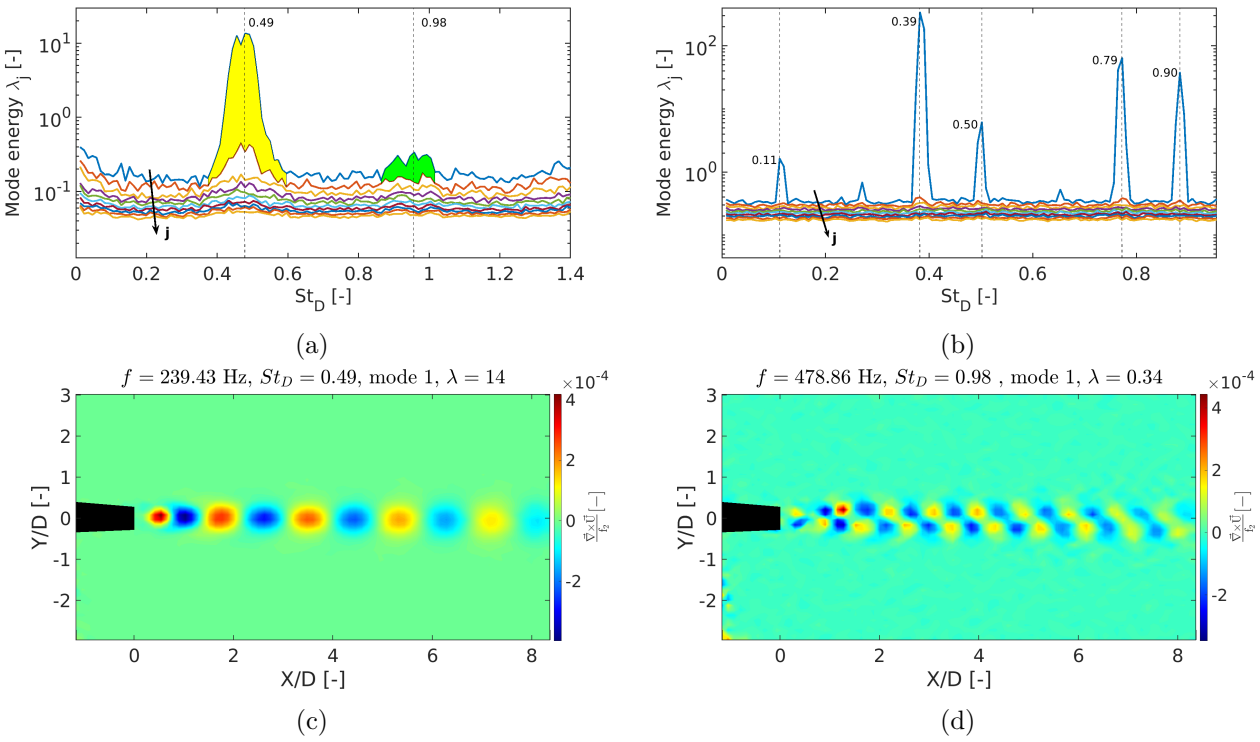

Figure 7: Enérgie des modes SPOD associée à (a) un régime non-résonant et (b) un régime d'accrochage vibratoire. Cartographies (x,y) du champ de vorticité associées au structures cohérentes les plus énergétiques du sillage identifiées par la méthode SPOD. $U_0 = 3.0$ m.s^{-1} ($Re_c = 2.55 \times 10^5$), régime non résonant. La figure (c) correspond à au phénomène de lâché tourbillonnaire de Karman et la figure (b) est associée à l'harmonique du lâché tourbillonnaire de Karman.

tourbillonnaire de Karman et son harmonique. Ces structures cohérentes sont la principale source d'excitation agissant sur la structure. Lors de l'accrochage avec le premier mode de torsion, le lâché de Karman et son harmonique sont renforcés et présentent des fréquences faibles bandes très marquées comme illustré par la figure 7b. Lorsque le shunt est activé, l'organisation générale du sillage proche n'est pas radicalement modifiée. Cependant pour le régime résonant avec accrochage avec le premier mode de torsion, l'activation du shunt rend les modes POD 1 et 2, représentatifs du lâché de Karman, moins corrélés en phase et le contenu multifréquentiel est réintroduit. Le tableau 2 présente l'impact du shunt sur les principales caractéristiques des tourbillons de Karman lors du régime d'accrochage. La taille des tourbillons de Karman est légèrement réduite, tandis que la circulation est réduite de 10%, ce qui tend à diminuer la composante fluctuante de la force de portance.

	Sans shunt	**Sh activéunt**
Position des tourbillons		
Vortex 3	X = 10.6 mm, Y = 0.14 mm	X = 11.3 mm, Y = −0.01 mm
Vortex 4	X = 16.78 mm, Y = −0.10 mm	X = 17.58 mm, Y = −0.08
Vortex 5	X = 23.10 mm, Y = −0.21 mm	X = 24.17 mm, Y = −0.29 mm
Surface des tourbillons		
Vortex 3	14.0 mm^2	13.0 mm^2
Vortex 4	15.6 mm^2	15.0 mm^2
Vortex 5	17.2 mm^2	16.0 mm^2
Rayon des tourbillons		
Vortex 3	2.1 mm	2.0 mm
Vortex 4	2.2 mm	2.2 mm
Vortex 5	2.3 mm	2.3 mm
Circulation des tourbillons		
Vortex 3	−2.06 $m^2.s^{-1}$	1.88 $m^2.s^{-1}$
Vortex 4	2.02 $m^2.s^{-1}$	−1.92 $m^2.s^{-1}$
Vortex 5	−1.99 $m^2.s^{-1}$	1.79 $m^2.s^{-1}$
Rapport d'aspect du sillage		
b_s/a_s	0.19	0.15

Table 2: Caractéristiques des tourbillons de Karman associés au mode POD 1. Accrochage avec le premier mode de torsion f_2 ($U_0 = 4.4\ m.s^{-1}$). Comparaison entre la configuration avec shunt activé et non-activé. b_s/a_s est le rapport d'aspect du sillage de Karman, rapport entre la distance normale et longitudinale entre les tourbillons successifs du sillage de Karman.

Conclusion

De nombreuses structures navales sont caractérisées par un grand allongement et un rapport d'aspect élevé. Pour ce type de structure, l'étude a permis de mettre en évidence la coexistence de deux types d'instabilités, notamment l'instabilité de bord de fuite et l'instabilité de la couche cisaillée due au détachement de la couche limite au bord d'attaque. Ces instabilités agissent comme des sources d'excitation vibratoires et sont à l'origine de deux régimes résonants différents : la résonance sans accrochage et la résonance avec accrochage. Afin d'atténuer les vibrations de forte amplitude propres aux régimes résonnants, un système de type shunt piézoélectrique résonant a été investigué expérimentalement et numériquement. Deux types de shunts ont été testés : le shunt à inductance bobinée et le shunt à inductance synthétique. Ces deux systèmes ont démontré des niveaux élevés d'atténuation des vibrations et sont simples, peu onéreux et adaptables, ce qui les rend particulièrement adaptés pour des applications marines. Cependant, seul le shunt à inductance bobinée peut

réduire les forts niveaux vibratoires associés au couplage de la structure avec les instabilités hydrodynamiques de bord de fuite. Un modèle numérique d'un hydrofoil équipé de patchs piézoélectriques et connecté à un shunt résonant a été modélisé avec les codes éléments finis COMSOL Multiphysics afin de prédire les modes propres de la structure, les facteurs de couplage et les paramètres du shunt. Ces simulations offrent un outil très efficace pour concevoir des structures équipées de patchs piézoélectriques. L'impact du shunt sur les caractéristiques du sillage proche de l'hydrofoil a finalement été étudié et a permis de mettre en évidence les effets d'une réduction vibratoire sur les propriétés hydrodynamiques. Cette étude ouvre la voie pour de nombreuses applications industrielles dans le domaine naval et maritime.

Contents

List of Tables

List of Figures

Chapter 1

General Introduction

“ La Terre est bleue comme une orange. ”

Paul Éluard

Content

1.1 Problem overview

Fluid-structure interaction (FSI) is defined as a bi-directional energy transfer in a domain composed of both fluid and solid. Among multiple engineering disciplines affected by FSI, flow-induced vibrations (FIV) appear to be crucial for the design of efficient and sustainable marine structures. Solid bodies, when placed in a steady flow at high Reynold number, induce hydrodynamic instabilities which are responsible for periodic and alternative vortex shedding. The pressure field in the near-wake of the body is directly impacted by the asymmetric inception of vortices leading to fluctuating lift and drag forces. This mechanism acts as a structural excitation source and is responsible for the body vibrations. When the vortex shedding frequency coincides with a natural frequency of the structure or one of its harmonics, a drastic increase of the vibration magnitude occurs. The instability mechanism leading to vortex shedding may couple with the body motion in case of high magnitude vibrations resulting in the synchronization of the vortex shedding frequency with the vibration frequency on a broad range of free-stream velocities. This phenomenon, known as lock-in, may have dramatic consequences for various engineering applications. The mechanism leading to vortex induced vibrations is particularly complex at high Reynolds number and in case of separated and reattached turbulent flows. Reattached turbulent flows are encountered for bodies of large chord-to-thickness ratio such as flat plates, hydrofoils or propeller blades. For these kinds of flows, the coupling between the leading-edge separation and the shedding vortices in the wake is much more complex than in strongly separated flows. When fluid–structure coupling occurs, the physical understanding and the modelling of these kinds of flows are still challenging.

Flow-induced vibrations interfere in various industrial systems, especially in the marine domain. The drastic growth of the world naval fleet in light of recent geopolitical events has put acoustic stealth concerns back at the forefront of research and engineering innovation. Structural vibrations are responsible of acoustic wave propagation in the fluid domain which may travel in the far-field if their energy is high enough, leading to a drastic increase of vessel's acoustic trace [22]. Reduction of flow-induced vibrations of propeller blades, rudders and fins is a major challenge for naval engineering. In the domain of marine wildlife preservation, the reduction of noise induced by human activities named anthropogenic noise, is also a major concern. Since the 1950's, the number of vessels sailing across the oceans has exploded due to global marine trade leading to excessive noise pollution. Many marine

organisms depend on the interpretation of acoustic information of their surrounding environment for their survival. Thus, noise pollution can affect marine organism's acoustic communication through auditory masking and through physiological damage of the hearing system [23, 24]. Nowadays, the reduction of noise pollution becomes a key consideration for the environmental politics of various states, for example the European legislation favours noise pollution reduction through the European Marine Strategy Framework Directive [25, 26]. These directives are of great relevance as numerous new types of marine vehicles navigate among the oceans at velocities prone to generate intense noise radiation.

Over the last decade, marine lifting surfaces have known a tremendous development in the field of nautical sports. New disciplines such as wing foil, kite foil, surf foil and windsurf foil have emerged, all based on the integration of hydrofoils on various types of surf boards. These devices have broadly contributed to the fast development of high efficiency, lightweight and competitive hydrofoils aiming to break world speed records or win international championships such as the Olympic games. The domain of competitive sailing has also been deeply impacted by the integration of lifting surfaces among the yachts hull's. Most of last generation mono and multihulls yachts use hydrofoils to lift their hull above the sea surface and drop down the hull resistance to reach maximal speed. Flow-induced vibrations are of prime importance for these applications because the reached velocities coincide with Reynolds numbers where hydrodynamic instabilities may couple with natural frequencies of the hydrofoils. Also, the increasing use of lightweight materials such as fibreglass composites or carbon may result in delamination of the material fibres due to the vibrations. Structural fatigue, resulting from high magnitude vibrations, may lead to early deterioration of the hydrofoils and the ship structure. Also, the comfort of last generation sailing yachts has been substantially reduced due to the acoustic noise radiated by the lifting surfaces. Nowadays, many professional sailors use noise-cancelling headphones to avoid the piercing tones induced by the underwater appendages which leads to early exhaustion and reduces the watch-keeping attentiveness.

In a different context, the increasing demand of energy by governments and the need for environmental friendly sources has contributed to the fast development of marine renewable energies. Most of the hydro-kinetic and hydro-generation power plants are composed of structural elements and impellers, often located in strong current regions prone to cause FIV. In a more general way, hydraulic machinery consisting of turbines and pumps containing stay and guide vanes are also strongly im-

pacted by FIV [11]. For these devices, post manufacturing modifications or repairs will often result in prohibitive expenses due to the remote location and the overall complexity of the systems. Also, onboard ships, many equipments are composed of rotatory pumps. The high rotation speed of their impellers is often prone to FSI occurrence and may lead to early wear and acoustic radiation which is particularly annoying for naval applications.

The list of industrial applications impacted by FSI developed in the present section is far from being exhaustive and demonstrates that FSI interferes in various mechanical systems. Over the years many research projects have investigated, both experimentally and numerically, the mechanism leading to FSI in order to find solutions to reduce the vibrations. Commonly adopted vibration mitigation methods consist in the modification of existing structures by suppression or addition of material in order to decouple the natural frequencies from hydrodynamic excitation sources. A different approach consists in modifying the geometry to alter the hydrodynamic instabilities. For example, the modification of a hydrofoil trailing-edge is able to drastically reduce the vibration magnitude and the range of flow velocities where coupling occurs [27, 28]. However, these solutions may also minimize the performance of the lifting surface which is often incompatible for applications where efficiency optimization is a major concern. More advanced systems such as wake control by acoustic waves generation [29] or boundary layer blowing and suction [30, 31], have also been investigated and provided promising solutions but in counterpart require the integration of complex systems often not adapted for marine devices. Regarding the high requirement level proper to modern marine applications, it is necessary to develop vibration mitigation devices which are highly adaptative, robust and easy to integrate on various types of structures. Systems based on piezoelectric materials may handle with these requirements.

Piezoelectricity is the ability of certain materials to generate an electric field when a mechanical force is applied and reversely to generate a deformation if it is exposed to an electric field. Since its discovery at the end of the 19^{th} century, manufacturing processes of piezoelectric materials have known a tremendous evolution giving rise to multiple industrial applications such as acoustic and pressure sensors, mechatronic actuators, sonars and, as presented through this study, for vibration mitigation devices. A major milestone was reached with the development of piezoceramics and more recently of piezocomposites. Transducers based on these materials consist of thin patches which are highly deformable and robust due to an encapsulating protective shell. These properties enable easy

integration on various complex structures such as propeller blades or hydrofoils. Vibration mitigation can be achieved when a piezoelectric transducer is connected to an inductor and a resistor. This simple electrical circuit is named a passive resonant shunt and is based on the tuning of an electrical frequency with a mechanical frequency to reach optimal energy transfer. Shunts have proven consequent vibration mitigation levels for in-air applications and are simple to implement. However, only few tests have been conducted to mitigate vibrations in water. Gaining new insight in this configuration will permit to use resonant piezoelectric shunts for marine lifting surfaces and will offer an effective system to reduce flow-induced vibrations.

1.2 Purpose of the study

The final purpose of this study is the design and test of an efficient vibration mitigation device based on a passive resonant piezoelectric shunt implemented with two different types of lifting surfaces. To reach this objective, two axes have been developed. The first axis consists in an experimental investigation of the hydrodynamic phenomena leading to high magnitude vibrations of elongated bodies at high Reynolds number. For this purpose, two different elongated structures have been immersed in the hydrodynamic tunnel of the French Naval Academy. The first structure consists in a cantilevered blunt aluminium plate of chord to thickness ratio 16.7. The second structure is a NACA 66-306 truncated aluminium hydrofoil of chord to thickness ratio 13.9. Both structures are studied at zero degrees of incidence for chord based Reynolds number ranging between 2.5×10^5 and 9.5×10^5 (corresponding to free-stream velocities between 2.5 and 9.5 $\mathrm{m.s^{-1}}$). Their wake dynamics, vortex shedding and structural vibrations have been investigated by using Time-Resolved Particle Image Velocimetry (TR-PIV) and laser vibrometry. Even if these kinds of structures have numerous industrial applications, it appears that only few studies have investigated the FIV of elongated bodies at high Reynolds number. Indeed, the physics proper to these configurations are complex due to the interaction of various hydrodynamic and structural phenomena. In order to gain new insights, advanced analysis methods were employed, namely Proper Orthogonal Decomposition (POD) and its Spectral variant (SPOD), vortex detection algorithms and statistical and spectral analysis tools. The accurate comprehension of fluid-structure interaction leading to FIV will enhance the design of marine structures and increase the efficiency of vibration mitigation devices.

The second axis is dedicated to the development of a passive resonant shunt based on piezoelec-

tric transducers integrated on a truncated hydrofoil profile. This system is autonomous in terms of energy and offers great integration simplicity for various marine structures. Experimental tests were achieved in various configurations: in air and in still water and at various flow velocities resulting in hydrodynamic excitation of the structure. Special attention was paid to the mitigation of the first twisting mode vibration in water. To our best knowledge, this type of vibration has not been mitigated using a passive resonant piezoelectric shunt before. To reach the highest vibration mitigation efficiency, a precise set-up of the shunt parameters is necessary. To facilitate this task, a numerical model of the hydrofoil embedded with piezoelectric transducers and connected to a passive resonant shunt was implemented using the software COMSOL *Multiphysics*. This approach will avoid several time consuming and expensive experimental iterations or post manufacturing modifications.

1.3 Structure of the document

The present document is composed of five chapters: Chapter I introduces the problem overview and the fundamental aspects developed in previous research works. Chapter II presents the experimental arrangement and the analysis methodology. The study of the flow-induced vibrations of the cantilevered blunt plate is discussed in chapters III. Chapter IV is dedicated to the vibration mitigation by passive resonant piezoelectric shunt and chapter V describes the impact of vibration mitigation on the near-wake specificities of the truncated hydrofoil.

Chapter I: General introduction

Chapter I presents the fundamental background proper to fluid structure interactions and describes the hydrodynamic features of flows past immersed structures based on previous research. Moreover, the main principles of flow-induced vibrations are discussed and an introduction to piezoelectric materials and vibration mitigation techniques is proposed. The problem overview and the purpose of the present study are also presented.

Chapter II: Experimental set-up and analysis methods

Chapter II describes the experimental arrangement and the test facilities in combination with a presentation of the geometry and the mechanical characteristics of the two studied structures. The measurement methods consisting in laser vibrometry and Time-Resolved Particle Image Velocimetry

(TR-PIV) are presented. Various post-treatment methods were employed, namely Proper Orthogonal Decomposition (POD) and its spectral variant (SPOD), a vortex detection algorithm and statistical and spectral analysis tools. The principle of these methods are presented, as well as the used setting parameters.

Chapter III: Fluid-structure interaction of elongated bodies

Chapter III is dedicated to the analysis of the vortex shedding and induced vibrations of a cantilevered blunt rectangular plate. Experiments were conducted at zero degrees incidence for Reynolds numbers Re_c (based on chord length) ranging from 2.5×10^5 to 9.5×10^5 , leading to turbulent wake conditions. The hydrodynamic properties of the wake were evaluated by statistical analysis, Proper Orthogonal Decomposition and vortex core identification of Time-Resolved Particle Image Velocimetry fields. The structural response of the plate was examined by laser vibrometry through modal analysis. The fluid-structure interactions were analysed for three different vibration regimes: out of resonance, lock-off resonance and lock-in resonance with the first twisting mode. The features of the first nine POD modes were investigated according to the different vibration regimes to understand the physics proper to the near-wake.

Chapter IV: Vibration mitigation by resonant piezoelectric shunt

Chapter IV is dedicated to flow-induced vibration mitigation by passive resonant piezoelectric shunt. In a first instance, the design and set-up of resonant piezoelectric shunts is introduced. The methodology to compute the shunt parameters is explained and two different types of resonant shunt circuits are presented: the synthetic inductor and the copper wired shunt. The ability of both circuits to mitigate vibrations is investigated experimentally in air and in water at zero flow velocity and at various flow velocities with the hydrofoil structure mounted in the hydrodynamic tunnel. The last section of the chapter describes a numerical model implemented with the software COMSOL *Multiphysics* involving the hydrofoil embedded with piezoelectric transducers and connected to a passive resonant shunt. Computations allow a prediction of the natural modes, coupling factors and shunt parameters and offer a very efficient tool to design structures embedded with piezoelectric transducers.

Chapter V: Impact of vibration mitigation on the near-wake properties

Chapter V deals with the impact of vibration mitigation on the near-wake properties. The Macro Fiber Composite (MFC) piezoelectric transducer integrated in the truncated hydrofoil was connected to a passive resonant shunt circuit in order to mitigate twisting mode vibrations. Chord based Reynolds numbers, including the lock-in regime and ranging between 2.55×10^5 and 4.68×10^5 were investigated using TR-PIV and laser vibrometry. POD and SPOD methods were employed to study the impact of piezoelectric shunt vibration mitigation on the wake instability mechanism. It was observed that the shunt offers a significant vibration mitigation level on a broad range of Reynolds numbers including the lock-in with the first twisting mode regime. The near-wake hydrodynamic properties were compared for the no-resonance, lock-in without shunt and lock-in with shunt regimes. An increase of two-dimensionality of the near-wake combined with a size reduction of the trailing-edge recirculation region was observed at the lock-in regime without shunt. When the shunt is activated, three-dimensional effects are increased and the recirculation region size increases tending to the features of a no-resonance regime. It was also noticed that the shunt impacts the SPOD and POD modes leading to a modification of the wake-dynamics. According to these observations, a vibration mitigation by passive resonant piezoelectric shunt impacts notably the hydrodynamic properties of the near-wake region generated by marine lifting surfaces and paves the way for future wake control studies.

1.4 Hydrodynamic features of flows around immersed structures

The present section consists in a general description of the boundary layer and the near-wake region generated by immersed bodies.

1.4.1 Boundary-layer

Generalities

Due to the viscosity of the fluid, the no-slip condition of the flow at the body's wall leads to the existence of a thin layer of fluid, characterized by high velocity gradients and named boundary layer. The characteristic parameters proper to the boundary layer are presented in figure 1.1. The boundary layer thickness is commonly defined as the vertical distance from the body surface where the flow

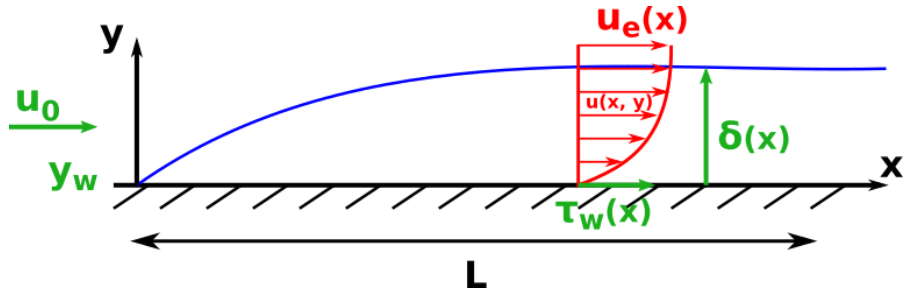

Figure 1.1: Boundary layer characteristic parameters.

reaches 99% of the external flow velocity u_e:

$$\delta = y|_{u=0.99u_e}. \tag{1.1}$$

The thickness of the boundary layer $\delta(x)$ evolves along the body from the leading-edge to the trailing-edge [10]. The wall shear stress is defined as:

$$\tau_w(x) = \mu \left(\frac{\partial u}{\partial y}\right)_{y=y_w}. \tag{1.2}$$

The local skin friction coefficient is expressed as:

$$c_f(x) = \frac{\tau_w(x)}{\frac{1}{2}\rho u_e^2}. \tag{1.3}$$

The integration of the wall shear stress over the surface of the body leads to the viscous drag force, characterized by its global coefficient:

$$C_{DV} = \frac{1}{L}\int_0^L \frac{u_e^2(x)}{U_0^2} C_f(x) dx. \tag{1.4}$$

For smooth bodies, $\delta(x)/x$ as well as $C_f(x)$ are strongly Reynolds dependant. The characteristic non dimensional parameter is the local Reynolds number Re_x which is expressed as

$$Re_x = \frac{u_e x}{\nu}, \tag{1.5}$$

with ν the kinematic viscosity. $\delta(x)/x$ and $C_f(x)$ are also sensitive to the external pressure gradient

$$\frac{dP_e}{dx} = -\rho u_e \frac{du_e}{dx} \tag{1.6}$$

Laminar to turbulent transition

The nature (laminar or turbulent) of the boundary layer is of great importance as it can influence the boundary layer thickness and the wall shear stress. For Reynolds numbers higher than a specific critical value, a laminar boundary-layer flow becomes unstable and transition to turbulence occurs. The transition Reynolds Re_{cr} for a smooth, flat plate boundary layer is found to be approximately:

$$Re_{cr} = \frac{u_e x_{cr}}{\nu} \approx 10^5, \tag{1.7}$$

where $x = x_{cr}$ is the critical distance from the trailing-edge at which transition occurs. Equation (1.7) stands for a turbulence intensity of the free-stream $Tu \approx 2\%$. The value of Re_{cr} may vary significantly due to fluctuations in the free-stream, surface shape (i.e. dP_e/dx) and roughness [32]. Progress in hydrodynamic stability theory and turbulence onset studies have demonstrated that transition starts long before the pronounced phenomena of breakdown are seen. As depicted in figure 1.2, the transition to turbulence in the boundary layer of a flat plate comprises three main stages: (a) receptivity, (b) linear stability and (c) non-linear breakdown.

The receptivity stage is characterized by the generation of instability waves, called Tollmien-Schlichting waves. The region of receptivity extends from the leading-edge of the plate up to the place where instability waves begin to amplify. The origin of instability waves is related to external disturbances such as acoustic [33], vortical [34], temperature and vibrational [35] fluctuations.

The linear stability stage is associated with the propagation of small amplitude waves downstream in the boundary layer, which are either amplified or attenuated [3]. The linear stability region is

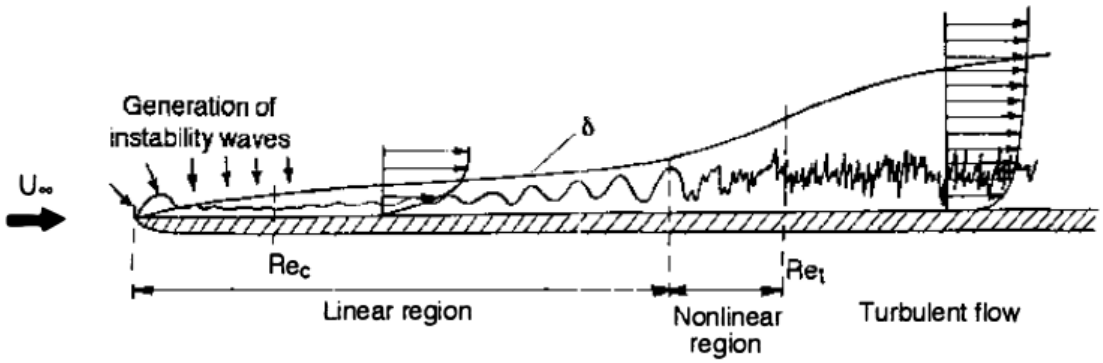

Figure 1.2: Sketch of the transition to turbulence in a boundary layer of a flat plate [3].

usually quite extensive and the phenomena which takes place in it can be simply described by linear stability theory and by receptivity theory [36].

The non-linear breakdown regime occurs when the amplitude of the instability waves reaches a considerable level (of order 1-2% of the free-stream velocity). The flow then enters a phase of non-linear breakdown, randomization and a final transition into a turbulent state. It results, that the flow is transformed from a deterministic, regular, two-dimensional laminar flow into a stochastic but ordered three-dimensional flow [3].

Many differences exist between a laminar and a turbulent boundary layer. A fully turbulent boundary layer produces substantially more average wall shear stress τ_w and viscous drag than an equivalent laminar boundary layer. This happens because turbulent fluctuations produce more wall-normal transport of momentum than viscous diffusion alone. The transition from laminar to turbulent boundary layer also results in a substantial increase in the boundary layer thickness δ. Also, a fully turbulent boundary layer has a different velocity profile and different parametric dependencies than a laminar one. As is presented in figure 1.3, the Reynolds dependent drag coefficient C_{DV} evolution is impacted when boundary layer transition occurs. The lower curve corresponds to a boundary layer that remains laminar over the entire length of the plate whereas the upper curve applies if the boundary layer is turbulent over the entire length. The section of the curve between $Re_x \simeq 5 \times 10^5$ and 10^7 corresponds to the transition between both regimes. The exact point where deviation from the laminar regime occurs depends on the upstream flow conditions, flow geometry and on the surface conditions [4].

Flow separation

Separation of a boundary layer is at the onset of high turbulence zones appearing in close vicinity of the body surface. This implies that the pressure gradient has a significant effect on the stability of the boundary layer. At the surface of the body, the momentum conservation law in the streamwise direction (i.e. the Prandtl's equation for the boundary layer) reduces to

$$\mu \left(\frac{\partial^2 u}{\partial y^2} \right)_{y=y_w} = \frac{dP_e}{dx}. \tag{1.8}$$

In an accelerating outer flow, $dP_e/dx < 0$ (*favorable* pressure gradient) there is no inflection point in the boundary layer profile. But in the case of a decelerating outer flow, the pressure gradient is

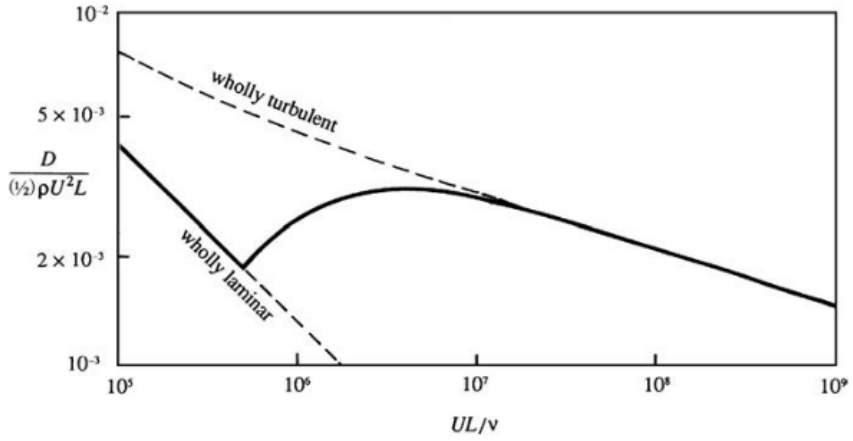

Figure 1.3: Drag coefficient evolution for a boundary-layer flow over a flat plate. The continuous line shows the drag coefficient for a plate on which the flow is originally laminar and then transitions to turbulent. The dashed lines show the behaviour if the boundary layer is either completely laminar or completely turbulent over the entire length of the plate [4].

positive, $dP_e/dx > 0$ (*adverse* pressure gradient) and equation (1.8) implies that the curvature of the velocity profile $u(y)$ changes its sign inside the boundary layer. This induces the occurrence of an inflexion point where $\partial^2 u/\partial y^2 = 0$. An adverse pressure gradient will result in an increase of the boundary layer thickness δ accompanied with a decrease in the wall shear stress τ_w. Also, the occurrence of the inflexion point in the velocity profile is responsible for the destabilisation of the flow in the boundary layer thus leading to an early onset of the turbulence.

If the adverse pressure gradient is strong enough, the wall shear stress τ_w will become null and changes its sign at the *separation point*. If the adverse pressure gradient continues to grow or if the streamwise distance increases further, a backflow will appear and the boundary layer will be separated from the surface of the body ($\tau_w < 0$). For high Reynolds values, a separated boundary layer will rapidly give rise to a vortex sheet and become unstable until generating a thick area of turbulence [4]. Figure 1.4 summarizes the different phases of the boundary layer separation. Due to the increase of the boundary layer thickness δ after separation, a wider wake behind the body will be observed.

Turbulent boundary layers characterized by higher τ_w have the specificity of separating less easily than laminar ones. After separation, the laminar boundary layer can become turbulent and can reattach to the surface and forms what is known as a laminar separation bubble (LSB) [37]. LSB, which occur at the leading-edge of air foils, are detrimental for the overall performance. There physical

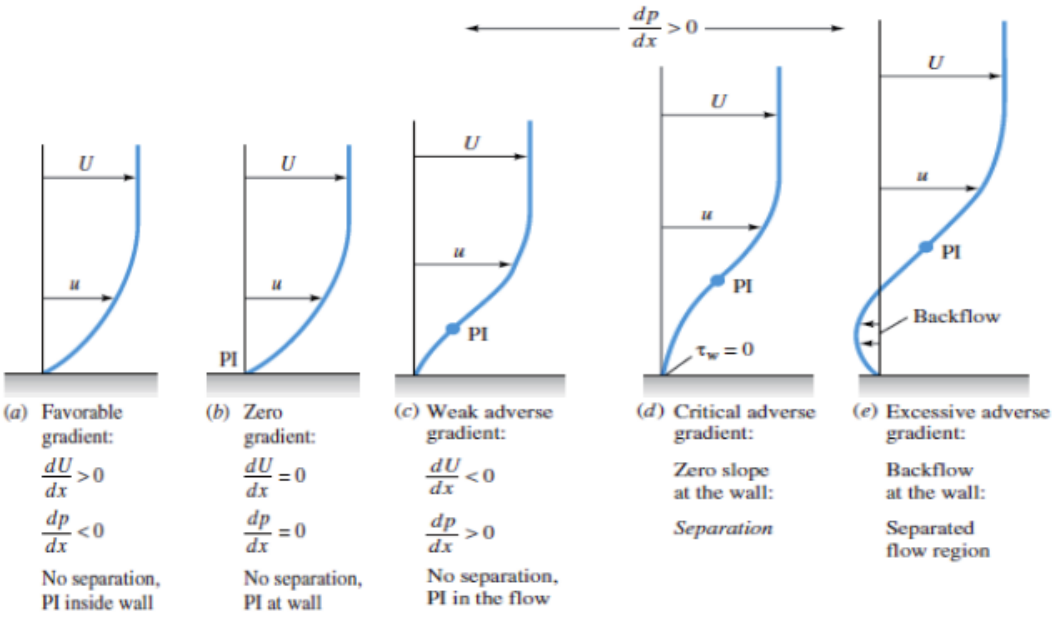

Figure 1.4: Phases of boundary layer separation according to the pressure gradient. PI stands for point of inflection in the u velocity profile. Figure by [5].

dimensions may vary in function of the Reynolds number, the body geometry, external disturbance and the angle of attack [38].

1.4.2 Vortex shedding mechanism downstream a cylinder

The hydrodynamic specificities of a uniform flow past a circular cylinder have been extensively studied over the years, see for example [6, 39, 40, 41, 42]. It has become a benchmark case for the description of the vortex formation and shedding in the near-wake region. The description proposed here is based on the reviews proposed by Gerrard [6] and Bearman [39]. No matter the shape of the body, the general ideas developed here are useful to understand the wake flow mechanisms and may be extrapolated for various types of immersed structures.

Bodies with continuous surface curvature such as circular cylinders generate a separated flow over a substantial portion of their surface. The point where flow separation occurs depends on the boundary layer state and on the geometry of the object. For low values of Reynolds number, the flow remains stable even after separation. Instabilities start to develop once the Reynolds number exceeds a critical

value and result in organized or disorganized unsteady wake motions. The part of the shear layer which is in contact with the cylinder surface moves much more slowly than the part which is in contact with the external flow. This has for consequence that the shear layers roll into the near-wake where they combine together and form discrete vortices [43]. Separating shear layers interact between each other and play a major role in the generation of a vortex street in the near-wake. According to Gerrard [6], an emerging vortex is fed by its attached shear layer and increases its size until it is strong enough to pull the opposing shear-layer across the near-wake region. The vortex detaches and travels downstream when the circulation supplied by the shear-layer is disrupted by the approach of oppositely signed vorticity.

Figure 1.5 illustrates the vortex formation model developed by Gerrard's [6] and demonstrates the prevalence of flow entrainment in the vortex formation mechanism. The growing vortex entrains part of the fluid (a) while another part (b) goes to the developing shear-layer. The eddy formation region is located between the base of the body and the emerging vortex. During this process, another part of the fluid is entrained (c) towards the base of the body (recirculating region). The major part of the entrained flow is located in (a) and represents the highest quantity of entrained fluid. It is responsible for the detachment of the emerging vortex when the adverse vorticity concentration reaches a high level. The whole mechanism described here alternates between the upper and lower boundary layer and leads to the periodical detachment of vortices giving rise to what is known as a Karman vortex street. When transposing to elongated bodies, such as blunt flat plates, this mechanism is identified as Trailing-Edge Vortex Shedding (TEVS). The recirculation region in very close vicinity of the trailing-edge is named a wake-bubble (WB).

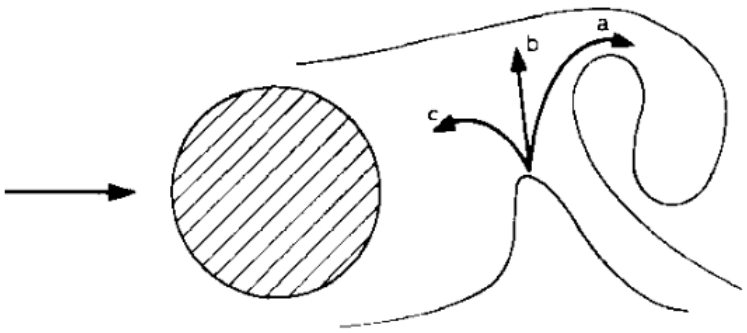

Figure 1.5: Illustration of the vortex-formation model showing entrainment flows [6].

1.4.3 Stability of the Karman vortex street

An object immersed into a stationary unidirectional flow will generate a wake flow structure known as Bénard-Von Karman (BVK) vortex street if the freestream velocity is high enough. According to von Karman [44], two parallel rows of isolated, equal, point vortices in a non-viscous fluid are stable if the ratio between lateral and longitudinal spacing between vortices b_s/a_s is equal to 0.28 and if the vortex arrangement is asymmetrical among the wake centre line. The stability criterion b_s/a_s increases if viscous effect is added. Figure 1.6 presents the arrangement of the wake behind a blunt body and the Karman vortex street stability parameters.

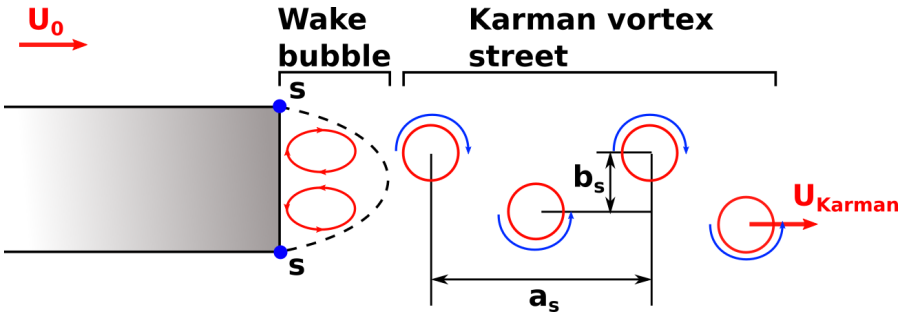

Figure 1.6: General arrangement of the wake behind a blunt body and Karman vortex street stability parameters. S indicates the separation points.

1.4.4 Strouhal number

The Strouhal number is a non-dimensional number which consists in a scaling of the vortex shedding frequency f_{vs}, using the representative length L of the body and the upstream velocity U_0.

$$St_L = \frac{f_{vs}L}{U_0}, \tag{1.9}$$

The thickness-based Strouhal number, often used in the field of FSI, is expressed as:

$$St_D = \frac{f_{vs}D}{U_0}, \tag{1.10}$$

where D stands for the maximum thickness of the body. Blake [45] has highlighted the fact that the boundary layer must be taken into account in the definition of the Strouhal number when the trailing-edge is blunt:

$$St_\delta = \frac{f_{vs}(h+2\delta)}{U_0}, \tag{1.11}$$

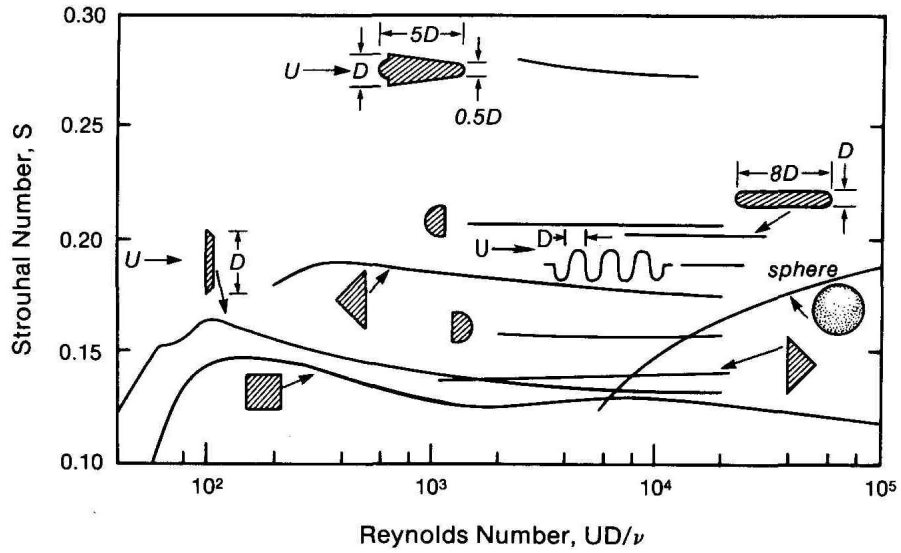

Figure 1.7: Thickness based Strouhal number St_D for different geometries. Image by [7]

where h is the trailing-edge thickness of the body and 2δ is the sum of the boundary layer thicknesses obtained at the trailing-edge. Also, according to Zobeiri [11] the thickness based Strouhal number St_D decreases when turbulence is triggered at the leading-edge of a foil. This is linked with the increase of the boundary-layer thickness.

Blevins [7] has conducted several studies to characterize the Strouhal number and to associate it with different geometrical sections. As a matter of fact typical Strouhal numbers have been associated with geometries such as spheres, cylinders, plates. Figure 1.7 reports the reference Strouhal numbers according to Blevins [7] for several geometries. It can be seen that a Strouhal number equal to 0.20 is associated to a flat plate with rounded edges at a thickness-based Reynolds Re_D between 10^4 and 10^5.

The Strouhal number is known to be linked to the Reynolds number. For elongated bodies, there is a discrepancy between the Strouhal number values according to the Reynolds number, but also according to the type of edge (leading/trailing-edges) [12] as well as the thickness ratio [46]. Indeed, the Strouhal number is very sensitive to the nature of the boundary-layers and it can vary with the chord to thickness ratio c/D. For a flat plate with sharp edges, the Reynolds number has a noticeable influence on the Strouhal number for small angles of attack at which flow reattachment occurs. The influence of the Reynolds number is weak at large incidence angles for which the boundary layer is

fully separated, [47].

1.4.5 Impact of chord to thickness ratio of elongated bodies on vortex shedding regimes

Previous studies have demonstrated that the geometrical characteristics of the structure have a direct impact on the vortex shedding regimes. For plates of square leading and trailing-edges, Stokes et al. [48] have summarized the results obtained by Parker et al. [46] and defined four different vortex shedding regimes depending on the ratio c/D. These regimes were confirmed by Shi et al. [49] and by Zhang et al. [50] for flat plates with c/D ranging from 1 to 9 at a thickness-based Reynolds number $Re_D = 1 \times 10^3$. These regimes are described as follow:

- For short plates ($c/D < 3.2$), the flow separation occurs at the leading-edge corner and there is a direct interaction of the shear-layer to generate a regular vortex street in the wake.
- For medium length plates ($3.2 < c/D < 7.6$), there is a reattachment of the boundary-layer to the trailing-edge surface forming a regular vortex street in the wake.
- For long plates ($7.6 < c/D < 16$), the boundary-layer is always reattached upstream of the trailing-edge and forms a leading-edge separation bubble which grows and divides in a random manner. In this case, there is a random distribution of the vortices throughout the boundary layer. This produces irregular shedding and no clear regular vortex street.
- For extra long plates ($16 < c/D$), the leading-edge separation bubble fluctuates in length the same way as described in the previous case but the randomly distributed vortices diffuse before reaching the trailing-edge. As a consequence, the fully developed turbulent boundary layer induces a regular vortex street at a short distance downstream the trailing-edge which is not directly related to the formation of the leading-edge separation bubble.

However, for Re_D from 1×10^3 to 3×10^3, Nakamura et al. [8] have put into light that the presence of square leading and trailing-edge corners induce a somewhat different interpretation of vortex shedding. According to their study, the vortex shedding in the wake is influenced by the impinging shear-layer instability (ISL) for $3 < c/D < 15$. As a consequence, for this range of c/D values and for $Re_D = 1 \times 10^3$, they have established that the chord based Strouhal number St_c increases stepwise with increasing values of c/D and that the wavelength of the impinging shear-layer

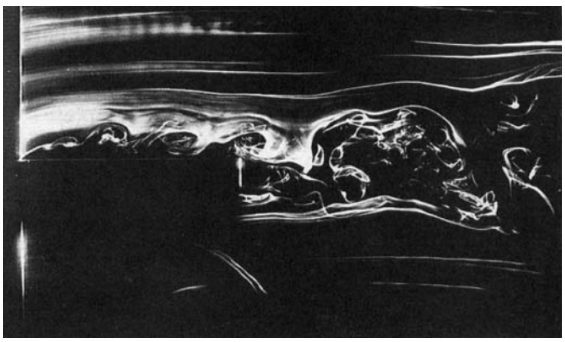

(a)

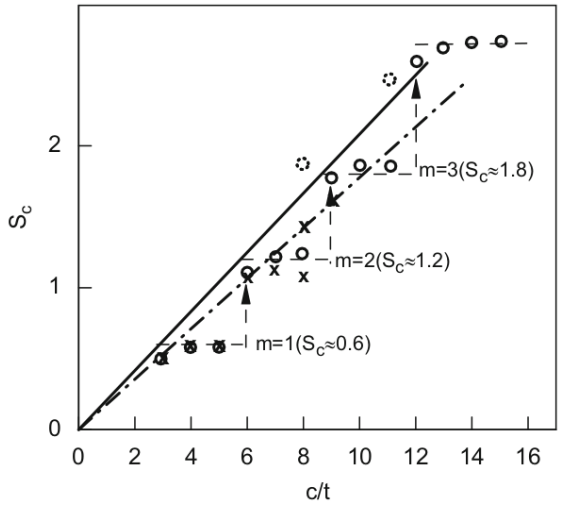

(b)

Figure 1.8: Visualization of the flow past a flat plate with square leading and trailing-edges of c/t=8 at $Re_D = 1.0 \times 10^3$, image of [8]. Chord based Strouhal number St_c versus chord-to-thickness ratio c/t at $Re_D = 1.0 \times 10^3$. Figure of [8].

instability is locked to the chord length. As presented in figure 1.8b, the chord based Strouhal number St_c increases to values that are approximately equal to an integral multiple m of 0.6. This value is representative of the ratio of the convective velocity of the instability over the upstream velocity. According to [8], the number of vortices that form in the separated shear-layer to cover the plate's chord is associated to m. Figure 1.8a shows a flow visualization of the vortices formed over a flat plate of c/t ratio 8 at $Re_D = 1.0 \times 10^3$.

This phenomenon of impinging shear-layer instability was also addressed by Naudascher et al. [51] who concluded that for $2 < c/D < 8$, it is rather vortex shedding by the separation bubble that interacts with the trailing-edge vortex, thus leading to what is called the impinging leading-edge vortex instability (ILEV) which is characterized by a feedback between the trailing-edge shedding and the

leading-edge shedding through pressure waves. However, for $Re_D > 2 \times 10^3$ and $c/D > 12$, no trace of forcing by the shear-layer or leading-edge vortex induced instability has been evidenced in the wake by Nakamura et al. [8]. This is consistent with the fact that the dependency with c/D of the Strouhal number vanishes for $Re_D > 2 \times 10^3$ [52].

Taylor et al. [53] have investigated at high Reynolds numbers the influence on the trailing-edge vortex shedding of a change in the length of the separation bubble by varying the geometry of the leading-edge. For thickness-based Reynolds Re_D ranging from 4.0 to 7.5×10^4 and elongated bodies characterized by $c/D = 7$, they have demonstrated that there is no forcing by the impinging shear-layer or leading-edge vortex instability and that the Strouhal number, which is weakly dependent on the Reynolds number, strongly varies with the leading-edge shape. A larger length of the leading-edge separation-reattachment bubble, which is achieved for a square leading-edge, plays in favour of a decrease in the Strouhal number.

Figure 1.9 summarizes the contribution of main mechanisms to the vortex shedding frequency according to the chord to thickness ratio of a flat plate at zero incidence. For square leading and trailing-edges and for $2 < c/D < 8$, the ILEV controls the vortex shedding in the wake (regime 2a on figure 1.9). n corresponds to the wave number of ILEV. For $c/D \geq 16$, the TEVS mechanism controls the vortex shedding in the wake (regime 3). In this case, the vortex shedding does not depend on the leading-edge shape of the plate and is very similar for round and square edges. For $8 \leq c/D \leq 16$, the ILEV is unstructured, leading to no regular vortex shedding (regime 2b). However, at high Reynolds number, high magnitude vibrations of the leading-edge may strongly influence the leading-edge vortex generation and revive the ILEV mechanism. For this configuration of c/D, both mechanisms ILEV and TEVS regimes may coexist and induce complex flow structures. This configuration deserves a special attention because it corresponds to standard dimensions of various marine lifting surfaces.

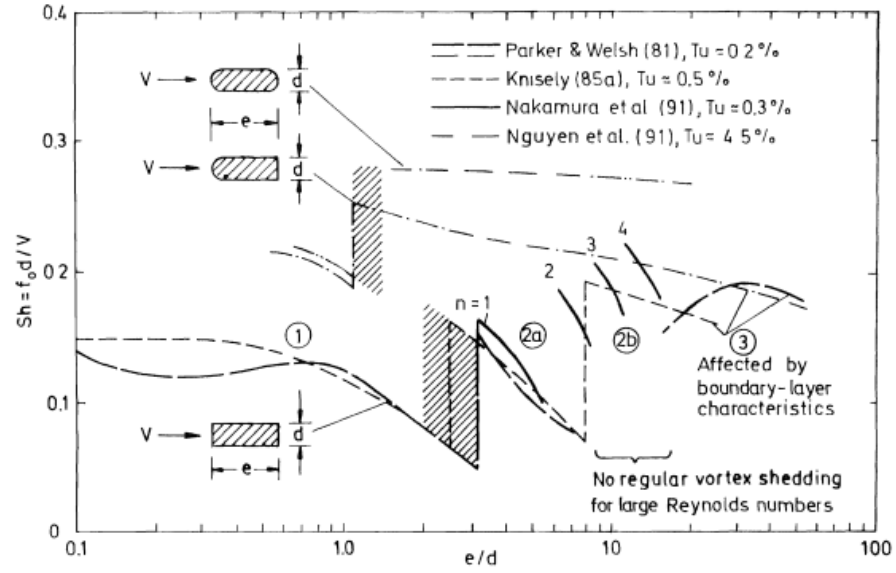

Figure 1.9: Strouhal number for stationary rectangular cylinders at zero degrees of incidence as a function of chord to thickness ratio c/D. Figure from [9].

1.5 Flow-induced vibrations

Flow-induced vibrations (FIV) is part of the fluid-structure interaction field and concerns the mechanical response of structures to oscillatory forces arising from hydrodynamic sources. FIV have been studied extensively over the years and appear in various engineering disciplines. Some unified descriptions can be found in [54, 9].

1.5.1 Fluid-structure interaction generalities

Fluid Structure Interaction (FSI) lies at the crossroads between fluid and solid mechanics. FSI is closely linked with the energy transfer between two domains. De Langre [55] defines FSI as the mechanical energy transfer between a fluid and a structure. However, the interaction between solid and fluid must be strong enough so that the action of the fluid on the structure is not negligible and conversely [56]. Several examples of FSI can be observed in nature, the movement of leaves on a tree [57], a flapping flag [58], deformations of oil rig pipelines [54] or even the movements of marine animals [59].

Although fluid mechanics and solid mechanics are two different domains, fluid and structure prob-

lems must not be treated distinctly. Axisa [60] explains that FSI problems can be classified under two criteria:

- The first criterion is based on the nature of the fluid flow. The flow can be rather negligible, in this case it is considered as fluid structure interaction, or non-negligible and then it is considered as flow structure interaction.
- The second criterion is based on the level of interaction between both domains.

Regarding the second criterion, the coupling can be strong or weak. Strong coupling means that there is a high level of interaction between both domains whereas weak coupling means that the effect of one domain is dominant on the other. De Langre [55] defines two dimensionless numbers to classify FSI problems:

- The mass number M_A compares the contribution of structural and fluid inertial effects. The more the mass number is close to 1, the more the fluid inertial effects contribute to the structure response. The mass number is defined as:

$$M_A = \frac{\rho_f}{\rho_s} \tag{1.12}$$

  with ρ_f the density of the fluid and ρ_s the density of the solid.

- The Cauchy Number C_y expresses the importance of the deformations induced by the flow. If it is small then the structural deformations induced by the flow will be small. The Cauchy number is defined as :

$$C_y = \frac{\rho_f . V^2}{E} \tag{1.13}$$

  with V the characteristic flow velocity and E the Young modulus of the solid.

In addition to these dimensionless numbers, the reduced velocity offers the opportunity to compare the advection time scale of the flow to the time scale of the structure motion. The reduced velocity is defined as

$$V_r = \frac{V}{fL} \tag{1.14}$$

where f is a characteristic frequency of the body's motion and L is the characteristic length of the flow. According to Chakrabarti [54], a strong interaction between a vibrating cylinder and its near-wake region occurs if the reduced velocity is lower than ten.

1.5.2 Damped Harmonic Oscillator

Naudascher and Rockwell [9] have identified two types of oscillators which are proper to flow-induced vibrations: body and flow oscillator. A body oscillator is defined as a rigid structure that is elastically supported, or a structure that is elastic in itself. Typical examples of body oscillators are risers, hydrofoils or the skinplate of a gate. Fluid oscillators consist of a fluid mass that can undergo oscillations usually governed by fluid compressibility or by gravity. A typical example of the interaction between a body and a fluid oscillator is the motion of water contained in an oscillating tank. For the present study, only body oscillators will be considered because the field of interest concerns vibrating solid structures immersed in an incompressible flow with negligible gravity.

A body oscillator can be represented by a simple system consisting of a mass oscillating over one degree of freedom, supported by a linear spring and a linear damper. This system is called a Damped Harmonic Oscillator (DHO) and is represented by the mechanical diagram displayed in figure 1.10. Studying the DHO permits to understand the fundamental principles of mechanical vibrations in a fluid medium and offers the opportunity to determine the natural frequencies of simple vibrating bodies [22].

An harmonic external force $f(t) = Fe^{j\omega t}$ with F the force magnitude and ω the pulsation, puts

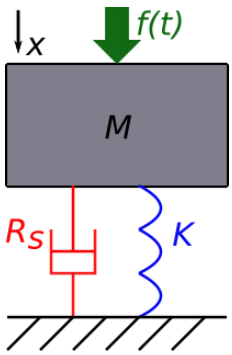

Figure 1.10: Forced, damped harmonic oscillator.

the mass M of the body into motion and is responsible for forced vibrations. The dashpot of linear damping coefficient R_s models a resistance opposed to the velocity which is associated with the viscous force arising from the interaction between the structure and the fluid. In its simplest expression (Stokes flow), such forces may be represented as a linear damping force proportional to the velocity $\dot{x}(t)$. K is representative of the stiffness of the structure. The Newton's second law of motion applied to the moving mass yields:

$$M\ddot{x}(t) = -R_s\dot{x}(t) - Kx(t) + f(t) - M_a\ddot{x} \tag{1.15}$$

where M_a is the added mass and $M_a\ddot{x}$ is the added mass force or inertia force linked to the fact that the accelerating body must displace some volume of surrounding fluid. The displacement can be replaced by the time-harmonic solution $x(t) = Xe^{j(\omega t+\phi)}$. By integrating these expressions in equation (1.15), the fundamental equation describing time-harmonic vibrations in the frequency domain is obtained:

$$[-(M + M_a)\omega^2 + j\omega R_s + K]Xe^{j(\omega t+\phi)} = Fe^{j\omega t}. \tag{1.16}$$

Equation (1.16) can be extended to multiple dimensions by expressing x as a multidimensional vector. Also, by superposing multiple DHOs, it is possible to predict the vibrational characteristics of complex structures. By solving equation (1.15), the damped resonance frequency is obtained:

$$\omega_d = \sqrt{\frac{K(1-\zeta^2)}{M + M_a}}, \tag{1.17}$$

where $\zeta = \frac{R_s}{2\sqrt{K(M+M_a)}}$ is the critical damping ratio. If the damping is small ($\zeta << 1$), equation (1.17) reduces to the undamped natural frequency ω_0:

$$\omega_0 = \sqrt{\frac{K}{M + M_a}}. \tag{1.18}$$

In a more advanced way, 2-D VIV can be described by considering a wake oscillator coupled with a structure oscillator. Such a model was developed by Facchinetti et al. [61] and allow accessible analytical considerations which help the understanding of the physics of VIV.

1.5.3 Sources of Flow-Induced Vibrations (FIV)

Movement-Induced Excitation (MIE)

A vibrating object surrounded by fluid generates an unsteady flow that affects the fluid forces applied to the object. A self-excited vibration may occur if energy is supplied to the moving body.

According to Naudaschher and Rockwell [9] this self-excitation is identified as movement-induced excitation (MIE). The main particularity of this type of excitation is that it is directly linked to the body motion and that it annihilates if the body comes to rest. A classical example of MIE is the fluttering of air-plane wings: when the wing is subjected to a disturbance in both the transverse and torsional mode, the flow will induce a pressure field that tends to increase that disturbance.

Extraneously Induced Excitation (EIE)

Extraneously Induced Excitation (EIE) defines excitation sources that are independent of any flow instability and structural motion and induce forced vibrations [9]. Various sources of EIE exist, among which the most common are:

- Turbulence buffeting;
- Oscillating flows such as waves;
- Cavitation;

For the present study, only turbulence buffeting will be considered. Turbulent vortices induced by an upstream turbulent flow may lead to a fluctuation of the structural load which can result in alternating deformations of the structure. Free-stream turbulence can be described using the turbulence intensity Tu:

$$Tu = \frac{u'_{rms}}{\overline{U_0}}, \tag{1.19}$$

where u'_{rms} is the root mean square of the fluctuating velocity component u' and $\overline{U_0}$ is the averaged free stream velocity. Real flows are characterized by various streamwise and transverse velocity fluctuations and length scales inducing multiple dominant frequencies. For a complete description about EIE and turbulence buffeting refer to [62, 63].

Instability Induced Excitation (IIE)

Instability induced excitation (IIE) is defined by Naudascher and Rockwell [9] as a flow instability which gives rise to flow fluctuations when a certain threshold value of flow velocity is exceeded, independently of any extraneously or movement-induced excitation. IIE includes excitation due to

vortices such as the impinging leading-edge vortex instability and, of particular interest for this study, the trailing-edge vortex shedding which appears to be the most energetic phenomenon responsible for transverse vibrations of marine lifting surfaces. Some pf the main differences between vortex induced vibrations (VIV) and turbulence buffeting are summarized below:

- Forces induced by turbulence buffeting act primarily in the direction of the flow in contrary to vortex-induced forces that act predominantly in the normal direction and result in fluctuations of the lift force.

- A greater diffusion of vorticity in the wake due to turbulence buffeting induces a reduction in vortex strength and shedding frequency [64].

- The force fluctuations induced by EIE are weakly dependent on the response of a fluid or body oscillator which is not the case of force fluctuations induced by IIE.

- The inception of background turbulence to the flow field makes the vortex shedding occur at a lower critical Reynolds number than for laminar flows. It is similar as increasing the surface roughness [65]

- In case of turbulence buffeting, the increase in the velocity is responsible for an increase of the vibration amplitudes. This is different for the VIV for which the vibration amplitude is enhanced in a narrow range of upstream velocities.

Also, there is another source of IIE, which can be linked to fluid oscillations due to the fluctuations of the volume enclosed into a separated pocket (laminar separation bubble of the boundary layer or recirculation region of the very near-wake also named wake bubble). Variations of the dimension of these recirculation regions which take place at a broadband frequency one order of magnitude smaller than those characterizing ILEV or TEVS are identified as flapping. This phenomenon may occur in combination with impinging shear-layer instability and trailing-edge instability. Figure 1.11 illustrates the mechanism of laminar separation bubble flapping above a fixed wall.

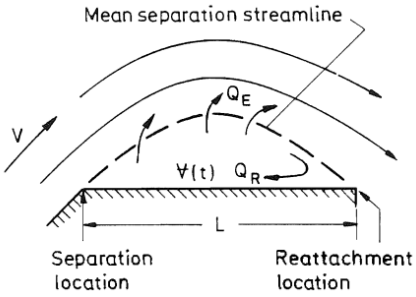

Figure 1.11: Illustration of a laminar separation bubble above a fixed wall.

1.5.4 Lock-in phenomenon

From a general point of view, the amplification mechanisms can be classified in two categories: the extraneous amplification and the feedback amplification. In the engineering field, extraneous amplification is mostly associated with the sound and pressure waves generated by engines or pumps but it is probable that the sound emitted by intensively vibrating hydrofoils may have an impact on the flow instabilities. In most cases, extraneously amplification does not induce severe structural vibrations. Feedback amplification can be fluid-elastic or fluid-resonant if a resonating body oscillator or fluid oscillator acts on the flow instability. It can also be fluid-dynamic when the exciting force is only dependent of the flow conditions. For the present study, the studied lifting surfaces are considered as resonating body oscillators which are exposed to instability-induced excitation. In consequence, the feedback amplification of interest is the fluid-elastic coupling. Figure 1.12 summarizes the amplification mechanisms by which instabilities may induce instability-induced vibration. Fluid-elastic feedback amplification is at the onset of the phenomenon called lock-in.

Severe vibrations occur when a body oscillator induces strong fluid-elastic amplification which results in the alignment of the natural frequency of the body oscillator with the flow oscillations frequency. This phenomenon, known as lock-in, is characterized by higher flow organization and stronger flow-induced forces. In a practical way, if a body periodically sheds vortices in its wake at a frequency near a natural frequency of the structure, vortex shedding may couple with structural vibration and generate a synchronous oscillating force on the structure [66]. Lock-in can generate vibration amplitudes hundreds of time higher than those caused by any other source. The lock-in is an inherently non-linear phenomenon, this means that it is very sensitive to small perturbations and

that it can appear and disappear due to minor variations of the physical parameters [22] such as, for example, the free-stream velocity.

According to Griffin et al. [67] and Stansby [68], the mechanical vibrations of a body may induce appreciable changes in the hydrodynamic properties of the flow. This is particularly true for the vortex shedding frequency during the lock-in regime. Parker et al. [69] have claimed that under these circumstances the vortex shedding frequency can change by as much as 25% of the value observed without lock-in. Under lock-in conditions, the vibration amplitude of a hydrofoil trailing-edge is very high and its motion takes control of the instability mechanism that leads to vortex shedding resulting in a synchronization of the shedding frequency with the structural motion frequency [11].

The torsional natural mode of an elongated structure is particularly compatible with cross-flow excitation forces which results in maximized transverse wall displacement at lock-in. Indeed, in the case of an elongated body, the maximal displacement amplitude occurs at the leading and trailing-edge meaning that the trailing-edge motion is in phase along the entire span which enhances two-dimensionality and strength of the vortex shedding.

Larger vibration amplitudes will induce a larger range of Reynolds numbers where lock-in occurs. Ausoni [10] claims that besides the lock-in, another fluid-elastic coupling occurs for flow velocities close to the ones of the lock-in. Although the structure is already under resonance, leading to higher vibration amplitudes, these are not high enough to impose the natural frequency to the vortex shedding

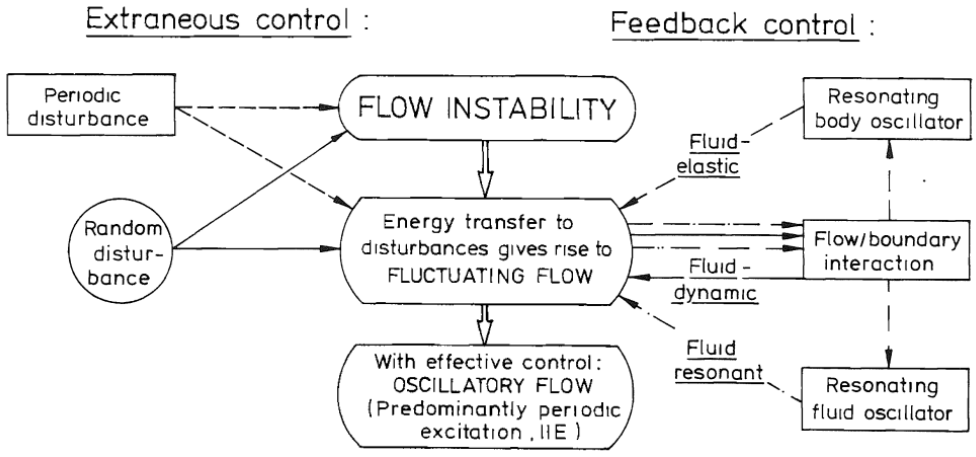

Figure 1.12: Amplifications mechanisms by which flow instabilities may lead to instability-induced excitation, [9].

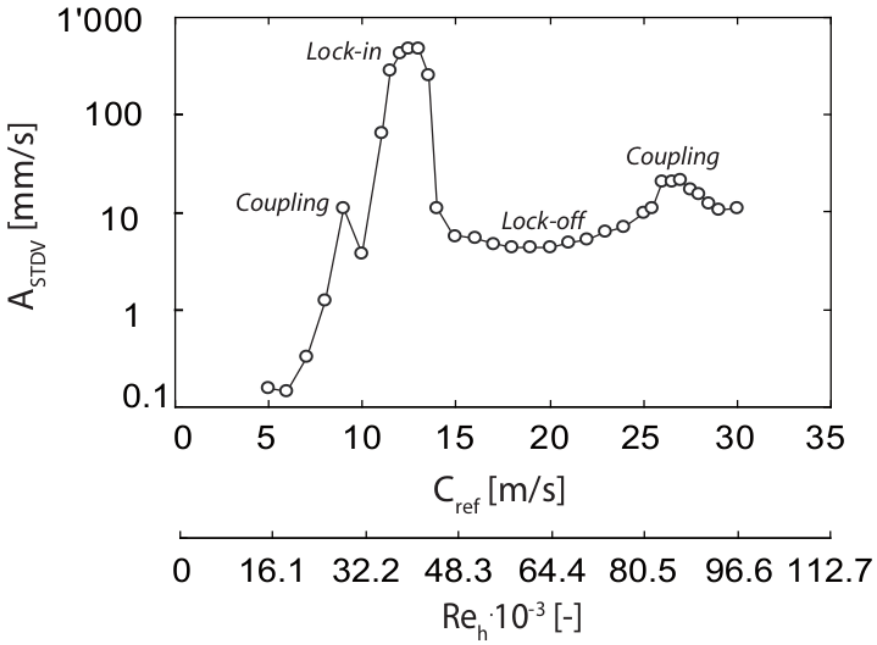

Figure 1.13: Standard deviation of the vibration amplitude of a hydrofoil for different free-stream velocities. Re_h stands for the trailing-edge thickness-based Reynolds number. Figure by [10].

on a free-stream velocity range. Both fluid-elastic coupling and lock-in are illustrated in figure 1.13 which presents the evolution of the vibration amplitude versus the Reynolds number for a truncated hydrofoil. If lock-in is clearly attributed to the vortex shedding, the nature of the flow instability that gives rise to the other fluid elastic coupling near lock-in has not been elucidated. This fluid-structure interaction regime is responsible for an early occurrence of resonance.

1.5.5 Impact of the trailing-edge shape on the vortex induced vibrations at lock-in

Significance and strength of vortex induced vibration is directly related to the geometry of the trailing-edge [12]. Even if the blunt trailing-edge is a very common shape for several industrial applications, other types of trailing-edges exist such as the oblique, rounded, beveled or cavity based trailing-edges. Over the years several experimental and numerical studies have been performed to analyse how the trailing-edge shape could modify the wake dynamics and the vibratory response. For a first approach, refer to Blake [45] for a synthesis of early studies.

Severe disparities between the vibrational features arise when the trailing-edge shape is modified. It is assumed that the instability of the separation points at the trailing-edge might contribute in a large measure to oscillations of the lift force and thus reinforce de vibrations. According to Toebes et al. [12] the modification of the vibration amplitude when changing the trailing-edge geometry is mainly related to:

- The differences to which the separating shear layers interact with each other.
- The differences to which two-dimensionality of the early wake is enhanced in the span-wise direction by transverse motions of the trailing-edge.

Figure 1.14 from Toebes et al. [12] presents the vibration amplitude as a function of the free-stream velocity for plates with different trailing-edge shapes. The re-entrant (plate n°2) and blunt (plate n°3) trailing-edges are assumed to have fixed flow separation points. Both geometries exhibit a small range of flow velocities where maximal vibration magnitude occurs. The re-entrant trailing-edge features the lowest vibration magnitude due to a trapping of the shed vortices which reduces their strength. Zobeiri [11] has studied experimentally the influence of three different trailing-edge geometries on the vortex induced vibrations sustained by a NACA009 hydrofoil for a chord based Reynolds number ranging between 5×10^5 and 3×10^6 at zero degrees of incidence. The tested geometries consisted of truncated, oblique and Donaldson trailing-edges which are known for their ability to reduce flow-induced vibrations [70, 71, 72].

Zobeiri's results [11] have confirmed that the highest vibration amplitudes under lock-in and lock-off conditions are observed for the truncated trailing-edge and the minimum vibration amplitude is found for the Donaldson trailing-edge. See figure 1.15 for the evolution of the vibration amplitude with regard to the flow velocity for the different trailing-edges. At lock-in, the flow separates on the pressure side somewhere at the lower part of the trailing-edge, for the oblique and Donaldson trailing-edges. This leads to a dissymmetry between the upper and lower shed vortices and a collision between them. In case of the Donaldson trailing-edge, the separation point position is free which induces a fluctuation in the phase shift between the upper and lower vortex detachment position, thus leading to the annihilation of lock-in. This study of Zobeiri [11] evidences that the control of the spatial shift of the separation points at the suction and pressure sides of a truncated trailing-edge is a way of controlling the vibrations of the hydrofoil, particularly at lock-in.

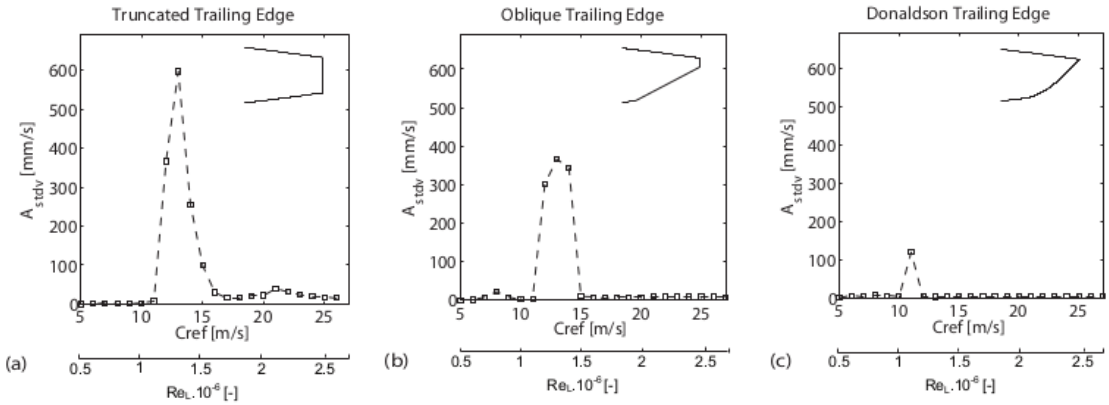

Figure 1.15: Standard deviation of the vibration amplitude versus Reynolds number for various trailing-edge geometries of a NACA0009 hydrofoil. Figure by Zobeiri [11].

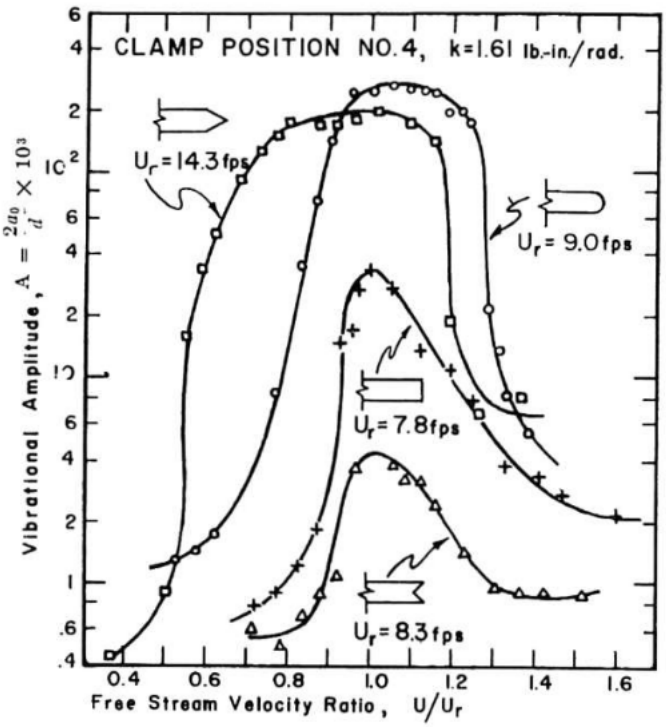

Figure 1.14: Evolution of the vibration amplitude with the ratio of free-stream velocity over reduced velocity at resonance for different trailing-edge geometries. Figure from [12].

1.5.6 Overview of FIV mitigation systems

Over the years, multiple systems aiming at reducing FIV have been developed and integrated in various industrial structures. A broadly adopted mitigation strategy consists in acting on the flow instability mechanism in order to cancel or reduce the fluid-elastic amplification mechanism. From a structural point of view, it is also possible to dissipate the energy of vibration without modifying the excitation source. Both approaches are reviewed in the present section.

Flow instability cancelling approach

This approach mainly consists in preventing or breaking up the shedding of vortices. Techniques for cancelling vortex shedding for aerodynamic and hydrodynamic applications may be classified as:

- shape adaptation: consists in adding surface protrusions to the structure in order to break the vortices directly after they have formed. Also, designing the structure with a special shape will avoid the formation of vortices or diphase their formation in the transverse direction (oblique trailing-edge) or in the spanwise direction to break the 2D arrangement at lock-in. A typical example is the helical strakes added to a cylinder surface presented in figure 1.17. It is also possible to act on the surface of the structure by integrating shrouds. For example by adding a porous cap or by perforating the surface. Shrouds aim at generating small vortices that can disturb the regular vortex shedding.

- near-wake stabilizers: based on the addition of splitter plates in the near-wake region in order to cancel coupling and displace the interaction further downstream.

- fluid injection: consists in bleeding fluid from the interior of the body into the recirculation region of the wake. This results in a decrease of the vortex strength associated to the increase in size of the wake bubble and a shift of the vortex formation region further downstream leading to a cancelling of the lock-in. Figure 1.17 illustrates the principle of fluid injection.

These methods are generally simple to implement, provided that they have been taken into consideration at the early design stages. However, they often interfere with the initial purpose of the system and may be detrimental in terms of aerodynamic or hydrodynamic performance.

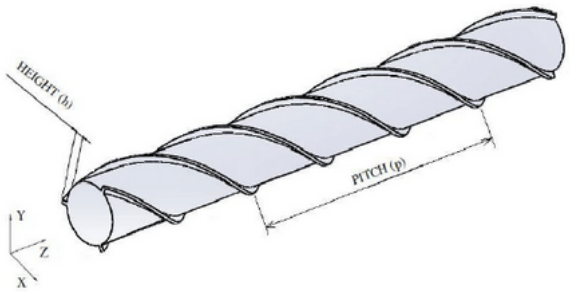

Figure 1.16: Circular cylinder fitted with helical strakes. Figure by [13].

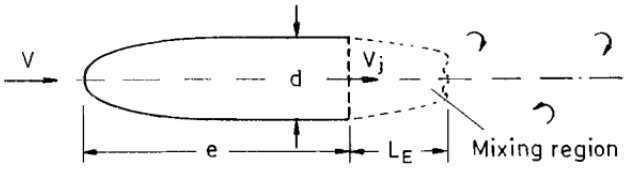

Figure 1.17: Cylindrical body bleeding fluid from its interior. Figure by [9].

Structural approach

The structural approach is based on the addition of mass or damping in the structure. Adding mass to the structure shifts the natural frequencies and cancels coupling. It acts directly on the mechanical vibrations and is independent of the excitation source. This solution is often not compatible with applications requiring lightweight structures which is often the case in the marine engineering domain. Also, if the flow velocity varies, coupling will occur even if the natural frequencies have been shifted.

A common approach in industry is the addition of viscoelastic material on the structure. These materials have the specificity of dissipating the energy of vibration when they are deformed [73]. Viscoelastic material addition is effective to reduce mid to high frequency vibrations and is simple to implement. However, for mitigating low frequencies, the amount of material to append may be prohibitive. It is also possible to combine a viscoelastic material with a Tuned Mass Damper (TMD) [74] which will absorb the vibration energy and dissipate it through the viscoelastic material.

Finally, some vibration mitigation systems are based on the electromechanical coupling between a mechanical structure and an electronic circuit. The coupling can be achieved through electromagnetic transducers consisting of magnets and coils or by means of piezoelectric transducers which are capable

of converting a mechanical strain into an electric current. This second technology is rather lightweight and easy to integrate on marine structures. Also, piezoelectric transducer are very thin and the electrical circuits can be located in a remote position which means that this solutions does not impact the hydrodynamic performances of marine structures. It will be investigated in detail and tested through this study. The next sections are thus devoted to the description of the piezoelectric principle for vibration mitigation.

1.6 Piezoelectric materials and vibration mitigation techniques

1.6.1 A brief history of piezoelectricity

Piezoelectricity was first introduced in 1880 by Pierre and Jacques Curie as they predicted the fact that some crystal materials such as topaz, quartz, tourmaline and even sugar could generate some electrical current while being exposed to some mechanical stress. Early practical application consisted mainly in laboratory instruments such as weight scales or radioactivity sensors as the one used by Pierre and Marie Curie in 1900 to measure the radioactivity of uranium, radium and polonium. In 1910, Woldemar Voigt published his Lehrbuch der Kristallphysik and defines twenty types of crystalline piezoelectric materials by introducing some rigorous physical constants. During the first World War, Paul Langevin designed the ultrasonic submarine detector which was the first industrial application of piezoelectricity. A major milestone was reached during the second world war with the discovery of synthesis ceramics such as Barium-Titanate and Lead-Zirconate-Titanate often designated as PZT. These materials are characterized by very high piezoelectric coefficients and their physical properties are simple to modify, offering a high range of adaptability. Today piezoelectric materials are used in various industrial applications such as pressure and acoustic sensors, sonars, energy harvesting devices and, as presented through this study, for vibration mitigation systems.

1.6.2 General definition of piezoelectricity

The term piezoelectricity derives from the Greek and means ”to press or squeeze” [75]. Piezoelectricity is the ability of certain types of materials to generate an electrical field when a mechanical force is applied to it, a phenomenon that is named direct piezoelectric effect [76]. Reversely, a piezoelectric material will deform if it is exposed to an electrical field, which is known as converse piezoelectric

(a) Direct effect.

(b) Inverse effect

Figure 1.18: Principle of piezoelectricity. Figure from [14].

effect [77]. As was mathematically demonstrated by Lippmann [78] in 1881, both effects coexist inside a piezoelectric material otherwise the material should be thermodynamically inconsistent. According to this principle, in the case of the direct effect, a mechanical strain and/or stress will generate an electrical voltage and/or current. Same principle applies to the inverse effect: an electrical voltage and/or current will generate a mechanical strain and/or stress. Figure 1.18 presents the principle of the direct and inverse piezoelectric effect. In appendix A, some basic theory about electrostatics can be found and may be useful to apprehend the principle of piezoelectricity.

To illustrate the principle of piezoelectricity, let's consider a simple quartz crystal located between two electrodes as illustrated by figure 1.19. This type of crystal has an asymmetric structure and is made of ionic bonds, which are the necessary criteria for a crystal to exhibit piezoelectricity. The electrostatic state of the material is described by the electric field $\mathbf{E}$, the polarization field $\mathbf{P}$ and the displacement field $\mathbf{D}$. Without a mechanical displacement, the centres of gravity of the negative and positive charges are located at the same position. In this case there is no polarization field and, the displacement field $\mathbf{D}$ is equal to $\epsilon_0\mathbf{E}$. By applying a mechanical stress on the crystal, its structure is modified and the electric charges of the ions are displaced inducing a polarization field. The centres of gravity of the charges are no longer confounded and a downward polarization vector is generated. The electrostatic state of the crystal has been altered by a mechanical stress, this constitutes the direct effect. Reversely, when the charges inside the crystal are exposed to an exterior electric field, the molecules are displaced and a deformation of the crystal occurs. The mechanical state of the crystal has been modified by an electrostatic action. This is representative of the inverse effect.

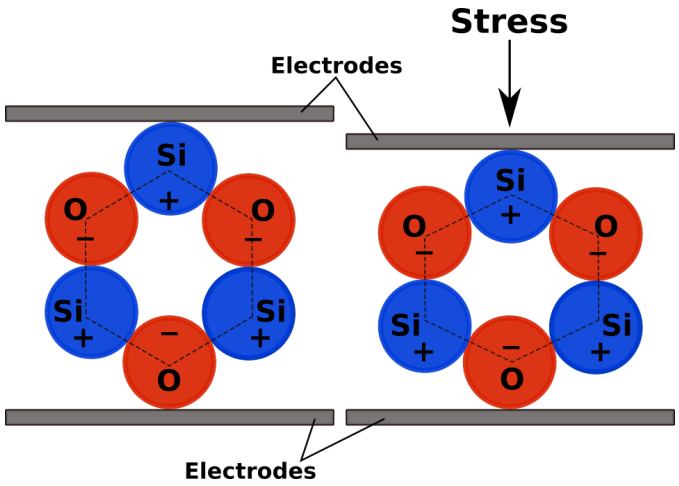

Figure 1.19: Cell of a quartz crystal exposed to a mechanical stress.

1.6.3 Piezoelectric coefficients

A brief description of the piezoelectric coefficients mentioned in the present study is presented below. For additional data about piezoelectric coefficients refer to [20, 79].

Piezoelectric coupling coefficient k_{ij}

The piezoelectric coupling coefficient k_{ij} is defined as the ability of a piezoelectric material to transform electrical energy to mechanical energy and *vice versa*. The ij index indicates that the stress, or strain is in the direction j, and the electrodes are perpendicular to the i-axis. Moheimani et al. [20] provide the following example: if a piezoelectric material is mechanically strained in direction 1, as a result of electrical energy input in direction 3, then the ratio of stored mechanical energy to the applied electrical energy is denoted as k_{31}^2.

Piezoelectric constant d_{ij}

The piezoelectric constant d_{ij} corresponds to the ratio of the strain along the j-axis over the electric field applied along the i-axis when all external stresses are equal to zero. d_{ij} can also be defined as the ratio of short circuit charge per unit area flowing between connected electrodes perpendicular to the j direction to the stress applied in the i direction.

Piezoelectric constant g_{ij}

This constant is representative of the electric field developed along the i-axis when the material is stressed along the j-axis. It can also be defined as the ratio of strain developed along the j-axis to the charge (per unit area) deposited on electrodes perpendicular to the i-axis.

1.6.4 Main types of piezoelectric materials

There exists a wide variety of piezoelectric materials. According to Safari et al [80], 30% of the materials in the world can exhibit piezoelectricity but only a few are used for practical applications. Some of these materials are naturally occurring while others are synthetic. A necessary, but not sufficient, condition is the non-centro symmetry feature of the material [81]. Uchino [82] suggest the following classification:

- Single crystals: Quartz, Lithium Niobate ($LiNbO_3$), Lithium Tantalate ($LiTaO_3$),
- Poly crystalline materials also known as ceramics: Barium Titanate ($BaTiO_3$), Lead Titanate ($PbTiO_3$), Lead Zirconate ($PbZrO_3$),
- Relaxor ferro-electrics: Lead Magnesium Niobate-Lead Titanate (PMN-PT), Lead Zirconium Niobate-Lead Titanate (PZN-PT),
- Polymers: PVDF, Poly (vinylidene diflouride- trifluoro ethylene) (PVDF-TrFE), Polymer-Ceramic composites.
- Piezo-composites

Naturally occurring piezoelectric materials

Naturally occurring piezoelectric materials mainly consist in single crystals. They were the materials used at the early days of piezoelectricity. As was cited previously, a necessary feature of the crystal is to exhibit a non-centro symmetric structure and possess ionic bonds. This specificity is proper to several types of crystals such as quartz, crystallized tartaric acid (also known as Rochelle Salt), tourmaline and even sugar. Crystals are classified in 32 classes [83] corresponding to the possible combinations of symmetry operations that define the external symmetry of crystals. Among these 32

classes, 20 present direct piezoelectricity and 10 of the 20 are polar crystals which means that they undergo spontaneous polarization in the absence of mechanical stress [16]. As is presented in figure 1.20, the crystal material class can be subdivided in several subclasses which consist in:

- Ferroelectric: materials with a reversible dipole moment when exposed to a large electric field.
- Pyroelectric: materials that generate a charge in presence of an oscillating thermal gradient.
- Piezoelectric materials: materials that convert mechanical and electrical energy in both directions.

The capability of a crystal to develop charge movements is described by the electro-mechanical coupling coefficient. Crystals are often characterized by low coupling coefficients, and also present the disadvantage of being brittle and difficult to assemble in large pieces [14]. Though, they are widely used in sensing devices.

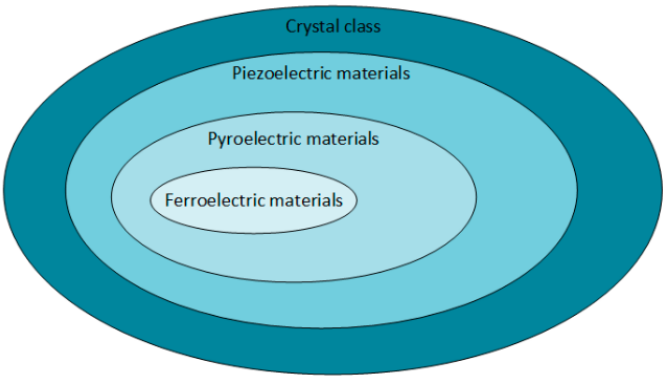

Figure 1.20: Relations between different crystal subclasses, Covaci et al. [15].

Piezoelectric ceramics

Piezoelectric ceramics consist in macroscopically homogenous polycrystals composed of microscopic grains [84]. These materials belong to the ferroelectric class and present a residual polarisation **Pr** once they have been exposed to an intense electrical field **E**; this process in known as polling. Ferroelectricity will only happen below a critical phase transition temperature introduced as the Curie temperature T_c [16]. When temperature is higher than T_c, ceramics become paraelectric and have a cubic crystal structure. In this case there is no polarization due to coincidence of charge barycentres [14]. This state corresponds to the initial structure of a piezoelectric ceramic and is isotropic.

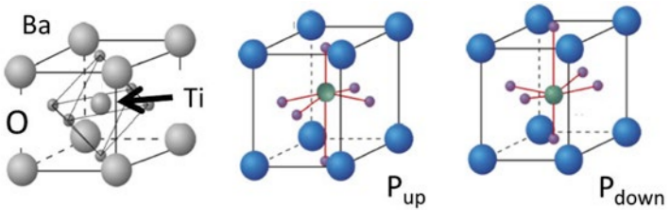

Figure 1.21: Crystal structure for $BaTiO_3$ showing effect of Ti^{4+} displacement on spontaneous polarisation of an elementary crystal cell [16].

The general formulation of a piezoelectric ceramic is written as $A^{2+}B^{4+}O_3^{2-}$ where A is a divalent metallic ion and B a tetravalent metallic ion. Figure 1.21 presents the crystalline structure of a common piezoelectric material known as Perovskites or Barium titanate $Ba^{2+}Ti^{4+}O_3^{2-}$. Below the Curie temperature spontaneous polarization will occur due to the displacement of the Ti^{4+} ion inducing an electrostatic dipole. Several adjacent cells form a ferroelectric domain characterized by a polarization vector **P**. Another very common type of piezoelectric ceramic material is Lead-Zirconate-Titanate $Pb^{2+}Zr^{4+}O_3^{2-}$, often referred as PZT.

Anisotropy is achieved by applying an intense electrical field to the piezoelectric ceramic through electrodes. The polarization field **P** grows non-linearly until reaching saturation as can be seen on the blue curve of figure 1.22. All the dipoles of the material are then aligned with the electrical field and each elementary cell is elongated in the electrical field direction and contracted in the orthogonal direction. At a macroscopic level, mechanical deformation is observed and anisotropy is reached. Remanent polarization $\boldsymbol{P_r}$ and displacement $\boldsymbol{D_r}$ remain when the electrical field is cancelled because most of the ions do not rearrange in a uniform way and remain oriented in the direction of the negative electrode. A free charge $\boldsymbol{Q_r} = \boldsymbol{P_r}A$ is visible at the surface of the electrodes, with A the area of the electrode. The material then deforms for small variations of the electrical field around the remanent polarization state as presented by the orange curve on figure 1.22. Coupling in the direction of the Polarization vector (known as "33" coupling) and in the orthogonal direction ("31" coupling) are frequently used because the same set of electrodes are used for polarization and for both deformation directions.

Piezoelectric ceramics are extensively produced and are employed for various industrial applications for more than 60 years [84]. Some of the main advantages of ceramics include:

- Low price due to large-scale commercial production [84].

- Manufacturing of various sizes and shapes including disks, plates, tubes.
- High coupling coefficients [14]

However, ceramics are also limited in use due to some disadvantages:

- Brittle, sensitive to temperature and time dependent. In order to avoid the ageing process of the material it is possible to achieve polling periodically.
- Failure of piezoelectric effect above the Curie temperature.
- Complex ceramic processes during manufacturing inducing hazardous reproducibility.
- Pyroelectricity induced by ferroelectricity of material [84].
- Higher electrical conductivity than single-crystalline material.

Relaxor ferro-electrics

Very common types of material compositions of relaxor-based single crystals consist of solid solutions of lead magnesium Niobate and lead Titanate (PMN-PT) as well as solid solutions of lead zinc Niobate and lead Titanate (PZN-PT). These materials can also be implemented for polycrystalline ceramics. However, by growing single crystals, the available properties are improved significantly. The chemicals formulas of these materials stand for:

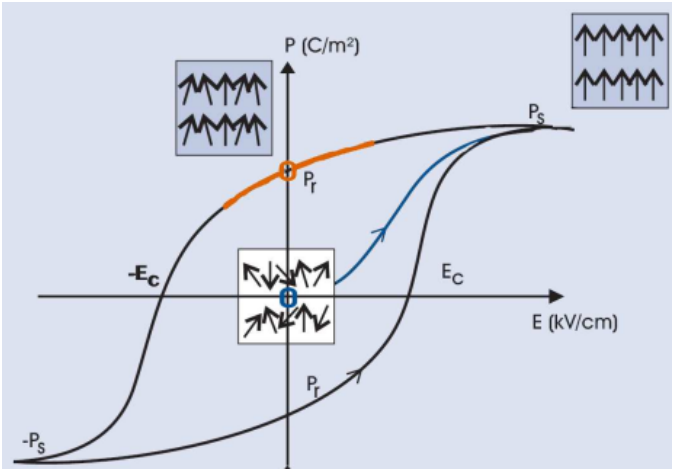

Figure 1.22: Evolution of Polarization field **P** with electrical field **E** [14].

- PMN-PT: $(1-\mathrm{x})\mathrm{Pb}(\mathrm{Mg}_{1/3}\mathrm{Nb}_{2/3})\mathrm{O}_3 \breve{}\ \mathrm{xPbTiO}_3$,
- PZN-PT: $(1-\mathrm{x})\mathrm{Pb}(\mathrm{Zn}_{1/3}\mathrm{Nb}_{2/3})\mathrm{O}_3 \breve{}\ \mathrm{xPbTiO}_3$,

where x ranges from 0 to 1. PMN-PT and PZN-PT materials are characterized by very high piezoelectric strain constants d_{ip}, electric permittivity ϵ and electromechanical coupling factor k_{33} [85]. Due to their excellent properties, relaxor ferro-electrics cover a wide range of practical applications such as ultrasonic transducers and electro-mechanical actuators [82]. However, at present it is complicated to manufacture large crystals with a homogenous composition and the dielectric and piezoelectric properties are dependent of temperature which makes industrial applications complex [86].

Polymers

Some types of polymers exhibit piezoelectric properties if they are stretched during the fabrication process [82]. Typical examples are Polyvinylidene Difluoride, PVDF or PVF2. Such materials are produced as thin sheets which makes it possible to use them as mechanically flexible sensors and actuators. Similarly to polycrystalline ceramic materials, the electromechanical coupling has to be activated with an appropriate polling process [85]. A brief description of one of the most common polymers, PVDF, is proposed below.

PVDF polymers consist of long-chain molecules that are alternately composed of methylene (CH_2) and fluorocarbon (CF_2) [87, 85, 88]. An example of a PVDF chain molecule is presented in figure 1.23 (a). The chain molecules are assembled together as thin lamellar crystal-like structures which are randomly arranged. This random orientation explains why the PVDF does not exhibit piezoelectric properties in its initial state. If the PVDF film is fitted with electrodes, polling can be achieved by applying high electric field intensities up to 100 $\mathrm{kV.mm^{-1}}$ in order to align the lamellar crystal-like structures. This will result in the alignment of the dipole moments and the activation of the electromechanical coupling.

Piezoelectric characteristics of PVDF materials are less marked than of piezoceramics such as PZT. PVDF films are well adapted as broadband piezoelectric components for directional microphones and ultrasonic hydrophones [82]. It is possible to implement copolymers of PVDF and Trifluoroethylene identified as P(VDF-TrFE) in order to enhance the electromechanical coupling factors. Also, these materials are soft which may be not adapted for integration on metallic or composite marine structures.

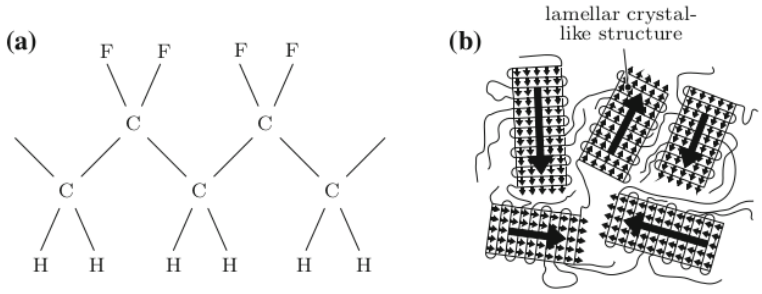

Figure 1.23: (a) Example of a chain molecule of PVDF. (b) Arrangement of the chain molecules inside the PVDF material; dipole moments inside lamellar crystal-like structures point in same direction. Image from [17].

Active and Macro Fibre Composites

Piezo-composites are constituted of a piezoelectric ceramic and a polymer [89]. The standard type of piezo-composites, identified as active fibre composite (AFC) consists of multiple ceramic fibres associated with a network of interdigitated electrodes and encased into an epoxy matrix as displayed in figure 1.24. When a voltage is applied, the electrodes induce a longitudinal electric field along the length of each fibre. For optimal piezoelectric coupling, the polling is achieved in the direction of the fibres (e.g. the direction of the stress applied on the transducer) and the high piezoelectric strain constant d_{33} is used rather than the d_{31} constant [20]. Macro Fibre Composites (MFCs) are similar to AFCs but instead of being constituted by individual fibres, a monolithic transducer is cut into a set of long stripes. This specificity offers a higher robustness to mechanical failure than monolithic patches. MFCs also take advantage of the d_{33} strain constant.

Due to their excellent tailorable properties piezo-composites are very promising materials for vari-

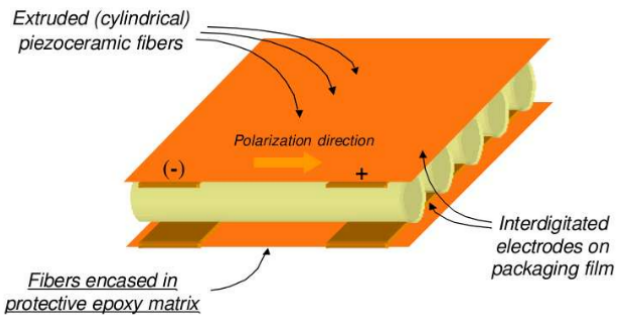

Figure 1.24: Piezoelectric composite with interdigitated electrodes. Figure from [18].

ous industrial applications. These materials also combine high piezoelectricity and mechanical flexibility [90] which makes them particularly suited for an integration on curved surfaces. The fact that the fibres are encapsulated by the printed polymer electrodes and the epoxy matrix increases significantly the robustness and reliability in hostile environments. Also, the transducers will remain operational even if some fibres are damaged. Some disadvantages of this type of transducer are their cost and the high voltage required to reach high actuation strain. Refer to [18, 91, 89] for additional information about this type of material.

1.6.5 Piezoelectric vibration mitigation techniques

General principle

Piezoelectric shunt damping, also known as piezoelectric vibration mitigation or reduction, includes all the concepts where an oscillating structure is damped with integrated piezoelectric transducers connected to electric networks [19]. The concept is mainly attributed to Hagood and von Flotow [92] who demonstrated that a series inductor-resistor network can significantly reduce vibration of a single structural mode. The principle consists in tuning the network to the resonance frequency of the mode to mitigate [20]. Similarly to a TMD, additional dynamics introduced by the shunt increase the effective structural damping [92]. Figure 1.25 presents the basic principle with the shunt network represented by the electrical impedance Z_1 which may consist of capacitive, resistive or inductive parts.

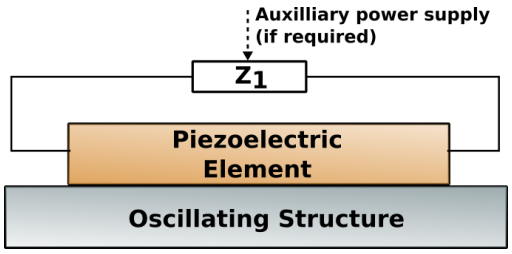

Figure 1.25: Principle of piezoelectric shunt damping, [19].

Classification

Vibration mitigation devices using piezoelectric transducers can be classified in three main categories: active, semi-passive and passive control systems [14, 93]. Affiliation to one of these categories is mainly influenced by the necessity of the system to be externally power supplied. Active control

systems have demonstrated high vibration mitigation levels and great adaptability to various vibration modes. However, these types of devices require a feedback control system which consists of sensors, actuators, signal processors, power amplifiers and external electric sources. This high amount of various components may not be convenient for integration in a submerged and confined environment proper to marine applications. Moreover, as active devices are externally power supplied their is an inherent risk of instability which may result in a self-excitation of the mechanical system in case of improper tuning.

Passive control systems do not require an external power supply and are fully autonomous [94, 95]. This type of system uses simple and low-cost passive components such as resistors, inductors or capacitors directly connected to the electrodes of the piezoelectric device. Considered at the early stages as less efficient than active systems, it appeared over the years that passive systems can provide high levels of vibration mitigation, subject however to a precise tuning of the electronic parameters. Moreover, there is no risk of instability due to the absence of external power supply. For some applications, control systems may require impractical electrical components (even with negative values) that are not feasible with classical passive components. In this case, an active electronic circuit can be implemented to generate synthetic components (i.e. synthetic inductor circuit described in chapter IV). This gives rise to the semi-passive category of vibration control systems which uses active components in the control circuit but without explicit feedback loop requiring signal processing. As the energy consumption is generally low it can be power supplied by low size batteries or by energy harvested by the piezoelectric transducer itself and making it suitable for autonomous and remote applications. The present study focuses on passive and semi-passive techniques.

Passive shunts

Various types of passive shunts have been developed over the years and can be classified depending of their linear or non-linear behaviour. Among the linear category three types of shunt circuits are identified:

- **Capacitive shunts** [96] adds capacitance to the terminals of a piezoelectric transducer and results in a variation of the stiffness of the structure. Purely capacitive shunts cannot be used for vibration damping but can be useful for slight adjustments of the resonance frequency of the structure.

- **Resistive shunts** [92] consist of a simple resistor connected to a piezoelectric transducer. Vibration mitigation is achieved by converting the mechanical energy into electrical energy which is then dissipated by Joule effect through the resistor. Although very simple, this type of arrangement is rarely used because it offers only a small amount of mitigation.

- **Resonant shunts** dedicated to control a single mode are composed of a resistor and an inductor which are either connected in parallel [97] or in series [92]. This type of shunt significantly increases the structural damping performance [20]. The inductor increases the electrical current circulating through the circuit and so raises the amount of energy dissipated by Joule effect. Some particular types of passive multi-resonant shunt identified as Hollkamp Current-Flow [98], Series-Parallel [99], Current Block [100] and Control Oriented [101] have been designed for multi-mode vibration control. These types of shunts, which mainly consist of various associations of inductors, resistors and capacitances, are out of our study range and won't be described in this document but the reader can refer in a first instance to [20] and [102] for further information about these types of shunts.

Switched shunts are identified as non-linear and integrate a controlled switch which opens and closes the circuit synchronously with the vibration of the structure. The associated circuit consists

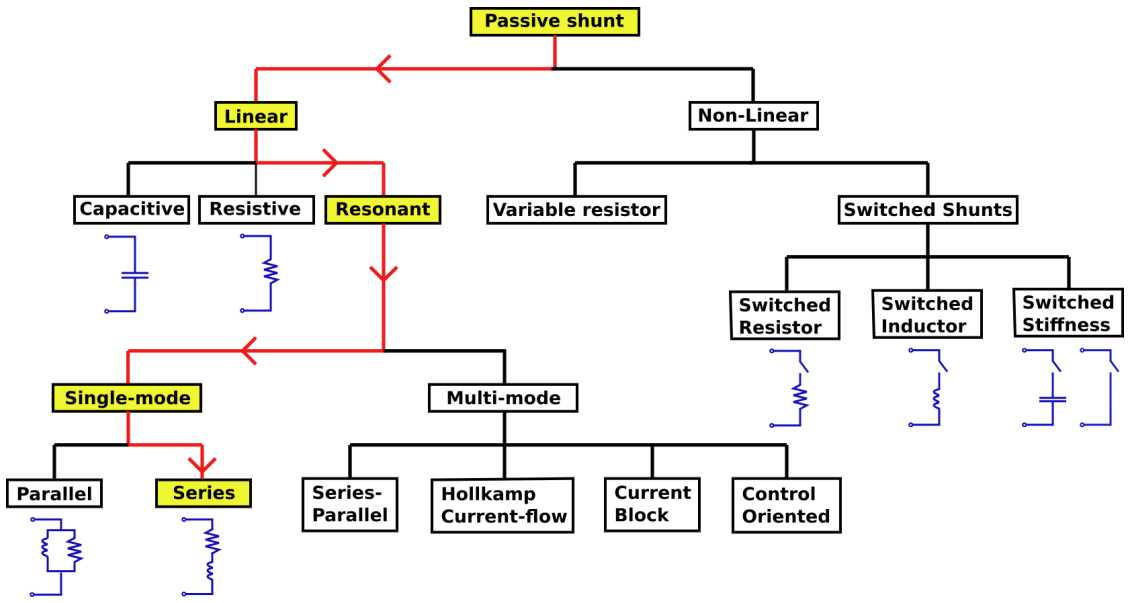

Figure 1.26: Passive piezoelectric shunt mitigation techniques. Figure inspired from [20]. The red path indicates the studied type of shunt.

of a single resistor or a resistor and an inductor. These types of circuits are respectively identified as Synchronized Switch Damping on Short (SSDS) [103] or on Inductor (SSDI) [91]. Non-linear inductor shunts offer interesting properties due to the introduction of a saturation phenomenon in which the amplitude of the mechanical mode becomes independent of the excitation amplitude after a threshold, and a non-linear anti-resonance in place of the linear resonance frequency, leading to high vibration mitigation [104, 105]. Switched stiffness shunts are made of a controlled switch connected directly at the poles of a piezoelectric transducer or in series with a capacitance [96], this type of shunt is out of the range of this study. Refer to figure 1.26 for a complete overview of the various types of linear and non-linear passive shunts. The present study will focus on resonant series passive and semi-passive shunts dedicated to single-mode vibration control. However, the study could be extended to multimodal or switched shunts by connecting the same piezoelectric fitted structure to various electrical circuits.

Conclusion of the chapter

The various topics handled through this chapter demonstrate that the phenomenon of flow-induced vibrations is complex and that despite numerous studies some aspects still require further investigations to accurately describe the physical mechanisms. The configuration consisting of an elongated body sustaining high magnitude vibrations is particularly complex because of the interaction between the ILEV and the TEVS mechanism. Elongated bodies are commonly encountered in the domain of marine engineering and an accurate understanding and prediction of the FIV phenomenon will greatly enhance the design of this type of structures. Also, the integration into a marine lifting surface of a piezoelectric resonant shunt vibration mitigation system offers great opportunities to avoid high magnitude vibrations leading to noise radiation and structural fatigue. The present study is dedicated to these aspects and both experimental and numerical investigations will be presented. Before introducing the obtained results through chapters III, IV and V, the next chapter describes in detail the experimental arrangement and the analysis methods.

Chapter 2

Experimental set-up and analysis methods

" The truth knocks on the door and you say, "Go away, I'm looking for the truth," and so it goes away. Puzzling. "

Robert M. Pirsig

Content

The present chapter is dedicated to the description of the experimental arrangement and the test facilities in combination with a presentation of the geometry and the mechanical characteristics of the two studied structures. The measurement methods consisting in laser vibrometry and Time-Resolved Particle Image Velocimetry (TR-PIV) are presented. Various post-treatment methods were employed, namely Proper Orthogonal Decomposition (POD) and its spectral variant (SPOD), a vortex detection algorithm and statistical and spectral analysis tools. The principle of these methods are presented, as well as the used setting parameters.

2.1 Experimental arrangement

2.1.1 Hydrodynamic tunnel

The hydrodynamic tunnel of the French Naval Academy Research Institute (IRENav) enables to study two or three dimensional fluid flows around obstacles with an average size of 100 mm. It has an overall size of 15 m long by 7 m high and contains 60 m^3 of fresh water. As presented in figure 2.1, it is made of three main parts:

- The resorbing tank (7).
- The test-section (1).
- The downstream free-surface tank (6).

The horizontal resorbing tank allows heat dissipation and is used to reduce the amount of bubbles. The flow circulates in an anti-clockwise direction using a 10 blades rotatory pump (2) driven by a 21 kW electric motor (3) with a maximum rotation velocity of 750 RPM. This unit is controlled by a speed variator of the type Elvovert XD of 37 kW and 400V which has an accuracy of 0,1 % on its rotational speed.

The downstream free-surface tank has a diameter of 2.2 m and a height of 7.5 m. The main purpose of this part of the tunnel is the reduction of the quantity of small sized air bubbles at the suction-side of the rotatory pump. This is achieved by fine meshed iron grids located inside the tank. Furthermore, the volume of air above the free-surface can be supplied to an additional 6 bars pressurised tank or to a vacuum tank. This process ensures the regulation of the pressure inside the tunnel between 0.1 and

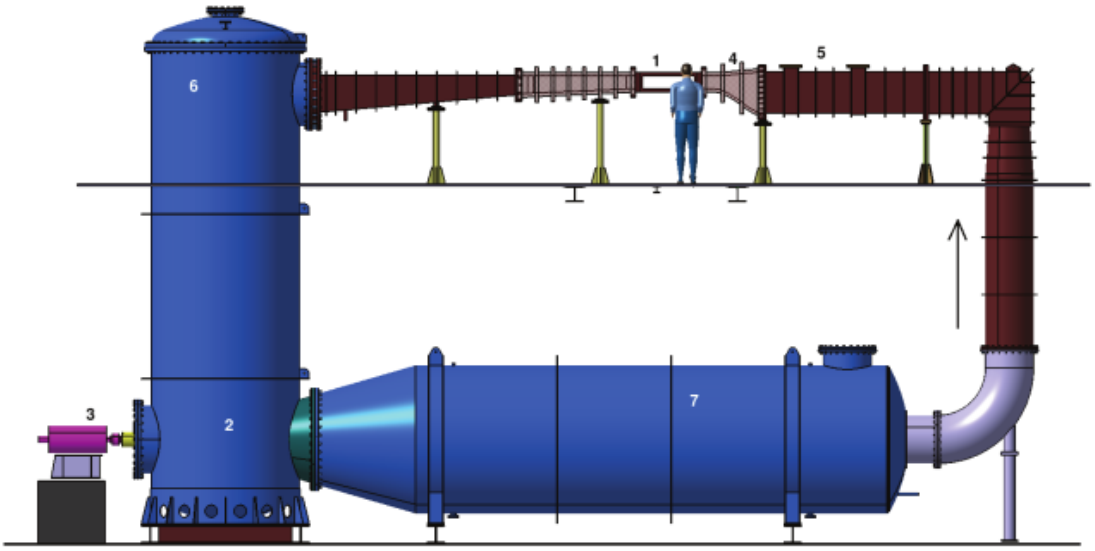

Figure 2.1: General arrangement of the IRENav hydrodynamic tunnel.

3 bars with a theoretical accuracy of 2.5 mbar. The automation of pressure regulation is achieved by a Yokogawa monitoring system which controls the servo-valves.

The test-section is 192 mm squared and 1 m long. The upper wall of the test-section is horizontal and makes it possible to ensure a zero pressure gradient in the test-section in the absence of obstacle. In order to reduce the impact of boundary layer generation on the flow, the bottom wall of the test-section is slightly inclined with regard to the upper wall. This inclination has been evaluated to be equal to 0.14° beside the horizontal plane reference. An asymmetrical converging section (4) made of Plexiglas is placed upstream of the test-section to reduce turbulence and to accelerate the fluid flow without unintended cavitation. In order to reduce as much as possible the turbulence rate in the flow, two honeycomb grids (5) are used. Consequently, the turbulence intensity at the entrance of the test-section is 2%. Two different diverging sections are located downstream of the test-section with an opening angle of 2.5° over 1.8 m and 5° over 2.93 m respectively. The first diverging section is made of Plexiglas and the second one is made of inox 316L. Refer to figure 2.2 for a general overview of the arrangement of the test-section. The vibrometer and the Particle Image Velocimetry (PIV) devices have been added to the figure.

A programmable logic controller is used for monitoring and regulation of the flow velocity in the tunnel. It is linked with two piezoresistive pressure sensors of the Paroscientific type. The first one

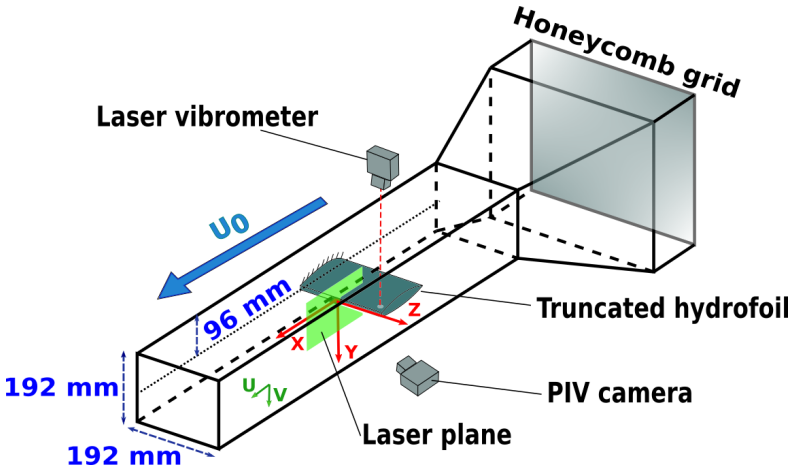

Figure 2.2: Test-section of the IRENav hydrodynamic tunnel.

records the mean pressure over three different locations upstream of the converging section. The second one records the pressure at the entrance of the test-section at a measurement point located on the bottom wall. Consequently, the controller is able to compute the flow velocity at the entrance of the test-section by pressure differential. The velocity set-point is then transmitted to the Elvovert speed variator and to the Yokogawa controller acting respectively on the electrical motor rotational velocity and on the free-surface tank air pressure. This process allows flow velocities ranging from 0 to 15 m.s^{-1}. The upstream velocity and pressure at the entrance of the test-section are regulated with a relative accuracy of $\pm 2\%$ and $\pm 2.5\%$ respectively.

2.1.2 Studied geometries

Two different types of marine structures were investigated through this study. The first one is a rectangular blunt plate used for the analysis of the fluid-structure interactions proper to elongated bodies. The second one is a truncated hydrofoil embedded with piezoelectric transducers dedicated to vibration mitigation by passive resonant shunt. The blunt trailing-edge geometry, proper to the flat plate and the truncated hydrofoil, ensures a fixed flow separation point. For both structures, the trailing-edge at mid-thickness and mid-span is chosen as the origin of the reference frame, x being the stream-wise direction, y being the downward vertical direction and z being the transverse direction, as shown in figure 2.2. Both structures were designed, build and equipped at the French Naval Academy Research Institute and at the LMSSC laboratory of the Conservatoire national des arts et métiers.

Blunt flat plate

The first studied structure consists of a blunt aluminium plate with a chord-to-thickness ratio c/D=16.7 and of mass M_s=0.38 kg. The span of the plate is s=191 mm, its chord is c=100 mm, and its thickness is D=6 mm. The fluid mass to the structure mass ratio $\rho Dsc/M_s$ is equal to 0.3. A rectangular extension of 80 mm × 31 mm × 10 mm is added at the base of the plate to clamp the structure at the backside of the test-section. The plate is mounted in the test-section with zero incidence, assuming a maximum uncertainty in the angle of attack of 0.1 °.

On the upper and under horizontal side of the plate there is a rectangular groove of dimension 61.5 mm × 71 mm × 1 mm intended to support two piezoelectric transducers on both sides. The piezoelectric transducers are attached to the plate surface using a vacuum bagging method with an epoxy adhesive. A thin layer of paraffin is added on top of the transducers to fill the residual depth of the cavity and reconstruct the surface in order to avoid added thickness and local roughness. Channels are also machined in the extension root to allow the passage of the electric wires of the piezo-electrodes. The piezoelectric transducers are of the type P-876. A15 DuraAct patches supplied by PI Ceramic. They consist of a PIC-255 active layer sandwiched between two soft thin encapsulating Kapton shell layers. Overall dimensions of the transducers (i.e. including the encapsulating material) are 61 mm × 35 mm × 0.8 mm, while the encapsulated active layer is 50 mm × 30 mm × 0.5 mm. Two

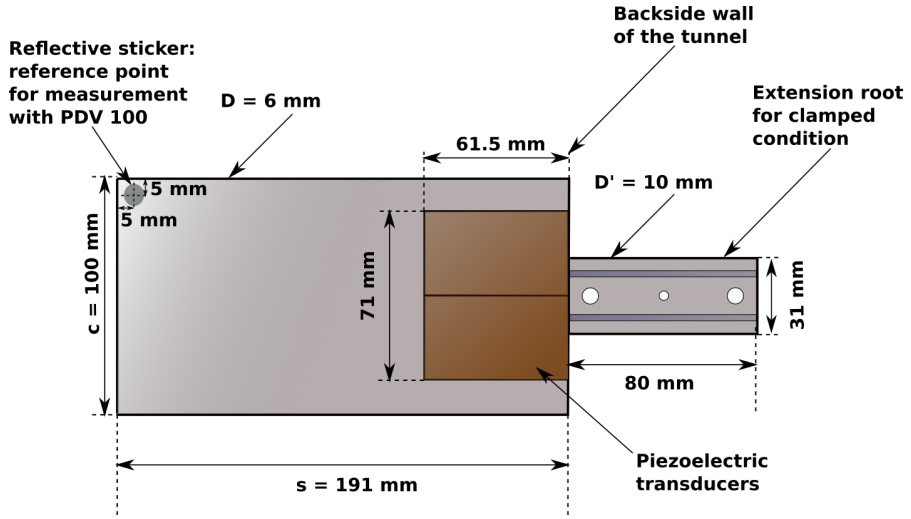

Figure 2.3: Geometry and dimension of the blunt flat plate embedded with piezoelectric transducers.

of the four transducers can be used as an excitation source for the plate vibration, while the output of the two others can be used to control the vibration or as sensors to convert the mechanical strain into a voltage signal. In the present work, only two transducers were used as a structural excitation source : they were power-supplied to characterize the natural frequencies and mode shapes of the plate at zero flow velocity. In this study, the vibration control was not activated and the remaining patches were connected in short-circuit. Figure 2.3 presents the geometry and dimensions of the aluminium flat plate. Refer to Pernod et al. [106] for a similar arrangement.

Truncated hydrofoil

The second geometry consists of a standard NACA 66-306 hydrofoil with a maximum thickness of 6% at 45.46% of the chord. The hydrofoil had an original chord of 100 mm but was truncated at 85% of the original chord. The final dimensions are 191.0 mm $\times$ 85.0 mm $\times$ 6.13 mm (span s, chord c, thickness D). The extra thickness of 0.13 mm is due to the surface treatment applied to reduce corrosion. The thickness at the truncated trailing-edge is equal to 3.4 mm. The mass is $M_s = 0.35$ kg and the fluid mass to the structure mass ratio $\rho Dsc/M_s$ is equal to 0.3. This hydrofoil, often defined as a laminar hydrofoil, has the specificity of being asymmetric along the chord which implies that it generates a lifting force at zero incidence. The root of the foil has been specially manufactured to form a cantilevered structure with a suitable clamping condition at the backside of the test-section. The hydrofoil is mounted in the test-section with zero incidence, assuming that the uncertainty in the angle of attack is 0.1 °. Refer to figure 2.4 for a representation of the hydrofoil profile.

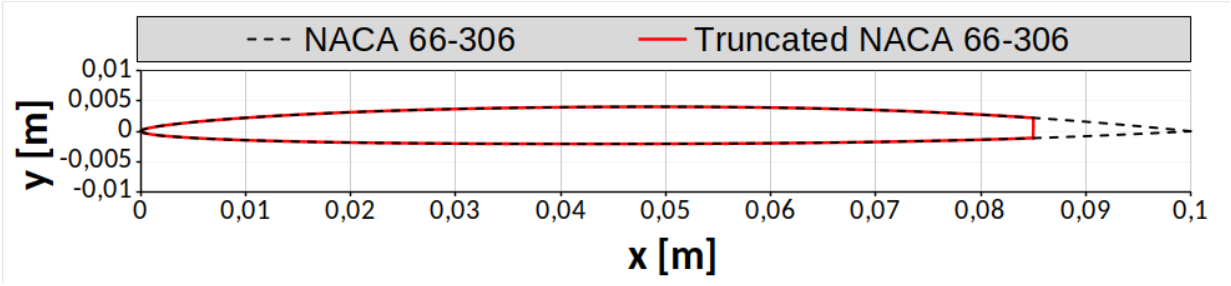

Figure 2.4: Truncated NACA 66-306 hydrofoil. Maximum thickness of 6% at 45.46% of chord. The thickness at the trailing-edge is 3.4 mm. The original NACA 66-306 hydrofoil is drawn in dotted lines.

On the suction-side, a rectangular cavity of dimension 108 mm × 68 mm × 0.5 mm was machined to host a MFC type piezoelectric patch of overall dimension 105 mm × 65 mm × 0.3 mm (includes the Kapton shell). The cavity follows the curvature of the foil. Consequently, the patch is in a pre-stressed position as it is slightly bend to follow the curvature of the foil. The selected MFC patch is primarily designed to sustain twisting type deformations due to the direction of the piezoelectric fibres equal to 45 °. The MFC patch is connected to an electrical shunt circuit and can be used for structural vibration mitigation, preferentially for the twisting vibration mode. On the pressure-side of the foil an other rectangular cavity of dimension 61.5 mm × 71 mm × 1 mm has been machined in order to insert two P-876.A15 DuraAct patches of 61 mm × 35 mm × 0.8 mm dimension each. This second cavity is aligned on the trailing-edge in order to force a twisting type deformation when the DuraAct patches are supplied by voltage and used as a structural excitation source. These patches also follow the curvature of the hydrofoil and a bore has been drilled at the root of the foil to enable the passage of the electrical cables connected to the piezoelectric patches. See figure 2.5 for a schematic representation of the transducers position.

The material of the hydrofoil is aluminium. An anodizing surface treatment was applied on the hydrofoil skin in order to prevent corrosion. The MFC transducer was covered with a thin epoxy layer to avoid water penetration inside the patch because tests demonstrated that the capacitance of the patch is altered when it is submerged in water for long periods without watertight protection. Smooth surface transition from aluminium to epoxy was achieved by sanding. The DuraAct transducers were

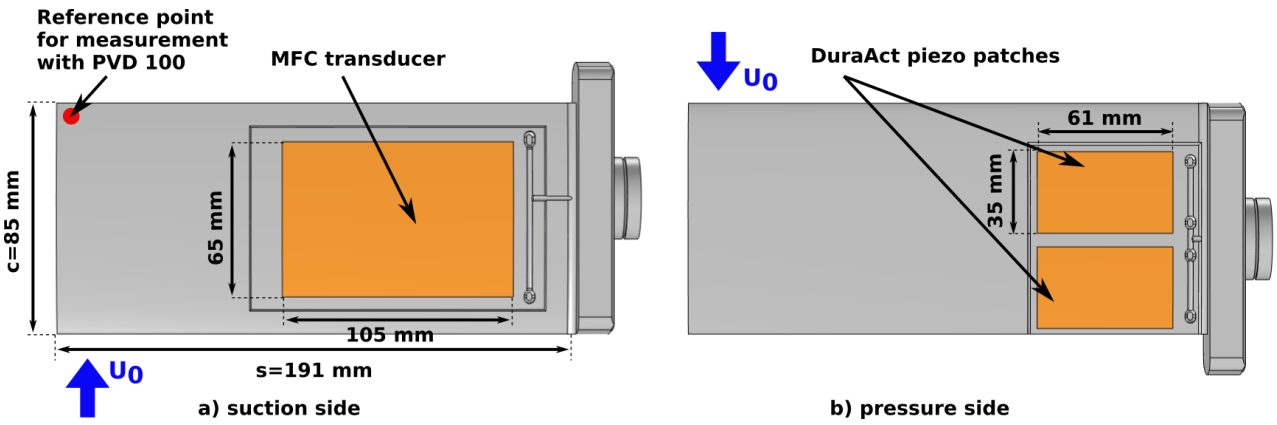

Figure 2.5: Truncated NACA 66-306 hydrofoil geometry and piezoelectric patch arrangement. Views of the suction and pressure-side.

covered with a thin layer of paraffin to avoid discontinuities on the foil surface. DuraAct transducers are less sensitive to water impregnation than MFC transducers and are not used for vibration mitigation so their capacitance drift is not a problem. An image of the truncated hydrofoil is presented in figure 2.6.

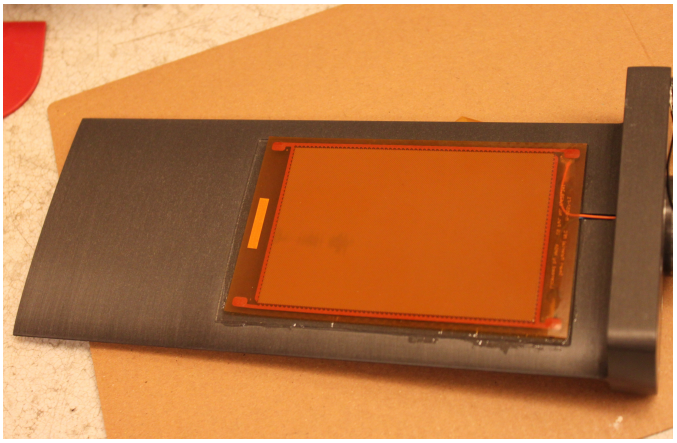

Figure 2.6: Image of the truncated hydrofoil. The MFC transducer is visible and was not covered by epoxy at this stage of the manufacturing.

2.1.3 Laser vibrometry

Laser vibrometry is a contactless vibration measurement method using the Doppler-effect principle. The phase-shift between the emitted and received laser signals provides a characterization of the displacement velocity related to the structure. Two Polytec® vibrometers were used: a PSV-400-B and a PVD-100. The main characteristics of these vibrometers are summarized in table 2.1. The PVD-100 is a single measurement point vibrometer while the PSV-400-B consists of a high precision scanning unit that can record the vibration velocity at different measurement points defined by a user-defined grid. This type of measurement enables to reconstruct the operational deflection shapes of the structure. The vibration velocity temporal evolution was measured at a reference point by the PSV-400-B vibrometer. This signal was then converted to frequency domain by Fast Fourier Transform (FFT). Because the bending and twisting mode amplitudes are maximal at the edges opposite to the clamping device, the reference point is placed at 5 mm from the trailing-edge on the upper-side of each structure. To enhance the reflection of the laser-beam at the reference point, a local reflective sticker was added on the structure. The deflection at various locations of the structure was measured by

the Polytec® PSV-400-B vibrometer, coupled with the PDV-100 used as a reference for phase-shift evaluation.

Mode shapes and natural frequencies were characterized in still air and in still water. The results are summarized in table 2.2. For both studied geometries this was made by analysing the vibration response of the structure at a reference point to a white-noise signal of bandwidth 0 to 2 kHz supplied to the two DuraAct piezoelectric transducers, an example of a similar arrangement can be found in [107]. Figure 2.7 presents the vibratory Frequency Response Function (FRF) of the blunt plate (2.7a) and the truncated hydrofoil (2.7b) to the piezoelectric voltage excitation in air and in water at the reference point. The FRF corresponds to FRF = Velocity(m.s^{-1})/Voltage(V) and its amplitude is expressed in decibels as FRF(dB) = 20.log(FRF/FRF$_{\text{reference}}$) with FRF$_{\text{reference}}$ = 1 m.s^{-1}.V^{-1}. The modes shapes associated with each natural frequency for the blunt plate and truncated hydrofoil geometry surrounded by water are presented in figures 2.8a and 2.8b.

PDV-100			**PSV-400-B**
Type	*Single point*	Type	*Scanner*
Laser type	*HeNe*	Laser type	*HeNe*
Laser wavelength	$\lambda = 633$ nm	Laser wavelength	$\lambda = 633$ nm
Velocity range	$0.01 - 10$ m.s^{-1}	Velocity range	10 m.s^{-1}
Frequency range	$0.5 - 22$ kHz	Frequency range	$0.5 - 40$ kHz
Working distance	$0.2 - 3$ m	Working distance	$0.4 - 100$ m
		Angular stability	$< 0.01°$/h
		Angular resolution	$< 0.002°$/h

Table 2.1: Main technical specifications of the Polytec® PDV-100 and PSV-400-B laser vibrometers.

	Blunt Plate	Hydrofoil	Deflection shape
First mode frequency in air f_1^{air}	61.0 Hz	92.5 Hz	Bending
First mode frequency in water f_1^{water}	25.8 Hz	39.4 Hz	
Second mode frequency in air f_2^{air}	308.1 Hz	518.4 Hz	Torsion
Second mode frequency in water f_2^{water}	180.7 Hz	281.2 Hz	
Third mode frequency in air f_3^{air}	482.2 Hz	637.2 Hz	Bending
Third mode frequency in water f_3^{water}	240.4 Hz	302.8 Hz	

Table 2.2: Natural frequencies and modes of the blunt plate and hydrofoil immersed in air and in water.

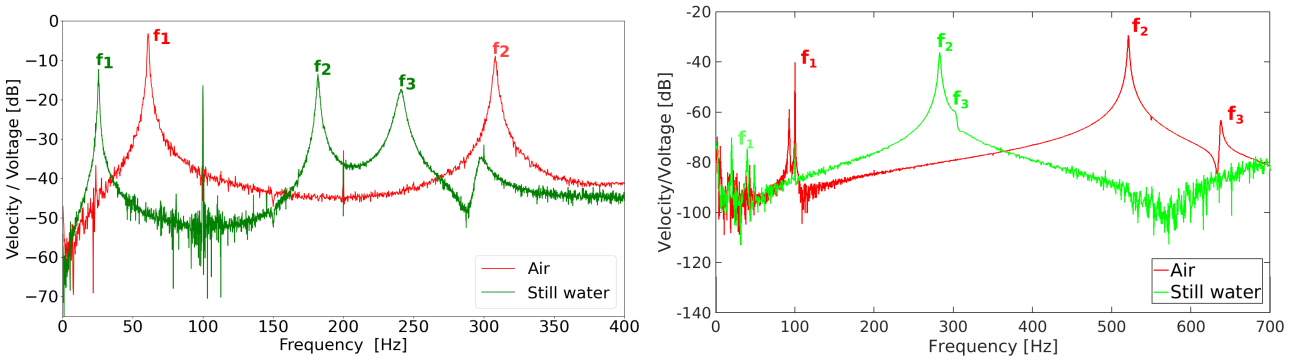

(a) Blunt plate (b) Hydrofoil

Figure 2.7: Vibration Frequency Response Function (FRF) of the (a) blunt plate and (b) truncated hydrofoil at zero flow velocity with piezoelectric excitation. Measurements are performed in air and in still water, they evidence peaks at the natural frequencies of the structure. Piezoelectric transducers are connected in open-circuit.

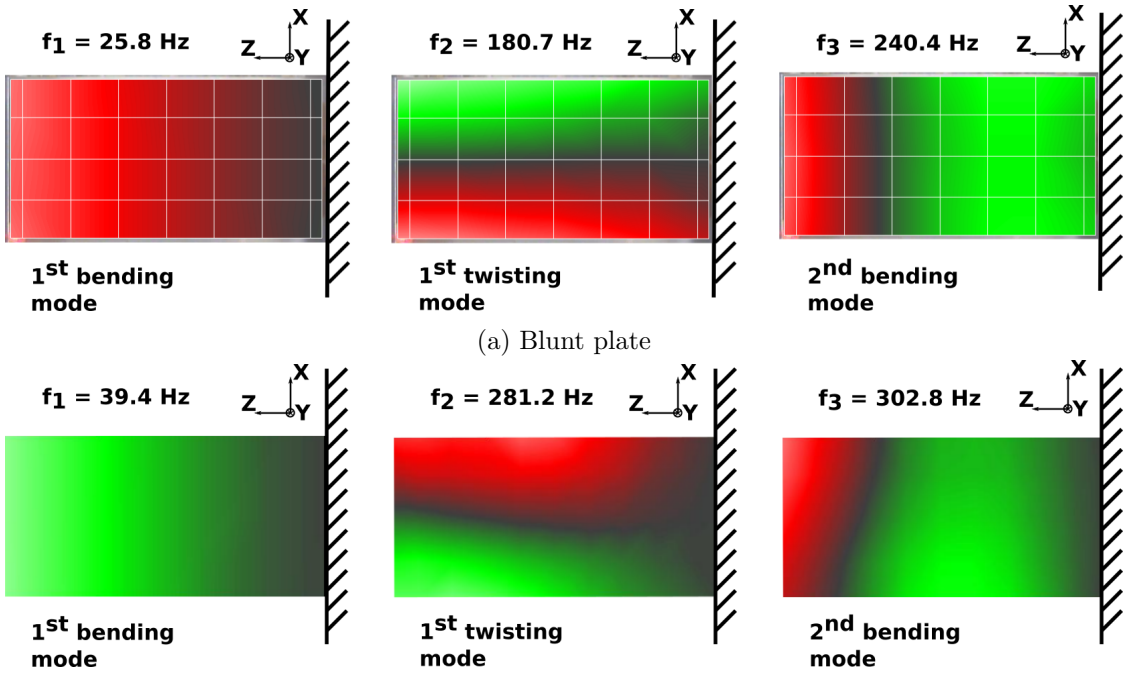

(a) Blunt plate

(b) Hydrofoil

Figure 2.8: Deflection shapes associated with the three first natural frequencies for the (a) plate and for the (b) hydrofoil immersed in water. Red and green areas correspond to the maximum of deformation and black areas to the lowest deformation.

2.1.4 TR-PIV

Particle Image Velocimetry (PIV) is a contactless and non-intrusive laser optical measurement technique. Two Components, two Dimensional (2C2D) Time-Resolved Particle Image Velocimetry (TR-PIV) has been used for the characterization of the flow downstream the structure in the symmetry plane of the tunnel (z=0). The method consists in illuminating an area of interest with a double pulsed laser in order to generate two light sheets with a small time-lag Δt_{pulse}. Each light-sheet is captured by a high-speed camera generating a set of double frames. A subdivision of each of the double frames into Interrogation Areas (IA) is then achieved and a spatial cross-correlation function is applied to each IA. The average particle displacement is computed by evaluating the maximum cross-correlation peak height in each IA of the double-frame. As the time between both images Δt_{pulse} is known, the velocity proper to each IA can be calculated and the entire velocity vector map of the area of interest can be reconstructed. Figure 2.9 describes the principle of the method. Refer to table 2.3 for the general specifications of the PIV system used for our study as well as for the optical (camera and lens) devices characteristics.

For the purpose, the flow has been seeded with polyamide particles. The time between laser pulses Δt_{pulse} and the sampling frequency of the double-frame were adjusted with respect to the upstream velocity. The laser-sheet was aligned with the vertical symmetry plane of the test-section (z=0). As illustrated in figure 2.10a and 2.10b, the viewing areas had dimensions 67.2×42 mm (i.e. $11.2D \times 7D$) for the blunt plate and 58.71×36.7 mm (i.e. $9.6D \times 6D$) for the truncated hydrofoil in the x and y directions respectively. The velocity field was processed with *DynamicStudio 2015c*, using an adaptative PIV method. Due to fluid–structure interactions under flow conditions, false velocity

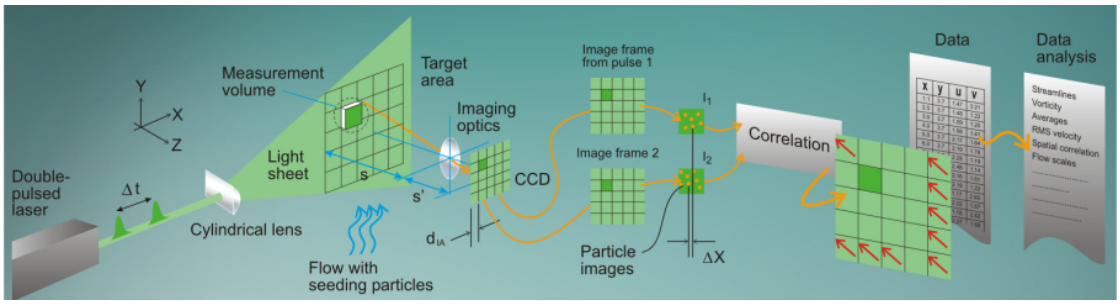

Figure 2.9: Principle of TR-PIV measurement. Image by *Dantec Dynamics*.

vectors at the first PIV measurement point in the close vicinity of the structure's wall may occur. The maximum amplitude of the structure motion under lock-in condition has been estimated to be 20% and 30% of the IA's size for the flat plate and the hydrofoil respectively. The first PIV measurement point in close vicinity of the trailing-edge is expected to be influenced by the structure motion. It was discarded for both structures on the time-averaged analysis and on the POD and SPOD assessments.

Specifications	
Laser type	Nd:YLF
Laser wave length	527 nm
Lasers pulse duration	158 ns
Lasers pulse peak power	11.7 mJ/pulse
High speed camera type	Phantom v611
High speed camera resolution	8 bit
High speed camera lens type	Zeiss Makro Planar 100 mm
High speed camera pixel size	20 μm
Picture size	1280 × 800 pixels
Particle type	Polyamide
Particle density	1.03 g.cm^{-3}
Particle diameter	10 ± 2 μm
Particle relaxation time	8.5 μs
Field of view size	plate: 11.2D×7D, hydrofoil: 9.6D×6D
Scale factor	plate: 52.5 μm/pixel, hydrofoil: 45.87 μm/pixel

Table 2.3: General specifications of the PIV optical device.

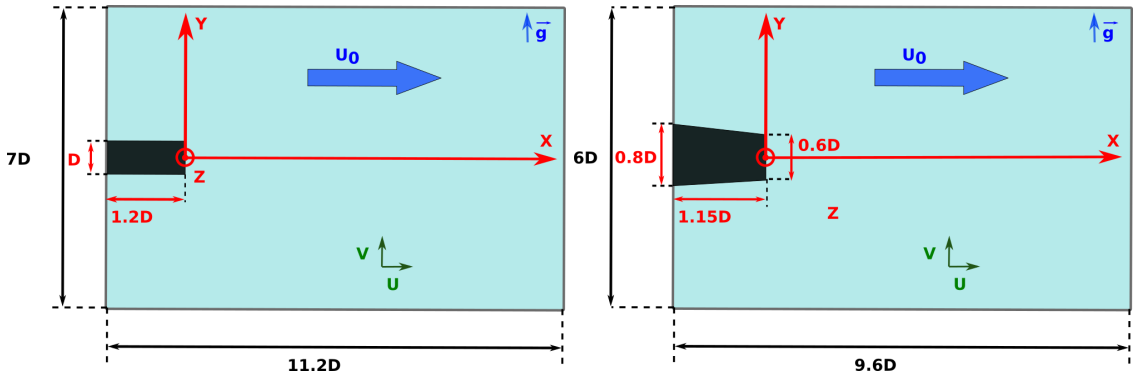

(a) (b)

Figure 2.10: PIV windows used for the (a) blunt plate and (b) truncated hydrofoil near-wake characterization.

For the blunt plate, a mask including the trailing-edge and the maximum vibration amplitude was used. For the hydrofoil no mask was used due to the complex trailing-edge shape and the high magnitude vibrations which would require a dynamic masking application. Table 2.4 summarizes the main acquisition settings of the PIV set-up for both configurations. Exhaustive informations about the PIV technique can be found in Willert et al. [108]. With all these adjustments, the near-wake was investigated from $X/D = -1.2$ to $X/D = 10$ for the flat plate and from -1.15 to 8.45 for the hydrofoil. Examples of (x,y) vorticity fields of a raw snapshot at $U_0 = 3.0$ m.s^{-1} for the blunt plate and hydrofoil geometries are presented in figures 2.11a and 2.11b. A review of recent developments in PIV can be found in Abdulwahab et al. [109].

	Blunt plate	**Truncated hydrofoil**
Time between pulses Δt_{pulse}	$438/U_0$(m/s)	$365/U_0$(m/s)
Recording duration	1 s	2 s
Sampling frequency	1000 or 1400 Hz	1495 Hz
IA size	16×16 pixels^2	16×16 pixels^2
Overlap	No	No
Spatial resolution	$0.14D \times 0.14D$	$0.12D \times 0.12D$
Default validation criteria:		
- Peak height correlation	1.15	0.25
- Kernel size	5×5 pixels^2	5×5 pixels^2
- Detection method	Universal outlier	Universal outlier

Table 2.4: Acquisition settings used for the blunt plate and hydrofoil PIV recordings.

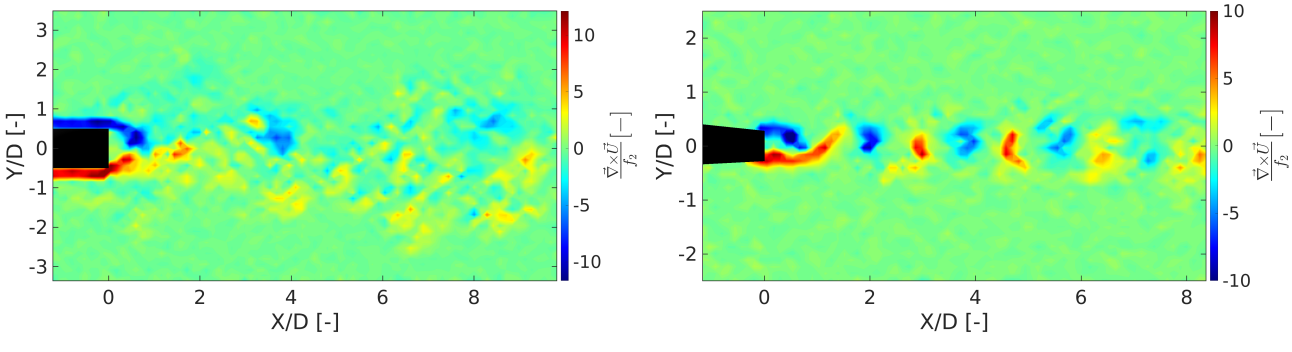

Figure 2.11: (x,y) vorticity field of a raw snapshot at $U_0 = 3.0$ m.s^{-1} for (a) the blunt plate geometry and (b) the truncated hydrofoil.

2.1.5 Non-dimensional numbers

Non-dimensional numbers have been used as control parameters in order to facilitate the analysis and comparison between different velocity conditions. The main basis quantities are the free-stream velocity U_0, the thickness D and chord c, the n order natural frequency of the structure f_n, the vortex shedding frequency f_{vs} in the near-wake and the kinematic viscosity $\nu = 1.10^{-6}$ m^2.s^{-1}. Accordingly, the chord-based and thickness-based Reynolds numbers Re_c and Re_D and the reduced velocity RU of order n can be expressed as

$$Re_c = \frac{U_0.c}{\nu}, \tag{2.1}$$

$$Re_D = \frac{U_0.D}{\nu}, \tag{2.2}$$

$$RU_n = \frac{U_0}{f_n.D}. \tag{2.3}$$

The Strouhal number based on the thickness has been used to characterize the flow-induced vibrations. It is expressed as:

$$St_D = \frac{f_{vs}.D}{U_0}. \tag{2.4}$$

For the purpose of the study, the free-stream velocity was varied from 2.5 m.s^{-1} to 9.5 m.s^{-1} for the blunt plate and from 3.0 m.s^{-1} to 5.5 m.s^{-1} for the truncated hydrofoil. Maximal velocity steps were equal to 0.5 m.s^{-1} and smaller steps of 0.1 m.s^{-1} were used at some particular vibration regimes to obtain an accurate characterization of the fluid-structure coupling. The experimental protocol consists in increasing step by step the free-stream velocity in its operational range. Table 2.5 summarizes the chord and thickness-based Reynolds numbers associated with both studies.

	Blunt plate	**Truncated hydrofoil**
U_0 range	2.5 to 9.5 m.s^{-1}	3.0 to 5.5 m.s^{-1}
Re_D range	1.50×10^4 to 5.70×10^4	1.84×10^4 to 3.37×10^4
Re_c range	2.50×10^5 to 9.50×10^5	2.55×10^5 to 4.68×10^5

Table 2.5: Studied free-stream velocities and associated thickness and chord-based Reynolds numbers.

2.2 Post-treatment methods

2.2.1 Proper Orthogonal Decomposition (POD)

Proper Orthogonal Decomposition (POD) was introduced in fluid mechanics in 1967 by Lumley [110] and has become over the years a powerful vector-field post processing tool applied to flow fields [111, 112]. POD aims at identifying the most energetic structures in the velocity field, which can be coherent structures in a wake, and also permits the filtering of the low energy flow structures. By identifying the most energetic wake structures, a reduced order model of a turbulent flow can be obtained [113]. Let $\mathbf{x}$ denote the position vector : $\mathbf{x}$=(x,y). In the case of a statistically stationary 2D flow with a well defined time-averaged velocity field $(\overline{u}, \overline{v})$, the fluctuating velocity components are decomposed into a sum of deterministic spatial functions $\Phi_k(\mathbf{x})$ or POD modes modulated by time-expansion coefficients $a_k(t)$. Let us denote (Φ_k^u, Φ_k^v) the components of the eigenvector (POD modes) of mode number k. The eigenvalue λ_k is representative of the average energy captured by mode k. For a set of N fluctuating velocity fields, the expansion is truncated at order N:

$$u'(\mathbf{x},t) = u(\mathbf{x},t) - \overline{u}(\mathbf{x}) = \sum_{i=1}^{N} a_k(t)\Phi_k^u(\mathbf{x}). \tag{2.5}$$

$$v'(\mathbf{x},t) = v(\mathbf{x},t) - \overline{v}(\mathbf{x}) = \sum_{i=1}^{N} a_k(t)\Phi_k^v(\mathbf{x}). \tag{2.6}$$

where u' and v' are respectively the stream-wise and vertical fluctuating velocity components. Figure 2.12 offers an example of a time-expansion coefficient $a_1(t)$ and its associated spatial distribution Φ_1^u. A detailed description of the POD method can be found in appendix B. For additional theoretical background and mathematical demonstrations in the infinite-dimensional space refer to the following studies [114, 115, 116, 117].

In the present study the snapshot method introduced by [118] has been employed. It has the specificity of speeding up the calculation. The method relies on the fact that the original POD equation is almost symmetric in t and $\mathbf{x}$ because mathematically there is no major difference between the temporal variable t and the spatial variable $\mathbf{x}$.

The kinetic turbulent energy (TKE) is a helpful criterion to associate POD modes and real physical phenomena. The TKE is directly related to the eigenvalues, hence the percentage of the total TKE contained in mode i on the total TKE is expressed as the eigenvalue of mode i divided by the sum of

all eigenvalues:

$$\%TKE_k = 100 \times \frac{\lambda_k}{\sum_1^N \lambda_k}. \tag{2.7}$$

Associating POD modes with real physical phenomena is much easier when a few number of modes contain a large portion of the TKE. According to the classification of the eigenvalues stated before, the first modes are necessarily the most energetic. As a result, an extensive analysis of the first modes will, in many cases, provide a reliable comprehension of the real flow characteristics.

The TKE also offers the opportunity to verify that the POD computation is fully converged (i.e. that the number of snapshots is large enough). Figure 2.13 presents the TKE level depending on the number of snapshots for the nine first POD modes. This analysis was done for the flat plate geometry at $Re_c = 3.0 \times 10^5$. It appears that the computation is fully converged for a number of snapshots N_t greater than 200. As the computation time was not prohibitive for the present studies, the total number of snapshots was used for the flat plate (1000 snapshots) and hydrofoil analysis (2990 snapshots). It is of prime importance to verify the convergence before performing the physical interpretation. Also, this verifications is useful for datasets with a very high number of snapshots because it enables to perform the POD computation on a reduced dataset which will considerably shorten the computation time.

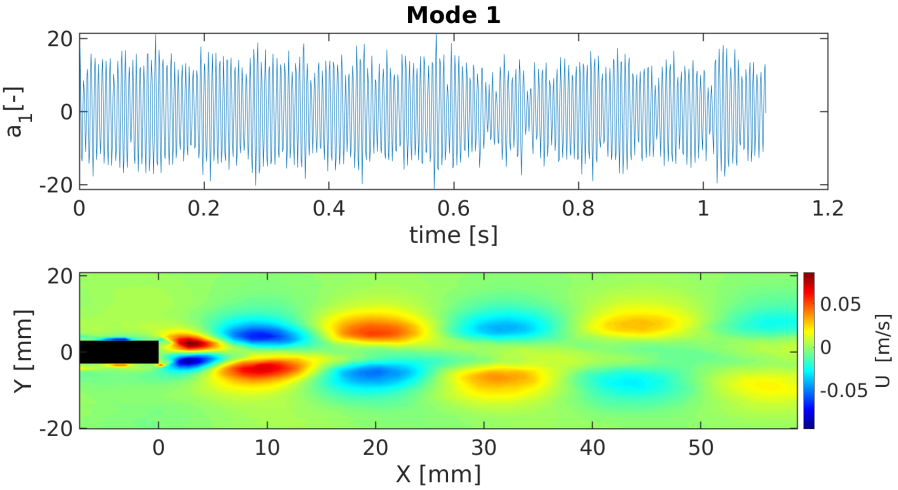

Figure 2.12: Example of time evolution of the expansion coefficients and spatial POD mode number 1 obtained with the stream-wise velocity dataset recorded by PIV at $U_0 = 3.0$ m.s^{-1} for the blunt plate geometry.

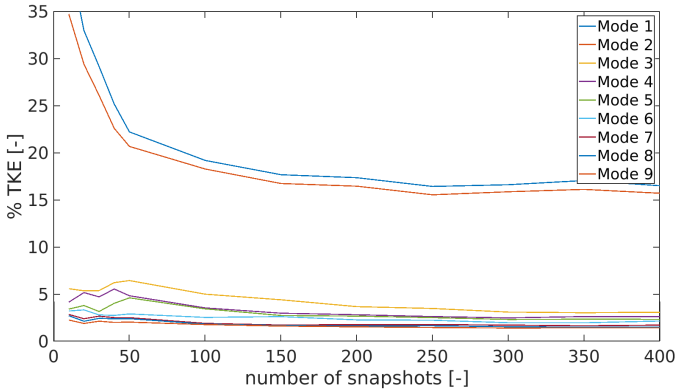

Figure 2.13: Analysis of the POD convergence for the flat plate geometry at $Re_c = 3.0 \times 10^5$. Computation is fully converged for a number of snapshots N greater than 200.

The POD approach has some limitations. When trying to identify coherent structures with the POD method, one should keep in mind that the observed modes are nothing else than mathematical objects representing spatial zones of correlation.The spatially coherent structures represented by space-only POD modes are composed of contributions from spatio-temporal coherent structures at many frequencies. Practically, this is manifested as broadband frequency content within the coefficients $a_j(t)$. This highlights the fact that each space-only POD mode typically represents flow phenomena at many different time-scales, which muddies their interpretation. Fluctuations are proper to each variable and these are not necessarily correlated. For the present study, the POD method was used to identify coherent wake structures. The most energetic POD modes obtained in the near-wake were compared by analysing their expansion coefficient $a_j(t)$ and their spatial distribution Φ_k^u and Φ_k^v.

2.2.2 Spectral Proper Orthogonal Decomposition (SPOD)

General principle

The limitations of the POD presented before can be avoided by using a variant of the standard POD called Spectral Proper Orthogonal Decomposition (SPOD). This method has the advantage of being spatially and time-optimal and was used for analysing the near-wake dynamics of the truncated hydrofoil. SPOD is often described as the frequency domain form of POD. The main advantage of the method is that it is optimal by construction for identifying flow structures that evolve coherently in both space and time [119] which is the case of most statistically stationary flows. The method

is particularly adapted to understand wake dynamics as flow phenomena are decoupled at various time-scales. SPOD involves the decomposition of the cross-spectral density (CSD) tensor and leads to modes that each oscillate at a single frequency and optimally account for the statistical variability of turbulence [21]. In practice, part of the flow described by a particular SPOD mode is perfectly correlated with the part of the flow described by that same mode at all times and entirely uncorrelated with the part of the flow described by all other modes at all times. The main algorithm behind SPOD is the Welch's method [120] which is an averaging technique that accurately predicts the cross-spectral density (CSD) tensor from a time-series [119]. The SPOD algorithm is briefly presented in appendix B as well as general principles to setup the SPOD parameters.

Figure 2.14 summarizes the Welch's method for estimating SPOD modes. The matrix Q of size $n \times N_t$ made of N_t time-series snapshots (i.e. time-series of the fluctuating velocity components measured at n grid points of the TR-PIV, is splitted into N_b blocks. The blocks can overlap. Each block is made of N_{FFT} successive time-series snapshots. The snapshots matrix $Q^{(i)}$, of size $n \times N_{FFT}$, denotes the snapshots matrix corresponding to the i^{th} block. A Fast Fourier Transform (FFT) is applied to the snapshots matrix of each block, leading to N_b datasets of frequency series of the fluctuating velocity components, arranged in a matrix $\hat{Q}^{(i)}$. The Welsh method is used to compute the FFT. Each column of $\hat{Q}^{(i)}$, corresponding to a given frequency f_k, is added into a new matrix $\hat{Q}_{f_k}$, which is an $n \times N_b$ matrix. Solving an eigenvalue problem into $\hat{Q}_{f_k}$ enables to decompose the

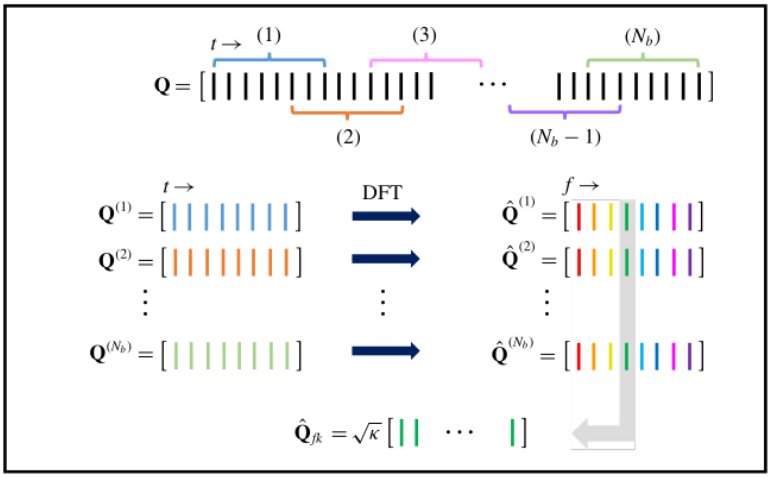

Figure 2.14: Schematic presentation of the Welch's method for estimating SPOD modes. Figure by Towne et al. [21].

fluctuating velocity component in the frequency domain $\mathbf{u}'(\mathbf{x}, f_k)$ into N_b modes, each mode i being characterized by the eigenvalue $\lambda^i(f_k)$ and the eigenvector $\phi^i(\mathbf{x}, f_k)$ of the covariance matrix. Table 2.6 summarizes the SPOD parameter employed for the analysis of the near-wake of the truncated hydrofoil at lock-in ($Re_c = 3.74 \times 10^5$). A MATLAB version of the SPOD algorithm is available at `https://github.com/SpectralPOD/spod_matlab`.

N_{FFT}	N_{ovlp}	N_b	Δf	windowing
256	50%	22	5.8 Hz	Hamming

Table 2.6: Parameters used for the SPOD analysis of the near-wake of the hydrofoil at lock-in ($Re_c = 3.74 \times 10^5$).

2.2.3 Vortex identification algorithm

Real flows are often characterized by a superposition of large scale vortices on a small scale turbulent velocity field [121]. It is of great interest to identify the main geometrical characteristics of these large scale vortices in order to understand the wake dynamics and the turbulence mechanisms. The present work has extensively used the identification method developed by Graftieaux et al. [122]. This method is based on two scalar functions, Γ_1 and Γ_2, which are derived from the velocity fields. These functions are able to detect the locations of the center and the boundaries of the large-scale vortices by considering only the topology of the velocity field and not its magnitude. This method is very robust and is able to process data sets resulting from large PIV recordings and LES or DNS simulations leading to statistical studies of the vortex characteristics. For the present study, the Γ_2 method was used preferentially. The principle of the method is described in appendix B.

Table 2.7 summarizes the applied criteria for the vortex core detection. An example of Γ_2 vortex detection applied on POD spatial mode 1 at $U_0 = 3.0$ m.s^{-1} for the blunt plate geometry is presented in figure 2.15. As can be seen, POD mode 1 is characterized by high alternating vorticity regions and identified as primary vortex shedding mode. The vortices cores are correctly detected by the Γ_2 method. The root mean square value of the circulation of each vortex of mode 1 is deduced from the relationship:

$$\Gamma_{rms} = \int_A \boldsymbol{\nabla} \times \mathbf{U}_{rms} \, ds, \tag{2.8}$$

Minimum value of $\|\Gamma_2\|$ in the vortex core	$2/\pi$
Minimum X distance from trailing-edge	1 mm
Maximum Y distance from the wake centreline	3 mm
Minimum number of detected points	10

Table 2.7: Vortex core centres detection criteria.

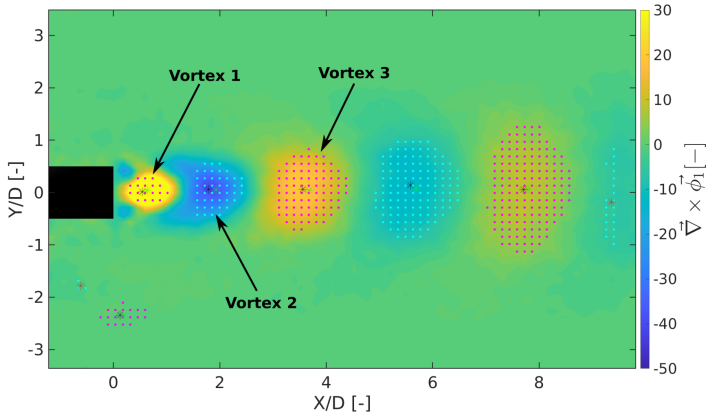

Figure 2.15: Example of vortex detection applied at $Re_c = 3.0 \times 10^5$ for the blunt plate geometry on spatial mode 1. Blue dots represent the detection of the negative rotation rate vortices, magenta dots the positive rotation rate vortices with the Γ_2 method. The vortex centres have been detected with the Γ_1 (black star) and Γ_2 methods (green star).

using the rms values of the expansion coefficients of mode 1:

$$u^1_{rms}\mathbf{x} = a_1^{rms}\phi_1^u\mathbf{x}, \tag{2.9}$$

$$v^1_{rms}\mathbf{x} = a_1^{rms}\phi_1^v\mathbf{x}. \tag{2.10}$$

2.2.4 Statistical and spectral analysis of the wake

For the statistical analysis, the measured spurious velocity vectors, as well as the velocity fluctuations induced by lowest energetic turbulent structures have been suppressed from the instantaneous velocity fields by reconstruction of the velocity field as a linear combination of the first modes, for which the cumulative energy is at least 90% of the total energy:

$$u_{reconstructed}(t,\mathbf{x}) = \overline{u}(\mathbf{x}) + \sum_{i=1}^{n_{90}} a_k^u(t)\Phi_k^u(\mathbf{x}), \tag{2.11}$$

$$v_{reconstructed}(t,\mathbf{x}) = \overline{v}(\mathbf{x}) + \sum_{i=1}^{n_{90}} a_k^v(t)\Phi_k^v(\mathbf{x}). \tag{2.12}$$

The local turbulent stresses in the stream-wise direction $\overline{u'^2}$, in the normal direction $\overline{v'^2}$, as well as the local turbulent shear stress $\overline{u'v'}$ have been deduced from the reconstructed velocity field, as follows:

$$\overline{u'^2}(\mathbf{x}) = \overline{(u_{reconstructed} - \overline{u_{reconstructed}})^2} = u_{rms}^2(\mathbf{x}), \tag{2.13}$$

$$\overline{v'^2}(\mathbf{x}) = \overline{(v_{reconstructed} - \overline{v_{reconstructed}})^2} = v_{rms}^2(\mathbf{x}), \tag{2.14}$$

$$\overline{u'v'}(\mathbf{x}) = \overline{(u_{reconstructed} - \overline{u_{reconstructed}})(v_{reconstructed} - \overline{v_{reconstructed}})}, \tag{2.15}$$

where $\bar{}$ denotes the time average.

The time-evolution (Figure 2.16a) of the expansion coefficients $a_k(t)$ has also been analysed for $1 \leq k \leq 9$ by applying a FFT algorithm. Figure 2.16b displays an example of frequency spectrum of the coefficient $a_1(t)$ of mode 1, characteristic of the Karman wake for the blunt plate configuration. The highest amplitude in the spectrum is associated to the frequency of the vortex shedding f_{vs} of the Karman vortices.

2.2.5 Spectral analysis of the flow-induced vibrations

For the characterization of the structural vibrations induced by the fluid flow, only the spectrums recorded by the PDV-100 vibrometer at the reference point have been analysed. The root mean square velocity of each spectrum was calculated by integration in the discrete frequency domain of each spectrum and is noted V_s^{rms}. The highest amplitude of each spectrum and it's associated frequency

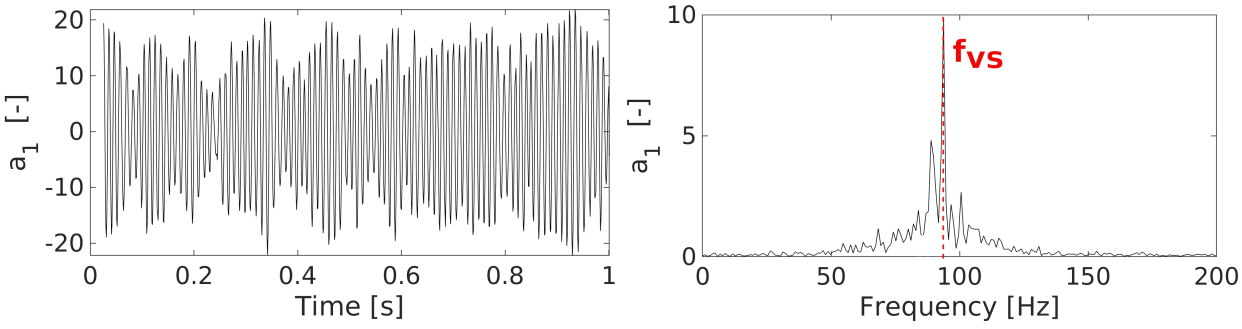

(a) (b)

Figure 2.16: Time evolution (a) and associated frequency spectrum (b) of the POD expansion coefficient $a_1(t)$, characteristic of the Karman wake at $U_0 = 3.0\ m.s^{-1}$ for the blunt plate geometry.

have also been extracted and are noted V_s^{max} and f_s^{max} respectively. Figure 2.17 presents an example of vibration velocity spectrum for the flat plate geometry at $U_0 = 4.5$ m.s^{-1} and its corresponding V_s^{max} and f_s^{max}. The analysis methods described here will be put into practice in te next chapter dedicated to the fluid-structure interaction sustained by the blunt plate.

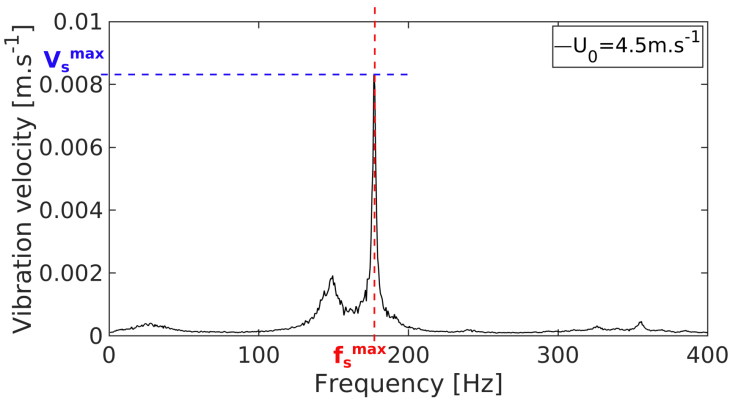

Figure 2.17: Vibration velocity spectrum at $Re_c = 4.5 \times 10^5$: V_s^{max} and f_s^{max} correspond respectively to the magnitude and frequency of the highest peak.

Chapter 3

Fluid-structure interaction of elongated bodies

" If you want to find the secrets of the universe, think in terms of energy, frequency and vibration. "

Nikola Tesla

Content

The present chapter aims at characterizing the structure of the near-wake and the flow-induced vibrations of a blunt plate with chord to thickness ratio c/D of 16.7. It provides new insight regarding vortex-induced vibrations for this specific configuration. To have a better control of the separating points, the leading and trailing edges are square. The plate was immersed at zero degrees of incidence in a uniform flow. The chord-based Reynolds Re_c is ranging into $[2.5\times10^5, 9.5\times10^5]$ and the thickness-based Reynolds Re_D number is varied in the range $[1.5\times10^4, 5.7\times10^4]$. The free stream velocity range has been selected in order to investigate different vibration regimes, including the lock-in resonance with the torsional vibration mode.

For this purpose, the structure of the near-wake is characterized by PIV (Particle Image Velocimetry) and analysed with the use of POD (Proper Orthogonal Decomposition). Different types of POD modes are identified. The contribution of these POD structures is discussed according to the vibration regime of the plate (out of resonance, lock-off resonance and lock-in with the first torsional mode). Also, the evolution with the Reynolds number of the characteristics of the Karman vortices is analysed according to the vibration regime.

The chapter is organized as follows: In section 1 the vibrations of the structure under flow excitation are analysed and in section 2 we present the general features of the near-wake. Section 3 presents the influence of Re_c on the properties of the Karman vortices. Finally in section 4, the POD decomposition of the near-wake is used to discuss about the energetic contributions of various types of structures at the different vibration regimes. Section 5 offers some conclusions.

3.1 Vibrations of the structure under flow excitation

The fluid structure interaction process has been identified as a vibratory response of the structure to hydrodynamic excitation sources consisting mainly in vortex shedding. The following sections aims at analysing the evolution with the Reynolds number of the vortex shedding frequency f_{vs} of the Karman wake together with the vibration characteristics of the structure. This analysis makes it possible to identify some particular vibratory regimes. A constant Strouhal number implies a linear evolution of the vortex shedding frequency f_{vs} with the free-stream velocity U_0 and is proper to non-resonant regimes.

The cartography of the power spectral density of the vibration velocity of the plate is displayed

in figure 3.1 and plotted in the (f_s/f_2,Re_c) plane. f_s corresponds to the vibration frequency of the structure measured by vibrometry and, as a reminder, f_2 is the second natural frequency of the structure (i.e. the natural frequency of the first torsional mode measured in still water). Figure 3.1 evidences the contribution of the natural frequency in the power spectral density of the vibration velocity. Vertical lines of maxima of the power spectral density evidences that the resonance vibration regimes of the plate occur for Re_c ranging in the intervals $[4.5\times10^5-6.0\times10^5]$ and $[7.0\times10^5-8.0\times10^5]$ for the resonance with the first twisting mode ($f_s^{max}=f_2$) and the resonance with the second bending mode ($f_s^{max}=f_3$) respectively.

For the purpose of the fluid-structure interaction regimes analysis, figure 3.2a presents the evolution, according to the Reynolds number, of both frequencies characteristic of the structure (f_s^{max}) and of the vortex shedding in the fluid (f_{vs}) and figure 3.2b presents the magnitude of the vibration velocity of the structure. Both quantities V_s^{max} and V_s^{rms} are normalized by f_2D. In Figure 3.2a, all the frequencies are scaled with the natural frequency of the first twisting mode f_2. The horizontal lines stands for the plateau achieved at the resonance regime with the twisting mode ($f=f_2$) and with the second bending mode ($f=f_3$). In Figure 3.2a, if the plate frequency f_s^{max} is coupled with the vortex shedding frequency f_{vs} (lock-in), the star and circle symbols overlap. The lock-in resonance regimes with the twisting and second bending modes occur for Re_c ranging in the intervals $[5.1\times10^5-6.0\times10^5]$ and $[7.5\times10^5-8.0\times10^5]$ respectively. The plate and the vortex shedding frequencies are together

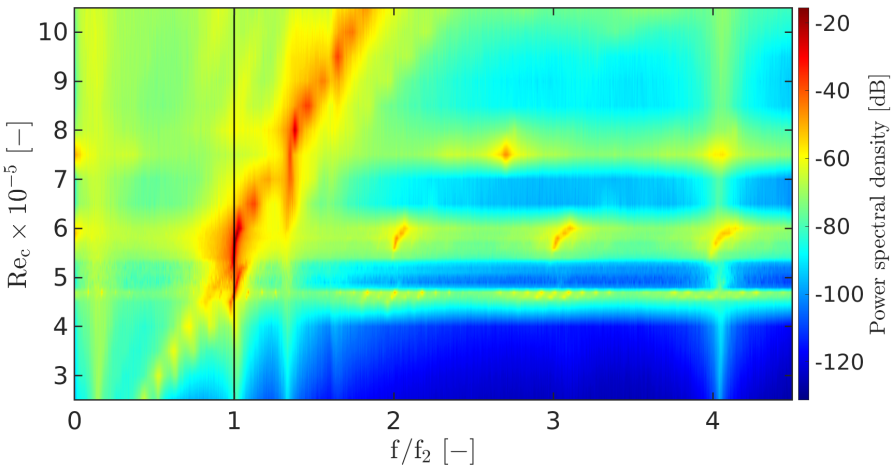

Figure 3.1: Cartography of the power spectral density of the structure vibration velocity. Cartography in the plane (f_s/f_2, Re_c). Power spectral density expressed in dB.

locked with the natural frequency of the structure. Figure 3.2b reveals that the highest vibration velocity magnitude appears at the lock-in resonance regime with the first twisting mode at Re_c equal to 5.7×10^5 ($RU_2 = U_0/f_2D = 5.25$). A second maximum of the vibration velocity is visible at Re_c equal to 8.0×10^5 ($RU_3 = U_0/f_3D = 5.56$) in the lock-in resonance regime with the second bending mode. From Figure 3.2a, the out of resonance regime is observed for Reynolds Re_c ranging in the intervals $[2.5 \times 10^5 - 4.5 \times 10^5]$, $[6.0 \times 10^5 - 7.0 \times 10^5]$ and $[8.0 \times 10^5 - 9.5 \times 10^5]$. For this regime, the plate's vibration frequency (f_s^{max}) is driven by the vortex shedding frequency (f_{vs}). We observe a linear scaling with respect to the Reynolds number of both frequencies, which is in agreement with a constant Strouhal number. The best linear fit leads to $St_D = 0.189(\pm 0.003)$. As expected for the lock-in resonance regime with the twisting mode, the reduced velocity $RU_2 = 5.25$ at the maximum vibration amplitude is in agreement with $1/St_D = 5.29(\pm 0.08)$, which confirms the measured value of St_D. Note that the reduced frequency $2\pi \times St_D = 1.2$ is of the order of unity, as been expected from the scaling of the Navier-Stokes equation in the wake.

In figure 3.2a, Reynolds number ranges where the star and circle symbols do not overlap indicate the lock-off regime. This appears for Re_c ranging in the intervals $[4.5 \times 10^5 - 5.1 \times 10^5]$ and $[7.0 \times 10^5 - 7.5 \times 10^5]$, where the dominant structural vibration frequency f_s^{max} is equal to f_2 and f_3 respectively. For this regime, the vortex shedding frequency is not coupled with the plate's frequency and the vortex shedding frequency obeys same Strouhal law ($St_D = 0.189$) as in the out of resonance regime. Interestingly, a local maximum of the vibration velocity amplitude is observed at $Re_c = 4.8 \times 10^5$ ($RU_2 = 4.42$) in the lock-off resonance regime. The occurrence of the lock-off regime is of particular interest for designers as it introduces the fact that high amplitude vibrations may occur for a Reynolds number range larger than those expected at the lock-in.

The occurrence of the lock-off resonance regime, which is not pointed out in the literature survey, may be due to the contribution of a secondary hydrodynamic excitation source, which is different from the vortex shedding primary excitation source. To confirm this statement, the vibration velocity spectra are plotted in Figure 3.3 for two different upstream velocities in the out of resonance regime. Two hydrodynamic excitation sources are visible on these spectra. The highest peak has a frequency $f_s^{primary} = f_s^{max} = f_{vs}$ and is associated with the Karman vortex shedding at the trailing-edge. A second excitation peak at $f_s^{secondary}$ is visible. The frequency of both hydrodynamic excitation sources evolve linearly while the Reynolds number increases and the corresponding Strouhal numbers $St_s =$

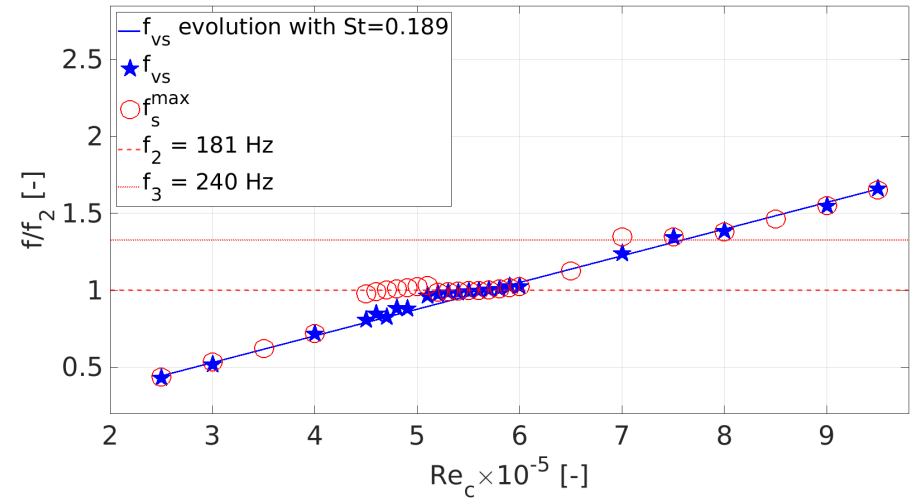

(a)

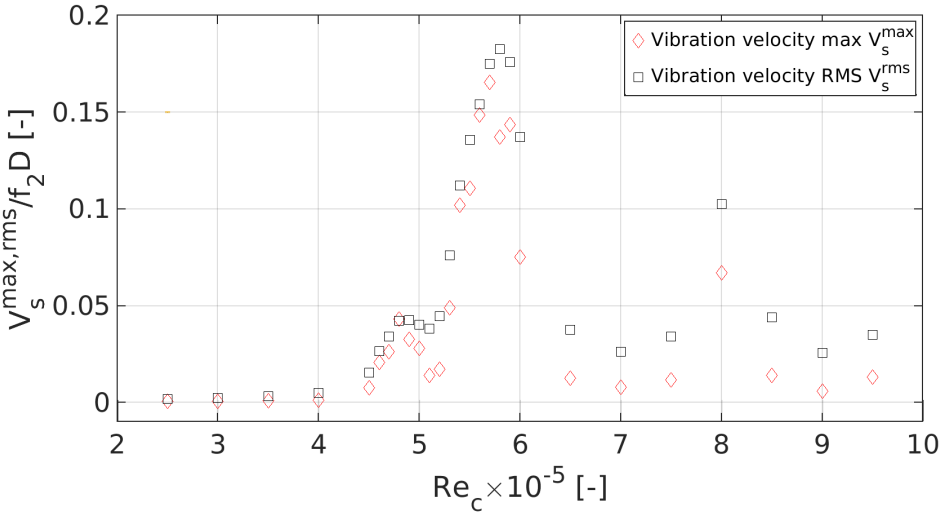

(b)

Figure 3.2: Evolution with Reynolds number of the structural vibration frequency f_s^{max} and Karman vortex shedding frequency f_{vs} scaled by f_2 (a). Maximal uncertainty is 0.6 Hz for f_s^{max} and 1 Hz for f_{vs}. Evolution of V_s^{rms} and V_s^{max} with Reynolds (b). Maximal uncertainty on V_s^{rms} is $\pm 2.17 \times 10^{-4}$ m.s^{-1}.

$f_s D/U_0$ are respectively $St_s^{primary} = 0.19$ and $St_s^{secondary} = 0.22$. Interestingly $1/St_s^{secondary} = 4.54$ is close to the value of the reduced velocity observed at the maximal vibration amplitude of the lock-off resonance regime ($RU_2 = 4.42$), which confirms that this regime occurs when $f_s^{secondary}$ locks with the natural frequency of the structure. This confirms the existence of a secondary hydro-elastic coupling mechanism in addition to the lock-in mechanism with the vortex shedding, as observed by [10].

Data about the Strouhal number, characteristic of the vortex shedding at the trailing-edge, are

missing in the literature survey for large c/D ratios and high Reynolds numbers. For $c/D > 12$ and $Re_D > 2.0 \times 10^3$, Nakamura et al. [8] did not observe an organised vortex shedding with a characteristic peak frequency. This disorganisation of the vortex street was confirmed by Parker et al. [46] in the range $[1.4 \times 10^4 - 3.1 \times 10^4]$. However, for larger c/D values ($c/D > 16$), the vortex shedding becomes more regular again and is characterized by a broadband peak in the velocity spectra. In this case, for large c/D values and Re_D in the range $[1.4 \times 10^4 - 3.1 \times 10^4]$ corresponding to a reorganized vortex shedding, the Strouhal number of the blunt plate approximates the values of plates with a similar geometry and rounded leading-edges [46].

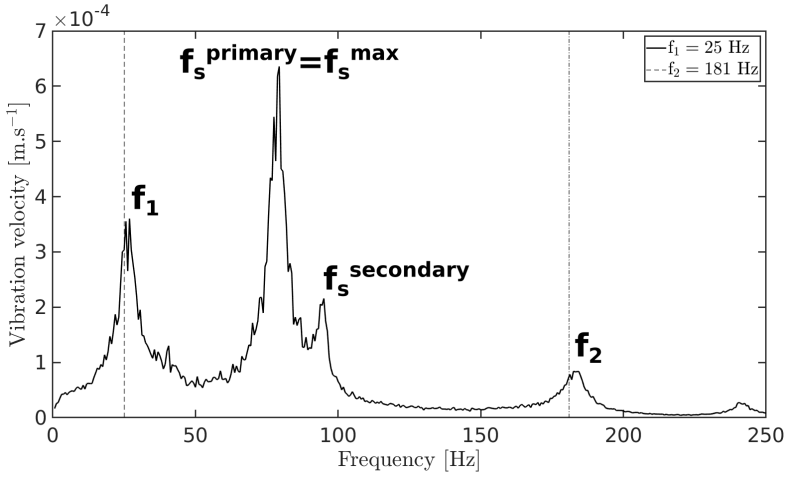

(a)

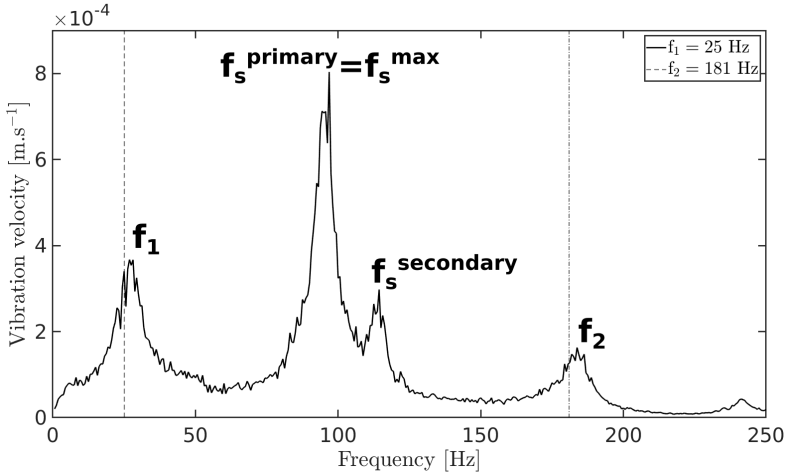

(b)

Figure 3.3: Vibration velocity spectrum at $U_0 = 2.5$ m.s^{-1} corresponding to $Re_c = 2.5 \times 10^5$ (a) and $U_0 = 3.0$ m.s^{-1} corresponding to $Re_c = 3.0 \times 10^5$ (b).

The value $St_D = 0.189$ of our experiments is consistent with the value $St_D = 0.20$ measured for a plate with rounded edges of same c/D [7] when the main hydrodynamic excitation source is the TEVS mechanism. Note that $St_D = 0.195$ is the Strouhal number observed in the wake of cylinders for turbulent shedding conditions and Re_D in the range $[1.0 \times 10^4 - 2.0 \times 10^4]$ [42].

Let us now discuss about the origin of the secondary excitation source source. For the secondary source the measured Strouhal number $St^{secondary}$ approximates $6 \times St_1$, with $St_1 = 0.6D/c$ where 0.6 is the stepwise increase in the Strouhal number based on the chord length measured by Nakamura et al. [8] when increasing the chord to thickness ratio up to 16 at low Reynolds numbers. This stepwise increase of the Strouhal number at low Reynolds number has been attributed by Nakamura et al. [8] to the impinging instability of the separated boundary layer in the presence of a sharp trailing-edge corner. According to Kaneko et al. [63] for a plate of $c/D = 16$, a transition between impinging leading-edge vortex (ILEV) and trailing-edge vortex shedding (TEVS) regimes exists. Because of the dimensions of our plate, both regimes may coexist and contribute to the excitation of the structure leading to two distinct excitation sources. The signature of $f_s^{secondary}$ in the flow, as part of an other hydrodynamic excitation source, will be examined further in section 3.4, when analysing POD modes of the near-wake.

Observations made in this section, have permitted to define different regimes of fluid-structure interaction which are summarized in table 3.1 depending on a specific Reynols number range or reduced velocity range. Based on these identified regimes, 3 operating points have been selected (A, B, C). Each of them corresponds to a particular regime with regard to the first twisting resonance mode. Indeed, the coupling of the first twisting mode of the structure with the two-dimensional vortices shed in the wake gives rise to the largest vibration velocity of the plate. Point A corresponds to no resonance, point B to resonance without lock-in (lock-off resonance) and point C to the lock-in resonance. Points B and C are conditions of local maxima of V_s^{rms}. The characteristics of these operating points are summarized in table 3.2.

Reynolds range	**RU range**	**Regime**	**Frequencies**
$2.5 \times 10^5 \leq Re_c \leq 4.5 \times 10^5$	$2.30 \leq RU_2 \leq 4.14$	No resonance	$f_{vs} = f_s^{max} = f_s^{primary} \neq f_2$ $f_s^{secondary} \neq f_2$
$4.5 \times 10^5 \leq Re_c \leq 5.1 \times 10^5$	$4.14 \leq RU_2 \leq 4.70$	Resonance lock-off	$f_{vs} = f_s^{primary} \neq f_2$ $f_s^{secondary} = f_s^{max} = f_2$
$5.1 \times 10^5 \leq Re_c \leq 6.0 \times 10^5$	$4.70 \leq RU_2 \leq 5.53$	Resonance lock-in	$f_{vs} = f_s^{max} = f_2$ $f_s^{primary} = f_s^{secondary} = f_2$
$6.0 \times 10^5 \leq Re_c \leq 7.0 \times 10^5$	$4.17 \leq RU_3 \leq 4.86$	No resonance	$f_{vs} = f_s^{max} = f_s^{primary} \neq f_2, f_3$ $f_s^{secondary} \neq f_2, f_3$
$7.0 \times 10^5 \leq Re_c \leq 7.5 \times 10^5$	$4.86 \leq RU_3 \leq 5.21$	Resonance lock-off	$f_{vs} = f_s^{primary} \neq f_3$ $f_s^{secondary} = f_s^{max} = f_3$
$7.5 \times 10^5 \leq Re_c \leq 8.0 \times 10^5$	$5.21 \leq RU_3 \leq 5.56$	Resonance lock-in	$f_{vs} = f_s^{max} = f_3$ $f_s^{primary} = f_s^{secondary} = f_3$
$8.0 \times 10^5 \leq Re_c \leq 9.5 \times 10^5$	$5.56 \leq RU_3 \leq 6.60$	No resonance	$f_{vs} = f_s^{max} = f_s^{primary} \neq f_3$ $f_s^{secondary} \neq f_3$

Table 3.1: Summary of the different fluid-structure interaction regimes according to Re_c range and RU range.

	Reynolds	RU_2	**Regime**	Local max of V_s^{rms}
(A)	$Re_c = 3.0 \times 10^5$ $Re_D = 1.80 \times 10^4$	2.76	No resonance	No
(B)	$Re_c = 4.8 \times 10^5$ $Re_D = 2.88 \times 10^4$	4.42	Lock-off, resonance with twisting mode	Yes
(C)	$Re_c = 5.7 \times 10^5$ $Re_D = 3.42 \times 10^4$	5.25	Lock-in resonance with twisting mode	Yes

Table 3.2: Points of interest and associated vibration regimes and characteristics.

The general features of the vibrational response of the plate have been investigated in order to understand the fluid structure interaction process responsible of high magnitude vibrations. Attention will now be paid to the hydrodynamic properties of the flow downstream the plate. In a first instance, the general features of the near-wake are studied.

3.2 General features of the near-wake

In this section, we initially present raw velocity fields and then we introduce general features of the near-wake based on the computation of time averaged velocity fields. At the end of this section, the evolution with Re_c of the total turbulent kinetic energy (TKE) repartition with respect to the number of POD modes is discussed.

A first inspection of the raw measured instantaneous velocity field reveals the presence of various scales of turbulence. Large vortices are rapidly dissipated into smaller structures that convect through the wake until vanishing. Figure 3.4 presents a raw snapshot of vorticity at $U_0 = 3.0$ m.s^{-1}.

The time averaged velocity fields of the U and V velocity components are presented in figures 3.5a and 3.5b at Re_c equal to 3.0×10^5. The wake region is characterized by a substantial decrease of the streamwise mean velocity component U. A strong gradient in the velocity profiles $\frac{\partial U}{\partial X}$ is visible for X/D included in [0-4] which is characteristic of the very near-wake. Two regions of high magnitude of vertical mean velocity components V are visible for X/D included in $[0-2]$ with a maximum of $|V|/U_0 \simeq 0.2$ at $X/D = 0.7$. This induces a recirculation region composed of two counter rotating vortices for X/D included in [0-1] and Y/D in [-0.5,0.5]. We will also refer to the term wake bubble (WB) to name the recirculation region. This recirculation region is highlighted when plotting the streamlines, as presented in figure 3.5d. This particular region is characterized by negative magnitudes of the horizontal velocity component U which induces a reversed flow. The reversed flow ends at the reattachment point of the wake at $X = L_R \simeq D$. This value is in agreement with the value measured by Taylor et al. [1] for $Re_c = 2.1 \times 10^5$ and $c/D = 7$.

Figure 3.5c presents a (x,y) cartography of the Reynolds shear stress $-\overline{u'v'}/U_0^2$. High magnitude positive and negative shear stress regions are visible for X/D included in [0-4]. These regions of high $|u'v'|$ delineate the recirculation area. Also, one can observe a region of zero Reynolds shear stress inside the recirculation area on both sides of the wake centreline. This particular region is expected

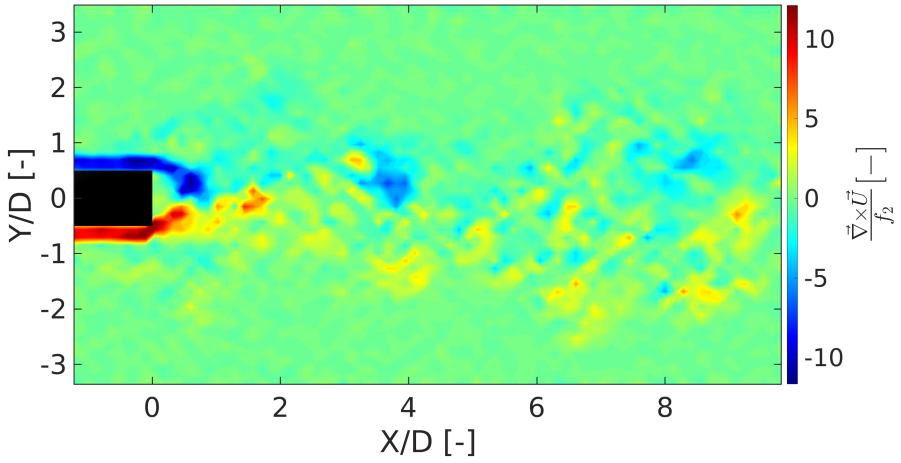

Figure 3.4: (x,y) vorticity field of a raw snapshot at $U_0 = 3.0$ m.s^{-1}.

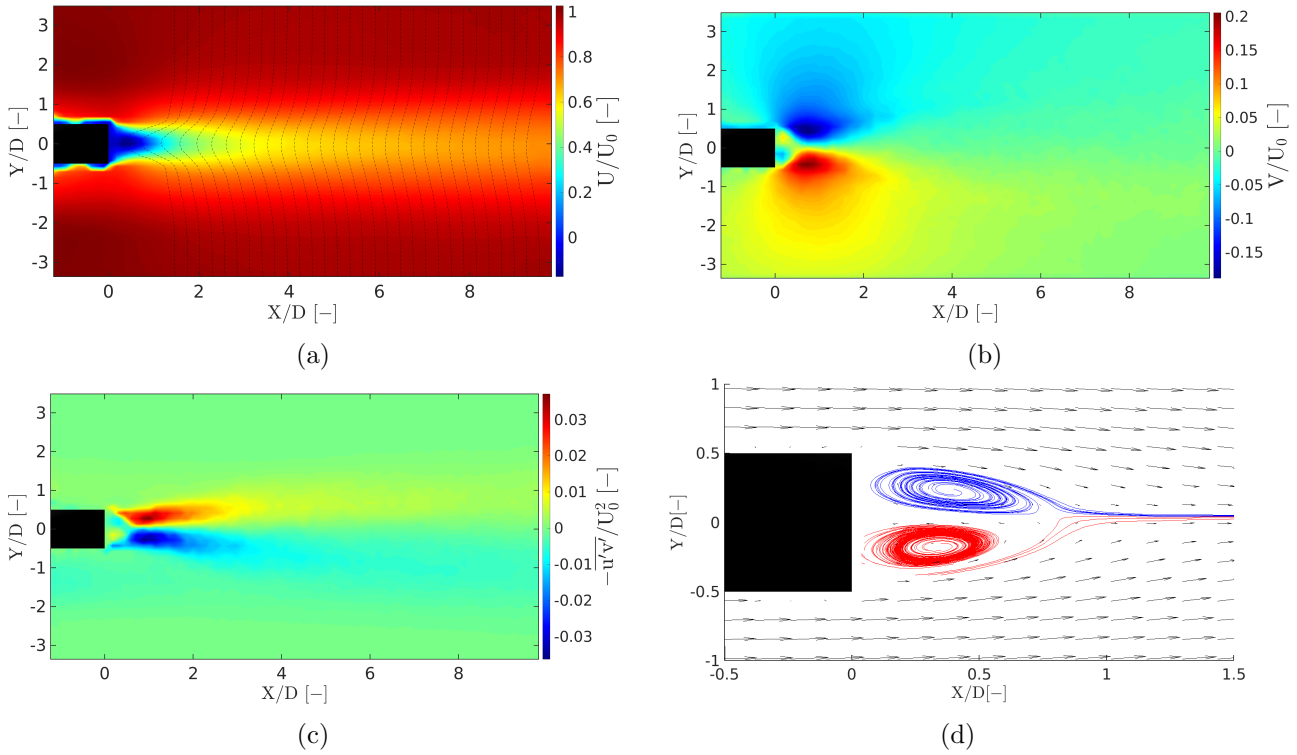

Figure 3.5: (x,y) cartography of the time averaged horizontal U (a) and vertical V (b) velocity components U and V, the Reynolds shear stress $-\overline{u'v'}/U_0^2$ (c) and streamline pattern superimposed to the time averaged (x,y) velocity field (d). For clarity purpose the streamlines under and above the plate have been hidden. Cartographies based on the reconstructed velocity field at $U_0 = 3.0$ m.s^{-1}.

to be the region where minimum pressure occurs, as discussed by Taylor et al. [1]. The patterns of shear stress observed are in agreement with earlier studies and highlight the assertion of Balachandar et al. [40] stating that the pattern of the shear stress regions is a consequence of the vortex shedding activity over a cycle.

The vertical profiles of the normalized velocity deficit $U_{defect}/U_0 = (U_0 - U)/U_0 = f(Y/D)$ measured at X=4D are displayed in figure 3.6 for Re_c of the different vibration regimes. According to the theory of self-similarity of the fully turbulent plane wake, in the far field, the velocity defect measured at the centreline U_{defect}/U_0 is scaled with $\sqrt{C_D.c/x}$. At fixed X positions, comparison of this velocity defect makes it possible to conclude about the drag coefficient C_D. The drag coefficient obviously decreases with increasing Re_c numbers, except at the lock-in with the twisting mode ($Re_c = 5.7 \times 10^5$).

Chopra et al. [123] defines the vortex formation length L_e as the distance over which the vortices

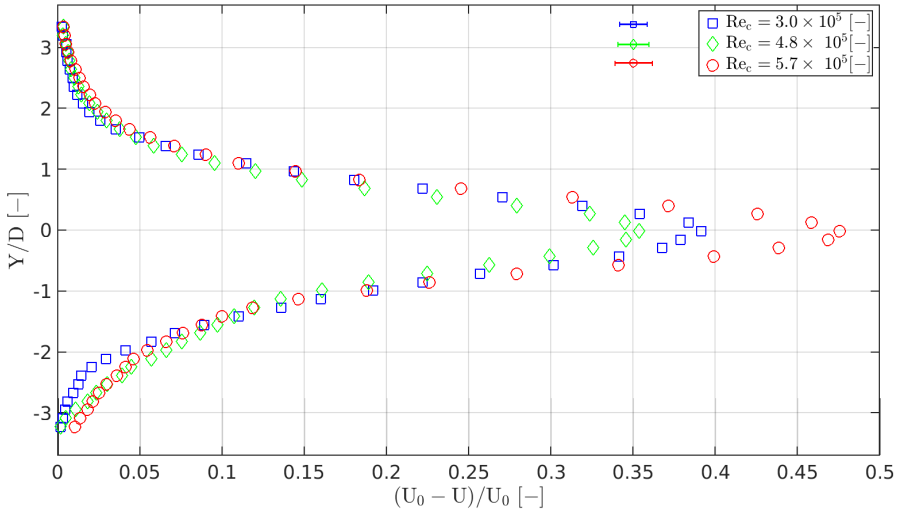

Figure 3.6: Vertical profiles of the normalized velocity defect $(U_0 - U)/U_0 = f(Y/D)$ measured in the streamwise direction at X=4D at various Re_c numbers. The error bars are representative of the maximum absolute error.

shed in the near-wake achieve their maximum strength while they convect. A popular method to asses L_e consists in evaluating the streamwise distance between the trailing-edge and the point along the wake axis where the time averaged Reynolds stress $\overline{u'u'}$ is maximum, see Bearman [124], Griffin [125], Kovasnay et al. [126]. Complementary to this definition we have investigated the location along the wake axis where the time averaged shear stress $-\overline{u'v'}$ reaches its maximum absolute value (maximum of $|\overline{u'v'}|$) for $Y < 0$ and $Y > 0$. These quantities have been assessed for various chord based Reynolds numbers in order to analyse the evolution of the vortex formation length as the inflow velocity U_0 increases.

As presented in figure 3.7 the vortex formation length using the location of maximum $\overline{u'u'}$ varies between $0.45D$ and $0.75D$, this variation is within the maximum uncertainty due to the spatial resolution of the PIV method. Therefore, it is hazardous to extract some general conclusions based on on $\overline{u'u'}$ maxima location. Regarding the evolution of the location of the maximums of $\overline{u'v'}$, a decrease is visible for Re_c ranging between 5.4×10^5 and 6.0×10^5. This corresponds to inflow velocities in the lock-in resonance regime which means that the length of the recirculation region is reduced at lock-in with the twisting mode. In general, a shorter vortex formation length is associated to a decrease in pressure at the base of the trailing-edge, Williamson et al. [127]. Indeed the minimum of pressure is shiffted closer to the trailing-edge, thus leading to an increase in the pressure drag.

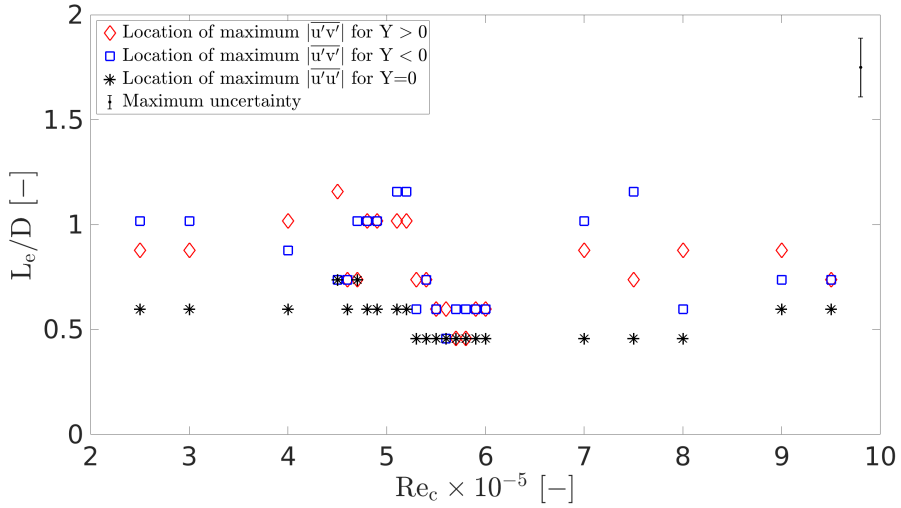

Figure 3.7: Evolution of the vortex formation length L_e with Re_c

The peak values of the turbulent shear stress $\overline{u'v'}$ have been investigated for various Reynolds numbers as is presented in figure 3.8. Interestingly, maxima of $|\overline{u'v'}/U_0^2|$ seems to be almost constant regardless of the Reynolds number, except at the lock-in with the twisting mode. A steep increase happens for Reynolds ranging between 5.1×10^5 and 6.0×10^5 with a maximum reached at 5.7×10^5. This Reynolds range corresponds to the highest vibration amplitudes occurring at the lock-in with the twisting mode which means that the recirculation is enhanced inside the recirculating region. The changes observed at the lock-in are: reinforcement of the recirculation and decrease of the eddy formation length play in favour of an increase in the minimum pressure and pressure drag at lock-in.

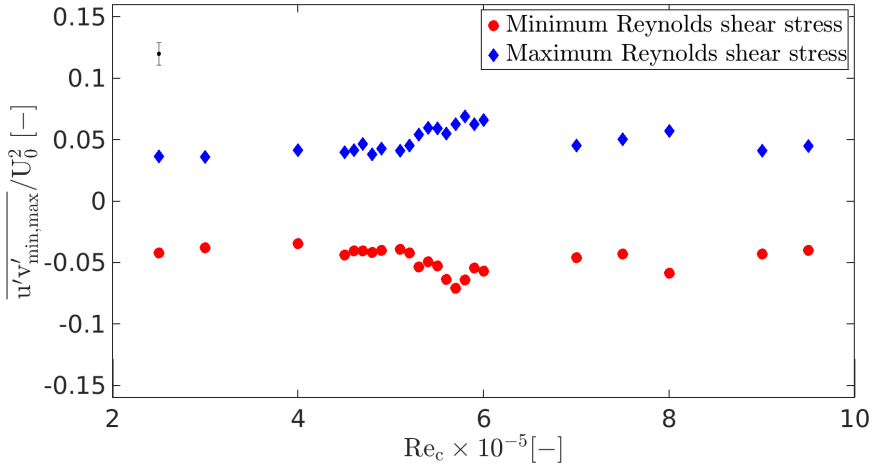

Figure 3.8: Evolution of min and max of $\overline{u'v'}$ with Re_c.

The distribution of the TKE was investigated at various Reynolds numbers in order to identify the hydrodynamic specificities at the various regimes. Figure 3.9a displays the number of modes $N_{90\%}$ necessary to reach 90% of total TKE. In general, without fluid-structure interactions, $N_{90\%}$ increases with the Reynolds number. In fact, a higher level of turbulence implies a broader distribution of the energy among the modes because of the contribution of various length scales proper to turbulent flows [128]. This trend is obviously observed for Reynolds numbers out of resonance. In the present study, due to fluid-structure interaction, the lowest value of $N_{90\%}$ is reached-out for Reynolds ranging between 5.7×10^5 and 6.0×10^5 which corresponds to the lock-in regime with the twisting mode. A local minimum is also observed at $Re_c = 8.0 \times 10^5$ corresponding to the lock-in with the second bending mode. The next part of our analysis will focus on the first two POD modes which contains the most energetic coherent structures in the near-wake.

3.3 Influence of the Re number and the vibration regimes on the primary Karman modes

The first two POD modes contain the highest percentage of TKE. For all Re_c, modes 1 and 2 are identified as primary Karman vortex shedding modes and present high spatial coherence. They are characterised by high alternating vorticity regions that are advected behind the trailing-edge, see figure 3.16b and 3.16c. Analysis of these structures is of great interest as they play an important

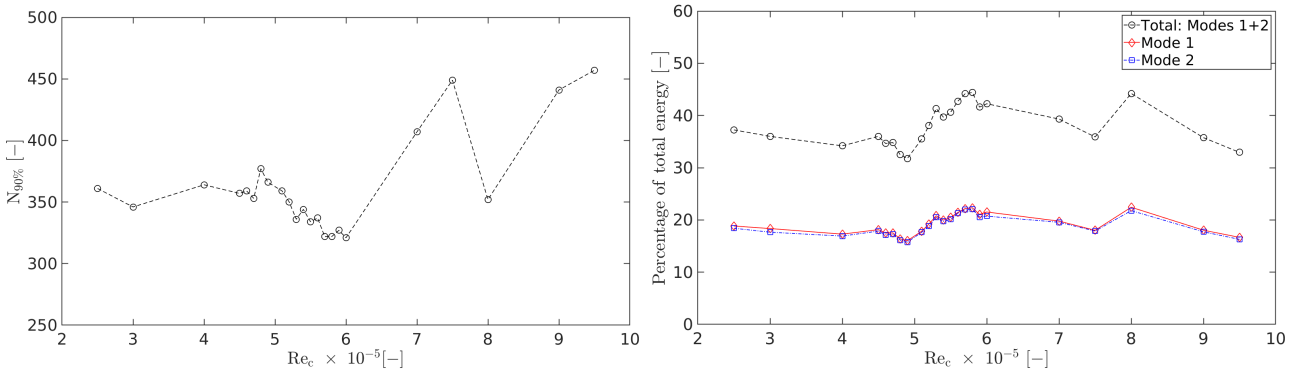

(a) (b)

Figure 3.9: Number of modes to reach 90% of the total energy according to Reynolds number (a). Mode 1 and 2 cumulated energy as a percentage of the total turbulent kinetic energy (b).

role in the flow-induced vibration mechanism. The present section aims at describing the evolution of the main characteristics of the Karman vortices with the Reynolds number. In particular, we focus on their contribution to the total kinetic energy, their size and their circulation, according to the Reynolds number and vibration regime. At the end of this section the coherence between modes 1 and 2 is compared for the different vibration regimes.

3.3.1 Contribution to the total TKE

Figure 3.9b offers a first insight into the contribution of the Karman modes to the total TKE with respect to Re_c. Modes 1 and 2 are characterized by similar contributions to the total energy and follow the same trend as Reynolds increases. Generally speaking, the part of the total TKE contained in modes 1 and 2 decreases with increasing Reynolds number, which is in agreement with an increasing contribution to the total TKE of smaller structures, with increasing Re_c. This trend is observed in the regime out of resonance of the plate. As expected the Karman vortex shedding modes reach the highest energy level at the lock-in resonance regime occurring at 5.7×10^5 for the synchronization with the first twisting mode (f_2) and at 8.0×10^5 for the synchronization with the second bending mode (f_3). A local maximum occurs at the lock-off resonance regime (4.8×10^5) which is in accordance with the local maximum of vibration velocity magnitude observed at this regime.

3.3.2 Vortex core properties

As modes 1 and 2 present similar spatial coherence, the Γ_2 vortex core detection algorithm is only applied to mode number 1 in order to reduce computation costs. The detection considers the first, second and third vortices arranged in the stream-wise direction, see figure 2.15 of chapter 2 for an example of the vortex arrangement. Vortex features of interest are the vortex area A and the vortex circulation Γ. The definition of each of these quantities is given in section 2. Note that in the following, the rms values of the vortex characteristics (namely the circulation Γ_{rms}) are determined using the rms values of the expansion coefficients of mode 1 combined with its modal vorticity field and integrated over the vortices core:

$$\Gamma_{rms} = a_1^{rms} \int_A \boldsymbol{\nabla} \times \boldsymbol{\phi}_1 dS \tag{3.1}$$

with

$$u_{rms}(\boldsymbol{x}) = a_1^{rms} \phi_1^u(\boldsymbol{x}), \tag{3.2}$$

$$v_{rms}(\boldsymbol{x}) = a_1^{rms} \phi_1^v(\boldsymbol{x}). \tag{3.3}$$

The variation of the vortex area of the first three vortices behind the trailing-edge is evaluated at various Reynolds numbers for mode number 1. It is made dimensionless by dividing by the squared thickness. According to figure 3.10a it is observed that the vortices grow when the distance from the trailing-edge increases in agreement with downstream expansion of the wake. The highest vortex area is detected for Reynolds ranging between 5.6×10^5 and 6.0×10^5. This Reynolds range corresponds to the flow velocities where the lock-in resonance occurs and where the maximum vibration amplitudes are reached. Accordingly, it can be affirmed that the lock-in resonance with the twisting mode is characterized by a sudden increase of the vortex area which is in agreement with the increase of the drag. A slight noticeable increase of the vortex area is also observed at the lock-in resonance with the second bending mode ($Re_c = 8 \times 10^5$). For Reynolds numbers out of the lock-in regimes, the vortex area of the vortex downstream (vortex 3) decreases with increasing Reynolds number. This is associated to a decrease with Re_c of the wake thickness (in the far-wake) as a consequence of a decrease with Re_c of the drag coefficient.

All the characteristics of vortex 2 measured for $Re_c = 4.8 \times 10^5$ (i.e $Re_D = 2.88 \times 10^4$) can be compared to characteristics of the vortices measured at $X/D = 2$ by Taylor et al. [1] at the same Re_D

for a plate of aspect ratio $c/D = 7$ with triangular edges giving same Strouhal number $St_D = 0.19$ as in our study. The characteristics measured by Taylor et al. [1] are approximate characteristics as the detection of the vortex core was subjected to the error in the vorticity measurement by PIV. Indeed, they approximated the vortex core by considering that it is delimited by 1% drop on the maximum local vorticity. All the characteristics measured by Taylor et al. [1] are displayed in table 3.3. At $Re_c = 3.0 \times 10^5$ ($Re_D = 1.8 \times 10^4$), for vortex 2 we measure $A/D^2 = 0.86 \pm 0.28$, which is larger than the value obtained in [1], as expected for a square trailing-edge.

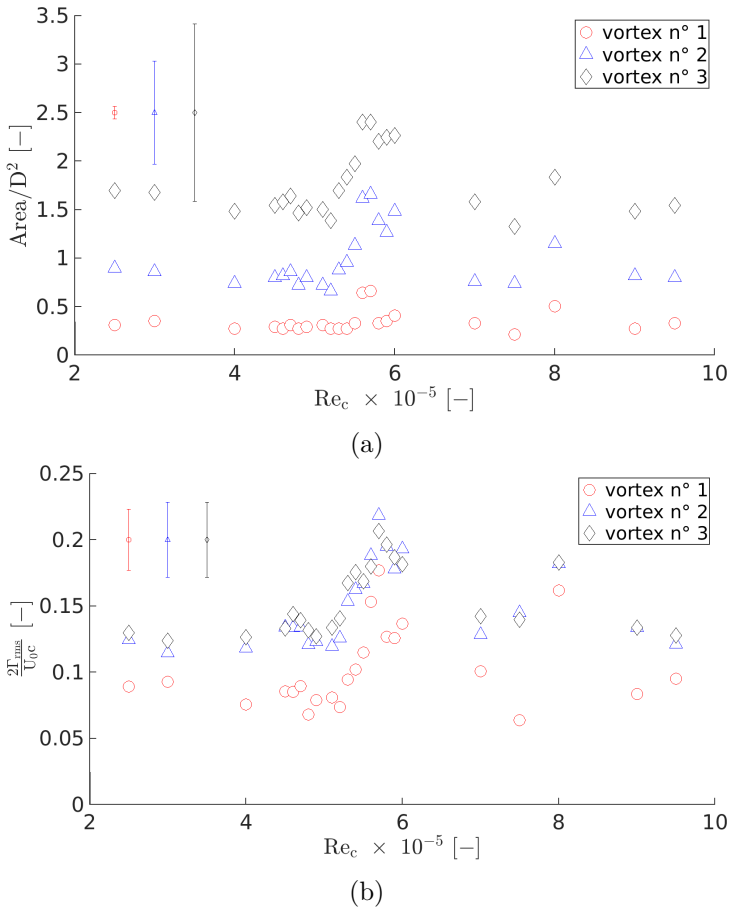

Figure 3.10: Non dimensional vortex core area evolution with the Reynolds number of the first three vortices downstream of the trailing-edge (mode1) (a). Vortex 1 is the upstream vortex and vortex 3 is the downstream vortex. Maximum uncertainty induced by the vortex core detection method is achieved at Re_c of the lock-in. Mode 1 rms circulation evolution with Reynolds of the first three vortices downstream of the trailing-edge (mode 1) (b). The circulation is scaled by $\frac{U_0 c}{2}$, which is representative of the lift coefficient. Vortex 1 is the upstream vortex, vortex 3 is the downstream vortex. The error bars are representative of the maximum absolute error.

	St_D	A/D^2	$\|\bar{\Gamma}\|_{max}/U_0D$
Taylor et al. [1]	0.19	0.78	1.7
Present study	0.19	0.86	1.4

Table 3.3: Characteristics of the wake vortices measured at X/D=2 and $Re_D = 3.0 \times 10^4$ by Taylor et al. [1]. Geometry with triangular edges of $c/D = 7$.

The vortex circulation downstream of an immersed structure induces an opposite circulation along the structure which results in a lift force. In a potential flow, the lift coefficient C_L is directly linked to the circulation Γ of the vortices in the wake. It yields

$$C_L = \frac{2\Gamma}{U_0.c}. \tag{3.4}$$

For the flat plate at zero incidence, the mean value of C_L is expected to be zero but the vortex shedding of the Karman wake induces alternative positive and negative C_L values. Therefore, Γ_{rms} of the Karman vortices scaled by $U_0c/2$ gives the magnitude of the rms value of C_L: $C_L^{rms} = 2\Gamma^{rms}/U_0c$. In figure 3.10b, the normalized values of Γ_{rms} have been plotted with regard to the Reynolds number for the first three vortices of mode 1. It appears that the rms value of the circulation of the vortices seems to converge downstream for vortices 2 and 3, which confirms the relationship between Γ of these two vortices and C_L. This is also in agreement with the expansion of the size of the vortices and a decrease of the vorticity observed downstream of the plate, see figure 3.16b. The lock-in regime can be associated with an abrupt increase of C_L^{rms} to reach a maximum value at Reynolds ranging between 5.6×10^5 and 5.7×10^5 which corresponds to the maximal structural vibration amplitude. Due to this high lift coefficient value, the structure will endure high level forcing resulting in high amplitude structural displacement in the transverse vertical direction. Vortex 2 and 3 also depict an increase in C_L^{rms} at the resonance regimes (lock-off resonance of the twisting mode and lock-in with the bending mode). For the Reynolds number range of the study and for the studied geometry of the plate, the C_L^{rms} of vortices 2 and 3 is of the order of 0.12 in the regimes out of resonance.

Generally speaking, there is a great discrepancy in C_L^{rms} measured in turbulent shedding condition downstream cylinders [42] and data of C_L^{rms} are not available for flat plates of large aspect ratio in the literature survey. However, we can compare our value of C_L^{rms} to $|\Gamma|_{max}/U_0D$ measured by Taylor [1], see table 3.3. In the work of Taylor, $|\Gamma|_{max}$ is the circulation of each vortex passing at $X/D = 2$, averaged among all the vortices at this position. Our approach is different as Γ_{rms} is the root mean square value in the POD mode 1. The relationship between Γ^{rms} and $|\Gamma|_{max}$ is $\Gamma_{rms} = |\Gamma|_{max}/\sqrt{2}$

when considering that the expansion coefficient $a_1(t)$ varies like a perfect sinusoid with time. For vortex 2 we obtain $|\Gamma|_{max}/U_0D = 1.4$. [1] have measured a value of $|\Gamma|_{max}/U_0D = 1.7$ which is same order of magnitude as the value we obtain. This means that the circulation of the primary vortices for $X/D > 2$ is imposed by the Strouhal and Reynolds numbers in the non-resonance regime.

3.3.3 Coherence of the primary Karman vortex shedding modes

Modes 1 and 2, as being both representative of the primary vortex shedding modes, are expected to be not independent but phase correlated. As inspired from the work of Oudheusden et al. [129], the phase plot of the POD coefficients $a_1(t)$ and $a_2(t)$ is useful for the analysis. The phase plot is modelled by a circle for ideal two-dimensional vortex shedding and scattering from the circle comes from the multi-frequency contents in the vortex shedding modes. Figure 3.11 evidences a certain coherence for all regimes, the highest coherence being achieved at the lock-in resonance regime. The lowest coherence is observed at the lock-off resonance regime. For this particular regime, this result will be discussed further in the chapter through the analysis of higher order POD modes contribution in section 3.4.

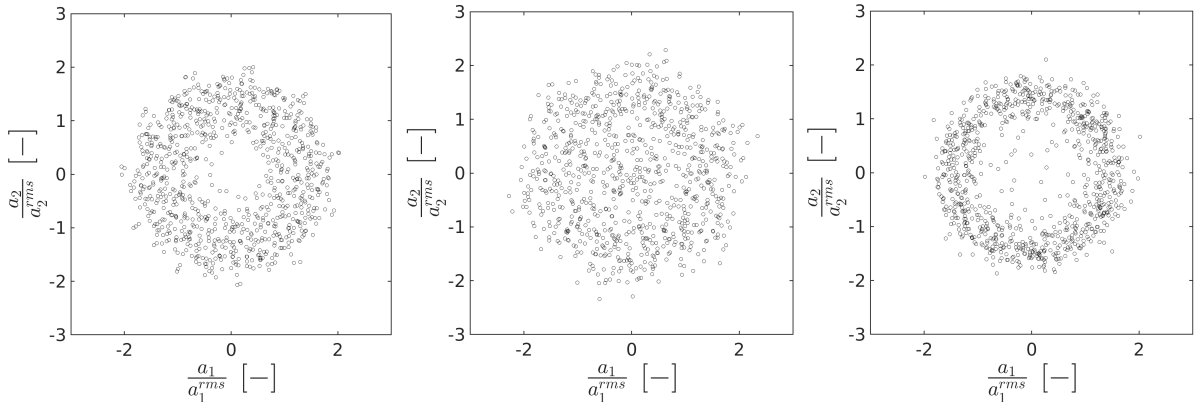

(a) $Re_c = 3.0 \times 10^5$ (b) $Re_c = 4.8 \times 10^5$ (c) $Re_c = 5.7 \times 10^5$

Figure 3.11: Phase diagram associated with modes 1 and 2 at the Reynolds numbers of interest.

3.3.4 Advection of the primary Karman vortex shedding modes

The advection of the primary Karman vortices has been investigated by using a spatio-temporal analysis of POD modes 1 and 2. Figure 3.12 displays a zoom of the space-time diagram of vertical velocity component $v_{1,2}$ associated to the contribution of both POD modes 1 and 2:

$$v_{1,2} = a_1(t)\Phi_1^v + a_2(t)\Phi_2^v. \tag{3.5}$$

The alternation of maxima of positive and negative $v_{1,2}$ values, representative of vortices, is propagating in the X downstream direction when combining modes 1 and 2. The associated wave length λ_{vs} as well as the frequency f_{vs} of the Karman shedding vortices is obtained from the 2D spectrum of the space-time diagram of $v_{1,2}$. A constant value of $\lambda_{vs} = 3.7D \pm 0.1D$ has been observed for the whole Reynolds range. f_{vs} is in agreement with f_{vs} determined from the FFT spectra of $a_1(t)$. The phase velocity can be deduced from $U_\Phi = \lambda_{vs} f_{vs}$ and is presented for various Reynolds numbers in figure 3.13. For the regime out of resonance, we obtain $U_\Phi/U_0 \approx 0.7$. This value is larger than the value measured by Taylor et al. [1] for a blunt plate of $c/D = 7$ which was $U_\Phi/U_0 = 0.5$ for $St_D = 0.15$ at $Re_D = 3.0 \times 10^4$ but as was demonstrated in [1] for different edge geometries, a larger U_Φ/U_0 value is in agreement with a larger vortex shedding frequency (i.e larger Strouhal). Indeed, Taylor et al. (2011) experienced the same value $U_\Phi/U_0 = 0.7$ with the same Strouhal number of 0.19 as in our experiment but it was obtained for triangular edges. At the lock-in with the twisting mode we also observed $U_\Phi/U_0 = 0.7$. Interestingly, a slight increase of the phase velocity is observed at $Re_c = 5.1 \times 10^5$ for the lock-in resonance. For this Reynolds number, $U_\Phi/U_0 = 0.75$.

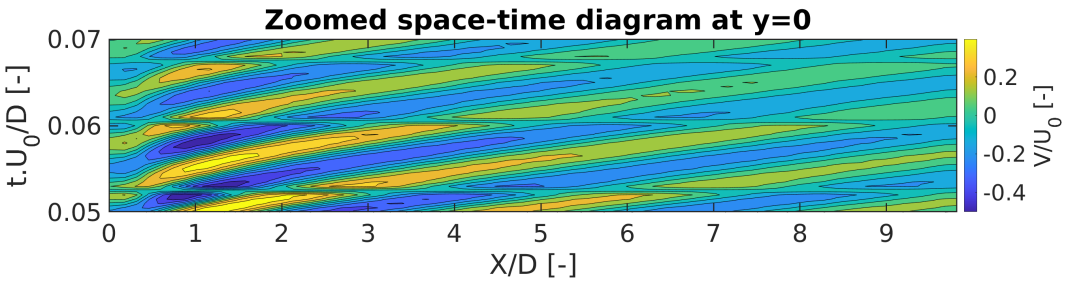

Figure 3.12: Space-time diagram of the Karman wake (modes 1 and 2) at $Re_c = 3.0 \times 10^5$.

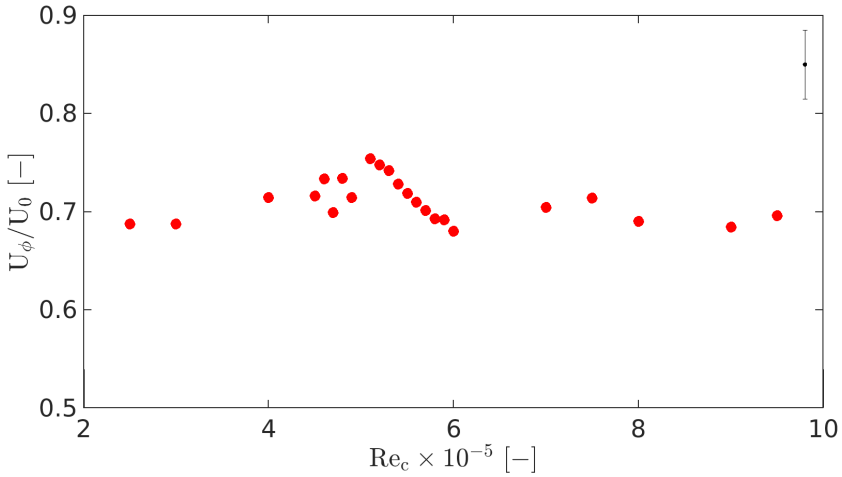

Figure 3.13: Evolution of the phase velocity obtained by space-time analysis of the reconstructed karman wake (modes 1 and 2).

3.4 Specificities of the POD modes in the near-wake for different vibration regimes

This section aims at analysing the main differences in the first nine POD modes observed in the near-wake of the plate for the three points of interest (A), (B), (C) summarized in table 3.2 and characteristic of the three vibration regimes: out of resonance, lock-off resonance and lock-in resonance. The analysis is based on the identification of the physical mechanisms responsible for the highest energetic POD modes.

Figure 3.14 presents the energy of the first nine modes as a percentage of the total energy for the three studied vibration regimes. These first nine modes account at least for 47% of the total energy. For this reason, we will limit the analysis to these modes. It appears that the highest energy percentages are associated with modes 1 and 2 as these modes cumulate on there own more than 35% of the total energy. During the lock-in regime ($Re_c = 5.7 \times 10^5$), the cumulated energy percentage of modes 1 and 2 reaches 44% of the total energy. The coupling with the high amplitude structural vibration, specific to this regime, is responsible of a strengthening of the first two modes. The cumulated energy percentage of modes 3 to 9 decreases at resonance and particularly at the lock-in resonance. See table 3.4 for a synthesis of the cumulated energy.

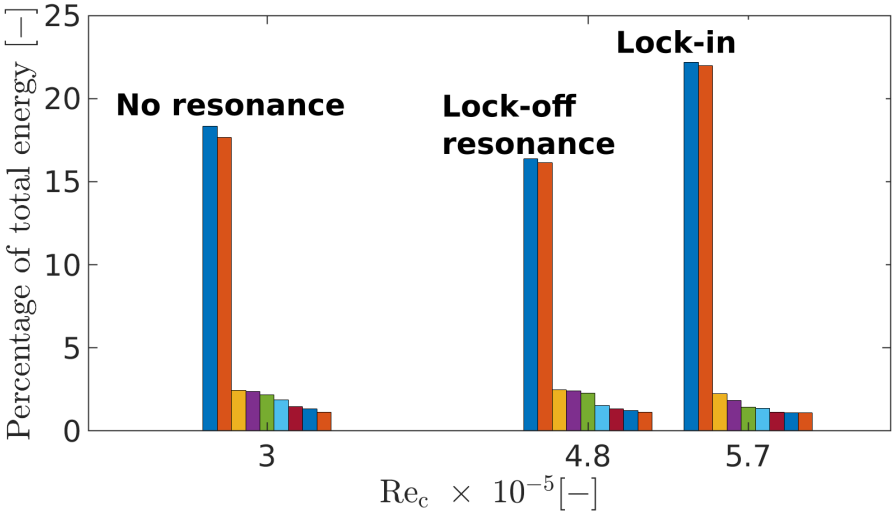

Figure 3.14: Respective percentage of the total energy of the first nine POD modes for each studied vibration regime.

Vibration regime	**(A)**	**(B)**	**(C)**
Re_c	3.0×10^5	4.8×10^5	5.7×10^5
Number of modes to reach 90% of total energy	346	377	322
Cumulated energy modes 1 to 2	36.0%	33%	44.1%
Cumulated energy modes 3 to 9	12.8%	11.6%	10.2%
Cumulated energy modes 1 to 9	48.8%	47.6%	54.3%

Table 3.4: Synthesis of the cumulated mode energy repartition of the 9 first POD modes for each studied vibration regime (in % of the total TKE).

3.4.1 Identification criteria of turbulent wake structures

Associating physical phenomena to POD spatial modes at high Reynolds can be challenging as the large-scale coherent structures are impacted by the smaller scale wake features proper to fully turbulent flows. This results in an alteration of the wake patterns by turbulence inducing some spatial distortion of the modes. The thickness of the turbulent boundary layer at the separation from the trailing-edge depends on both the Reynolds number and c/D. However, different periodic mechanisms taking place in the boundary layer can influence the near-wake [130]:

- Low frequency flapping of the separated shear layer with a characteristic Strouhal number.

$St_D^f = f_f D/U_0 \approx 0.02 - 0.03$ where f_f is the characteristic frequency of the flapping [130].

- Laminar separation bubble (LSB) vortex shedding of characteristic Strouhal numbers $St_R = f_R L_R/U_0 \approx 0.6 - 0.7$ and $St_{DR} = f_R D/U_0 \approx 0.12 - 0.14$, where f_R is the LSB vortex shedding frequency. This can induce the phenomenon referred as impinging leading-edge vortices (ILEV). For a blunt plate with a square leading-edge of chord to thickness ratio $6 \leq c/D \leq 36$ and for thickness based Reynolds numbers Re_D in the range $[1.5 \times 10^4 - 7.5 \times 10^4]$, a LSB has been systematically observed with a length L_R in the range $[4.2D, 5D]$, see [1], [53], [131], [112], [130].

For large c/D ratios, the ILEV is expected to be strongly reduced [131] because of the important diffusion of the leading-edge vortices. However, the chord to thickness ratio $c/D = 16$, which corresponds to the geometry of the study, is at the transition of two mechanisms: either the impinging leading-edge vortices (ILEV) or the trailing-edge vortex shedding (TEVS) could be the major mechanisms of influence for the vortex shedding and induced vibrations [63]. If the main mechanism is the TEVS, then the Strouhal number is close to the Strouhal number of bluff bodies ($St_D \approx 0.2$). This is what is observed in our experiment.

In order to facilitate the identification of physical modes, we propose to base our analysis of the first 9 modes on both:

- The symmetry or anti-symmetry of the vorticity distribution $\boldsymbol{\nabla} \times \boldsymbol{\Phi}^k$ of the modes in the (x,y) plane according to the wake centreline,

- The time evolution and the dominant frequencies exhibited by the frequency spectrum of their expansion coefficients $a_k(t)$.

The physical mode identification method based on symmetry is inspired from the work proposed by Miyanawala et al. [128] for the study of a square cylinder at low to moderate Reynolds number. We can consider that antisymmetry of the vorticity distribution is characteristic of shear layer modes (SL) and near-wake bubble (WB) modes (i.e recirculation region of the wake). Symmetry distribution is characteristic of the Karman vortex shedding (KVS). For scientific robustness we have limited our identification to the modes that present an unambiguous spatial distribution of vorticity and well established narrow banded frequency spectrums of their expansion coefficients. Modes that do

not respect these criteria may result from the recombination of several turbulent structures and are identified as combined modes (CM).

3.4.2 Modes identification at the non-resonant regime

The non-resonant regime studied at $Re_c = 3.0 \times 10^5$ is associated with low magnitude vibrations. As a consequence there should be weak influence of the vibrations on the wake. This case is used as a reference for comparison with resonant regimes. Figure 3.16 presents the vorticity cartography of the first nine modes. As discussed previously, modes 1 and 2 are symmetric modes of highest vorticity which are characteristic of Karman vortices. Also, by regarding the frequency spectrum of the POD coefficients in figure 3.15, it appears that modes 1 and 2 have a similar well established dominant frequency equal to 93 Hz, which is in agreement with the frequency of the primary excitation source (i.e. $St_D \approx 0.19 \approx St_{primary}$). Modes 1 and 2 are identified as the primary Karman vortex shedding mode (KVS1). For highly turbulent flows, as evidenced by Miyanawala et al. [128], the identification method fails for regimes out of resonance. The spatial distributions associated to modes 3 to 9 do not highlight well defined energetic structures and broadband spectra are observed for these modes. This comes from the multi-frequency approach of the POD analysis. Mode 8 is characterized by a broadband spectrum at low frequency of dominant frequency (f=10 Hz, i.e. $St_D = 0.02$) in the range expected for the low frequency flapping mechanism. No particular feature is evidenced on the spatial distribution of the vorticity of mode 8, except in the wake bubble ($X/D \leq 1$). For these reasons, mode 8 will be identified as a low-frequency flapping wake bubble mode (WB mode). The frequency spectra of modes 3, 4 and 5 show similar behaviour. Their dominant frequency is in the order of magnitude of the expected frequency of the LSB vortex shedding (f=60 Hz, i.e. $St_D = 0.12$). Their spatial distribution also evidences the presence of alternate vortices travelling in the region at $Y/D = \pm 2$. For this reason, these modes can be identified as ILEV modes, but this assertion must be taken with caution as they also combine with the low frequency wake bubble mode. Modes 6, 7 and 9 result from the combination of KVS1, WB, ILEV modes and higher frequency modes. These modes are thus identified as combined modes (CM). The spectra of mode 7 and 9 also evidence the contribution of the frequency of the mechanisms identified as the secondary hydrodynamic excitation mechanisms ($f_{secondary}$=110 Hz, i.e. : $St_{secondary} = 0.22$), but the multi-frequency approach of the POD limits the structure identification of these modes 7 and 9.

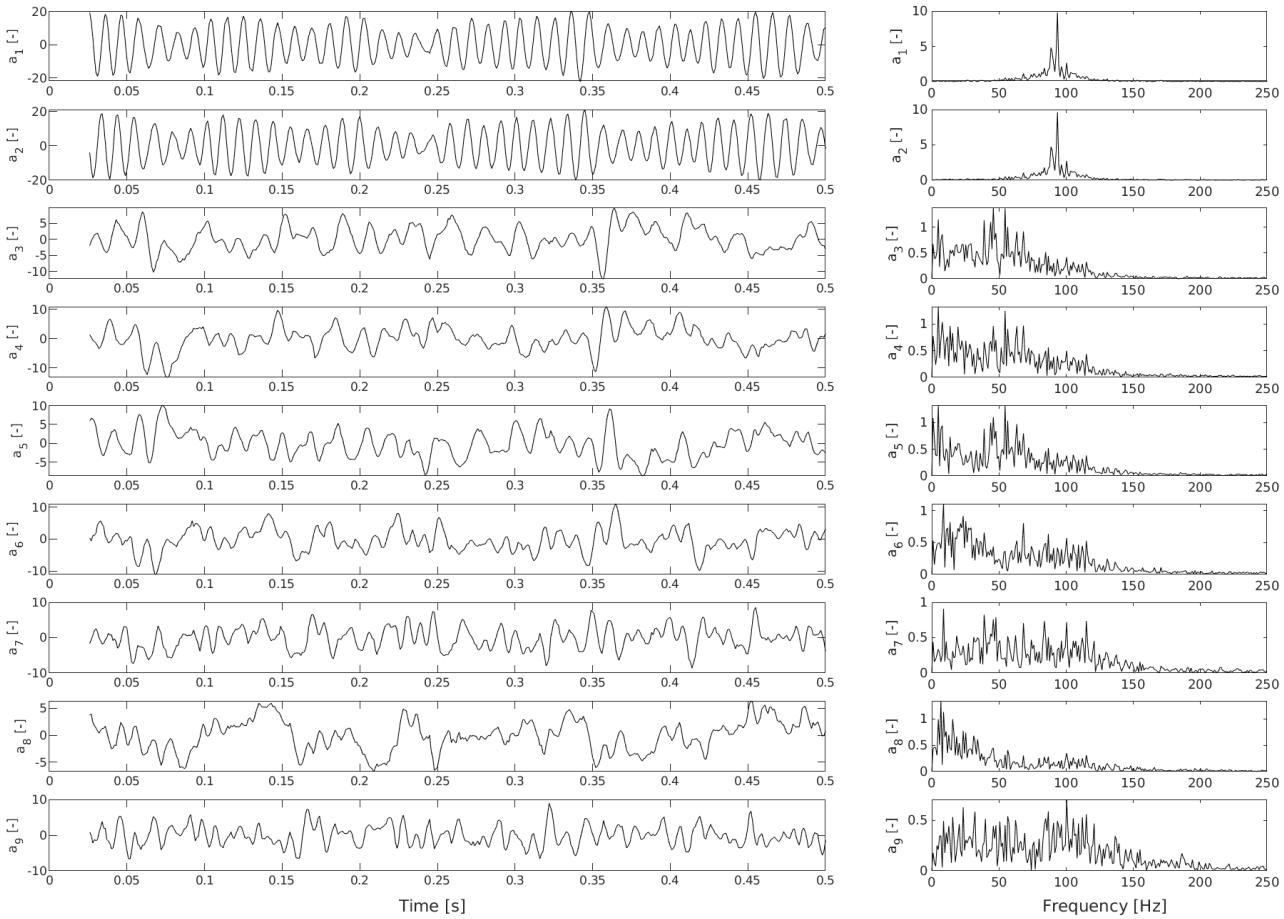

Figure 3.15: Temporal coefficients and associated frequency spectrum of POD modes 1 to 9 at $U_0 = 3.0$ m.s^{-1} ($Re_c = 3.0 \times 10^5$, non-resonant regime).

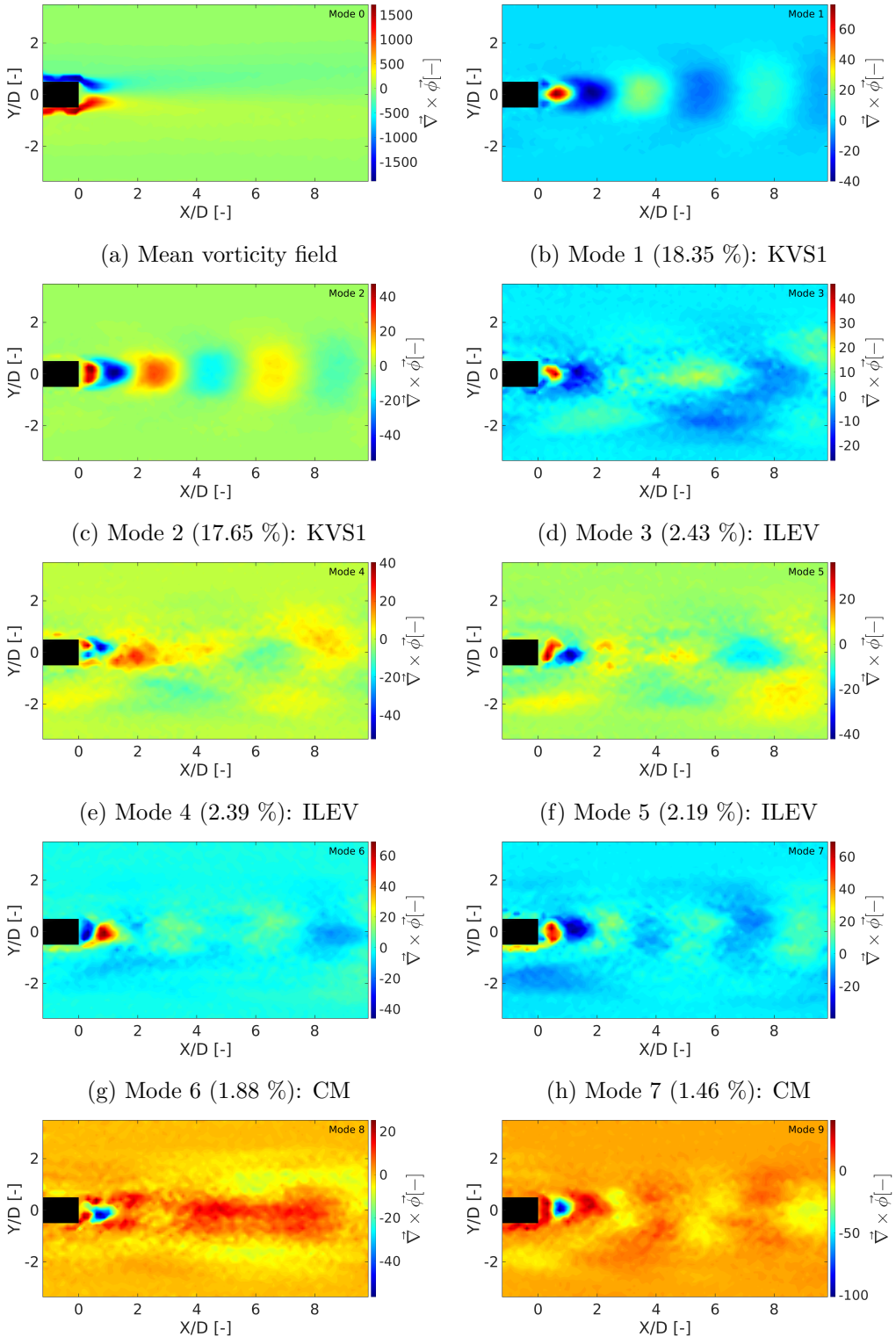

(a) Mean vorticity field

(b) Mode 1 (18.35 %): KVS1

(c) Mode 2 (17.65 %): KVS1

(d) Mode 3 (2.43 %): ILEV

(e) Mode 4 (2.39 %): ILEV

(f) Mode 5 (2.19 %): ILEV

(g) Mode 6 (1.88 %): CM

(h) Mode 7 (1.46 %): CM

(i) Mode 8 (1.34 %): WB

(j) Mode 9 (1.14 %): CM

Figure 3.16: (x,y) cartography of vorticity. Mean vorticity field and spatial POD modes from 1 to 9 at $U_0 = 3.0$ m.s^{-1} ($Re_c = 3.0 \times 10^5$, non-resonant regime).

3.4.3 Mode identification at the lock-off resonance regime

The lock-off resonance regime studied at $Re_c = 4.8 \times 10^5$ is characterized by a local maximum amplitude of vibrations at a frequency equal to the natural frequency of the twisting mode f_2 but with an excitation frequency f_{vs} that is still different from f_2. For modes 1 to 9, figures 3.17 and 3.18 present the frequency spectrum of their expansion coefficients as well as their spatial distribution of vorticity. It appears that the most energetic POD modes, modes 1 and 2, are still characterized by symmetric vortical structures representative of the primary Karman vortex shedding (KVS1 mode). The frequency of modes 1 and 2 is $f_{vs} = 156\ Hz$ in agreement with the Strouhal number of the primary excitation mode ($St_D \approx 0.19 \approx St_{primary}$). The spatial distribution of the vorticity of modes 3 and 5 is also symmetric and is very similar to the ones of modes 1 and 2. However, modes 3 and 5 exhibit a higher wave number in the streamwise direction than modes 1 and 2 and a higher dominant frequency, which is 182 Hz (i.e. $St_D \approx 0.227 \approx St_{secondary}$). Modes 3 and 5 are identified as a second Karman mode (KVS2 mode), and considered as being the signature of the second excitation source regarding their Strouhal number. For this Reynolds number, the frequency of the KVS2 mode is locked with the resonant frequency f_2, which makes this KVS2 mode contribute to the turbulent kinetic energy of the most energetic modes and is responsible for the early occurence of a resonance regime of the structure. This observation is proper to the lock-off resonance and it demonstrates the fact that two dominant Karman wakes modes coexist for this regime. As a consequence of this coexistence, the phase diagram $(a_1 - a_2)$ of the primary Karman modes coefficients (figure 3.11b) shows that modes 1 and 2 are much less phase correlated for this regime than for the other regimes. An other important feature is the emergence in mode 4 of an antisymmetric structure which is clearly identified as the wake bubble. This observation is of great interest as it seems to be the particularity of a resonance regime. Mode 4 is characterized by a low frequency broadband spectrum of maximum TKE centered near the flapping frequency ($f \approx 25\ Hz$, i.e. $St_D \approx 0.03$). This is consistent with a flapping of the wake bubble (WB mode). Modes 6,7, 8 and 9 are identified as combined modes (CM).

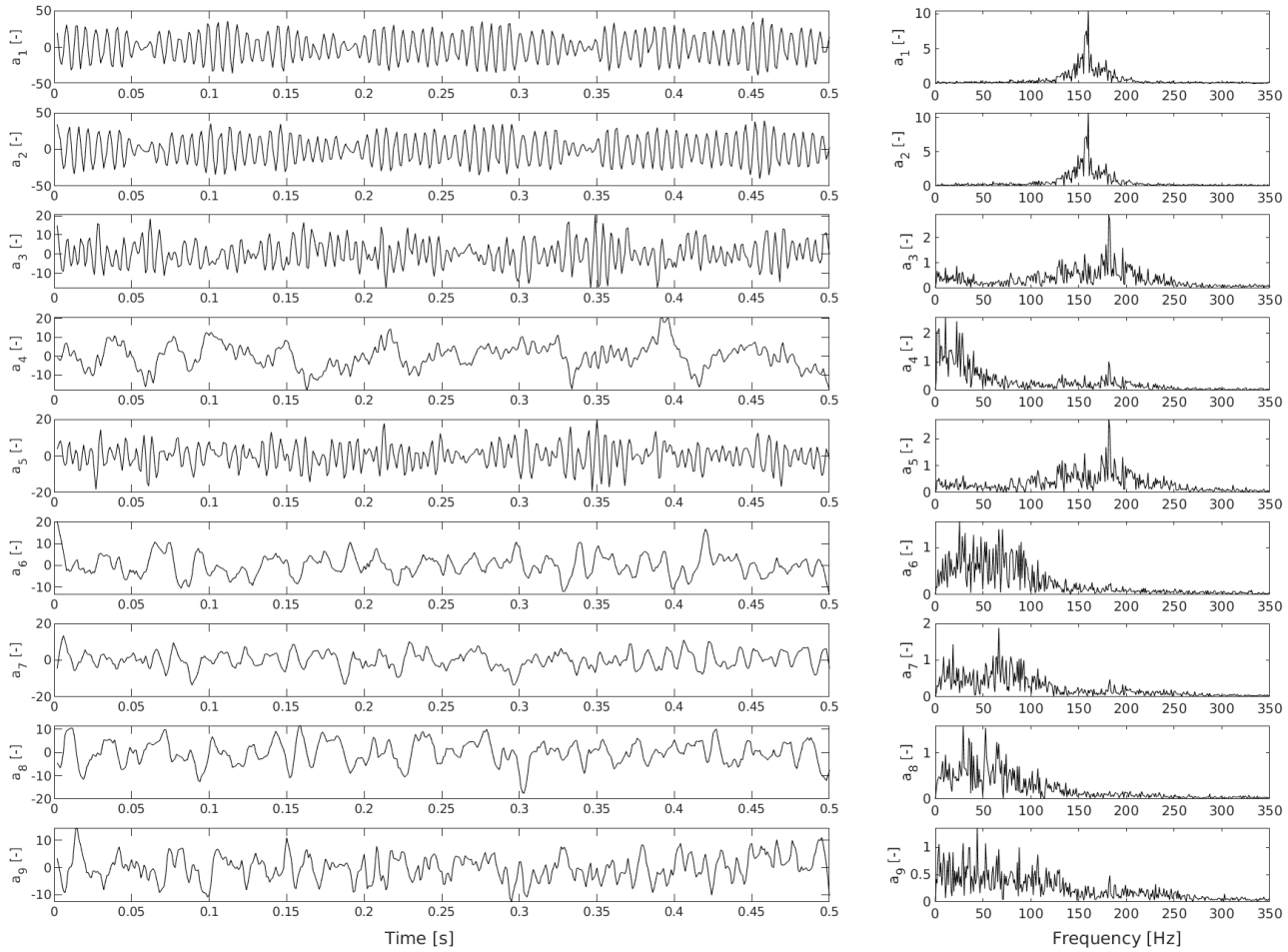

Figure 3.17: Temporal coefficients and associated frequency spectrum of POD modes 1 to 9 at $U_0 = 4.8$ m.s^{-1} ($Re_c = 4.8 \times 10^5$, lock-off resonance regime).

3.18

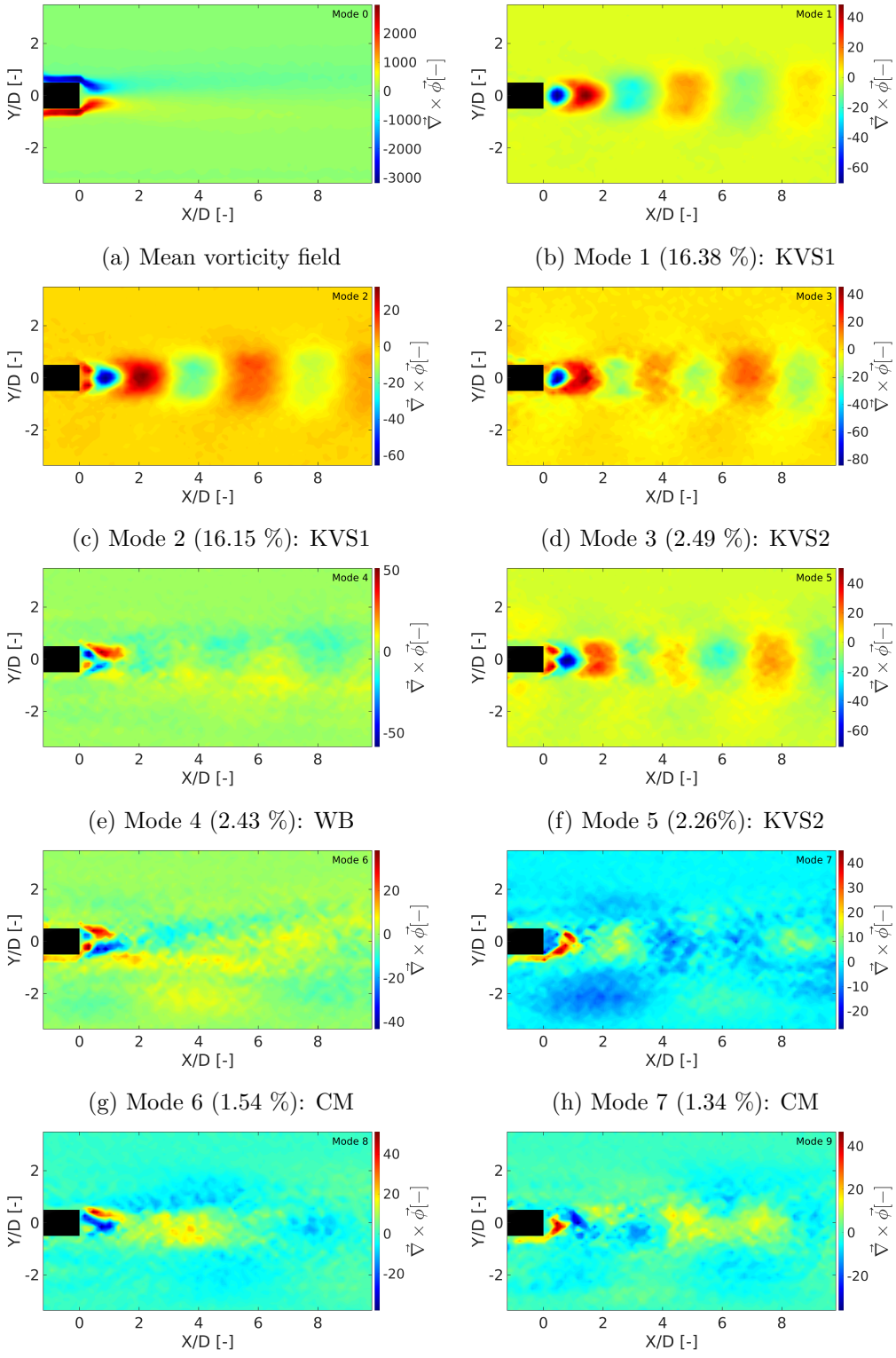

(a) Mean vorticity field

(b) Mode 1 (16.38 %): KVS1

(c) Mode 2 (16.15 %): KVS1

(d) Mode 3 (2.49 %): KVS2

(e) Mode 4 (2.43 %): WB

(f) Mode 5 (2.26%): KVS2

(g) Mode 6 (1.54 %): CM

(h) Mode 7 (1.34 %): CM

(i) Mode 8 (1.23 %): CM

(j) Mode 9 (1.11 %): CM

Figure 3.18: (x,y) cartography of vorticity. Mean vorticity field and spatial POD modes from 1 to 9 at $U_0 = 4.8$ m.s^{-1} ($Re_c = 4.8 \times 10^5$, lock-off resonance regime).

3.4.4 Mode identification at the lock-in resonance regime

The lock-in resonance regime occurring at $Re_c = 5.7 \times 10^5$ is characterized by the highest amplitude vibrations at a frequency equal to the Karman vortex shedding frequency. Major fluid-structure interaction is expected to occur at this regime due to an important energy transfer from the wake to the structure. For modes 1 to 9, figures 3.19 and 3.20 present the frequency spectrum of their expansion coefficients as well as their spatial distribution of vorticity. As presented in figure 3.20 modes 1 and 2 are still representative of symmetric vortex shedding of the primary Karman modes (KVS1 modes). The time evolution of their expansion coefficient shows a periodic behaviour at $f_{vs} = f_2$ (i.e. $St_D \approx St_{primary}$) with the highest phase correlation between a_1 and a_2 (figure 3.11 c) by comparison to the other vibration regimes. In comparison with the previous regimes an enlargement of the wake in the cross-flow direction is visible. A particular feature of this lock-in regime is the appearance of a very well defined coherent and antisymmetric structure visible on modes 7, 8 and 9. These modes exhibit propagative vortices developing at the corner of the trailing-edge. The spectra of the POD coefficients of these modes are narrow banded similarly to the ones of modes 1 and 2 and have a dominant frequency equal to twice the vortex shedding frequency of the primary Karman modes ($f_{7,8,9} = 2 \times f_{vs} = 2 \times f_2$). These modes are identified as harmonics of the primary Karman vortex shedding (KHVS1) and they are expected to modulate the drag force at $2 \times f_2$ [128]. These modes are standard modes observed in case of vibrating cylinders, see [41] and [132]. Karman harmonic modes were also highlighted for a flat plate of high aspect ratio with an elliptic leading-edge and a blunt trailing-edge by Chiekh et al. [133]. This type of wake structure is not specific to lock-in resonance but in case of high amplitude vibrations its turbulent kinetic energy is amplified and it is observed as a lower rank POD mode. The vorticity map of mode 3 exhibits an antisymetric structure characteristic of the wake-bubble. It is also a low frequency mode of characteristic frequency f=21 Hz (i.e. $St_D \approx 0.02$) which could be associated with the flapping of the separated shear layer. Mode 3 is then identified as the low-frequency flapping wake-bubble mode (WB mode). Other modes 4, 5 and 6 are combined modes because they present no distinct spatial coherence or narrow banded frequency spectra.

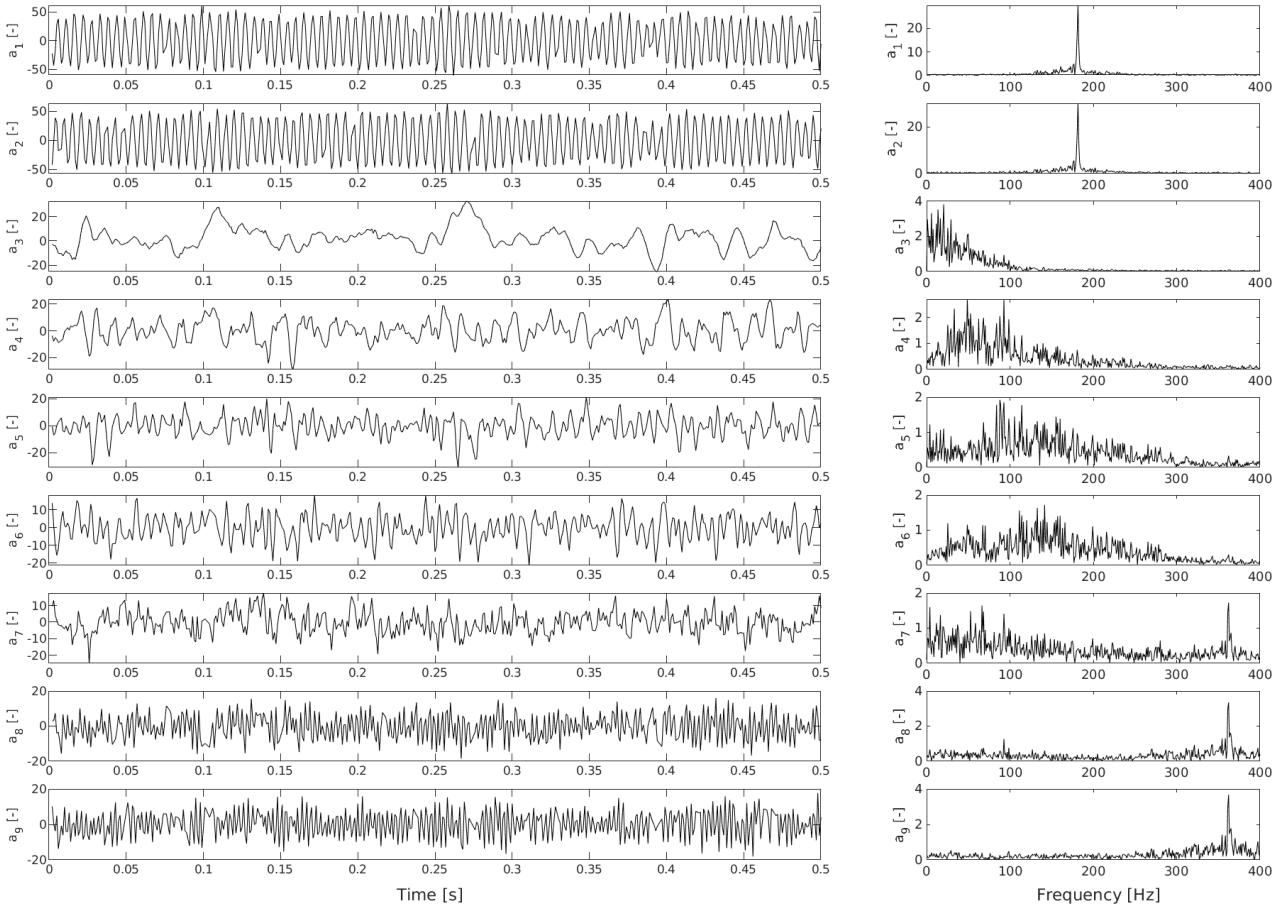

Figure 3.19: Temporal coefficients and associated frequency spectrum of POD modes 1 to 9 at $U_0 = 5.7$ m.s^{-1} ($Re_c = 5.7 \times 10^5$, lock-in resonance regime).

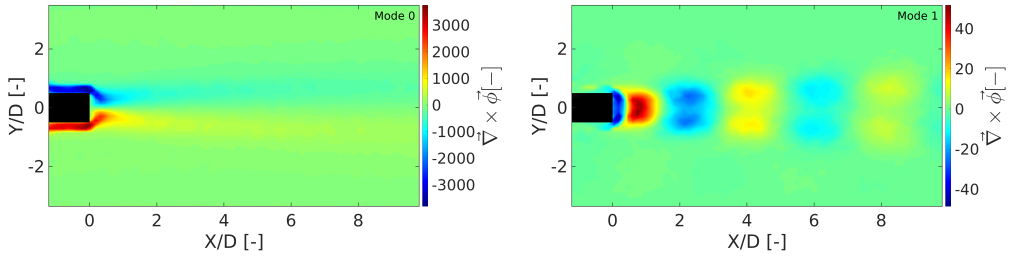

(a) Mean vorticity field

(b) Mode 1 (22.18 %): KVS1

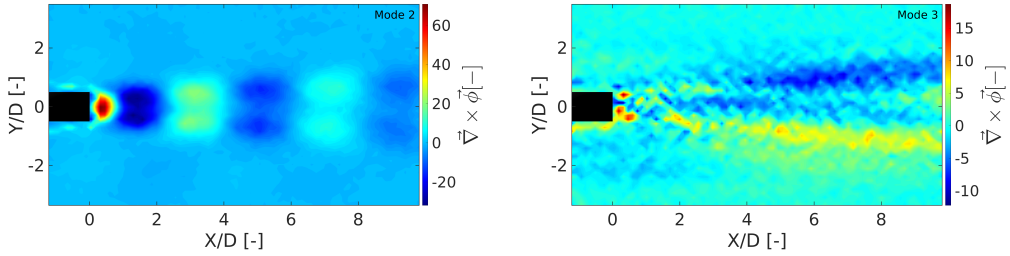

(c) Mode 2 (21.98 %): KVS1

(d) Mode 3 (2.25 %): WB

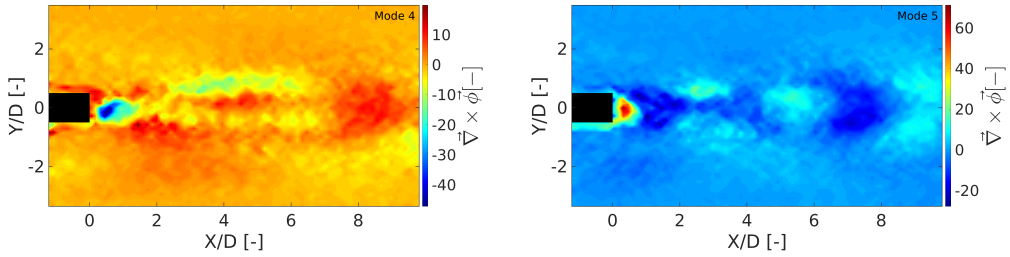

(e) Mode 4 (1.85 %): CM

(f) Mode 5 (1.42 %): CM

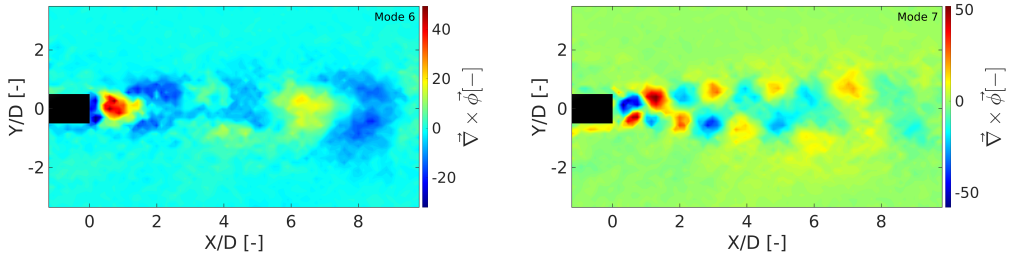

(g) Mode 6 (1.35 %): CM

(h) Mode 7 (1.13 %): KHVS1

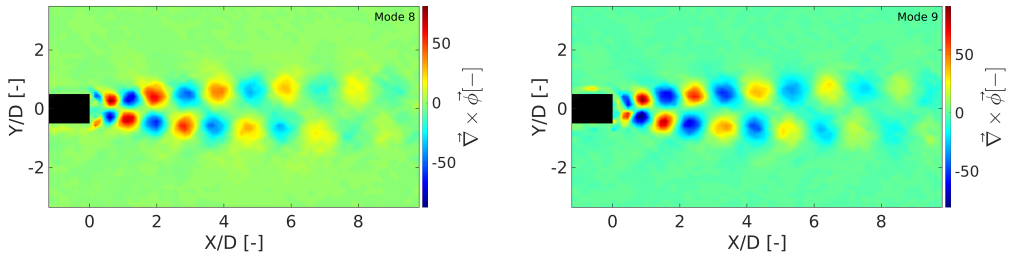

(i) Mode 8 (1.09 %): KHVS1

(j) Mode 9 (1.09 %): KHVS1

Figure 3.20: (x,y) cartography of vorticity. Mean vorticity field and spatial POD modes from 1 to 9 at $U_0 = 5.7$ m.s^{-1} ($Re_c = 5.7 \times 10^5$, lock-in resonance regime).

Conclusion of the chapter

An experimental study was conducted to investigate the vortex shedding and induced vibrations of a cantilevered blunt rectangular aluminium plate of chord to thickness ratio 16.7 immersed in a uniform water flow at zero degrees of incidence. The chord based Reynolds number Re_c was varied from 2.5×10^5 to 9.5×10^5 corresponding to turbulent flow conditions. The first nine POD modes of the near-wake were analysed in terms of spatial distribution of their vorticity and characteristic frequencies of their expansion coefficients.

A special attention has been paid to the characterization of the Karman vortex shedding corresponding to the first two POD modes. In particular, the frequency, as well as the area and circulation of the vortices shed have been systematically characterized with respect to the Reynolds number. This characterization is useful for reduced order modelling. Interestingly, the area and circulation of the Karman vortices seem to be controlled by two parameters which are the Strouhal and Reynolds numbers, whatever the geometry of the trailing-edge and the chord-to-thickness ratio. The measured Strouhal number $St_D = 0.195$ is in agreement with the Strouhal of bluff bodies and plates of large c/D ratio. Two hydrodynamic excitation sources of different Strouhal number are present. These excitation sources may be attributed to the coexistence of two mechanisms, a chord to thickness ratio of 16 being at the transition between these two regimes of excitation. The primary excitation source which is identified as trailing-edge vortex shedding instability consists in primary Karman vortex shedding of characteristic Strouhal number $St_D = 0.195$. The secondary excitation source which is identified as the impinging shear layer instability is attributed to a square leading-edge. It has a Strouhal number $St_D = 0.227$.

Three vibration regimes have been highlighted and consist of non-resonance ($Re_c = 3.0 \times 10^5$), lock-off resonance ($Re_c = 4.8 \times 10^5$) and lock-in resonance ($Re_c = 5.7 \times 10^5$) regimes. At the lock-off resonance, the secondary excitation source synchronizes with the twisting mode natural frequency resulting in a local maximum of the vibration magnitude. In the near-wake, this regime is characterized by the coexistence of two distinct Karman vortex shedding modes. To our best knowledge, it is the first time that such a lock-off resonance regime is analysed. This regime is of particular importance for the design of structures subjected to flow-induced vibrations as it implies the early occurrence of a resonance regime. Accordingly, high amplitude vibrations may appear for a Reynolds and reduced

velocity range larger than the one expected for lock-in resonance. The highest vibration magnitudes were observed during the lock-in resonance regime with the twisting mode, resulting in a strong fluid-structure synchronization. This regime is characterized by an enlargement of the wake and an increase in the contribution to the total turbulent kinetic energy of the harmonics of the primary Karman vortex shedding. Another interesting point is the emergence in the most energetic modes of a low frequency wake-bubble structure for all resonance vibration regimes (lock-off resonance and lock-in resonance). This is consistent with the observations of Miyanawala et al. [128] for a resonant square cylinder. The next chapter will be dedicated to the vibration mitigation by passive resonant piezoelectric shunt.

Chapter 4

Vibration mitigation by resonant piezoelectric shunt

" *Il est grand temps*
de ralumer les étoiles "

Guillaume Apollinaire

Content

Resonant piezoelectric shunts offers the opportunity to mitigate high amplitude flow-induced vibrations by using a simple passive or semi-passive electronic circuit. However, to reach maximal efficiency, this type of system requires an accurate tuning of its electrical parameters consisting in the transducer capacitance and the circuit inductance and resistance. The adopted vibration mitigation strategy consists in reducing the maximal vibration magnitude on a given frequency range by tuning the electrical resonance frequency on the target mechanical resonance frequency. The aim of the present chapter is to design, setup and test resonant shunts connected to piezoelectric transducers integrated in marine lifting surfaces. A MFC piezoelectric transducer with a fibre direction of 45° dedicated to twisting mode mitigation is integrated on the hydrofoil and investigated experimentally and numerically.

After introducing the calculation principle of the shunt parameters, the present chapter describes two types of resonant piezoelectric shunts: the first one is fully passive and is based on a copper wired inductor, the second one is semi-passive and uses a synthetic inductor circuit. The copper inductor shunt was tested in various flow conditions whereas the synthetic inductor shunt was tested only in calm air and calm water. The last section of the chapter introduces a numerical model implemented with COMSOL *Multiphysics* for the hydrofoil structure embedded with DuraAct and MFC piezoelectric transducers and connected to a passive resonant shunt. The aim of this model is to predict accurately the natural frequencies and coupling factors of a structure embedded with piezoelectric transducers in order to facilitate future designs of prototypes.

4.1 Design and setup of resonant piezoelectric shunts

The following sections are dedicated to the design an setup of resonant piezolelectric shunts. The computation principle of the shunt parameters is presented and different types of inductors are investigated.

4.1.1 General setup and calculation of the parameters

The present study focuses on the series resonant piezoelectric shunts which are composed of a piezoelectric transducer of capacitance C (at zero strain) connected to a resistance R and an inductance L. The piezoelectric effect of the patch is exploited to convert mechanical energy into electrical energy which is then dissipated through the resistance of the circuit by Joule effect. A simple solution to

maximise the mitigation level consists in connecting an inductance L in series with the resistance R thus creating a RLC circuit. This introduces an electrical resonance which has the specificity of increasing the electrical current flowing through the resistor and thereby maximises the dissipation. The electrical resonance of the circuit is usually tuned to a mechanical natural frequency of the structure in order to mitigate a mechanical resonance responsible of high magnitude vibrations [106]. The resonant circuit behaves then similarly to a mechanical vibration absorber consisting of a tuned mass-spring oscillator mounted to the mechanical structure [134]. The electrical resonance frequency is directly linked to the value of the inductance so it is necessary to set-up precisely its value. Two types of inductors used for resonant shunts are discussed below: the copper wired inductor and the synthetic inductor. Figure 4.1 presents the general arrangement of a passive resonant piezoelectric shunt paired with a hydrofoil type structure. The efficiency of the shunt to reduce the vibrations depends on the coupling factor k_c which is expressed as

$$k_c = \sqrt{\frac{\omega_{oc}^2 - \omega_{sc}^2}{\omega_{sc}^2}}, \tag{4.1}$$

where ω_{oc} corresponds to the natural angular frequency of the foil structure when the piezoelectric transducer is in open-circuit (zero electric charge displacement condition) and ω_{sc} is the natural angular frequency of the structure when the piezoelectric patch is in short-circuit (zero voltage condition). To obtain a significant vibration mitigation, the coupling factor should usually be higher than 5%. In order to reach the highest levels of mitigation, the parameters R, L and C must be calculated in agreement with the mechanical angular frequency to mitigate a resonance at ω_{oc}. For relatively low piezoelectric coupling factors, the optimal values of the shunt parameters are depicted from the following equations [14, 135].

$$L = \frac{1}{C\omega_{oc}^2}, \tag{4.2}$$

$$R = \sqrt{\frac{3}{2}}\frac{k_c}{C\omega_{oc}}. \tag{4.3}$$

Passive shunts offer the opportunity to mitigate vibrations without major modifications of the structure. Moreover, the electrical circuit may be located in a remote position which offers great flexibility for an usage in restricted spaces. Depending on the selected inductor technology (see paragraph below), resonant shunts can be operational without an external power supply and are then totally autonomous. The fact that there is no external power injected in the system is an advantage for acoustic

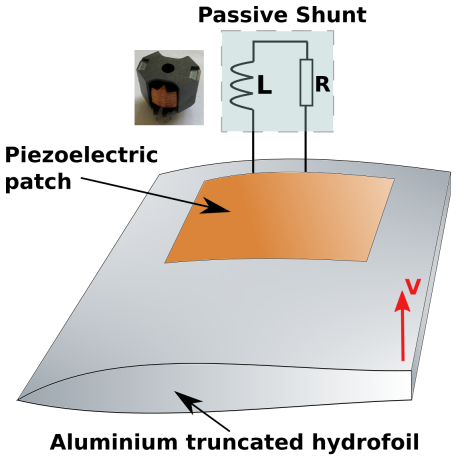

Figure 4.1: Passive resonant piezoelectric shunt principle.

stealth applications because there is no risk of vibration amplification by external energy injection in case of dysfunction. The absence of external sensors and control units also demonstrate the simplicity and adaptability of this kind of vibration mitigation system and avoids the risk of instability.

4.1.2 Coper wired inductor

The most elementary type of inductor consists in a coper winding around a ferrite core. The value of the inductance is directly dependent of the magnetic properties of the coper windings and can be calculated with the following equation

$$L[H] = \frac{N^2 \times \mu_0 \times \mu_r \times A}{l}, \tag{4.4}$$

where N [-] is the number of windings, l [m] is the equivalent length of the magnetic circuit, A [m^2] is the equivalent section of the magnetic circuit, $\mu_0 = 4\pi \times 10^{-7}$ T.m.A^{-1} is the permeability of the air and μ_r [T.m.A^{-1}] is the relative permeability of the inductor core. The main advantage of this type of inductor is that it is simple to implement and it can sustain high voltage levels if this is taken into consideration during the design phase. However, it is complicated to modify the winding afterwards, so the design of the inductor must be done precisely and in accordance with the vibration frequency to mitigate. For many mechanical applications, vibrations to damp are low frequency which implies high values of inductance. A disadvantage of this type of inductor is that the internal resistance is high in case of significant length of the coper wire. In some situations, this could induce a lower vibration

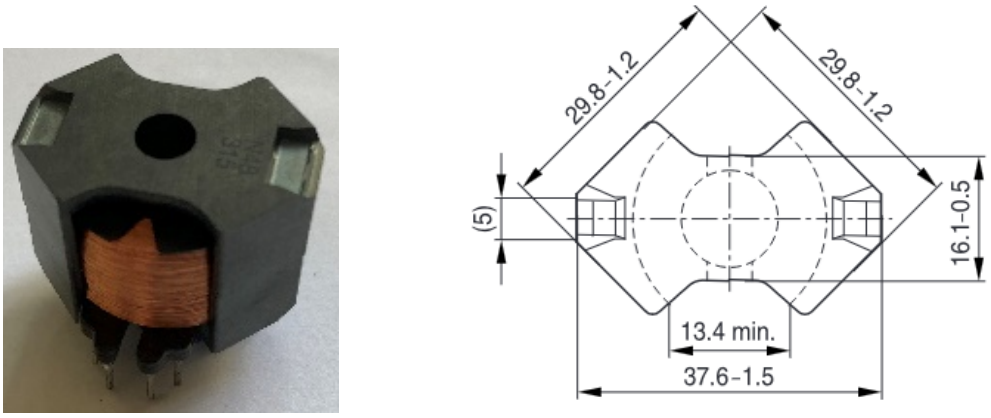

(a) (b)

Figure 4.2: (a) Picture of the used coper wired inductor and (b) its dimensions according to the datasheet.

mitigation level due to an over resistive electrical circuit.

Passive shunts aiming to reduce vibration frequencies lower than 1 kHz with a coper wired inductor require a high number of windings and are seldom available at suppliers. Most of the time, it will be necessary to manufacture the inductor by oneself using a linear winding machine. Some inductors are embedded with a screw inside the inner core which makes it possible to slightly adjust the inductance. According to equation 1.2 it is also possible to reduce the required inductance by adding an additional capacitor in parallel of the piezoelectric patch. This solution should only be used for small adjustments because it will also reduce the equivalent coupling factor. Refer to figure 4.2a for a picture of the coper wired inductor used for the present study and to figure 4.2b for its dimensions. The hole at the top of inductor corresponds to the location of the adjustment screw.

4.1.3 Synthetic inductor

As was demonstrated by equation 1.2, it is of prime importance to be able to modify the value of L to set up precisely a resonant shunt because the highest vibration mitigation is reached when the electrical resonance frequency is equal to the frequency of the mechanical resonance to mitigate. In 1969, Antoniou [136] developed an electronic circuit based on operational amplifiers identified as a synthetic inductor (also known as gyrator). A modification of this circuit was proposed in 1996 by von Wangenheim [137] in order to compensate the internal resistance by including a negative resistance

component. Refer to figure 4.3 for a schematic view of this type of circuit. The synthetic shunt circuit designed by Julien Ducarne [14] during his PhD was used for our tests and is displayed in figure 4.4.

The synthetic inductor is characterized by an equivalent impedance Z_{eq} consisting in an equivalent inductance L_{eq} and an equivalent resistance R_{eq}. The equivalent impedance can be calculated with the following equation, depending on the internal parameters of the circuit:

$$Z_{eq} = \frac{V}{I} = jL_{eq}\omega + R_{eq}. \tag{4.5}$$

Equivalent inductance and resistance can be identified as

$$L_{eq} = \alpha_{th} P_2 \tag{4.6}$$

with

$$\alpha_{th} = C_1 R_3 \frac{R_1}{R_2}. \tag{4.7}$$

and

$$R_{eq} = -P_1 \frac{R_1}{R_2}, \tag{4.8}$$

where the internal variable resistances of the synthetic shunt circuit are P_1 and P_2, the internal fixed resistances are R_1, R_2, R_3 and the internal capacitance is C_1 (see figure 4.3 for the electric diagram and table 4.1 for the numerical values). The parameter α_{th} is constant. For the values presented in

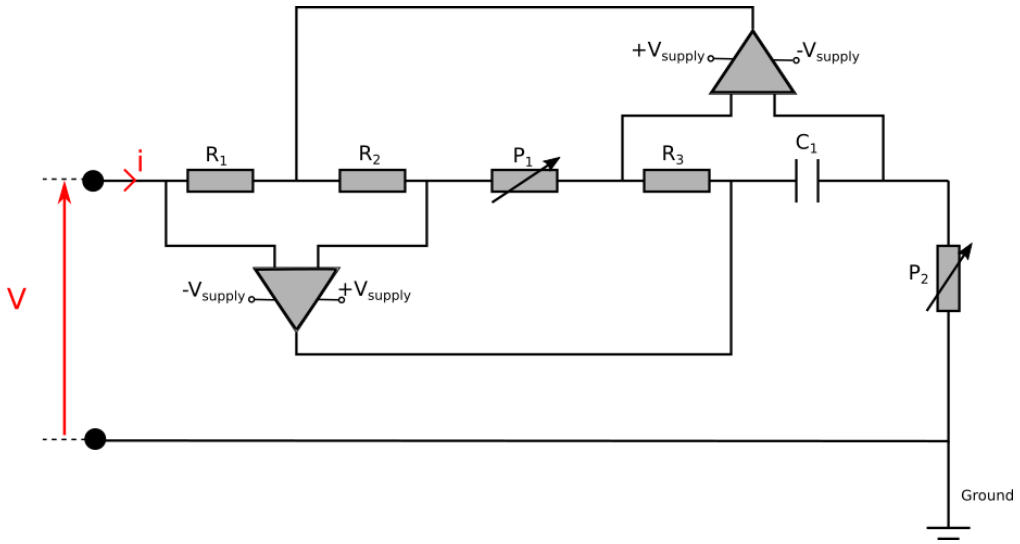

Figure 4.3: Electric diagram of the synthetic inductor.

Synthetic inductor	
R_1	2 kΩ
R_2	1 kΩ
R_3	1 kΩ
P_1	0 to 1 kΩ
C_1	10 μF
V_{supply}	+/- 30 V
P_2	0.1 to 10 kΩ
Simulated piezo patch	
C_t	1 μF
R_t	100 Ω
V_1	Sweep 2 Hz-2 kHz

Table 4.1: Electrical parameters implemented for the experimental characterization of the synthetic inductor.

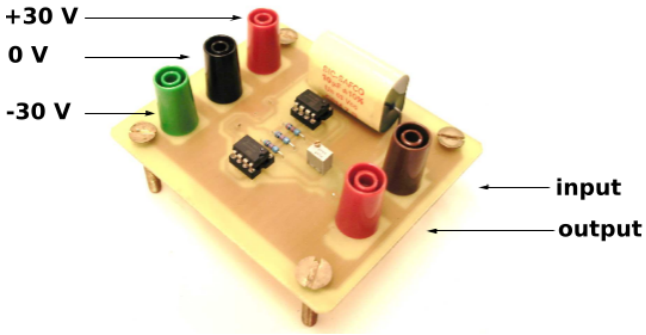

Figure 4.4: Synthetic inductor circuit. The same circuit was used in the thesis of Ducarne [14]. Image from [14].

table 4.1, α_{th} is equal to 20 H.kΩ^{-1}. This implies that the evolution of L_{eq} in function of P_2 is linear. In accordance with equation 1.6, a variation of P_2 results in a variation of the electrical resonance frequency. Knowing the exact value of α_{th} is critical to set-up correctly a synthetic inductor. The specificities of the components presented in a data sheet are often not precise enough to compute α_{th} accurately, so an experimental characterization of the synthetic inductor is necessary and will be investigated in the next subsection.

The negative resistance of the inductor is varied with the potentiometer P_1. When implementing piezoelectric vibration mitigation, the tuning was done manually in order to reach the highest mitigation level. The operational amplifiers require an external power supply but this power is not injected directly in the system, so a shunt using a synthetic inductor is still considered as passive. This type

of system offers great adaptability in terms of setup of the inductance but it is restricted to moderate input voltage due to the operational amplifiers which have a voltage limit of 45 V. For the present study, the synthetic inductor was used to mitigate vibrations in still air and in still water when the two DuraAct piezoelectric transducers embedded in the foil act as a structural excitation source. For flow-induced vibrations and especially at lock-in, the voltage at the output of the piezoelectric patch appeared to be to high for the standard synthetic inductor. For this reason the copper wired inductor was still required for flow-induced vibration mitigation.

4.1.4 Experimental characterization of the synthetic inductor

An experimental characterization of the synthetic inductor was achieved in order to evaluate precisely the characteristics of the system and verify that it is operating correctly. A piezoelectric transducer was simulated by an alternative source of voltage (V), a capacitor (C_t) and a resistor (R_t). The output signal (V_2) is measured at the connecting terminals of the synthetic inductor. See figure 4.5 for an illustration of the electrical circuit and table 4.1 for an overview of the parameters. At each value of P_2, a frequency response function (FRF) is obtained by computing V_2 over V_1 as presented in figure 4.6a. The highest peak of the FRF is associated with the electrical resonance at ω_e. By using equation 1.6, the inductance associated with each value of P_2 is computed. As can be seen in figure 4.6b, the evolution of L_{eq} is linear. By using a linear regression, the experimental coefficient α_{exp} is computed and is equal to 21.1 H.kΩ^{-1} which is in agreement with the analytical prediction of equation 1.8.

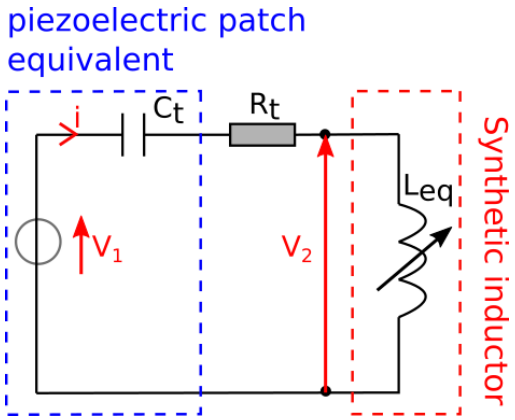

Figure 4.5: Electric circuit used for the synthetic inductor characterization.

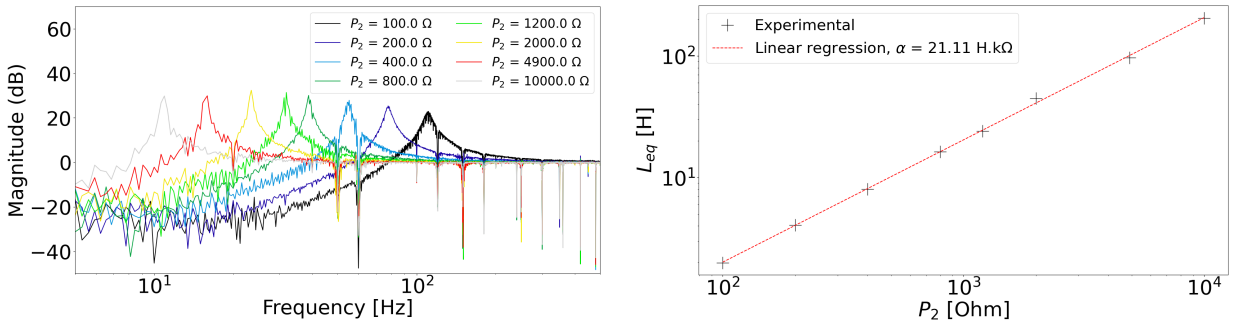

(a) (b)

Figure 4.6: Experimental characterization of the synthetic inductor. (a) presents various electrical frequency response functions depending on P_2. Each peak corresponds to an electrical resonance at pulsation ω_e. (b) stands for the evolution of L_{eq} with regard to P_2.

4.2 Vibration mitigation at zero flow velocity

The vibration mitigation by passive resonant piezoelectric shunt was first investigated experimentally at zero flow velocity. Both synthetic and copper wired inductor configurations were tested and compared. The zero flow velocity requires the use of an external excitation source to generate the mechanical vibrations. This offers the opportunity to totally control the excitation in terms of energy and signal type. The two DuraAct transducers were used as a structural excitation source by converting an electrical signal into a mechanical stress.

4.2.1 Twisting mode mitigation with the synthetic inductor

The synthetic inductor shunt was first tested with the hydrofoil mounted in the test section of the hydrodynamic tunnel and surrounded by air. Thereafter, the test section was filled with water. The main difference between water and air is that the natural frequencies of the structure are lower in water than in air due to the added mass effect. A pseudo-random excitation signal was used as an excitation source and applied to the structure by the two DuraAct patches embedded in the hydrofoil. This type of signal excites all the natural vibration modes which is helpful to investigate the natural frequencies of the structure. Connection of the DuraAct transducers electrodes has been done in order to emphasis the twisting deformation meaning that the twisting modes are more excited than the bending modes. This is achieved by connecting the (+) electrode of the first DuraAct patch with the (-) electrode of the second DuraAct patch (and thus the (-) electrode of the first patch with the (+)

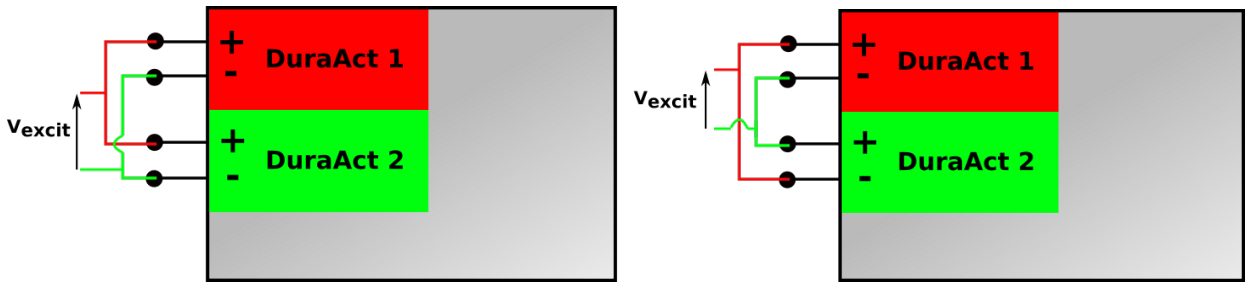

(a) Bending excitation (b) Twisting excitation

Figure 4.7: Illustration of the two types of DuraAct connections : (a) for bending excitation and (b) for twisting excitation. The voltage V_{excit} is the input of the excitation signal.

electrode of the second patch). It is also possible to emphasis the bending modes by connecting the (+) and (-) electrodes of the first and second patch together. Figure 4.7 illustrates the connections associated with the two types of excitations. The vibration velocity was measured with the PDV-100 vibrometer at a single location near the trailing edge. This location is expected to undergo the highest twisting vibration magnitude. Refer to chapter 2 for additional information abut the measurement point.

The frequency response functions obtained for both types of excitations (bending or twisting) are presented in figure 4.8. It is obvious that the type of excitation significantly impacts the response of the structure leading to higher magnitude vibrations of the modes associated with the type of excitation. Refer to table 4.3 for a complete overview of the tuning parameters used for the air and water recordings. The difference between the calculated and experimental resistances could be due to the fact that the capacity used to compute α_{th} may have varied from its nominal value ($C_t = 1$ μF).

A slight offset between the short-circuit and the open-circuit natural frequency is representative of the coupling factor k_c (figure 4.9a). When the shunt is used to mitigate the vibrations of the hydrofoil

Structural excitation features	
Signal type	Pseudo-random
Maximum voltage	6 V
Signal amplification	28 dB
Excitation type	twisting by DuraAct

Table 4.2: Parameters of the piezoelectric excitation. The same parameters were used in air and in water.

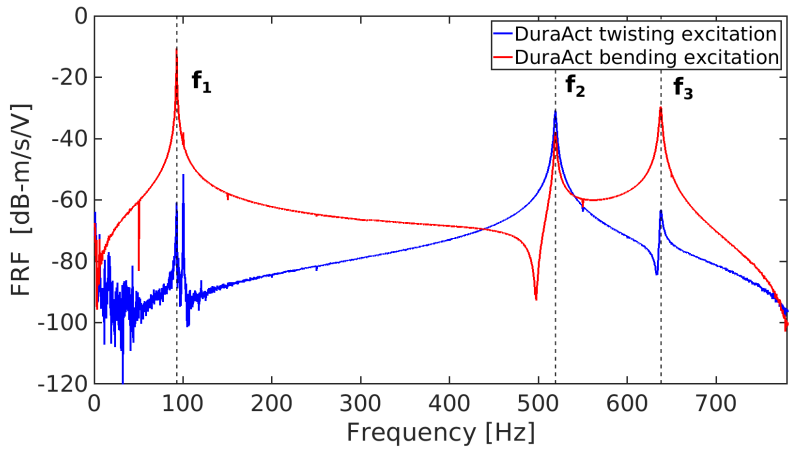

Figure 4.8: Frequency response function associated with a bending or twisting DuraAct excitation, no shunt connected. Hydrofoil surrounded by air.

Calculated shunt parameters	Air	Water
Type of control patch	MFC, PZT fibres at 45°	MFC, PZT fibres at 45°
Controlled mode	1^{st} twisting mode	1^{st} twisting mode
Open-circuit natural frequency	f_2^{co}=519.1 Hz	f_2^{co}=280.9 Hz
Short-circuit natural frequency	f_2^{sc}=516.8 Hz	f_2^{sc}=279.9 Hz
Coupling factor	$k_c = 9.53\%$	$k_c = 8.57\%$
Patch capacitance	$C_t = 14.4\ nF$	$C_t = 14.3\ nF$
Equivalent inductance	$L_{eq} = 6.3\ H$	$L_{eq} = 22.5\ H$
Series resistance	$R_t = 2.4\ k\Omega$	$R_t = 4.2\ k\Omega$
Variable resistance	$P_2 = 316\ \Omega$	$P_2 = 1123\ \Omega$
Experimental shunt parameters		
Serie resistance	$R_t = 0\ \Omega$	$R_t = 0\ \Omega$
Internal resistance compensation	$P_1 = 344\ \Omega$	$P_1 = 326\ \Omega$
Variable resistance	$P_2 = 271\ \Omega$	$P_2 = 840\ \Omega$

Table 4.3: Parameters of the synthetic inductor shunt used for the vibration mitigation with the hydrofoil surrounded by air or by water. The calculated parameters were obtained with equations 1.2 and 1.3 and then adjusted manually to reach the highest vibration mitigation level by varying P_1 and P_2. As the equivalent circuit is naturally too resistive due to non negligible dissipation in the OPA and in the MFC patch, R_t was set to zero and negative resistance was added.

surrounded by air, a vibration reduction level of 31 dB (equivalent of dividing the magnitude by 36) of the twisting mode peak ($f_2 = 518\ Hz$) is observed. The off-peak, also known as antiresonance, appearing is characteristic of a shunted frequency and its magnitude varies with the resistance of the electrical circuit. The deepness of the off-peak can be varied with the potentiometer P_1 which

compensates the internal resistance of the circuit. However, the magnitude of the two secondary peaks at 490 Hz and 540 Hz increases with the deepness of the off-peak which can be problematic in terms of vibration mitigation. When configuring the synthetic inductor shunt, a correct ratio between the deepness of the off-peak and the magnitude of the secondary peaks should be obtained in order to minimize the maximum amplitude over the frequency range of interest. A circuit that is slightly too resistive will exhibit a "plateau" instead of an off peak and in the worst cases a single peak [135]. The location of the off-peak in terms of frequency is controlled by the potentiometer P_2 which is equivalent to vary the inductance of the circuit. A difference between the magnitudes of the two secondary peaks

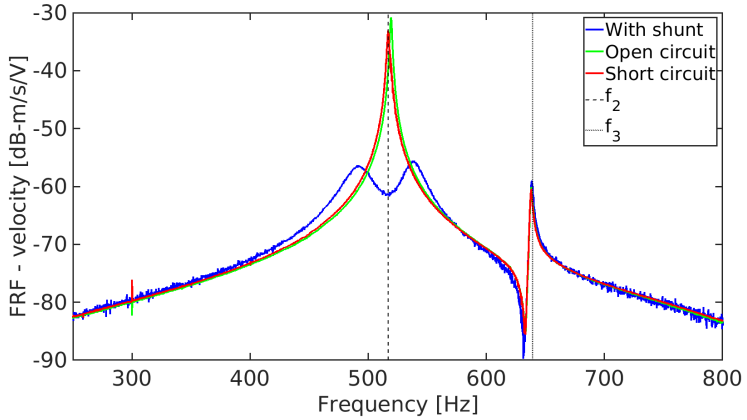

(a) air

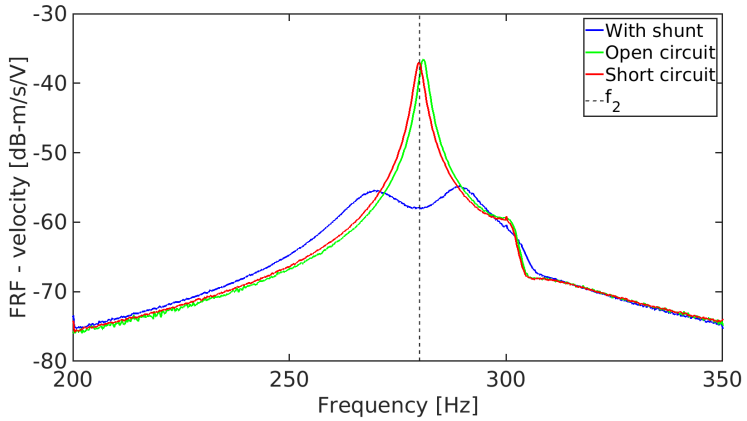

(b) water

Figure 4.9: Frequency response function with the piezoelectric transducer in short-circuit, open circuit and with the synthetic shunt in (a) air and in (b) water. Structural excitation is produced by the DuraAct patches. Vibration mitigation of 31 dB (equivalent of dividing the magnitude by 36) and 21 dB (equivalent of dividing the magnitude by 11) are obtained in air and water respectively.

means that the electrical resonance frequency is different from the mechanical frequency of the mode to control (f_2). It appeared that the shunt parameters calculated analytically with the equations described before had to be adjusted manually to reach the highest mitigation level. The value of capacitance considered for the calculations is an approximation of the real capacitance of the patch, this implies that a manual tuning of the shunt is necessary to maximize the vibration mitigation. Also, the circuit used for these experiments had a high value of internal resistance and the MFC transducer has also its own internal resistance which was not taken into consideration when implementing the equations used to compute the shunt parameters. Consequently, no series resistance was needed and negative resistance was added with P_1 (see table 4.3 for the numerical values of the parameters).

The same arrangement was used to mitigate vibrations with the hydrofoil immersed in still water. The synthetic inductor shunt parameters were adapted to control the same twisting mode but at a lower frequency (f_2=282 Hz) caused by the added mass. According to figure 4.9b, a vibration level reduction of 21 dB (equivalent of dividing the magnitude by 11) of the twisting mode peak ($f_2 = 280\ Hz$) amplitude is observed when the shunt is used to mitigate the vibrations of the hydrofoil surrounded by water. Interestingly, the level of mitigation is lower in water than in air. Independently of the shunt effect, the damping in water is higher than in air which implies that the peak magnitude in open-circuit is lower in water than in air. This explains the lower mitigation level in water than in air. Also, the coupling factor in water is slightly lower than in air. This could also explain the difference between both mitigation levels. The frequency of the first twisting mode is nearly divided by two when the foil is immersed in water but the synthetic inductor shunt is capable to mitigate both frequencies depending on its tuning. This demonstrates the high adaptability of the synthetic inductor and its capacity to target variable vibration frequencies.

4.2.2 Twisting mode mitigation with the copper wired inductor

The passive shunt system implemented with the copper wired inductor was tested with the hydrofoil immersed in water at zero flow velocity. A dedicated inductor was designed for this purpose. The structure was excited by using the two DuraAct patches connected to a signal generator as was done with the synthetic inductor. This configuration can, for example, be used to verify that the shunt parameters are correctly set-up before mitigating the vibration under flow excitation. The reader can refer to table 4.4 for a complete overview of the parameters. As displayed in figure 4.10 showing the

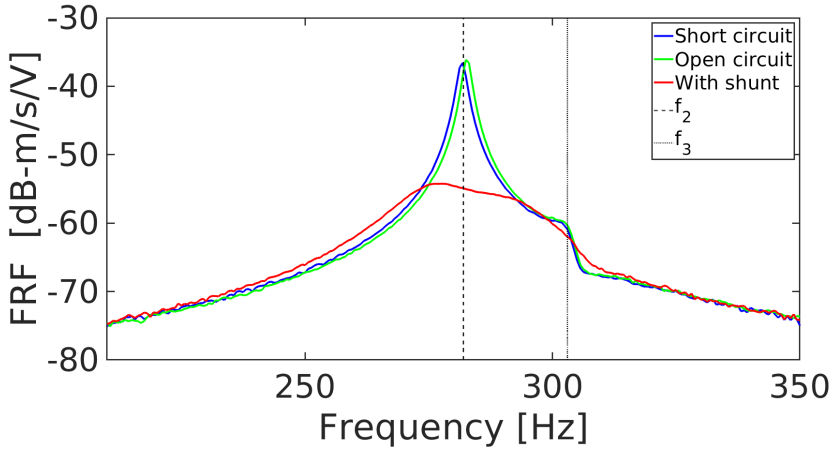

Figure 4.10: Frequency response function with the piezoelectric transducer in short-circuit, open circuit and with the copper wired inductor shunt at zero flow velocity in water. Structural excitation is produced by the DuraAct patches. A vibration mitigation of 18 dB (equivalent to a reduction ratio of 1/8) is observed.

frequency response functions in short-circuit, open-circuit and with the shunt activated, an attenuation level of 18 dB (equivalent to a reduction ratio of 1/8) of the first twisting mode was reached. The open-circuit and short-circuit configurations have nearly the same FRF peak magnitude at f_2. Ideal tuning of the shunt should provide an off-peak centred on the natural frequency to attenuate as was observed for the synthetic inductor shunt. However, it is rather a broadband peak with a "plateau" centred on f_2 that is observed here. This specificity is due to the fact that the electrical circuit is slightly too resistive, mainly because of the copper losses in the coil of the inductor. This could be reduced by using a different design of magnetic component. The fact that the "plateau" has a slope with regard to the horizontal demonstrates that the inductance is slightly too low and implies that the electrical resonance frequency is a bit different of the first twisting mode frequency. By adjusting accurately L_{eq} a higher mitigation level could be attained.

Experimental shunt parameters	
Series resistance	$R_t = 0\ \Omega$
Self inductance	20.4 H (100 Hz) and 21.46 H (1 kHz)
Inductor equivalent series resistance (iron and copper)	618 (100 Hz) and 750 Ohm (1 kHz)

Table 4.4: Parameters of the copper wired inductor shunt used for the vibration mitigation with the hydrofoil surrounded by water.

In comparison with the the synthetic inductor shunt, the copper wired inductor shunt offers less flexibility in terms of variation of the shunt parameters (R_t and L_{eq}) which implicates that the wired inductor must be designed accurately, even if a slight adjustment is possible with the screw inside the inductor core. The main advantages of this type of shunt is that it is able to sustain higher values of voltage and it requires no external power supply which makes it totally autonomous. Under flow excitation conditions, the output voltage of the MFC piezoelectric transducer can reach values higher than 100 V which is not adapted for standard operational amplifiers as the ones used in the synthetic shunt.

4.3 Vibration mitigation under flow excitation

Critical situations in terms of structural vibration occur when an hydrodynamic excitation frequency is equal to a natural frequency of the structure. This induces the lock-in phenomenon described previously. The synthetic shunt was first tested in these conditions but it appeared that the high voltage at the output of the MFC patch caused a saturation of the OPAs. For this reason, the vibration mitigation level proper to the copper wired inductor and the MFC transducer was investigated by comparing the vibration velocity signal root mean square value V_s^{rms} when the shunt is activated and when it is not. The value of the equivalent inductance L_{eq} was adjusted manually to reach the lowest value of V_s^{rms}. Table 4.5 summarizes the experimental shunt parameters. It appears that the optimal value L_{eq}=12 H, is much lower than the computed one. This is probably due to the fact that the MFC patch suffers from water infiltration which induces an increase of the patch capacitance and high internal dissipation. Figure 4.11a presents the vibration velocity signal at $Re_c = 3.74 \times 10^5$ corresponding to the lock-in with the first twisting mode (f_2). It appears that V_s^{rms} is reduced by 59% which offers a considerable reduction of structural fatigue and acoustic radiation.

Experimental shunt parameters	
Series resistance	$R_t = 0\ \Omega$
Self inductance	11.9 H (100 Hz) and 12.2 H (1 kHz)
Inductor equivalent series resistance (iron and copper)	638 (100 Hz) and 745 Ohm (1 kHz)

Table 4.5: Parameters of the copper wired inductor shunt used for the vibration mitigation with the hydrofoil surrounded by water.

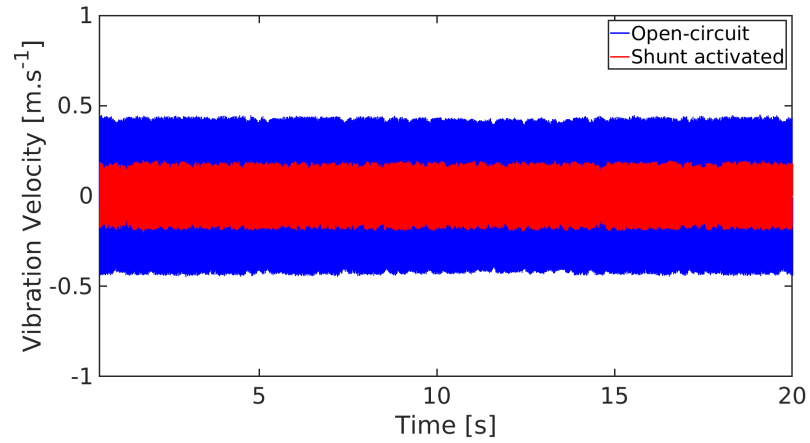

(a)

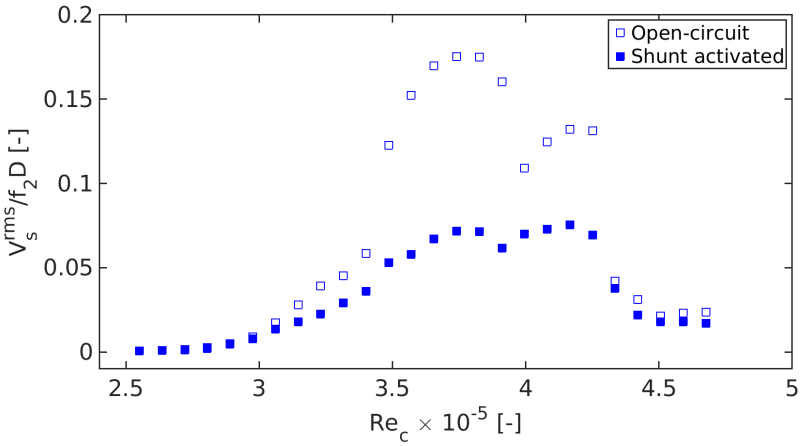

(b)

Figure 4.11: (a) Vibration velocity time signal at $U_0 = 4.4$ m.s^{-1} ($Re_c = 3.74 \times 10^5$, lock-in). (b) Evolution of V_s^{rms} with Reynolds number.

The vibration reduction level has then been investigated at various chord based Reynolds numbers Re_c ranging between 2.55×10^5 and 4.68×10^5. The Reynolds number was varied by increasing the inflow velocity U_0. As is presented in figures 4.11b, it appeared that the shunt provides a vibration reduction level for Reynolds comprised between 2.98×10^5 and 4.68×10^5 with a maximum reduction of 62% at $\mathrm{Re_c} = 3.57 \times 10^5$. This broad range of Reynolds numbers where the shunt induces a vibration mitigation demonstrates that the setup of the shunt parameters offers a certain adaptability. These parameters where initially calculated to control the lock-in with the twisting mode (f_2) at $Re_c = 3.74 \times 10^5$, however a high vibration reduction level was also observed during the lock-in with the second bending mode (f_3). The vibration mitigation level appears to be lower under flow excitation than in

still water conditions. This could be due to the fact that the internal dissipation of the piezoelectric transducer may be increased by the high level of deformation under flow excitation and by water infiltration. Also, the hydrodynamic phenomena involves a non-linear fluid-structure interaction that does not necessarily induces similar mitigation levels as in the linear case. A predictive estimation of the vibration levels requires a more advanced modelling of the dynamics of the VIV that is out of the scope of the present study.

Tests of a passive resonant shunt used to mitigate a twisting mode vibration in a water flow have, to our best knowledge, not been investigated before and the results presented here will pave the way to various industrial applications in the naval domain. We believe that higher vibration mitigation levels could be reached if a better insight on the internal resistance of the piezoelectric transducer is obtained and if water infiltration inside the MFC patch is avoided. The following section is dedicated to a numerical characterization of the mechanical properties of the hydrofoil embedded with piezoelectric transducers and a numerical model of the passive resonant shunt is implemented. The experimental results obtained before is used as a reference to verify the accuracy of the numerical results and validate the model as an efficient design tool for future prototypes.

4.4 Numerical simulations at zero flow velocity

The design of structures embedded with piezoelectric transducers requires a precise identification of the mechanical properties of the system in order to achieve optimal integration of the transducers among the structure. As hydrodynamic phenomena may act as structural excitation sources and induce resonance, it is necessary to determine the natural frequencies and deflection shapes at the early design stages in order to avoid critical vibration magnitudes. The determination of the coupling factor, which is of prime importance to appreciate the ability of a resonant shunt to mitigate vibrations efficiently, requires an experimental assessment at each modification of the structure if a numerical model is not available. Also, the determination of the optimal shunt parameters may require several iterations resulting in the replacement of the shunt components due to the reduced variability range proper to most standard passive electrical components.

The use of a numerical tool to predict the modal properties and the coupling factors of structures embedded with piezoelectric transducers is of great interest because it will avoid several, time

consuming and expensive, experimental iterations. In addition, the modelling of a piezoelectric resonant shunt integrated to an immersed structure will provide an appreciation of the optimal vibration mitigation level and shunt parameters. The commercial code COMSOL *Multiphysics*, based on finite elements computations, was employed to implement a numerical model of the previously described hydrofoil connected to a resonant passive shunt. No Computational Fluid Dynmics (CFD) modelling was implemented even if this offers interesting perspectives for future investigations. Special attention was paid to the modelling of a piezocomposite active layer of the type MFC-P1 elongator (d_{33}). The modelling of such a transducer is still challenging and we present here a calibration method of its piezoelectric constants which could be employed for the design of other structures embedded with MFC piezocomposites.

The experimental results described previously were used as a reference to validate the numerical computations. Also, when using a numerical model, it is effortless to vary the parameters and to realize multiple tests which has permitted to gain new insights on the studied system. After describing the setup of the numerical model, the present section compares the computed modal properties and coupling factors to the experimental results. A model of a resonant passive shunt is assessed numerically in order to study the vibration mitigation proper to the hydrofoil first twisting mode.

4.4.1 Modelling of the hydrofoil structure

In a first instance, the geometry of the hydrofoil exempt from piezoelectric transducers was generated by using a computer aided design (CAD) tool and was imported in COMSOL. The same CAD file, which includes the foil root used for the mounting in the test section, was used for the machining of the experimental hydrofoil. As the general arrangement of the hydrofoil is complex due to the presence of channels machined for the passage of the electric cables and due to the presence of curved surfaces, it is necessary to generate the geometry by using a dedicated CAD software. Nevertheless, in the case of simple geometries such as flat plates, beams or cylinders, the build-in CAD tool of COMSOL is appropriate. The initial geometry file was employed for the evaluation of the modal properties of the hydrofoil without embedded transducers.

A second geometry CAD file includes the DuraAct and MFC active layers and the soft layers representative of the Kapton shell and the epoxy used to integrate the transducers on the hydrofoil surface. The piezoelectric active layers follow the curvature of the hydrofoil. The second geometry

	Value	Units
Aluminium		
Density	2650	$kg.m^{-3}$
Young's modulus	70	GPa
Poisson's ratio	0.33	
Soft layer		
Density	1420	$kg.m^{-3}$
Young's modulus	2.8	GPa
Poisson's ratio	0.30	

Table 4.6: Material properties of the hydrofoil body and soft layers implemented for the COMSOL numerical model.

file was used to investigate the modification of the modal properties by the addition of piezoelectric transducers, for the evaluation of coupling factors and for the modelling of the resonant passive shunt. Refer to table 4.6 for an overview of the hydrofoil mechanical properties. As can be seen in figure 4.12a, a fixed constraint condition was applied at the root of the hydrofoil in order to model a perfect clamping. This element is important because the clamping conditions may affect the mode shapes and thus the coupling factor, see for example [106].

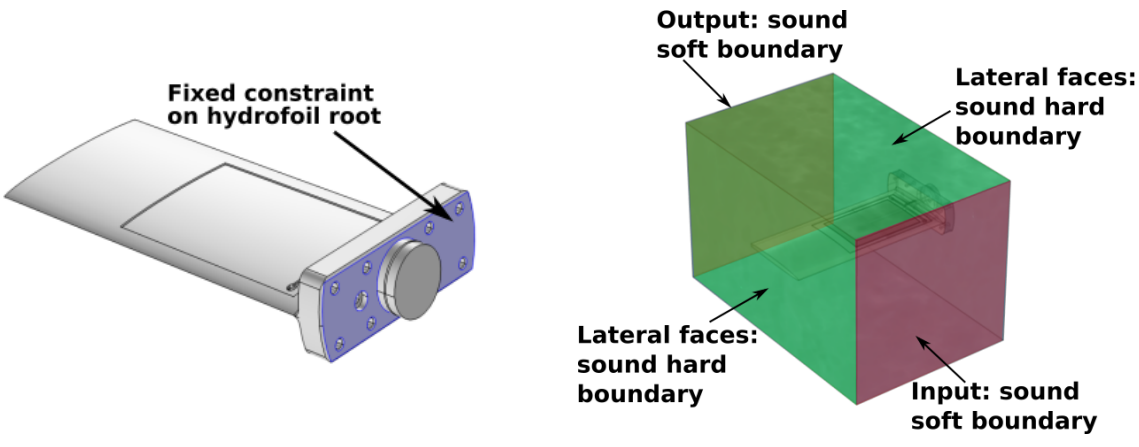

(a) (b)

Figure 4.12: (a) Illustration of the hydrofoil geometry with a fixed constraint applied at the root of the profile. (b) fluid domain surrounding the hydrofoil for numerical computation in still water.

4.4.2 Fluid modelling

The numerical study in still water requires an additional domain representative of the test section and the fluid. A parallelepiped bloc of same dimensions as the test section (193 mm × 193 mm × 300 mm) was implemented with the hydrofoil located at the center of the bottom wall, as displayed in figure 4.12b. This arrangement respects the experimental conditions in order to achieve realistic comparisons between numerical and experimental results. The fluid domain, which consists of an acoustic fluid medium surrounding the hydrofoil, is representative of the water present in the test section. Rigid walls boundary conditions were applied to the lateral faces of the fluid domain. This type of boundary implies that the normal component of the acceleration (and thus the velocity) is zero which means that the fluid and thus the acoustic radiation, is restricted by the walls.

The input and the output of the fluid domain represents the locations where the flow enters the test section and where it goes out. These surfaces have been configured as sound soft boundaries which means that the acoustic pressure vanishes at these locations. Test were also done with the input and output of the domain configured as sound hard boundaries. Table 4.7 presents the three first natural frequencies in open-circuit for both types of boundaries. It appears that the difference between natural frequencies is lower than 1% which implies that the type of boundary has weak impact on the natural frequencies computation for the present arrangement. The fluid was considered at rest (zero flow velocity) for all the computations, the fluid-structure interaction induced by the vibrations of the hydrofoil were not taken into account because this is prohibitive in terms of computation costs and it requires additional CFD modules which is not the purpose of this study. Also, the main aim of this study is to extract the natural frequencies and coupling factors to facilitate the design of future prototypes.

	Sound soft boundaries	Sound hard boundaries	Difference
f_1^{oc}	38.43 Hz	38.22 Hz	0.55%
f_2^{oc}	285.54 Hz	285.37 Hz	0.06%
f_3^{oc}	302.28 Hz	301.79 Hz	0.16%

Table 4.7: First three natural frequencies in open-circuit for the input and output of the fluid domain configured as sound soft or sound hard boundaries.

4.4.3 Modelling of DuraAct transducers

The DuraAct piezoelectric transducers commercialized by PI Ceramic are of the type P-876.A15 and consist of a PIC-255 lead zirconate titanate active layer sandwiched between two soft Kapton shell layers. This encapsulation induces a pre-stress on the active layer which increases the admissible curvature of the transducer. This point is of prime importance for the present application because it reduces drastically the brittle specificity of piezoelectric materials and allows integration on curved geometries such as hydrofoils or propeller blades.

The PIC-255 active layer belongs to the category of "soft" piezo ceramics which is characterized by relatively easy polarization due to its ferro-electric properties. The main features of this type of active layer consists in high Curie temperature ($T_C = 350\ ^\circ C$), high permittivity and coupling factor and a high charge constant. According to PI Ceramics, this type of active layer is particularly suitable for actuator applications in dynamic operating conditions and at high ambient temperatures. A description of the arrangement and thickness of each constitutive layer (Kapton shell, electrodes and active layer) of the patch is presented in figure 4.13.

The DuraAct patches were used as structural excitation sources when computing the frequency response function, depending on the connection of the electrodes, bending or twisting deformations can be simulated similarly as for the experimental arrangement. The main mechanical and piezoelectric characteristics of the P-876.A15 DuraAct active layer are presented by table 4.8.

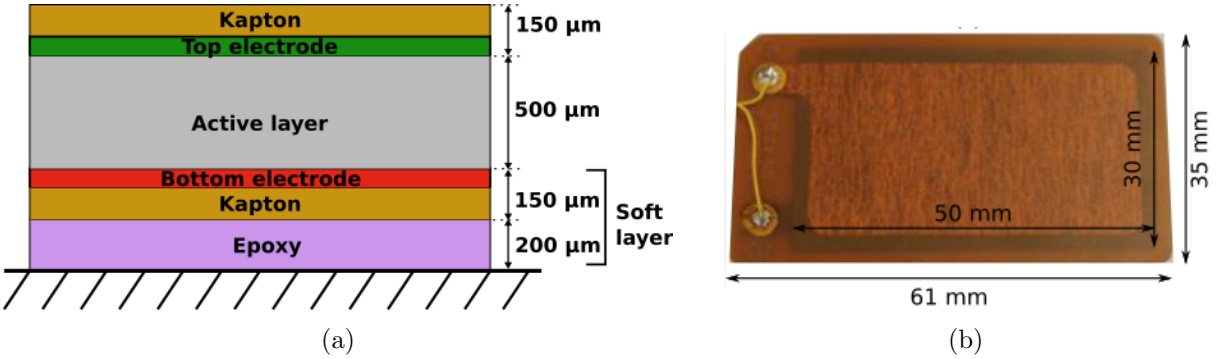

(a) (b)

Figure 4.13: Sequence of layers of the DuraAct P-876.A15 transducer (a) and image of DuraAct P-876.A15 with dimensions (b).

Density	7800	kg/m^3
Compliance matrix		
S_{11}^E	16.06×10^{-12}	m^2/N
S_{12}^E	-5.685×10^{-12}	m^2/N
S_{13}^E	-7.454×10^{-12}	m^2/N
S_{33}^E	19.09×10^{-12}	m^2/N
S_{44}^E	46.99×10^{-12}	m^2/N
S_{55}^E	46.99×10^{-12}	m^2/N
S_{66}^E	43.50×10^{-12}	m^2/N
Charge constants		
d_{31}	-186.7×10^{-12}	m/V
d_{33}	399.6×10^{-12}	m/V
d_{15}	617.4×10^{-12}	m/V
Relative permittivity		
ϵ_{11}^σ	1852	
ϵ_{22}^σ	1852	
ϵ_{33}^σ	1751	

Table 4.8: Material properties of the PIC-255 active layer in strain-charge form.

4.4.4 Modelling of a MFC transducer

General considerations

Macro Fiber Composites (MFCs) have been developed at NASA around the year 2000 [18]. They consist of rectangular piezo-ceramic fibres sandwiched between layers of adhesive, electrodes and polyamide film. The electrodes are attached to the film in an interdigitated pattern. This type of arrangement enables in-plane polling, actuation and sensing. The MFC transducer used for this study is a $M8557F1$ manufactured by *Smart Material* and is of the type d_{33} (elongator) with a fiber direction equal to 45°. This fiber direction is favourable for twisting mode vibration control because the principal stress directions can then be aligned or orthogonal to the fibers. Refer to figure 4.14 for an illustration of the internal arrangement of this type of MFC. The nominal capacitance of the transducer provided by the data sheet is equal to 13.26 nF. This value corresponds to the capacitance when the patch is free. In our case, the patch is curved and prestressed because it is embedded on the hydrofoil surface. For the present configuration, we experimentally measured a capacitance equal to 14.4 nF at a recording frequency of 1 kHz for the MFC integrated on the hydrofoil surface and surrounded by air. This value of capacitance will be employed as a reference to set-up the model and

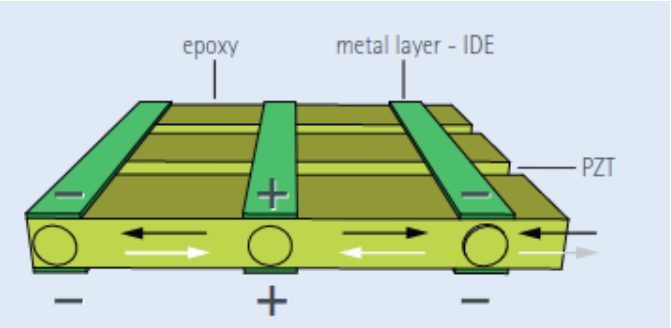

Figure 4.14: Internal arrangement of a d_{33} MFC P1 type. Image by Smart Material.

calibrate the piezoelectric constants (ϵ_{ij} and d_{ij}).

Mixing rules

Piezocomposites are composed of several layers of different materials (electrodes, kapton, epoxy, active layer) which means that an accurate numerical modelling is not straightforward. A detailed description of the layer sequence, thickness and equivalent homogenous mechanical, piezoelectric and dielectric properties of each constitutive material is required to obtain realistic simulations. These technical informations are not fully provided by the manufacturers which complicates the modelling of structures embedded with piezocomposites. Various attempts have been made over the years to model piezocomposites, see for example [138], [139] and [140]. Though, it appears that there exists only few analytical simple mixing rules for the characterization of the longitudinal and transverse piezoelectric coefficients for piezocomposites with rectangular fibres such as d_{31} and d_{33} MFCs. The present study proposes to use the homogenized mechanical properties derived from analytical mixing rules in [2] combined with a calibration of the piezoelectric and permittivity parameters in order to match with the experimental coupling factors and the capacitance. The homogenized properties of the MFC d_{33} active layer proposed by [2] are summarized in table 4.9.

The electric field generated inside a d_{33} MFC does not have a constant direction due to the arrangement of the interdigitated electrodes. It is however reasonable to consider that the polling direction is that of the fibres and that the electric field is in the same direction. At the local level, the orthotropic direction offering properties that differ from the two other directions is the one that is in the plane of the MFC patch but orthogonal to the fibers. It is considered as the first direction. The

d_{33} MFC transducer is then considered as a transversely isotropic material which is a special form of orthotropic material [141]. The compliance matrix of a transversely isotropic material is expressed as

$$[S] = \begin{bmatrix} \frac{1}{E_1} & -\frac{\nu_{21}}{E_2} & -\frac{\nu_{21}}{E_2} & 0 & 0 & 0 \\ -\frac{\nu_{21}}{E_2} & \frac{1}{E_2} & -\frac{\nu_{23}}{E_2} & 0 & 0 & 0 \\ -\frac{\nu_{21}}{E_2} & -\frac{\nu_{23}}{E_2} & \frac{1}{E_2} & 0 & 0 & 0 \\ 0 & 0 & 0 & \frac{1}{G_{23}} & 0 & 0 \\ 0 & 0 & 0 & 0 & \frac{1}{G_{12}} & 0 \\ 0 & 0 & 0 & 0 & 0 & \frac{1}{G_{12}} \end{bmatrix}, \tag{4.9}$$

where the direction 1 corresponds to the in-plane orthogonal to the fibres direction, 2 the normal out-of-plane direction and 3 the fibres direction. It has been considered that $\nu_{12}/E_1 = \nu_{21}/E_2$. Note that it is direction 1 that offers different properties (and not the direction of the fibers) because a 3D representation of this equivalent material would actually be a stack of piezoelectric layers normal to direction 1. The numerical values computed with the compliance matrix used for the MFC transducer model are presented in table 4.10.

d_{33} **MFC homogenized properties**	**Symbol**	**Unit**	**Mixing rules**
Young's modulus	E_1	GPa	16.97
	E_2	GPa	42.18
Shear modulus	G_{12}	GPa	6.06
	G_{23}	GPa	17
Poisson's ratio	ν_{21}	-	0.38
	ν_{23}	-	0.24
Piezoelectric charge constants	d_{32}	pC/N	-176
	d_{33}	pC/N	436
Dielectric relative constant (free)	$\epsilon_{33}^T/\epsilon_0$	-	1593

Table 4.9: Homogenized properties of the active layer of a d_{33} MFC calculated by [2] using analytical mixing rules.

Density	5440	kg/m^3
Compliance matrix		
S_{11}^E	58.93×10^{-12}	m^2/N
S_{12}^E	-9.009×10^{-12}	m^2/N
S_{13}^E	-9.009×10^{-12}	m^2/N
S_{23}^E	-5.704×10^{-12}	m^2/N
S_{33}^E	23.71×10^{-12}	m^2/N
S_{44}^E	58.82×10^{-12}	m^2/N
S_{55}^E	165.0×10^{-12}	m^2/N
S_{66}^E	165.0×10^{-12}	m^2/N

Table 4.10: Mechanical properties of the MFC d_{33} piezocomposite computed for the compliance matrix.

Material coordinate system

The MFC body coordinates (x, y, z) have to be related with the piezoelectric material coordinates named O_{123}. An illustration of the coordinate systems disposal is proposed in figure 4.15. In the O_{123} coordinate system, the direction e_3 is aligned with the fibres direction, e_2 is the normal out-of-plane direction aligned with the z axis and e_1 is the in-plane normal direction to the fibres and also the electrodes direction. It has been considered that both the material and the body coordinate systems are orthogonal in the three directions. An example of coordinate system configuration can be found in [142]. Also, with respect to the COMSOL notation format, the transformation matrix between both coordinate systems is expressed as:

$$[T] = \begin{bmatrix} \sin\frac{\pi}{4} & -\cos\frac{\pi}{4} & 0 \\ 0 & 0 & -1 \\ \cos\frac{\pi}{4} & \sin\frac{\pi}{4} & 0 \end{bmatrix}. \tag{4.10}$$

As stated before, the MFC transducer is curved by the integration on the hydrofoil surface. This property was taken into account when setting up the numerical model. The curvilinear coordinates function of COMSOL was implemented so that the material coordinate system follows the curvature. It is especially meaningful to take this property into consideration when modelling piezoelectric transducers integrated on high curvature radius bodies such as cylinders for example.

A last complexity that arises when modelling MFC transducers is related to the interdigitated electrodes. As seen in Figure 4.14 they are responsible for the direction of the electric field that is oriented along the piezoelectric fibers. However, modelling such an interdigitated pattern may be difficult in a

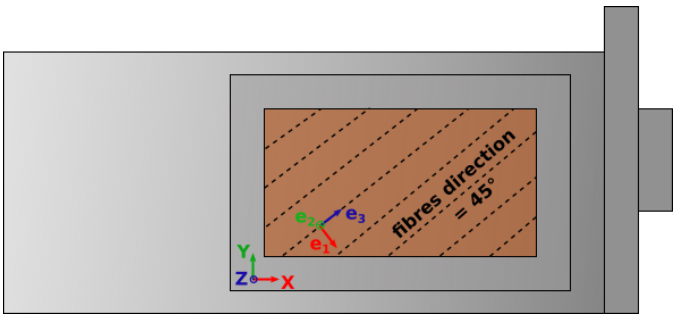

Figure 4.15: Illustration of the material and body coordinate systems. The colors of the axes respects the COMSOL formalism.

macroscopic finite element model, that is why it is here decided to virtually modify the orientation of the electric field to retrieve a model closer to the one used for the DuraAct patches. Two electrodes are actually defined on the top and bottom of the patches and both the piezoelectric permittivity and coupling matrices undergo a permutation to orientate the electric field along the e_2 axis that corresponds to the thickness direction. Since the related constants are then calibrated, the macroscopic coupling and capacitive effects reach representative values even if the proposed multiphysics model does not represent the actual local state inside the material.

Arrangement of the material layers

In addition to the Kapton encapsulation of the patches, epoxy was used as an adhesive to integrate the transducers on the hydrofoil surface. A material identified as a soft layer was modelled between the hydrofoil surface and the electrode delimiting the piezoelectric active layer. As was mentioned by [106] it is important to include the soft layer in the numerical model as it reduces the electromechanical coupling level because of stiffness loss. The soft layer includes the Kapton shell, the epoxy layer and one electrode. The total thickness of the transducer (soft layer + active layer) was close to the depth of the cavity. Because the thickness of the epoxy is difficult to evaluate, it was considered that it is equal to the gap between the Kapton shell and the base of the cavity. The thickness of the electrodes is very small so it was not taken into account. The length and width of the soft layer domain have the same dimensions as the piezoelectric active layers which means that it is smaller than the span wise and chord wise dimensions of the cavity. This approximation is acceptable because there is weak impact of the uncovered area on the electromechanical coupling. Because the epoxy layer

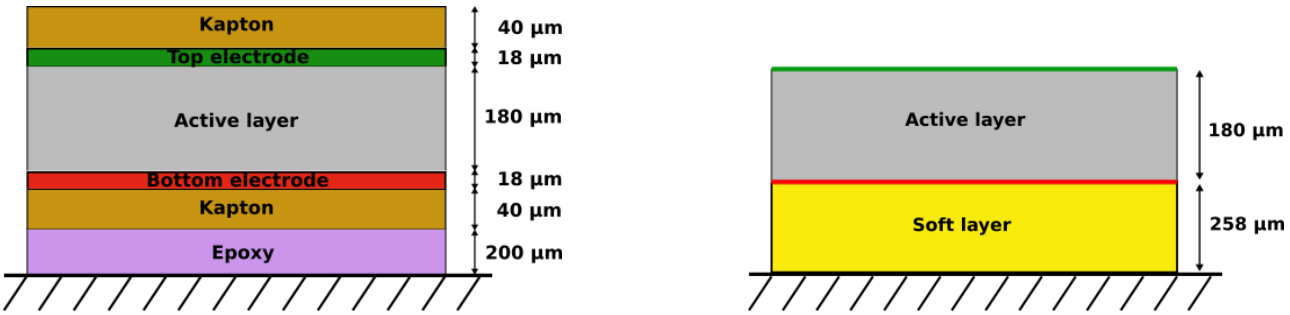

Figure 4.16: Sequence of layers of the MFC transducer (a). Data provided by Smart Material and presented in the work of [2]. Arrangement of the layers for the numerical model (b).

thickness is not precisely determined, it could be used as a variable parameter to align the numerical and experimental coupling factors as was done by [106]. For this study we have rather adjusted the piezoelectric charge and relative permittivity constants. Refer to table 4.6 for the material properties of the soft layer used in the numerical model. A description of the arrangement and thickness of each MFC constitutive layer (Kapton shell, epoxy, electrodes and active layer) is presented in figure 4.16a. The COMSOL layer arrangement is presented in figure 4.16b.

Calibration of the piezoelectric properties

A calibration of the model was performed by multiplicating the relative permittivity parameters proposed in [2] by a constant value. The capacitance of the model was evaluated by integrating with COMSOL the surface charge density of the modelled active layer at a single frequency ($f = 1000$ Hz, same as the experimental capacitance recording frequency). Recall that the model used for the present study replaces the interdigitated electrodes by more traditional top and bottom electrodes which virtually modify the orientation of the electric field from the e_3 to the e_2 direction. The calibration of the permittivity then naturally leads to non-physical values with respect to the considered homogenized piezoelectric material but we can still retrieve the global capacitance of the MFC patch, which is what is actually seen from the electrical circuit. The same process is proposed for the piezoelectric constants that are now related to the e_2 direction to be consistent with the virtual direction of the electric field. The initial charge constants $d_{31} = d_{32}$ and d_{33} are all multiplied by an identical constant value to compute the updated d_{21}, d_{22} and d_{33} constants used in the COMSOL model.

The piezoelectric charge constants of the active layer (d_{21}, d_{22}, d_{23}) were adjusted to match the

	Value	Units
Charge constants		
d_{21}	-25.5×10^{-12}	m/V
d_{22}	-25.5×10^{-12}	m/V
d_{23}	63.2×10^{-12}	m/V
Relative permittivity		
$\epsilon_{11}^T/\epsilon_0$	92.0	-
$\epsilon_{22}^T/\epsilon_0$	75.2	-
$\epsilon_{33}^T/\epsilon_0$	92.0	-

Table 4.11: Material properties of the MFC active layer in strain-charge form.

experimental coupling factors. A first computation of the coupling factors associated with the first, second and third natural modes was achieved with the hydrofoil surrounded by air and with the piezoelectric parameters proposed by [2].

The modified charge constants and permittivities were not modified for the in-water configuration and were kept the same for all the upcoming computations. It is interesting to notice that the coupling factors and capacitance depends on both the piezoelectric charge constants and the relative permittivities, so it is necessary to reach a suitable value for both parameters when calibrating the model, in other words to find the best compromise. A synthesis of the calibrated piezoelectric properties is presented by table 4.11.

4.4.5 Meshing of the domains

The mechanical system has been decomposed into three meshed subdomains consisting in the hydrofoil body, the fluid region representative of the test section and the thin layers consisting of the piezoelectric active layers (DuraAct and MFC transducers) and the soft layers (Kapton and epoxy). This has been achieved in order to control the meshing of each part of the mechanical system and to potentially induce local refinement. The COMSOL automatic meshing algorithm was employed for the three subdomains.

A convergence study was realized based on the first two natural frequencies (first bending and first twisting modes) and on their corresponding coupling factors. Computations were achieved in air with the DuraAct transducers connected in short-circuit and the MFC connected in open and short-circuit. Figure 4.17 (a) present the mesh convergence results in open-circuit for the first bending mode f_{1oc}

and the first twisting mode f_{2oc}, while figure 4.17 (b) presents the mesh convergence analysis for the coupling factors. We have considered that the mesh is fully converged for 93 234 elements in the in air configuration. A similar mesh size was used for the hydrofoil and thin layers when studying the in water configuration but an additional subdomain corresponding to the fluid was appended and meshed independently. The complete parameters of the mesh are presented in table 4.12.

The complexity of the geometry, in particular the presence of the channels machined for the wires, is responsible for the high number of elements required to reach convergence. Figure 4.18 is an illustration of the meshed hydrofoil and thin layers domains (here the MFC transducer is represented).

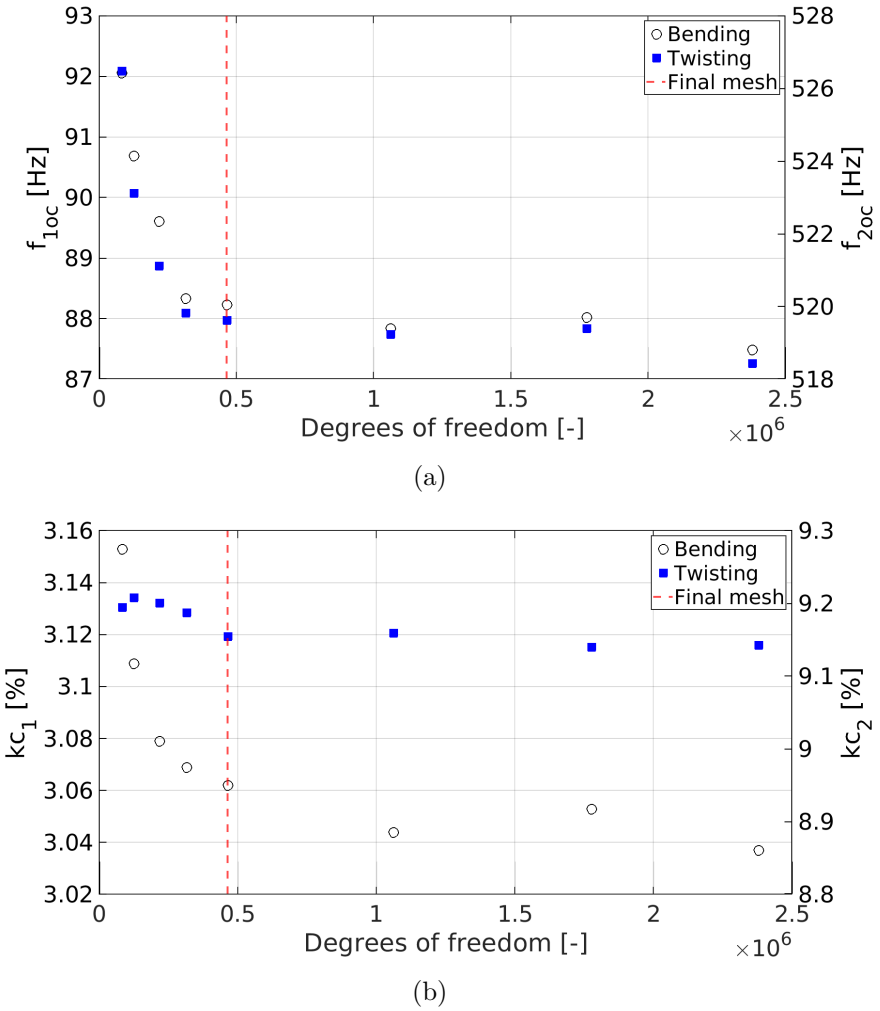

Figure 4.17: Mesh convergence study on (a) the in-air natural frequencies and (b) the corresponding coupling factor.

	In air configuration	**In water configuration**
Type of elements	Tetrahedral	Tetrahedral
Shape function	Quadratic serendipity	Quadratic serendipity
Number of degrees of freedom	464 495	468 318
Number of elements		
Hydrofoil	67 490	49 958
Thin layers	25 744	14 142
Fluid domain	-	98 071
Total	93 234	162 171

Table 4.12: Mesh specifications for the in air and in water configurations.

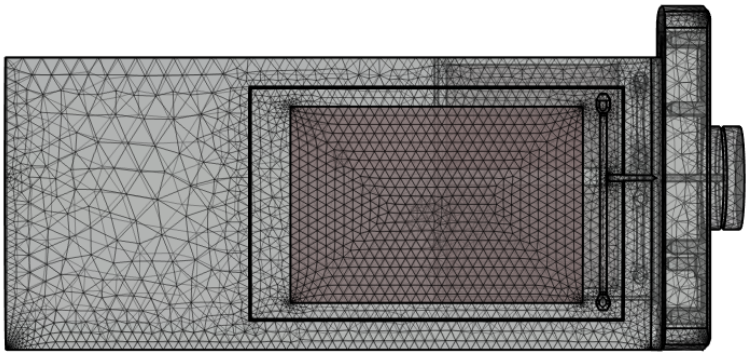

Figure 4.18: Illustration of the hydrofoil and thin layers mesh for the in-water configuration.

It may appear that some narrow regions are over-sampled in terms of mesh elements, especially the channels dedicated to the wire passage and the corners of the geometry. Further improvement of the mesh could be obtained by meshing these regions independently, however for the present applications these regions are not critical and the computation time is still low so we have considered that the COMSOL automatic meshing function offers satisfactory results.

4.4.6 Comparison between numerical and experimental results

Computation of the natural frequencies and deflection shapes

The numerical model of the hydrofoil embedded with piezoelectric transducers was employed to achieve a modal analysis. The natural frequencies and associated deflection shapes were computed for the in-water configuration with all the transducers in open-circuit mode (equivalent to a zero

voltage condition at the electrodes). This type of analysis offers substantial informations about the deformation of the structure and may help to identify critical stress regions and critical vibration regimes. Figure 4.19 presents the deflection shapes of the three first natural modes and their associated natural frequencies. The highest deformation magnitude is represented by dark blue regions and lowest by light green regions. The transparent frame represents the structure without deflection. The first mode is a bending mode, the second mode is a twisting mode and the third mode is close to a second bending mode but the non symmetric geometry leads to a combination of bending and twisting deformation. These deflection shapes are in agreement with the ones observed with the scanning vibrometer and presented in chapter 2.

The experimental and numerical natural frequencies are presented in table 4.13. For the first three modes, the difference between experimental and numerical values is lower than 3% without recalibration of the mechanical properties. These results demonstrate the benefits of preliminary numerical computations. Especially, knowing the natural frequencies at the early design stage will prevent post-manufacturing modifications of the structure in order to adapt the modal properties of the structure. Also, it may help to properly set-up an experimental campaign, for example the knowledge of the deflection shapes is useful to determine the regions were the highest vibrations will be observed and knowing these regions is also useful to setup the vibrometer recording points. As was explained in the previous chapter, high magnitude vibrations occur when the vortex shedding frequency couples with a natural frequency. Knowing the natural frequencies makes it possible to avoid critical flow velocities where coupling occurs.

	Open-circuit, numerical	Open-circuit, experimental	error
f_1	38.43 Hz	39.38 Hz	2.4%
f_2	285.54 Hz	281.2 Hz	1.5%
f_3	302.28 Hz	302.8 Hz	0.2%

Table 4.13: Numerical and experimental frequencies of the three first modes in water. Connection of the MFC electrodes in open-circuit and excitation by the DuraAct transducers in twisting configuration.

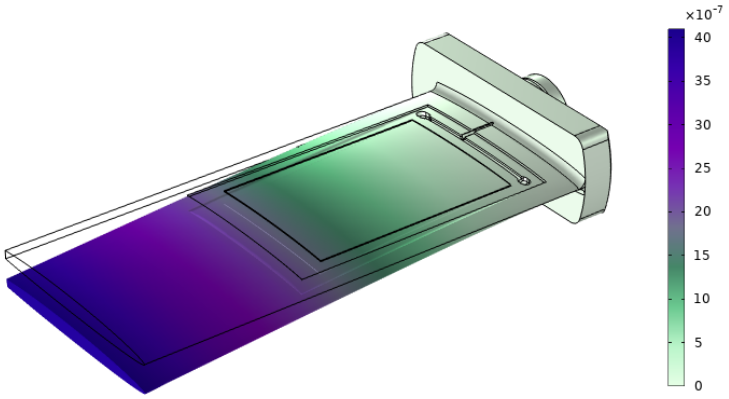

(a) Mode 1: $f_1 = 38.43\ Hz$

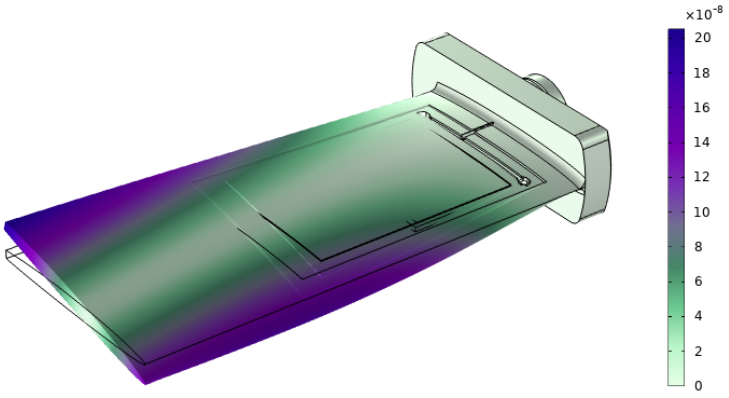

(b) Mode 2: $f_2 = 285.54\ Hz$

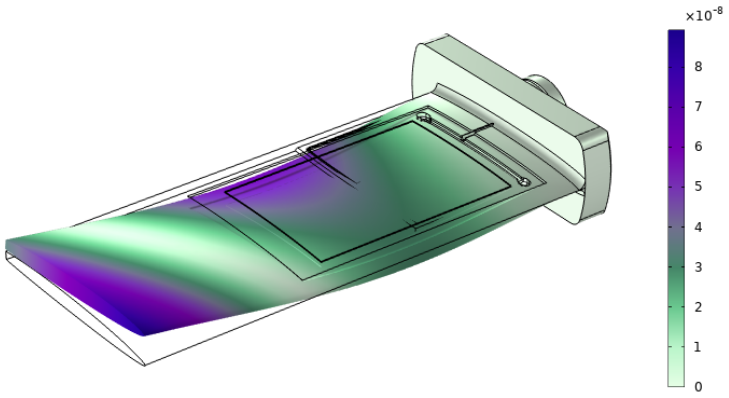

(c) Mode 3: $f_3 = 302.28\ Hz$

Figure 4.19: Deflection shapes of the hydrofoil structure obtained by numerical simulation with COMSOL Multiphysics. The hydrofoil is immersed in water.

Modification of the modal properties by piezoelectric transducer integration

Computations in air were achieved in order to compare the frequency response functions (FRF) of the vibration velocity for a configuration without integrated piezoelectric transducers and with DuraAct and MFC transducers embedded on the hydrofoil surface and connected in short-circuit. The FRFs were computed for both configurations with a mechanical excitation source applied on the upper corner of the trailing edge and aligned with the z axis of the body coordinates. As displayed in figure 4.20, the frequency of the peaks corresponding to the first bending mode (f_1) and the first twisting mode (f_2) are increased by 8 Hz and 37 Hz respectively whereas the frequency of the second bending mode is decreased by 8 Hz when the transducers are integrated on the structure.

The large frequency offset observed for the first twisting mode demonstrates that it is necessary to take into account the integration of the transducers when evaluating the natural frequencies and deflection shapes of a structure. It is important to specify that the natural frequencies of the structure could also vary according to the position of the transducers so it is not possible to determine a general rule when regarding the difference between natural frequencies of non-integrated and integrated transducers configuration.

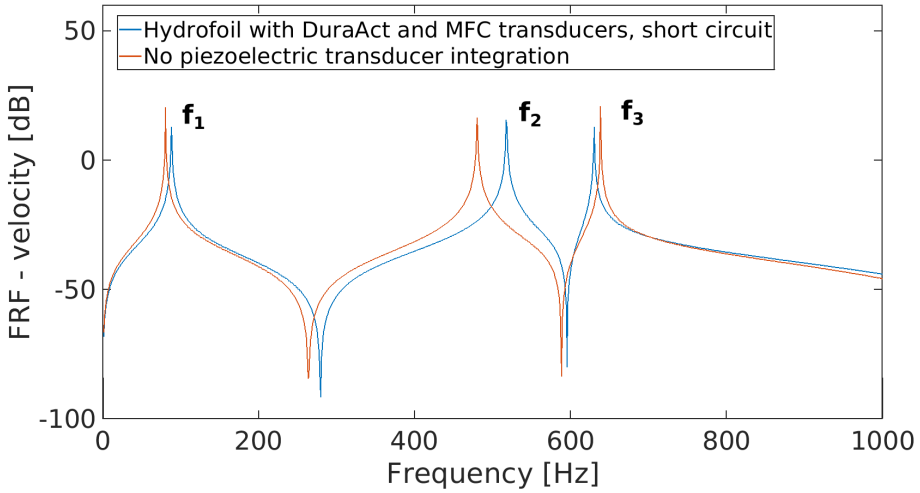

Figure 4.20: Frequency response functions of the vibration velocity in air corresponding to a configuration without piezoelectric transducers (orange curve) and with the DuraAct and MFC transducers embedded on the hydrofoil surface (blue curve).

	No patch, numerical	With patch, numerical	With patch, experimental	error
f_1	80.0 Hz	88.0 Hz	92.5 Hz	5%
f_2	480.0 Hz	517.0 Hz	518.4 Hz	0.3%
f_3	638.0 Hz	630.0 Hz	637.2 Hz	1%

Table 4.14: Natural frequencies in air of the first three modes obtained with numerical computations with and without transducer and experimental values for the integrated transducers configuration. Connection of the electrodes in short-circuit for all configurations. The error column represents the difference between numerical and experimental results.

A comparison between numerical and experimental natural frequencies in air and with integrated transducers (DuraActs and MFC) was also achieved. As demonstrated by table 4.14, the difference between numerical and experimental is lower than 2% which proves the high accuracy of the numerical computations and confirms the previous results in-water.

Computation of the Piezoelectric coupling factors

The capability of a resonant piezoelectric shunt to mitigate vibrations is directly dependent of the coupling factors. High coupling factor values will result in significant vibration reduction levels induced by the shunt. The coupling factor relies on the piezoelectric material properties but also on the positioning of the transducer on the structure and on the soft layer features. Piezoelectric coupling factors were computed numerically in air and in water for the following configurations:

- Coupling factors of the MFC transducer.
- Coupling factors of the DuraAct transducers in bending mode.

A comparison between numerical and experimental results is presented by table 4.15. Computation of the coupling factors was done by using a RFP algorithm which evaluates the natural frequencies in short (sc) and open-circuit (oc) of the selected mode. Coupling factors lower than 2% should be taken with caution because the difference between sc and oc frequencies is very small. As stated in the previous section, the piezoelectric constants of the MFC patch were calibrated in air so that the experimental an numerical coupling factors of the second bending mode (kc_2) match together. After calibration, it appears that the coupling factors proper to modes one (kc_1) and three (kc_3) are also aligned. Results for the in water configuration reveals also a proper match of the numerical and

experimental coupling factors. These observations validate the calibration principle and demonstrate that a transition from air to water is not strongly impacting for a piezoelectric coupling related to the first modes of the structure.

The coupling factors of the DuraAct transducers were also investigated. Even if these patches were initially integrated on the hydrofoil surface to act as a structural excitation source, they could also be used to mitigate vibrations, depending of the connection of their electrodes. The coupling factors were computed when the DuraAct patches are connected in bending mode. No calibration of the DuraAct patches was achieved. It appears that the numerical coupling factor proper to the first bending mode is nearly equal to the experimental value in air which demonstrates the correct set-up of the DuraAct numerical model and also the high capability of this type of arrangement to mitigate the first bending mode.

	Air			**Water**		
	f_n^{num}	kc_n^{num}	kc_n^{exp}	f_n^{num}	kc_n^{num}	kc_n^{exp}
MFC						
	f_1^{sc}=87.688 Hz f_1^{oc}=87.718 Hz	3.04%	3.3%	f_1^{sc}=38.416 Hz f_1^{oc}=38.434 Hz	3.10%	3.70%
	f_2^{sc}=517.412 Hz f_2^{oc}=519.572 Hz	9.15%	9.2%	f_2^{sc}=284.58 Hz f_2^{oc}=285.54 Hz	8.20%	8.50%
	f_3^{sc}=629.710 Hz f_3^{oc}=629.925 Hz	2.61%	2.6%	f_3^{sc}=301.91 Hz f_3^{oc}=302.28 Hz	4.95%	4.70%
DuraAct Bending						
	f_1^{sc}=87.678 Hz f_1^{oc}=88.689 Hz	15.23%	15.0%	f_1^{sc}=38.416 Hz f_1^{oc}=38.860 Hz	15.25%	N.C.
	f_2^{sc}=517.411 Hz f_2^{oc}=517.412 Hz	0.14%	0.5%	f_2^{sc}=284.583 Hz f_2^{oc}=284.586 Hz	0.47%	N.C.
	f_3^{sc}=629.710 Hz f_3^{oc}=629.712 Hz	0.19%	1.8%	f_3^{sc}=301.911 Hz f_3^{oc}=301.922 Hz	0.88%	N.C.

Table 4.15: Numerical natural frequencies in open and short-circuit and there associated numerical coupling factors. Comparison with the experimental coupling factors. In-air and in-water configurations.

Numerical modelling of a resonant piezoelectric shunt

The proposed model offers the possibility to simulate a passive resonant shunt circuit by defining at the electrodes of the active layer a floating potential condition of the type

$$Q_0 = \frac{V_0}{L_{eq}(2\pi f)^2 - iR_t(2\pi f)} \tag{4.11}$$

where L_{eq} and R_t are the shunt equivalent inductance and total series resistance respectively, Q_0 is the charge and V_0 is the applied voltage. The MFC piezoelectric transducer integrated on the hydrofoil surface was connected numerically to the simulated shunt in order to mitigate the first twisting mode vibrations. The structure was excited by the DuraAct transducers with the electrodes connected in twisting configuration.

In a first instance the inductance L_{eq} was computed with equation 1.2 described in section 1.1 of the present chapter. However, as is visible on figure 4.21 (blue curve), the antiresonance induced by the shunt is not aligned with the first twisting mode frequency f_2 due to approximations on the piezoelectric capacitance. As for the experimental case, a manual adjustment of the inductance is possible to obtain optimal vibration mitigation conditions. A good practice to adjust the antiresonance on the vibration frequency to mitigate is to use a very low value of R_t, this will increase the antiresonance and calibration of L_{eq} becomes easier. The calibrated value of L_{eq} was equal to 24.1 H for the present analysis, whereas the initial value of L_{eq} was equal to 22.5 H.

Once the inductance is properly set-up, it is interesting to study the impact of a variation of R_t on the FRF features. Figure 4.22 presents various FRFs corresponding to increasing values of R_t. Low values of R_t are characterized by a very deep antiresonance surrounded by two secondary peaks. When increasing R_t, the antiresonance progressively reduces until becoming a single peak for very high values of resistance. It is seductive to consider that the lower the value of R_t, the higher the vibration mitigation level. However, a very deep antiresonance results in secondary peaks which may be inappropriate for acoustic stealth applications. Also, very low values of resistance induce very high values of current which is often destructive for standard electrical components. For broadband considerations, if the control strategy is to reduce the maximal magnitude of a FRF on a given frequency range, the best compromise consists in minimizing the secondary peaks magnitude. This aspect is reasonably respected when setting-up the shunt with the value of R_t computed with equation 1.3.

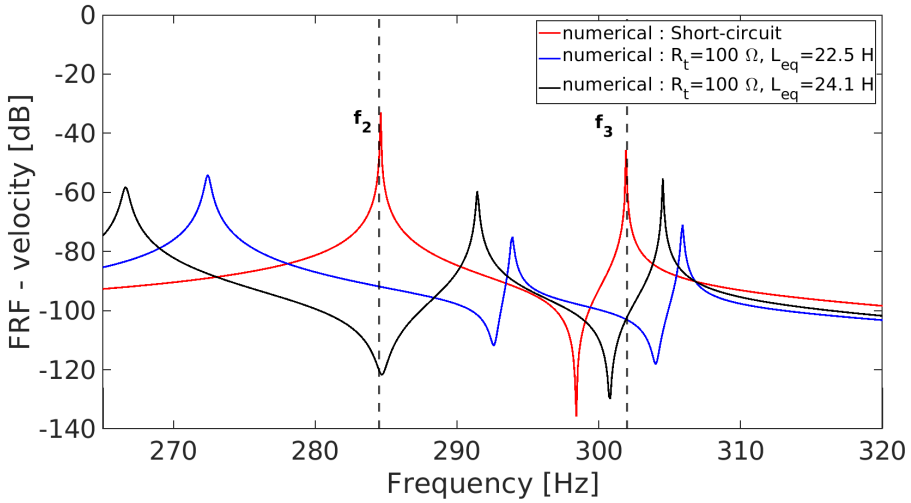

Figure 4.21: Numerical frequency response functions of the vibration velocity in water corresponding to a configuration in short circuit (red curve) and with connection to a resonant piezoelectric shunt configured with an equivalent inductance $L_{eq} = 22.5\ H$ computed with equation 1.2 (blue curve). The black curve corresponds to the inductance $L_{eq} = 24.1H$. For the two connected shunt FRFs, $R_t = 100\ \Omega$.

In complement to the previous observations, an effect on the second bending mode (f_3) is also visible: for low values of R_t, the f_3 peak is shifted towards the higher frequencies and its magnitude also decreases. The frequency shift is even higher when the resistance is low. This aspect was observed experimentally and is here confirmed by the numerical model. It shows that a single resonant shunt may be able to mitigate simultaneously close vibration modes.

Figure 4.23 presents the FRF obtained with the shunt parameters computed with equations 1.2 and 1.3 and the FRF obtained after manual calibration. Even if there is an offset between the numerical and experimental value of f_2, the experimental FRF with shunt has been added on figure 4.23. It appears that the general aspect of the numerical and experimental FRFs with activated shunt are similar which demonstrates the accuracy of the numerical model. The aforementioned results demonstrate that a numerical model implemented with COMSOL *Multiphysics* is a very valuable tool for designing structures embedded with piezoelectric transducers and connected to a passive resonant shunt. It offers the opportunity to test various shunt set-ups and control strategies in a cost effective way and with high flexibility.

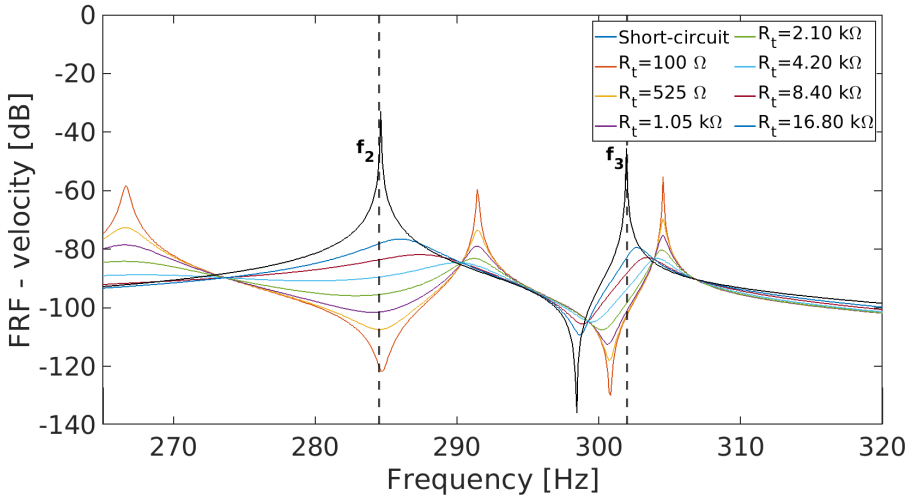

Figure 4.22: Frequency response functions of the vibration velocity in water corresponding to a configuration in short circuit and with connection to a resonant piezoelectric shunt configured with an equivalent inductance $L_{eq} = 24.1\ H$ and with various values of total resistance R_t.

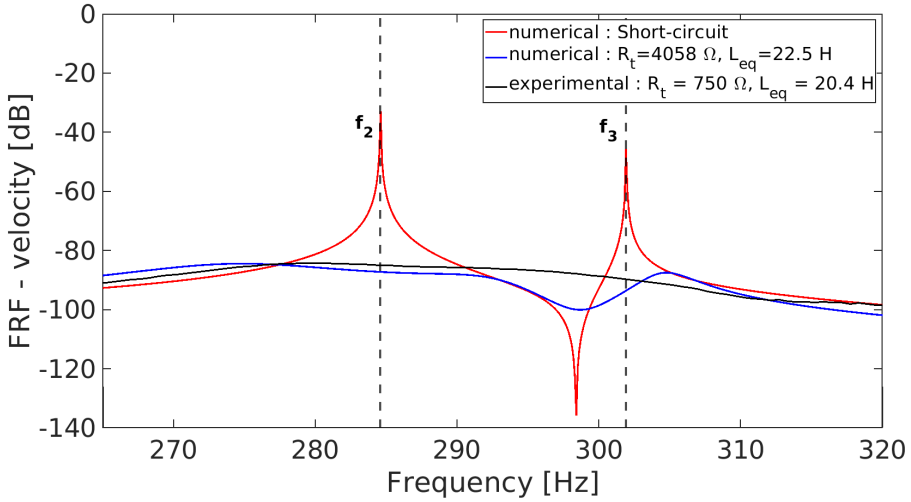

Figure 4.23: Frequency response functions of the vibration velocity in water obtained with numerical computations for the short-circuit (red curve), activated shunt configuration with shunt parameters computed with equations 1.2 and 1.3 (blue curve). The activated shunt experimental FRF (black curve) was obtained with L_{eq}=20.4 H and a measured inductor resistance R_t= 638 Ω.

Conclusion of the chapter

The present chapter was dedicated to the study of the vibration mitigation induced by passive resonant piezoelectric shunts. After describing the general principle of this type of vibration mitigation

device, two types of shunt circuits were presented: the copper wired inductor and the synthetic inductor. Both shunts were tested experimentally in air, steady water and under flow excitation. It appeared that the copper wired inductor shunt is well adapted for high vibration magnitudes such as those induced by the flow and resulting in a high voltage level at the electrodes of the piezoelectric transducer. However, this type of shunt requires an accurate design and manufacturing of the inductor because the variability range of the inductance is small. The synthetic inductor offers adaptability in terms of variation of the inductance and internal resistance. It is restricted to low vibration levels because the constitutive electronic components are not able to sustain high voltage. Both shunt circuits have demonstrated high vibration mitigation levels and are simple, cost effective and adaptable which makes them particularly suitable for marine applications.

A numerical model of a hydrofoil embedded with MFC and DuraAct transducers was then implemented by using the finite element computation code COMSOL *Multiphysics*. The aim of this part of the study is to obtain an accurate design tool to predict the natural frequencies and coupling factors of structures embedded with piezoelectric transducers. Special attention was paid to the MFC active layer because the modelling of such a piezocomposite appeared not being straightforward in the literature review and a calibration method for the MFC was proposed. The computed modal properties (deflection shapes and natural frequencies) and coupling factors were compared to the experimental results. A passive resonant shunt was also simulated in order to predict the frequency response functions proper to the structure and to the shunt. This has permitted to simply adjust the shunt parameters in order to reach the highest and most effective vibration mitigation. Both numerical and experimental results appeared to be in good agreement, which demonstrated the high benefit of the numerical model when designing piezoelectric vibration mitigation devices. Using this numerical tool will avoid several expensive experimental iterations and guarantee an optimal set-up of resonant shunts for future applications.

Chapter 5

Impact of the vibration mitigation on the near-wake of the truncated hydrofoil

" *Il arrive qu'une vérité vous échappe, parce qu'elle est infime.*
Il arrive aussi que vous ne la voyiez pas à cause de son évidence et de son énormité. "

Robert M. Pirsig

Content

The present chapter is dedicated to the impact of vibration mitigation through resonant piezoelectric shunt on the different vibration regimes and on the near-wake hydrodynamic specificities of an hydrofoil under flow excitation. The truncated NACA 66-306 of chord c=85 mm, maximum thickness D=6.13 mm and trailing edge thickness t_{TE}=3.4 mm was used for the present analysis. Vibrations were mitigated by coupling the hydrofoil to a resonant piezoelectric shunt based on a copper wired inductor. Particle image velocimetry and laser vibrometry were used to characterize the fluid-structure interaction process at zero incidence and at various vibration regimes consisting of no-resonance, lock-in without shunt and lock-in with shunt.

5.1 Hydrofoil vibration under flow excitation

A preliminary study of the flow-induced vibrations of the truncated hydrofoil was carried-out. Different vibration regimes corresponding to no-resonance, lock-in with the first twisting mode (f_2) and lock-in with the second bending mode (f_3) were identified and analysed in order to understand the vibrational behaviour of this particular type of lifting surface. The impact of the resonant piezoelectric shunt on the vibration features was then characterized at various Reynolds number in order to evaluate the capability of this type of vibration mitigation system to break strong fluid-structure coupling regimes.

5.1.1 Vibration regimes identification for the non-activated shunt configuration

For the non-activated shunt configuration, the MFC piezoelectric transducer is in open-circuit. The truncated hydrofoil is subjected to various vibration modes. For frequencies lower than 1 kHz, the modes of interest are the first bending mode (f_1=40 Hz), the first twisting mode (f_2=282 Hz) and the second bending mode (f_3=305 Hz). The fluid-structure interaction analysis was restricted to the coupling with f_2 and f_3 in the chord-based Reynolds number range $[2.55 \times 10^5; 4.68 \times 10^5]$.

The cartography of the power spectral density is plotted in the $(f_s/f_2, Re_c)$ plane and is presented in figure 5.1 for the non-activated shunt configuration. It appears that the resonance with f_2 occurs for a broad range of Reynolds numbers from $Re_c = 2.72 \times 10^5$ ($U_0 = 3.2$ m.s^{-1}) to $Re_c = 3.91 \times 10^5$ ($U_0 = 4.6$ m.s^{-1}). This range is smaller for the resonance with f_3 as it occurs from $Re_c = 4.0 \times 10^5$ ($U_0 = 4.7$ m.s^{-1}) to $Re_c = 4.25 \times 10^5$ ($U_0 = 5.0$ m.s^{-1}). Also, a resonance regime with $f_4 = f_2 + f_1$ is

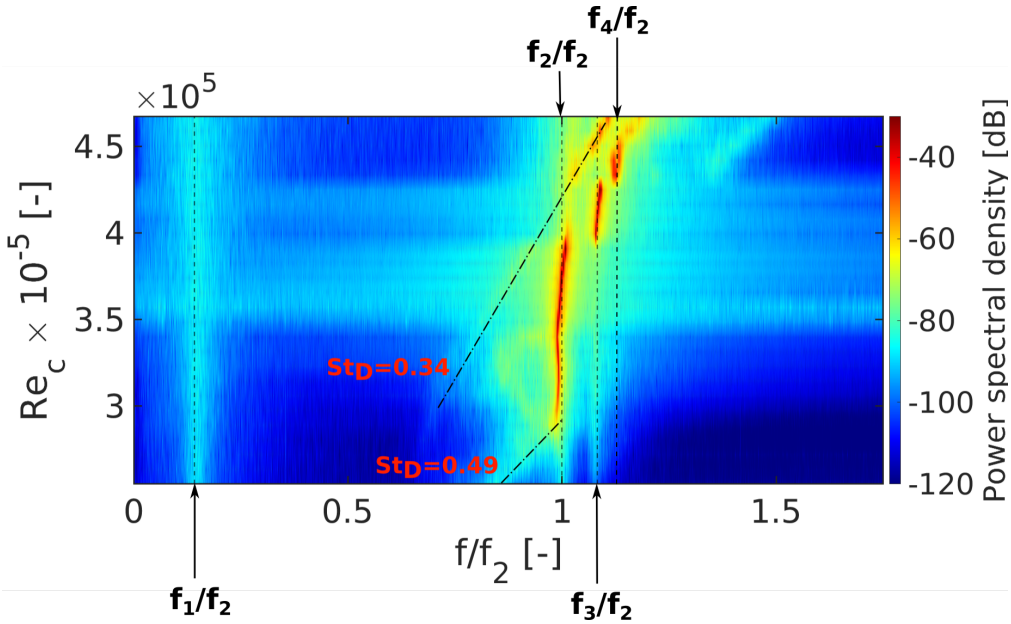

Figure 5.1: Cartography of the power spectral density of the structure vibration velocity. Cartography in the plane (f_s/f_2 , Re_c) with non-activated shunt configuration. Power spectral density expressed in dB ($Vs_{ref} = 1\ m.s^{-1}$). The dashed-lines correspond to excitation sources which evolve at a constant Strouhal number when the Reynolds number increases.

visible for Re_c in the range $[4.34\times10^5; 4.51\times10^5]$. This regime is characterized by weaker fluid-structure interaction than for other resonance regimes. The transition between these resonance regimes is very abrupt as the structural vibrations locks directly from $f_s^{max} = f_2$ to $f_s^{max} = f_3$ and from $f_s^{max} = f_3$ to $f_s^{max} = f_4$. The regime of lock-in with f_2 takes place in the Re_c range $[3.4 \times 10^5; 3.9 \times 10^5]$ and is characterized by an increase of the power spectral density of the vibration velocity. Same is observed for the regime of lock-in with f_3 in the Re_c range $[4.0\times10^5; 4.25\times10^5]$. In figure 5.1, two hydrodynamic excitation sources are identified in the no-resonance regimes. They have a dominant frequency that increases linearly with the Reynolds number. Their best linear fits have been represented in figure 5.1 by dashed lines. The corresponding Strouhal number is obtained with the value of the slope. Both excitation sources are characteristic of Karman vortex shedding. The first excitation which is associated with a first Karman mode is characterized by a Strouhal $St_{D1} = 0.49$ which stands for $Re_c < 2.72 \times 10^5$, before the occurrence of the different resonance regimes sequences. The second excitation source which is associated to a second Karman mode has a Strouhal number $St_{D2} = 0.34$ which stands for $Re_c \geq 4.6 \times 10^5$, after the foil has experienced different resonance regimes. The

No resonance	$Re_c < 2.72 \times 10^5$ $Re_c \geq 4.6 \times 10^5$ $U_0 < 3.2$ m.s^{-1} $U_0 \geq 5.4$ m.s^{-1}	$f_s^{max} \neq f_1, f_2, f_3, f_4$
Resonance with f_2	$2.72 \times 10^5 \leq Re_c \leq 3.9 \times 10^5$ 3.2 m.s$^{-1} \leq U_0 \leq 4.6$ m.s^{-1} $1.85 \leq RU_2 \leq 2.66$	$f_s^{max} = f_2$
Lock-in with f_2	$3.4 \times 10^5 \leq Re_c \leq 3.9 \times 10^5$ 4.0 m.s$^{-1} \leq U_0 \leq 4.6$ m.s^{-1} $2.31 \leq RU_2 \leq 2.66$ $0.38 \leq 1/RU_2 \leq 0.43$ $2.13 \leq RU_3 \leq 2.46$	$f_s^{max} = f_2 = f_{vs}$
Resonance with f_3	$4.0 \times 10^5 \leq Re_c \leq 4.25 \times 10^5$ 4.7 m.s$^{-1} \leq U_0 \leq 5.0$ m.s^{-1} $2.51 \leq RU_3 \leq 2.68$ $0.37 \leq 1/RU_3 \leq 0.40$	$f_s^{max} = f_3$
Lock-in with f_3	$4.0 \times 10^5 \leq Re_c \leq 4.25 \times 10^5$ 4.7 m.s$^{-1} \leq U_0 \leq 5.0$ m.s^{-1} $2.51 \leq RU_3 \leq 2.68$ $0.37 \leq 1/RU_3 \leq 0.40$	$f_s^{max} = f_3 = f_{vs}$
Resonance with f_4	$4.34 \times 10^5 \leq Re_c \leq 4.51 \times 10^5$ 5.1 m.s$^{-1} \leq U_0 \leq 5.3$ m.s^{-1} $2.72 \leq RU_3 \leq 2.83$ $2.58 \leq RU_4 \leq 2.68$ $0.37 \leq 1/RU_4 \leq 0.39$	$f_s^{max} = f_4$ $f_s^{max} \neq f_{vs}$

Table 5.1: Characteristics of the different vibration regimes for the non-activated shunt configuration.

value $1/St_{D1} \approx 2.04$ is close to the value of the reduced velocity at the resonance with f_2 occurrence ($RU_2 = U/f_2D = 1.85$). Also, $1/St_{D2} \approx 2.94$ is close to the value of the reduced velocity ($RU_3 = U/f_3D = 2.83$) reached at the end of the lock-in sequence with f_3. Table 5.1 summarizes the vibration properties of the different regimes.

Figure 5.2 displays the vibration velocity spectra of three different operating points associated with different vibration regimes. Figure 5.2a presents the vibration velocity spectrum at $U_0 = 3.0$ m.s^{-1} ($Re_c = 2.55 \times 10^5$) corresponding to the no-resonance regime. The peaks associated to the three first natural frequencies (f_1, f_2, f_3) have same order of magnitude. The hydrodynamic excitation source identified as vortex shedding is characterized by a broadband peak with its highest magnitude at $f_s^{max} = 239$ Hz. The associated thickness-based Strouhal number is equal to $St_D = 0.49$. For this flow velocity the vortex shedding frequency f_{vs} is not equal to a natural frequency ($f_{vs} \neq f_1, f_2, f_3$). Accordingly, this flow velocity is associated with a no-resonance regime and will be used as a reference for weak fluid-structure coupling. It is important to stipulate that due to the fact that the different

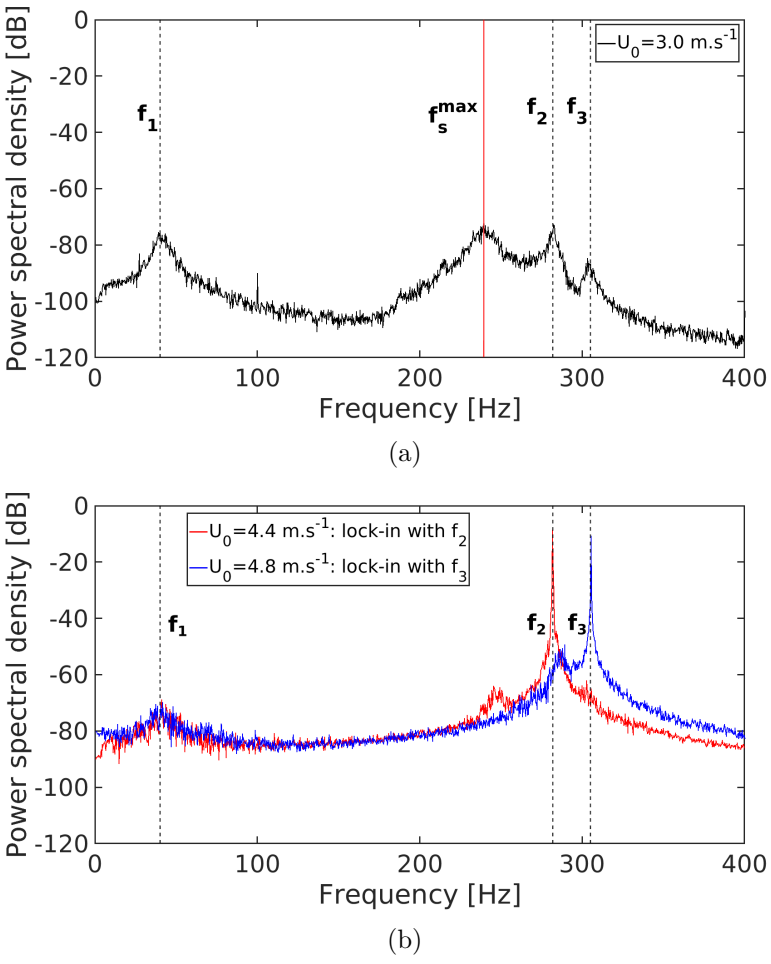

Figure 5.2: Vibration velocity spectrum at $U_0 = 3.0\ m.s^{-1}$ ($Re_c = 2.55 \times 10^5$) corresponding to a non-resonant regime (a) and at $U_0 = 4.4\ m.s^{-1}$ ($Re_c = 3.74 \times 10^5$) and $U_0 = 4.8\ m.s^{-1}$ ($Re_c = 4.08 \times 10^5$) corresponding to a lock-in regime with f_2 and f_3 respectively.

peaks have nearly the same magnitude, the total displacement of the structure is a combination of the different modal shapes associated with each peak. In other words, there is no dominant type of deflection shape as can be observed for a resonance regime with a specific natural mode. This combination of displacement will impact the wake and probably disorganise the wake-dynamics leading to three-dimensional effects in the vortex shedding as those observed by Zobeiri [11].

Figure 5.2b presents the vibration velocity spectra at $U_0 = 4.4$ m.s^{-1} ($Re_c = 3.74 \times 10^5$) and $U_0 = 4.8$ m.s^{-1} ($Re_c = 4.08 \times 10^5$) which correspond to the lock-in regimes with f_2 and f_3 respectively. For both lock-in regimes, the maximal vibration magnitude is of same order. The lock-in with f_2 is even more interesting because it maximizes the transverse motion of the structure against the incoming flow field leading to high fluid-structure interaction [54]. For this reason, this regime will be studied in detail. Also, for the lock-in with f_2, an additional peak is visible and is attributed to a vortex shedding excitation at $f_{vs} = f_s = 245$ Hz. At this velocity, the corresponding Strouhal number is $St_{D2} = 0.34$ in agreement with the second Karman vortex shedding mode. Interestingly, there seems to be a transition in the Strouhal numbers of the vortex shedding from St_{D1} to St_{D2} which takes place in the lock-off resonance regime with f_2 for Re_c in the range $[2.72 \times 10^5; 3.40 \times 10^5]$. This decrease of the Strouhal number can be linked to an increase in the wake thickness at the resonance with f_2.

Figure 5.3a describes the evolution of f_s^{max} and f_{vs} with Re_c. Here, f_{vs} is obtained with the frequency spectrum of POD mode 1 expansion coefficient measured by PIV in the wake. In complement, figure 5.3b describes the evolution of the vibration velocity root mean square value with the Reynolds number. Maximum vibration magnitude is reached at $U_0 = 4.4$ m.s^{-1} ($Re_c = 3.74 \times 10^5$) for the lock-in with f_2 and at $U_0 = 4.8$ m.s^{-1} ($Re_c = 4.08 \times 10^5$) for the lock-in with f_3. The corresponding reduced velocities at the maxima of the vibration amplitude correspond to 0.38 and 0.39 respectively and are in the range $[St_{D1}; St_{D2}]$, which confirms the transition in Strouhal number from St_{D1} to St_{D2} induced by the successive resonance regimes.

5.1.2 Vibration regimes identification for the activated shunt configuration

The level of vibration mitigation obtained with the passive piezoelectric resonant shunt was investigated for the complete range of studied Reynolds numbers. The parameters of the shunt were adjusted manually in order to obtain the highest mitigation of the vibration velocity signal root mean square value at the lock-in with f_2. These parameters are summarized in table 5.2 and were used

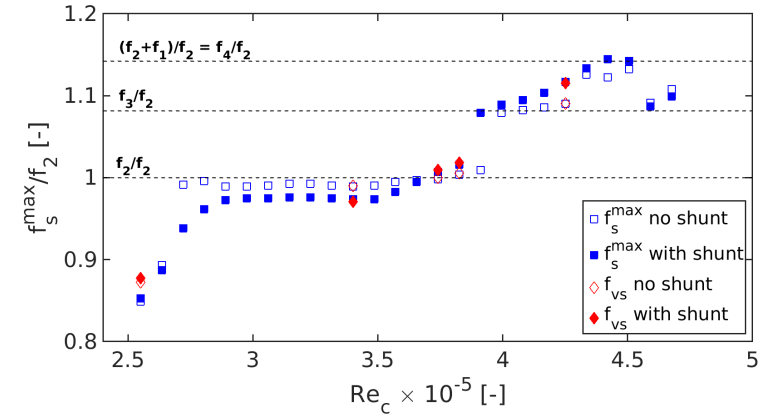

(a)

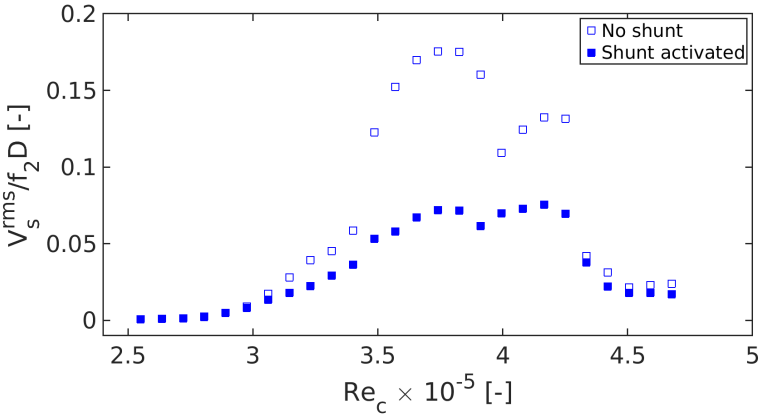

(b)

Figure 5.3: (a) Evolution of f_s^{max} and f_{vs} and (b) V_s^{rms} with Reynolds for non-activated and activated shunt configurations. Maximum uncertainty for f_s^{max} is 0.6 Hz and 0.7 Hz for f_{vs}.

for the complete set of Reynolds numbers. The inductance and total resistance of the copper wired inductor were recorded at two different recording frequencies (100 Hz and 1 kHz).

The evolutions of f_s^{max}, f_{vs} and V_s^{rms} according to the Reynolds number for the activated shunt configuration have been added in figure 5.3. Also, according to figure 5.3b, the highest vibration

Patch type	MFC
Patch capacitance	13.8 nF
Inductance	11.9 H (100 Hz) and 12.2 H (1 kHz)
Equivalent series resistance	638 Ω (100 Hz) and 745 Ω (1 kHz)

Table 5.2: Passive resonant piezoelectric shunt parameters used for vibration mitigation under flow excitation. Copper wired inductor with MFC patch.

mitigation is obtained at $Re_c = 3.74 \times 10^5$ for the lock-in with f_2 and at $Re_c = 4.17 \times 10^5$ for the lock-in with f_3. For these two regimes, the vibration velocity signal root mean square V_S^{rms} value was reduced by 59% and 43% respectively. Interestingly, the shunt offers a significant vibration mitigation level for Reynolds ranging in $[3.5 \times 10^5; 4.25 \times 10^5]$ corresponding to both regimes of resonance with f_2 and f_3. This demonstrates that the shunt is operational for a certain range of incoming flow velocities.

Figure 5.4 presents the cartography in the (f_s/f_2, Re_c) plane of the vibration velocity power spectral density when the shunt is activated. The two hydrodynamic excitation sources represented by $St_D = 0.49$ and $St_D = 0.34$ are not impacted by the activation of the shunt. For the activated shunt configuration, the transitions between different lock-in regimes (from lock-in with f_2 to lock-in with f_3 and from lock-in with f_3 to lock-in f_4) are smoother.

A modification of the twisting mode natural frequency is also observed. Initially equal to f_2=282 Hz, it is decreased of 7 Hz (f_2'=275 Hz) for the activated shunt configuration. This behaviour is confirmed in figure 5.3a when analysing the dominant vibration frequencies f_s^{max}. This could be due to a slight offset between the electrical frequency and the twisting mode frequency. Also, a reduced Reynolds range for the resonance with f_2' regime from $Re_c = 2.89 \times 10^5$ to $Re_c = 3.83 \times 10^5$ is highlighted. Observations made by Bearman [39] have demonstrated that the larger the vibration amplitude, the larger the range of Reynolds numbers at resonance. This statement is in accordance

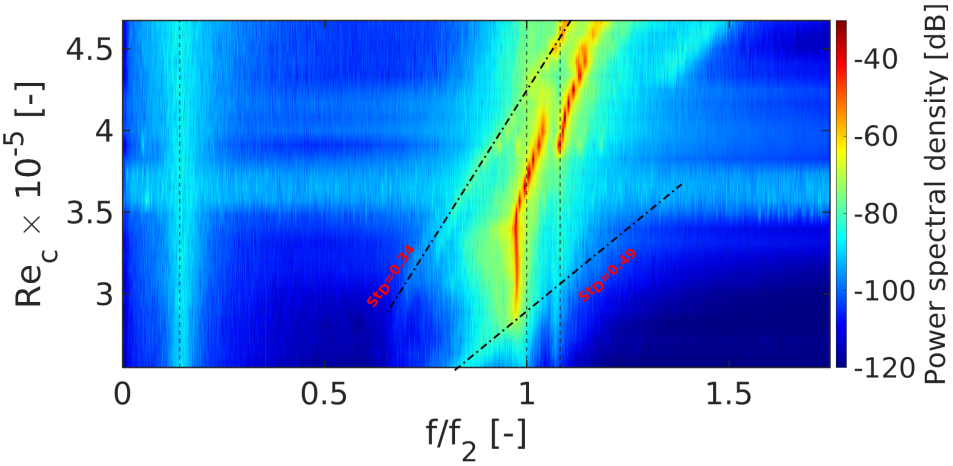

Figure 5.4: Cartography of the power spectral density of the structure vibration velocity. Cartography in the plane (f_s/f_2 , Re_c) with activated shunt configuration. Power spectral density expressed in dB ($Vs_{ref} = 1\ m.s^{-1}$).

with the observations made when the shunt is activated leading to a smaller vibration amplitude and a narrower range of Reynolds numbers where resonance occurs. Also, figure 5.4 evidences that the lock-in with the twisting mode remains a lock-in with f_2 when the shunt is activated. Due to the shift from f_2' to f_2, the lock-in with the twisting mode has its Re_c number range reduced to $[3.57\times10^5; 3.83\times10^5]$.

The Re_c range of resonance and lock-in resonance with f_3 and f_4 have not been impacted by the activation of the shunt. The smooth transition between different lock-in regimes induced by the shunt is also characterized by a coexistence of both lock-in with f_2 and f_3 in the Re_c range $[3.83\times10^5; 4.17\times10^5]$ which is expected to distribute the TKE in the wake and different Karman vortex shedding modes (at $f_{vs} = f_2$ and $f_{vs} = f_3$). This mechanism may be partially responsible for the attenuation of V_{rms} observed in the Re_c range of the resonance with f_3 regime (see figure 5.3b). The characteristics of the different vibration regimes when the shunt is activated are summarized in table 5.3.

The above mentioned results have demonstrated that the piezoelectric shunt mainly acts by inducing an additional damping in the mechanical system leading to the reduction of vibration magnitude. Since the resonance adds a new degree of freedom , it may also create a slight modification of the vibration frequency which implies that the $f_{excitation} = f_{natural}$ criteria is no longer verified. The next stage of the analysis consists of a characterization of the near-wake hydrodynamic properties in order

Resonance with f_2'	$2.89\times10^5 \leq Re_c \leq 3.83\times10^5$ $3.4\ \text{m.s}^{-1} \leq U_0 \leq 4.5\ \text{m.s}^{-1}$	$f_s^{max} = f_2$
Lock-in with f_2'	$3.57\times10^5 \leq Re_c \leq 3.83\times10^5$ $4.2\ \text{m.s}^{-1} \leq U_0 \leq 4.5\ \text{m.s}^{-1}$	$f_s^{max} = f_2 = f_{vs}$
Resonance with f_3	$4.0\times10^5 \leq Re_c \leq 4.25\times10^5$ $4.7\ \text{m.s}^{-1} \leq U_0 \leq 5.0\ \text{m.s}^{-1}$	$f_s^{max} = f_3$
Lock-in with f_3	$4.0\times10^5 \leq Re_c \leq 4.25\times10^5$ $4.7\ \text{m.s}^{-1} \leq U_0 \leq 5.0\ \text{m.s}^{-1}$	$f_s^{max} = f_3 = f_{vs}$
Resonance with f_4	$4.34\times10^5 \leq Re_c \leq 4.51\times10^5$ $5.1\ \text{m.s}^{-1} \leq U_0 \leq 5.3\ \text{m.s}^{-1}$	$f_s^{max} = f_4$ $f_s^{max} \neq f_{vs}$

Table 5.3: Characteristics of the different vibration regimes for the activated shunt configuration. The resonance with f_3 and f_4 and the lock-in with f_3 have same specificities as for the non-activated shunt configuration.

to demonstrate the capability of the shunt to modify the vortex dynamics.

5.2 General hydrodynamic features of the near-wake

The near-wake region is often characterized by high velocity gradient regions leading to the inception of large-scale turbulence. Pressure fluctuations in close vicinity of the trailing edge caused by vortex shedding results in periodic deformations of the structure which are proper to flow-induced vibrations. Studying the hydrodynamic properties of the near-wake is of prime importance to understand the fluid-structure coupling leading to high magnitude vibrations.

The truncated hydrofoil geometry studied here, is particular because the trailing edge acts as a geometrical discontinuity responsible for the detachment of the flow at a fixed position and leading to vortex shedding. The rounded leading edge offers a smooth transition for the flow and the high aspect ratio of the hydrofoil ($c/t = 13.9$) reduces the probability of leading edge vortices impacting the near-wake. Yet, it is probable that the boundary layer separates from the hydrofoil surface at a location close from the trailing edge leading to an interaction between the detached shear layer and the near-wake. Figure 5.5 presents a (x,y) vorticity field of a raw snapshot at $U_0 = 3.0$ m.s^{-1} ($Re_c = 2.55 \times 10^5$). It appears that, even without any low-order reduction or filtering process, the near-wake is characterized by very coherent and well identifiable convective trailing edge vortices. The stability criterion b_s/a_s [143] was computed for the non-resonant regime as illustrated in figure 5.5

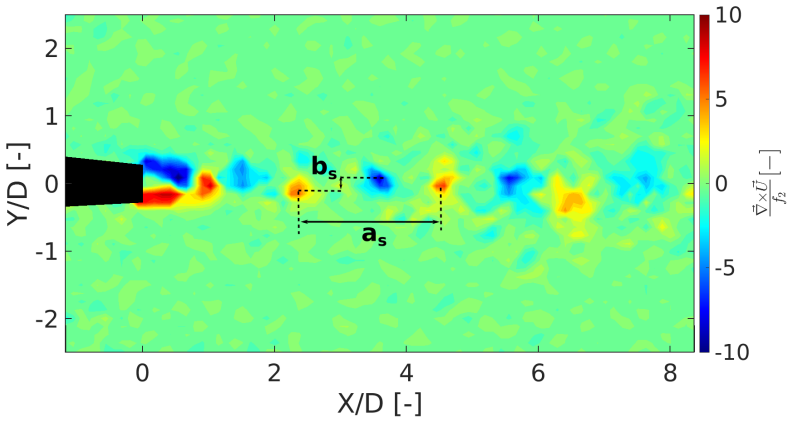

Figure 5.5: (x,y) vorticity field of a raw snapshot at U_0=3.0 m.s^{-1}. Non activated shunt configuration. The stability criteria b_s/a_s was computed and is equal to 0.11.

Reynolds	**Reduced velocity**	**Regime**	**Frequencies**	**Strouhal**
$Re_c = 2.55 \times 10^5$	$Ru_2 = 1.75$	No resonance	$f_{vs} = f_s^{max}$	St_D=0.49
$Re_c = 3.74 \times 10^5$	$Ru_2 = 2.56$	Lock-in with f_2	$f_{vs} = f_s^{max} = f_2$	St_D=0.39=1/RU_2

Table 5.4: Summary of the different fluid-structure interaction regimes at two characteristic operating points. Non activated shunt configuration.

and was found equal to 0.11.

The present section is dedicated to the description and analysis of the near-wake of the hydrofoil for the non-activated shunt configuration. Two operating points are examined: $U_0 = 3.0$ m.s^{-1} ($Re_c = 2.55 \times 10^5$) corresponding to the no-resonance regime and $U_0 = 4.4$ m.s^{-1} ($Re_c = 3.74 \times 10^5$) corresponding to the lock-in regime with f_2 and characterized by the maximum of vibration velocity. The time-averaged hydrodynamic properties are firstly presented in order to understand the general features of the near-wake of the hydrofoil and identify the impact of high magnitude vibrations, occurring at lock-in, on the mean flow. Then, POD and SPOD analysis methods are employed. The SPOD method is used to identify some characteristic coherent structures of the fluctuating flow. POD is implemented to characterize the coherent structures proper to the Karman vortex shedding. Table 5.4 describes the main properties of the studied operating points. The impact of vibration mitigation induced by the resonant piezoelectric shunt on the near-wake properties will be investigated in another dedicated section.

5.2.1 Time-averaged properties of the near-wake

For the two operating points of interest, the time-averaged velocity fields are computed in the near-wake based on the reconstructed velocity fields and using 90% of total Turbulent Kinetic Energy (TKE) in order to filter small scale turbulent noise. Figures 5.6 (a,b), 5.7 (a,b) and 5.8 (a,b) present the stream-wise and normal time-averaged velocity components as well as the Reynolds shear-stress. Characteristic time averaged features of the near-wake region are summarized in table 5.5. As observed in figure 5.6a, for the no-resonance regime the very near-wake region is characterized by a significant reduction of the stream-wise velocity component U for X/D included in [0;1] in combination with two regions of high magnitude of normal velocity component V visible in figure 5.7a for X/D included in [0;2] and with a maximum $|V|/U_0 = 0.24$ at X/D=0.5. These specificities are at the origin of a recirculation region or wake-bubble in close vicinity of the trailing-edge.

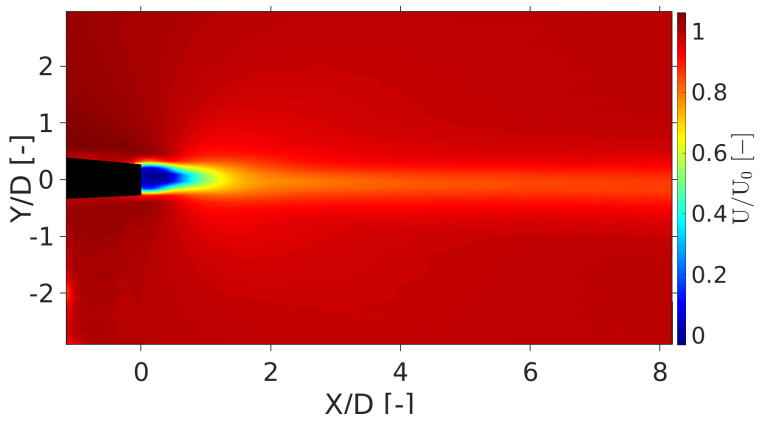

(a) $U_0 = 3.0$ m.s^{-1}, no shunt.

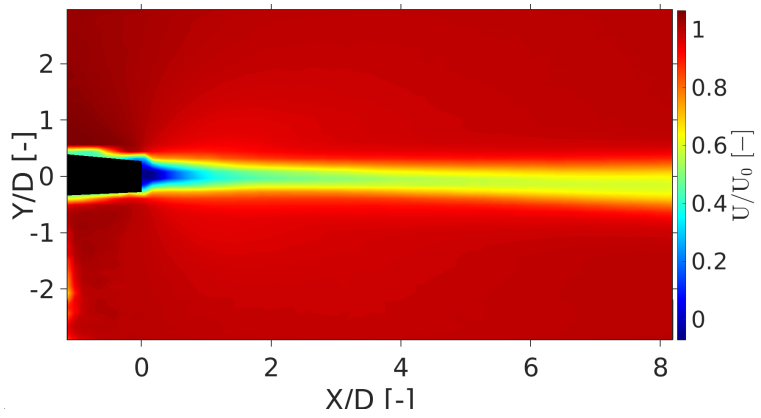

(b) $U_0 = 4.4$ m.s^{-1}, no shunt

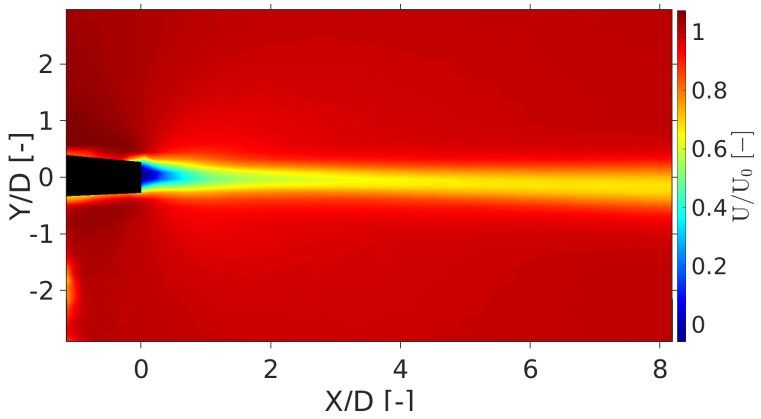

(c) $U_0 = 4.4$ m.s^{-1}, shunt activated

Figure 5.6: (x,y) cartography of the time-averaged stream-wise velocity component U. Flow velocity is equal to U_0=3.0 m.s^{-1} ($Re_c = 2.55 \times 10^5$) for figure (a) and U_0=4.4 m.s^{-1} ($Re_c = 3.74 \times 10^5$) for figures (b,c). Shunt is not activated except for figure (c). Cartographies are based on the reconstructed velocity field.

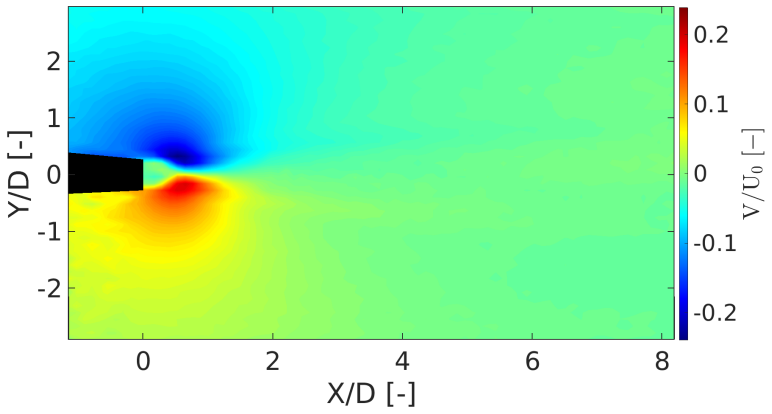

(a) $U_0 = 3.0$ m.s^{-1}, no shunt

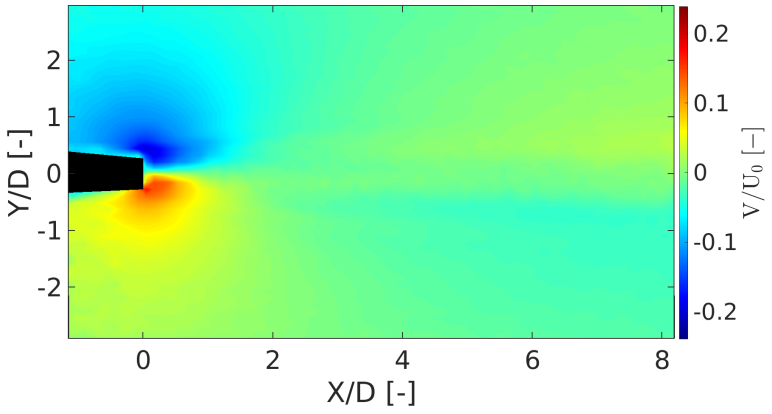

(b) $U_0 = 4.4$ m.s^{-1}, no shunt

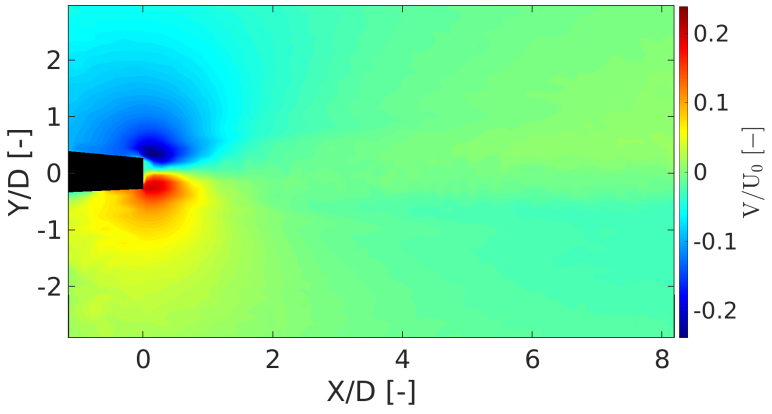

(c) $U_0 = 4.4$ m.s^{-1}, shunt activated

Figure 5.7: (x,y) cartography of the time-averaged normal velocity component V. Flow velocity is equal to U_0=3.0 m.s^{-1} ($Re_c = 2.55 \times 10^5$) for figure (a) and U_0=4.4 m.s^{-1} ($Re_c = 3.74 \times 10^5$) for figures (b,c). Shunt is not activated except for figure (c). Cartographies are based on the reconstructed velocity field.

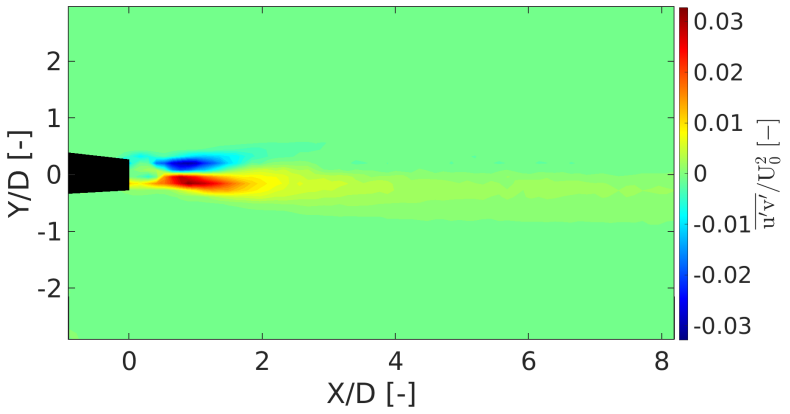

(a) $U_0 = 3.0$ m.s^{-1}, no shunt

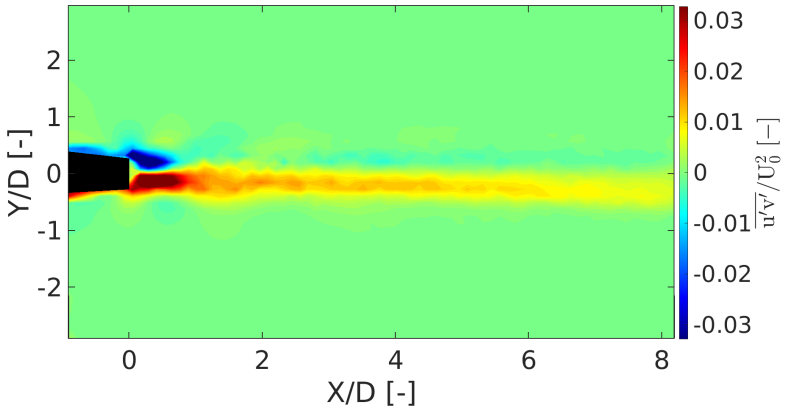

(b) $U_0 = 4.4$ m.s^{-1}, no shunt

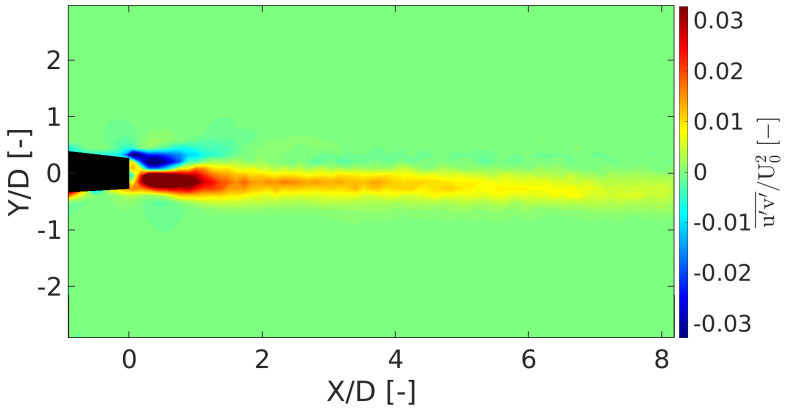

(c) $U_0 = 4.4$ m.s^{-1}, shunt activated

Figure 5.8: (x,y) cartography of the time-averaged Reynolds shear-stress $\overline{u'v'}/U_0^2$. Flow velocity is equal to U_0=3.0 m.s^{-1} ($Re_c = 2.55 \times 10^5$) for figure (a) and U_0=4.4 m.s^{-1} ($Re_c = 3.74 \times 10^5$) for figures (b,c). Shunt is not activated except for figure (c). Cartographies are based on the reconstructed velocity field.

Regions of high Reynolds shear-stress presented in figure 5.8a delineate the wake bubble and eddy length. As observed for the flat plate in chapter 3 and as stated by [40], the pattern of Reynolds shear-stress is the consequence of vortex shedding over one cycle. The distance from the trailing-edge of the stream-wise positions of $|\overline{u'v'}|/U_0^2$ maxima is representative of the eddy length. Also, the region of small $|\overline{u'v'}|/U_0^2$ and small $|V|/U_0$ right downstream of the trailing-edge delineates the wake-bubble. It is interesting to notice that the negative and positive Reynolds shear-stress regions are non-symmetric among the wake centre-line. This may be due to the non-symmetric geometry induced by the camber of the NACA 66-306 truncated profile.

When the free-stream velocity is equal to 4.4 m.s^{-1}, lock-in with f_2 occurs leading to high magnitude vibrations. When observing figures 5.7b and 5.8b, it appears that the size of the recirculation bubble is reduced from $X/D \approx 0.25$ at the no-resonance to $X/D \approx 0.10$ at the lock-in. The region of high positive Reynolds shear-stress is shifted towards the trailing-edge during the lock-in which denotes a reduction of the eddy length at the lock-in. Also, the value of $|V_{max}|$ is slightly decreased during the lock-in regime which implies a reduction of the time averaged lift coefficient.

Figure 5.9 presents the vertical profiles of the normalized velocity defect at X/D=4 for the two operating points of interest for the non-activated shunt configuration. It appears that the velocity defect is doubled when the free-stream velocity is changed from 3.0 m.s^{-1} at no-resonance to 4.4 m.s^{-1} at lock-in. The velocity defect measured at the wake center line U_{defect}/U_0 follows the same trend as the time-averaged drag coefficient. Here it appears that C_D increases during the lock-in. This observation was also mentioned for the blunt plate geometry and seems to be specific to lock-in.

	No resonance, no shunt.	lock-in, no shunt.	lock-in, with shunt
Velocity U_0	3.0 m.s^{-1}	4.4 m.s^{-1}	4.4 m.s^{-1}
$\|V_{max}\|/U_0$ for $Y < 0$	0.20	0.17	0.20
$\|V_{max}\|/U_0$ for $Y > 0$	0.24	0.20	0.25
Eddy length L_e/D with max. of $\|\overline{u'v'}\|$ for $Y > 0$	0.89	0.29	0.41
Eddy length L_e/D with max. of $\|\overline{u'v'}\|$ for $Y < 0$	0.89	0.41	0.53
Velocity Defect $(U_0 - U)/U_0$ at $X/D = 4$	0.17	0.45	0.35

Table 5.5: Synthesis of the time-averaged quantities specific to the near-wake region at the no-resonance, lock-in for the non-activated shunt configuration regime and lock-in for the activated shunt configuration.

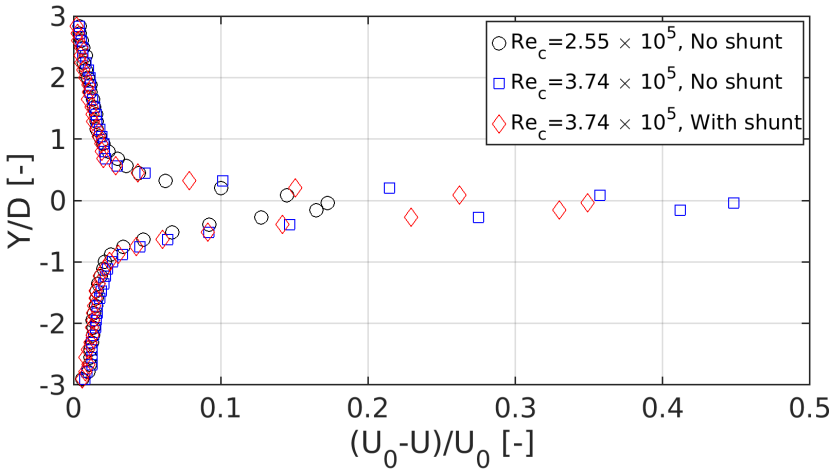

Figure 5.9: Vertical profiles of the normalized stream-wise velocity defect $(U_0 - U)/U_0 = f(Y/D)$ measured at $X = 4D$ for flow velocities equal to U_0=3.0 m.s^{-1} ($Re_c = 2.55 \times 10^5$) and U_0=4.4 m.s^{-1} ($Re_c = 3.74 \times 10^5$). Comparison between non-activated and activated shunt configuration at U_0=4.4 m.s^{-1} ($Re_c = 3.74 \times 10^5$).

5.2.2 Identification of turbulent wake patterns with SPOD

High amplitude vibrations proper to the lock-in regime could impact the flow properties of the near-wake region leading to a reorganization of the vortex dynamics. The Spectral Proper Orthogonal Decomposition (SPOD) is employed to compare the most energetic turbulent wake patterns at the no-resonance and at the lock-in with f_2 regimes.

Figure 5.10a presents the energy spectrum of the different SPOD modes at the no-resonance regime. Peaks correspond to the most energetic frequencies present in the wake and each peak is associated with a type of coherent wake structure. For the no-resonance regime, SPOD mode 1 contains most of the energy and a broadband peak ranging between 187 Hz (St_D = 0.38) and 300 Hz (St_D = 0.61) (yellow area) is dominant. The maximum of the peak is located at a frequency f = 239 Hz ($St_D = St_{D1}$ = 0.49) and its Strouhal number corresponds to the excitation source at St_{D1} identified in section 1 (see figure 5.1 and table 5.4). According to [119], the first SPOD mode is particularly representative of a dominant physical process at a given frequency if the ratio between the first and second modes energy (yellow and green areas in figure 5.10a) is large. The broadband aspect of the peak is in agreement with the observations obtained with the vibration spectrum at the same velocity. The vorticity cartography associated with mode 1 at the frequency f = 239 Hz (St_D=0.49)

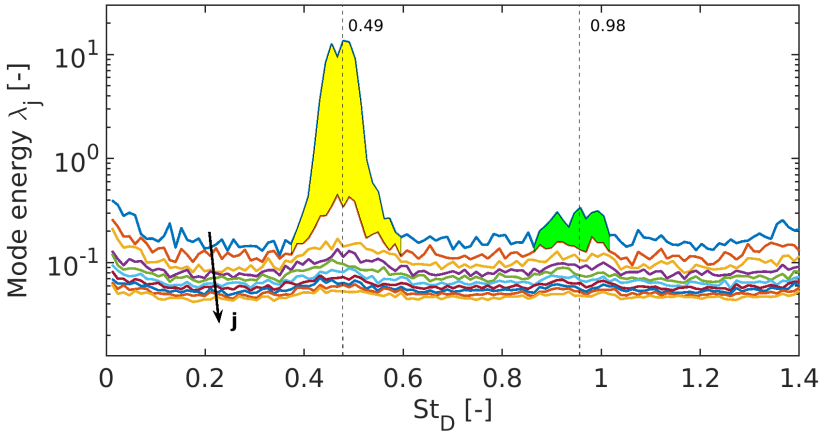

(a) No-resonance

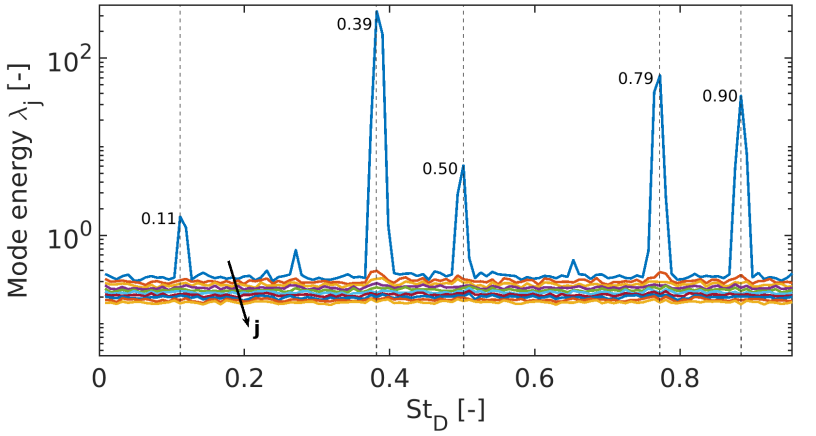

(b) Lock-in with f_2

Figure 5.10: Energy spectra of the first SPOD modes for the non-resonant (U_0=3.0m.s^{-1}, $Re_c = 2.55 \times 10^5$) regime and the lock-in with the first twisting mode f_2 (U_0=4.4m.s^{-1}, $Re_c = 3.74 \times 10^5$). Uncertainty of the frequency is equal to 6 Hz for both regimes.

is presented in figure 5.11a and displays a set of well organized contra-rotative vortices. This type of wake structure is proper to a Karman vortex shedding (KVS). At this dominant frequency associated with St_{D1}, this mode will be denoted KVS1.

All the vorticity cartographies associated with SPOD mode 1 for the frequency range [187;300] evidence a KVS type wake structures. This broadband frequency behaviour could be due to the fact that three-dimensionality of vortex shedding is important in the case of a no-resonance regime resulting in fluctuations of the vortex shedding frequency [11]. As was stated in section 1, the total displacement of the hydrofoil at the no-resonance regime is a combination of various deflection shapes

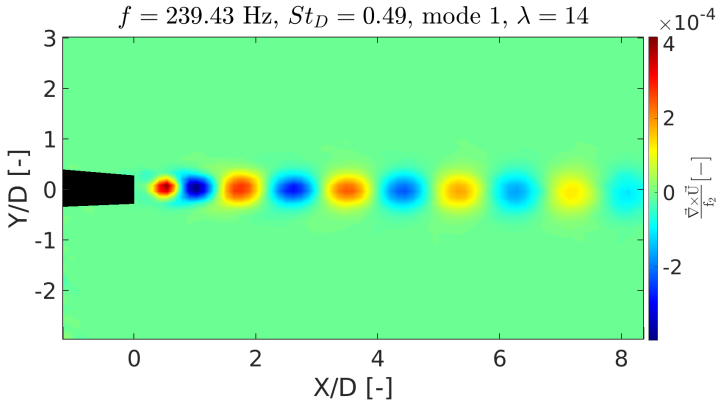

(a) KVS

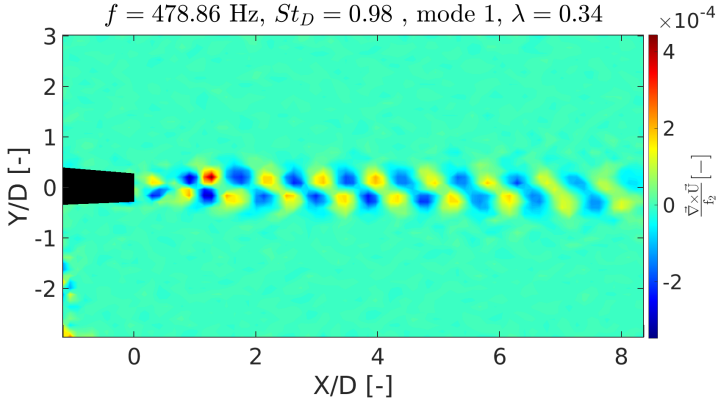

(b) KHVS

Figure 5.11: (x,y) vorticity cartography of the two most energetic coherent wake structures identified with SPOD at $U_0 = 3.0\text{m.s}^{-1}$ ($Re_c = 2.55 \times 10^5$). (a) corresponds to Karman Vortex Shedding (KVS) and (b) is an harmonic (KHVS).

which may result in a disorganisation of the near-wake and increase three-dimensionality. Also, the large dimension of the near-wake bubble and its flapping may impact the Karman vortex formation mechanism and favour multi-frequency shedding.

A second broadband peak is visible in figure 5.10a (green area) with a maximum at f=478 Hz (St_D=0.96). Even if this peak has a low energy level, it is associated with a very coherent wake structure illustrated in figure 5.11b and identified as the harmonic of Karman vortex shedding. This type of wake pattern will be denoted as KHVS1. Indeed, its frequency is equal to twice the Karman vortex shedding frequency: $f_{KHVS1} = 2 \times f_{KVS1}$. KHVS wake patterns seems to be the key specificity of near-wake flows generated by blunt trailing edges.

The SPOD energy spectrum associated with the lock-in with f_2 is presented in figure 5.10b. The

highest energy is still contained in mode 1 but the aspect of the spectrum is drastically different from the no-resonance case: five different high magnitude narrow-banded peaks are clearly identifiable. This demonstrates a discrete repartition of energy among various single-frequency wake structures. According to the literature, high magnitude trailing edge vibrations generate more organized wake patterns and vorticity lines parallel to the trailing edge in the span-wise direction [11]. As presented in figures 5.12a and 5.12b, the two most energetic wake patterns correspond to Karman vortex shedding and to its harmonic and are characterized by a frequency f_{KVS}=280 Hz (St_D^{KVS}=0.39) and f_{KHVS}=567 Hz (St_D^{KHVS}=0.79). In comparison with the no-resonance regime, these two coherent structures have significantly gained in energy.

Interestingly, for the lock-in regime, a new type of coherent structure, which contributes significantly to the energy, is observed at a frequency f_{SSL}=648 Hz ($St_D^{SSL} = 0.88$). As presented in figure 5.12c, it is characterized by well organized contra-rotative vortices which diffuse symmetrically towards the far-wake. A dominant stream-wise gradient $\partial/\partial x >> \partial/\partial y$ is also observed. The frequency associated with this type of wake structure has not been detected with the vibrometry measurements so obviously it does not act as an excitation source on the structure. With the data available for the study, a reliable identification of this type of wake pattern is not straightforward but a possible hypothesis is that it is generated by the flow separation upstream from the trailing edge at lock-in. In the rest of the study, this type of coherent structure will be named Separated Shear Layer (SSL) wake pattern. A similar arrangement was observed by Ribeiro et al. [144]. Also, the peaks associated with the frequencies 358 Hz ($St_D = 0.50$) and 79 Hz ($St_D = 0.11$) have a very low level of energy ($\lambda_j / \sum \lambda_j$<1%). They may be the consequence of combined patterns such as: $St_D = St_D^{KVS} + (St_D^{SSL} - St_D^{KHVS}) = 0.5$ and $St_D = St_D^{SSL} - St_D^{KHVS} = 0.11$. Also, the frequency of the low frequency energetic SPOD mode is an harmonic of the first bending mode natural frequency $f_{SSL} - f_{KHVS} = 2f_1$, which means that the amplification of the bending of the hydrofoil at the lock-in with the twisting mode may contribute to the emergence of combined patterns in the flow. Additional data is necessary to confirm this hypothesis.

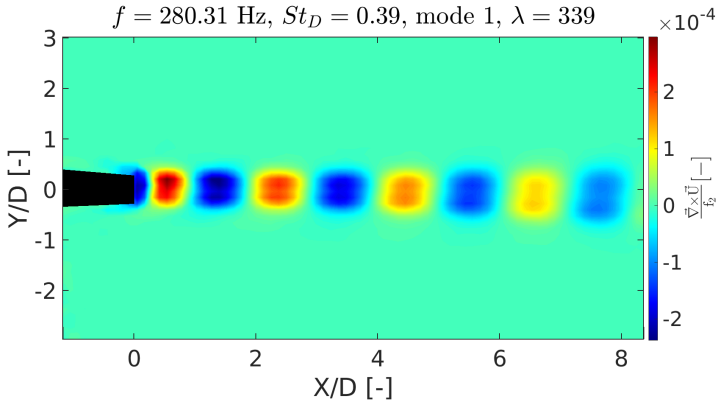

(a) KVS

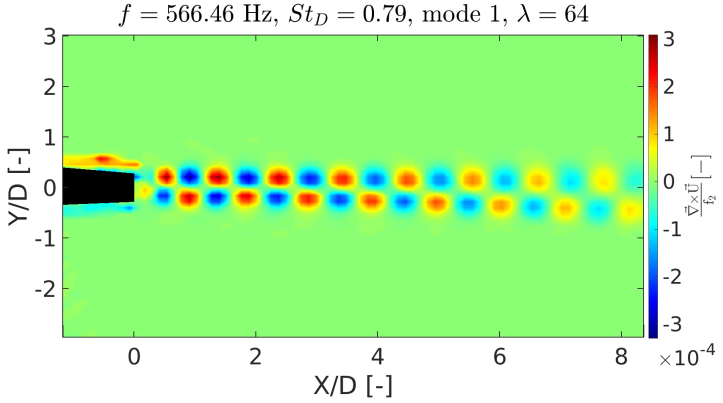

(b) KHVS

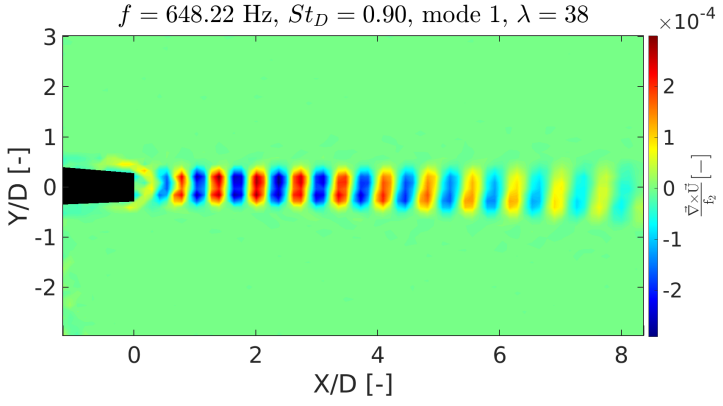

(c) SSL

Figure 5.12: (x,y) vorticity cartography of three most energetic coherent wake structures identified with SPOD mode 1 at $U_0 = 4.4$ m.s^{-1} ($Re_c = 3.74 \times 10^5$) corresponding to the lock-in with f_2 regime. Non-activated shunt configuration.

5.2.3 Analysis of the Karman vortices

To analyse more precisely the dynamics of KVS patterns, the POD method was employed. The POD method offers the opportunity to study the phase correlation between modes by analysing their expansion coefficients. Also, a reduced-order model of the Karman vortex shedding can be obtained by reconstructing the velocity field with the associated POD spatial modes and their expansion coefficients. It makes it possible to analyse the dynamics of the vortex shedding in the Karman street.

Karman modes energy

Figure 5.13 presents the percentage of total TKE of the first four POD modes for the no-resonance ($Re_c = 2.55 \times 10^5$) and for the lock-in with f_2 for the non-activated shunt configuration ($Re_c = 3.74 \times 10^5$). These modes acount for a least 50% of the total TKE at the no-resonance regime and at least 70% at the lock-in regime. The highest level of TKE is attributed to modes 1 and 2 for both regimes. As was observed for the plate, modes 1 and 2 are still associated with the Karman vortex shedding. At the no-resonance regime, modes 1 and 2 cumulate 40% of the total energy. During the lock-in regime this percentage reaches 68% which implies that there is a transfer of energy from the lower rank modes to modes 1 and 2 at lock-in. This reinforcement of the Karman modes can be associated with the synchronization between the high magnitude vibrations and the vortex shedding occurring at lock-in.

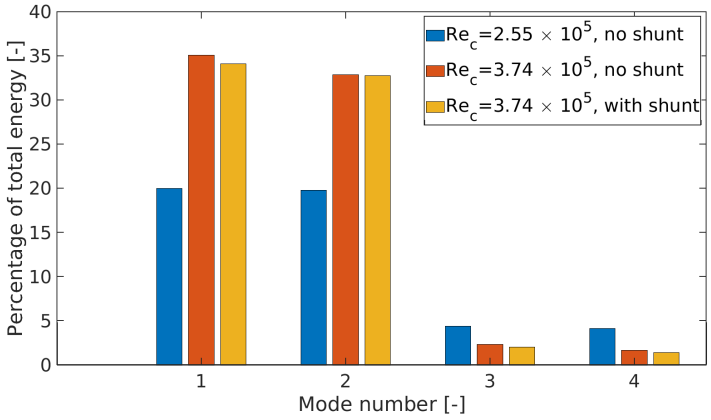

Figure 5.13: Turbulent Kinetic Energy (TKE) of the four first POD modes. No resonance regime (blue), lock-in with f_2 without shunt (orange) and lock-in with f_2 with activated shunt (yellow).

Expansion coefficients

The study of the POD expansion coefficients enables to analyse the temporal evolution of each POD mode and to identify some periodic phenomena occurring in the wake. In figure 5.14, the time signal associated with the expansion coefficient $a_1(t)$ is presented as well as the corresponding frequency spectrum and the dominant frequencies of the mode can be extracted. Mode 2 presents similar temporal features as mode 1 so the analysis can be restricted to the first POD mode. According to figure 5.14a, at the no-resonance regime $a_1(t)$ is characterized by a broadband frequency content ranging between 200 Hz and 280 Hz. The dominant frequency extracted (i.e. the main vortex shedding frequency) is equal to f_{vs}=246 Hz ($St_D \approx 0.50$). As stated before, three dimensionality of the turbulent

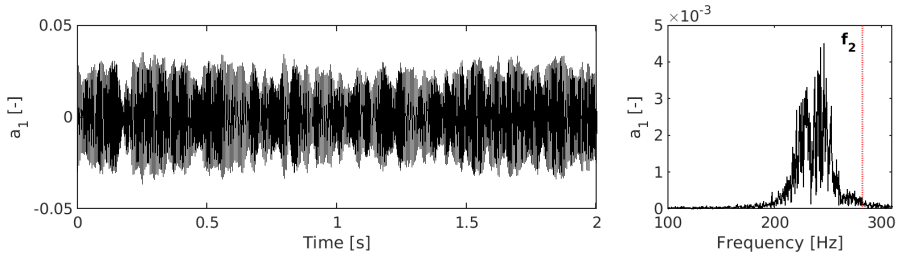

(a) No resonance, no shunt.

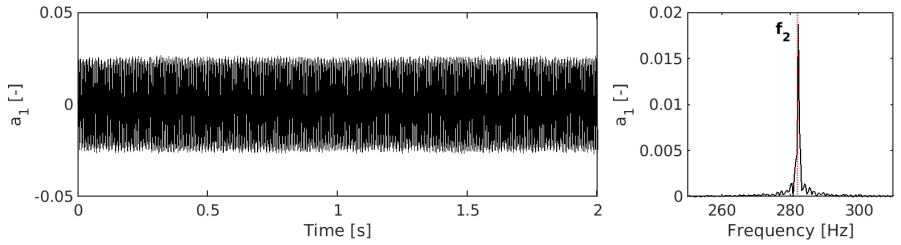

(b) Lock-in, no shunt.

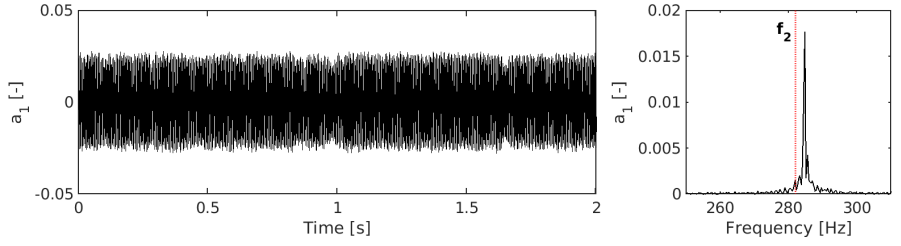

(c) Lock-in, with shunt.

Figure 5.14: Temporal coefficients and associated frequency spectrum of POD mode 1 at the (a) no-resonance regime with non-activated shunt ($U_0 = 3.0$ m.s^{-1}, $Re_c = 2.55 \times 10^5$), (b) the lock-in with non-activated shunt ($U_0 = 4.4$ m.s^{-1}, $Re_c = 3.74 \times 10^5$) and (c) the lock-in with activated shunt ($U_0 = 4.4$ m.s^{-1}, $Re_c = 3.74 \times 10^5$).

wake structures is a specificity of a low magnitude vibration regime [11] and could result in fluctuations of the vortex shedding frequency. Also the higher length of the wake-bubble highlighted before and its probable flapping could also impact the Karman vortex shedding. These hypotheses may explain the multi-frequency features of a_1. Also, the observations made here, illustrate clearly the fact that a POD mode can contain various frequencies which can complicate the identification of coherent wake patterns. This constitutes a limitation of the POD method which is avoided by SPOD.

At the lock-in with f_2, the spectrum of a_1 (figure 5.14b) is narrow-banded and the dominant frequency is equal to f_{vs}=282 Hz ($St_D = 0.39$). This is in agreement with the frequency of the most energetic SPOD mode. This observation confirms the synchronization between the structural motion and the vortex shedding and is in accordance with the hypothesis of increased two-dimensionality proper to the lock-in. The comparison with the activated shunt will be achieved below.

Figure 5.15a presents the phase diagram of POD coefficients $a_1(t)$ and $a_2(t)$ at the no-resonance and at the lock-in for the non-activated shunt configuration. Modes 1 and 2, as being both representative of the Karman vortex shedding, are expected to be phase correlated. The phase plot is modelled by a circle for ideal two-dimensional vortex shedding. Scattering from the circle comes from the multi-

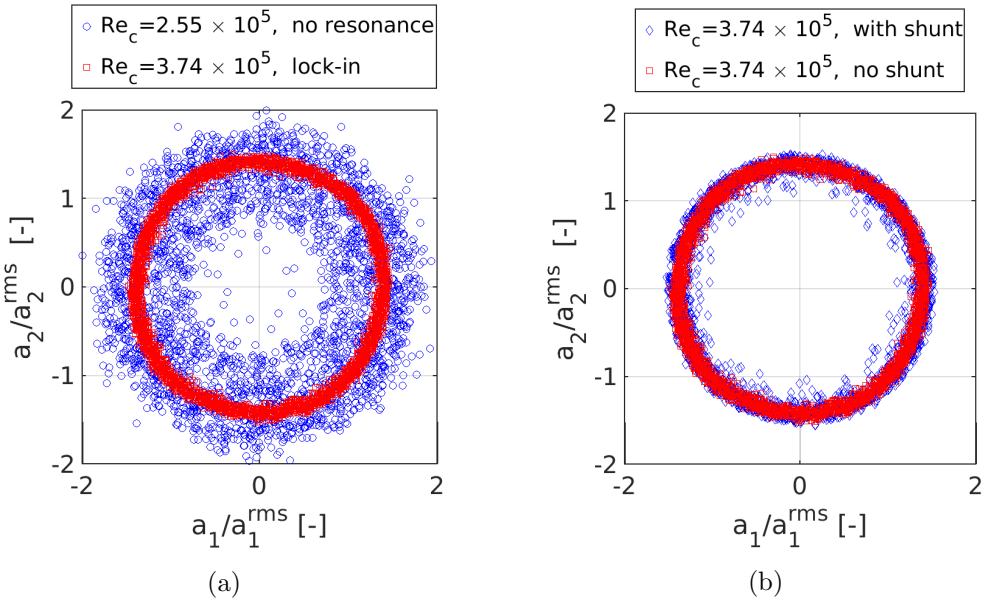

Figure 5.15: (a) Phase diagram associated with modes 1 and 2 at the no-resonance regime and at the lock-in with f_2, non activated shunt configuration. (b) Phase diagram associated with modes 1 and 2 at the lock-in with f_2, activated shunt configuration

frequency contents in the vortex shedding modes. High scattering is observed for the no-resonance regime which confirms the multi-frequency properties of a_1 observed before (figure 5.14a). For the lock-in regime, scattering is highly reduced and modes 1 and 2 are strongly phase correlated.

Arrangement of the Karman wake

A reduced order model of the vorticity map in the near-wake region was obtained by reconstructing the fluctuating vorticity field with POD modes 1 and 2 superimposed to the time-averaged vorticity field. Figures 5.16a and 5.16b display an instantaneous reconstructed vorticity field for the no-resonance and lock-in with f_2 with non-activated shunt configuration. At the no-resonance regime, the vortex centres are located on the wake center-line and the spatial aspect of each vortex is circular. For this configuration the vortex arrangement is symmetrical. The diameter of each vortex is equal to the trailing edge thickness. The region were a vortex is detached from its connecting shear layer is approximately X/D=1, which is the order of magnitude of the eddy-length. It appears that the further a vortex detaches from its connecting shear layer, the less it will interact with the other vortex being generated. This results in vortex centres located close to the wake center-line. The reconstructed Karman wake demonstrates that the vortex arrangement is also modified at the lock-in regime, passing from a symmetrical to an asymmetrical vortex arrangement.

The lock-in regime offers a different spatial arrangement as the location of the vortex centres are shifted beneath and above the wake center-line. This property has permitted to compute the b_s/a_s criterion which is equal to 0.19 for this regime when the shunt is not activated. The aspect of each single vortex is also modified and is no longer circular. The vortices are elongated in the direction normal to the flow. This shape is in agreement with the stability of large area vortices with an arrangement $0.2<b_s/a_s<0.36$ [145, 143]. The region were the vortices are generated is located much closer to the trailing edge than for the no-resonance regime which goes together with a reduction of the wake-bubble length and the eddy-length.

In summary, lock-in increases the coherence of the Karman wake. In our opinion, the main cause of this is the extend to which two dimensionality of the Karman vortices is enhanced by a single deflection shape, leading to a more organized wake. Additional PIV recordings in the span-wise direction are necessary to confirm this hypothesis. The next section is dedicated to the characterization of the effect of the shunt on the hydrodynamic features of the near-wake.

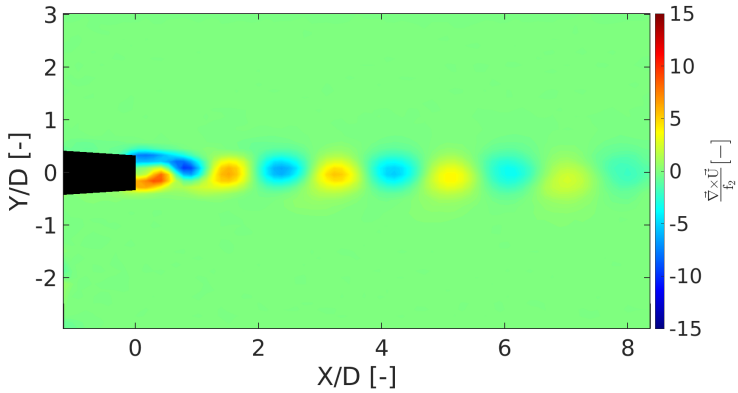

(a) No resonance, no shunt

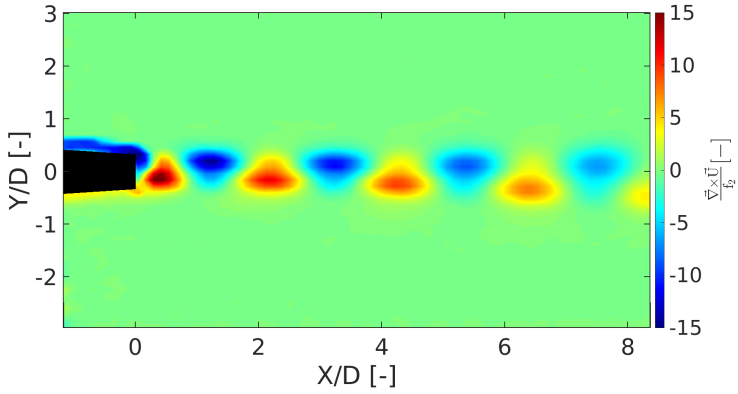

(b) Lock-in, no shunt

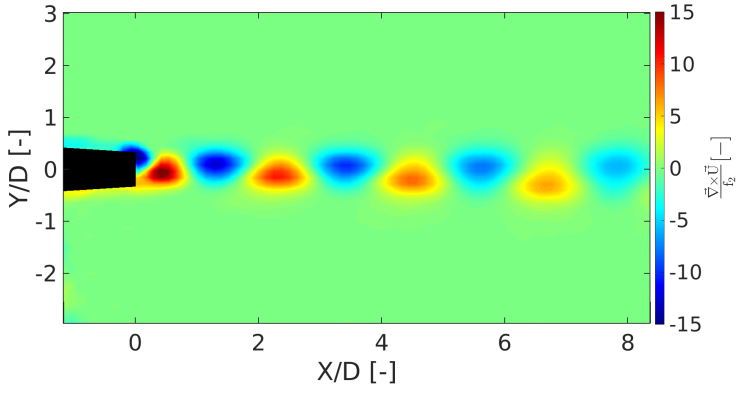

(c) Lock-in, activated shunt

Figure 5.16: (x,y) cartography of the reconstructed vorticity field including POD modes 1 and 2 superimposed to the mean field. For the (a) no-resonance ($U_0 = 3.0$ m.s^{-1}, $Re_c = 2.55 \times 10^5$), (b) lock-in with f_2 without shunt activation ($U_0 = 4.4$ m.s^{-1}, $Re_c = 3.74 \times 10^5$) and (c) lock-in with shunt activation ($U_0 = 4.4$ m.s^{-1}, $Re_c = 3.74 \times 10^5$) regimes.

5.3 Effect of the resonant shunt on the hydrodynamic features of the near-wake

5.3.1 Impact on the time averaged properties

In this section, the characteristics of the time-averaged quantities, SPOD patterns and POD Karman modes are compared at lock-in with f_2 between no-shunt and activated-shunt configurations. Figures 5.6c, 5.7c and 5.8c present the (x,y) cartographies of the stream-wise and normal averaged velocity components and the averaged Reynolds shear-stress at lock-in with shunt activation. When visually inspecting these cartographies, there is no major difference between non-activated (figures 5.6b, 5.7b and 5.8b) and activated shunt configurations. However, it appears that the area corresponding to the near-wake bubble is slightly increased in the stream-wise direction and that the velocity defect in the wake is reduced. In figure 5.8c, the area of high magnitude Reynolds shear-stress (red area) is still longer in the stream-wise direction than the negative shear stress region (blue area). The time averaged quantities specific of the near-wake, obtained for the activated shunt configuration are summarized in table 5.5, together with quantities for the non-activated shunt configuration.

When the shunt is activated, the eddy-length (L_e), based on the stream-wise distance from the trailing-edge of the maximum of $|u'v'|$ is increased of $0.12D$. These observations also confirm that the wake-bubble size is increased and thus that it is sensitive to the vibration magnitude which is decreased. Also, with the activation of the shunt, $|V_{max}|_{y>0} - |V_{max}|_{y<0}$ is increased at lock-in which suggests an increase of the lift force by comparison to the non-activated shunt configuration.

The normalized velocity deficit $U_{defect}/U_0 = (U_0 - U)/U_0 = f(Y/D)$ vertical profile measured at $X = 4D$ is displayed in figure 5.9 for the lock-in with activated shunt configuration. The velocity deficit measured at the centreline significantly decreases when the shunt is activated resulting in a reduction of the drag coefficient. According to this observation, vibration mitigation by piezoelectric shunt could enhance the performance of lifting surfaces by drag reduction and also by increase of the lift force.

5.3.2 Alteration of the near-wake turbulent structures

The impact of the vibration mitigation on the vortex dynamics was investigated by using the SPOD method. The energy associated with the first SPOD mode is presented in figure 5.17 for the

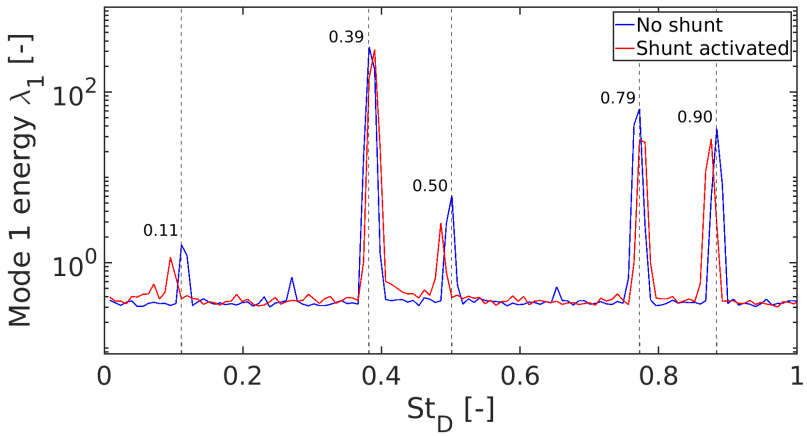

Figure 5.17: Energy spectra of the first SPOD mode for the non-activated and activated shunt configuration at $U_0 = 4.4$ m.s^{-1} ($Re_c = 3.74 \times 10^5$).

non-activated and activated shunt configuration at the lock-in with f_2 regime. The distribution of the energy is not drastically modified as the peaks are still narrow-banded. Table 5.6 summarizes the characteristics of the three most energetic peaks for the non-activated and activated shunt configuration. It appears that the frequency of the peaks are slightly modified when the shunt is activated for the KVS and the SSL patterns. It is necessary to specify that the frequency resolution of the energy spectra is of 6 Hz which may make accurate frequency evaluation doubtful. The eigenvalues representative of the energy associated with the KVS, KHVS and SSL wake structures have sustained an energy reduction. The highest reduction of the energy is attributed to the KHVS structure which has its energy nearly divided by two. The spatial distributions associated with each type of coherent structure were not modified by the shunt as is illustrated in figures 5.18a, 5.18b and 5.18c, the most energetic patterns are still KVS, SSL, KHVS.

Even if the vibration level is maximised during the lock-in, its order of magnitude remains small compared to the characteristic length scales of the KVS and SSL structures which is of the order of the foil thickness D. This could explain why these types of wake structures are weakly influenced by the vibrations of the hydrofoil. Smaller wake structures such as the KHVS are more prone to suffer from the vibrations due to similar characteristic length scales. Also, the KHVS are asymmetric among the wake center-line and consist of two contra-rotative vortices (see figure 5.18b). This kind of spatial distribution is particularly prone to couple with a twisting type deflection as the movement of the

	No shunt	**Shunt activated**
Karman Vortex Shedding		
f_{KVS}	280 Hz	286 Hz
St_D^{KVS}	0.39	0.40
λ_1^{KVS}	338.60	314.50
Karman Harmonic Vortex Shedding		
f_{KHVS}	566 Hz	566 Hz
St_D^{KHVS}	0.79	0.79
λ_1^{KHVS}	64.01	27.72
Separated Shear Layer		
f_{SSL}	648 Hz	642 Hz
St_D^{SSL}	0.90	0.89
λ_1^{SSL}	37.56	28.42

Table 5.6: Characteristics of the coherent wake structures identified with SPOD for the lock-in regime with non-activated and activated shunt configurations.

trailing edge may impact the rotational motion of the vortices. In order to investigate in detail the impact of the shunt on the Karman vortices, the POD method was employed and the obtained results are commented in the next section.

5.3.3 Alteration of the Karman vortices

As illustrated in figure 5.13, the highest level of energy when the shunt is activated is still associated to POD modes 1 and 2 which correspond to Karman type coherent structures. Only the energy of POD mode 1 is slightly reduced when the shunt is activated. The spectra of the expansion coefficient $a_1(t)$ presented in figure 5.14c exhibits an increase of 3 Hz of the dominant peak frequency with regard to the natural frequency of the twisting mode. This frequency offset was also observed with the SPOD analysis and also with the vibrometry measurements (see figure 5.4 in section 1).

The phase correlation of the expansion coefficients $a_1(t)$ and $a_2(t)$ is illustrated by the phase diagram in figure 5.15b. When the shunt is activated, the scattering from the ideal circle is higher which implies that the expansion coefficients are less phase correlated and that multi-frequency content

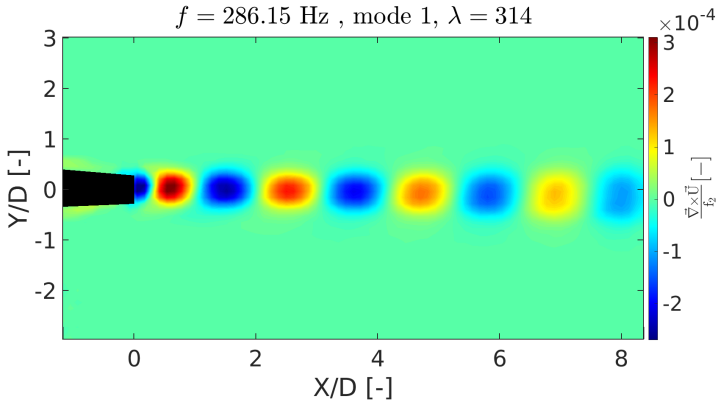

(a) KVS

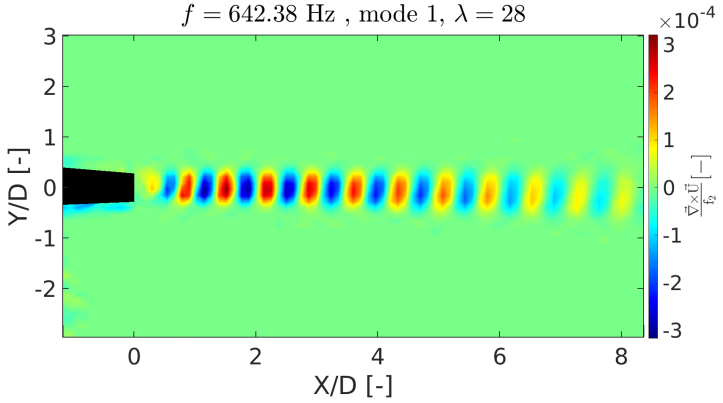

(b) SSL

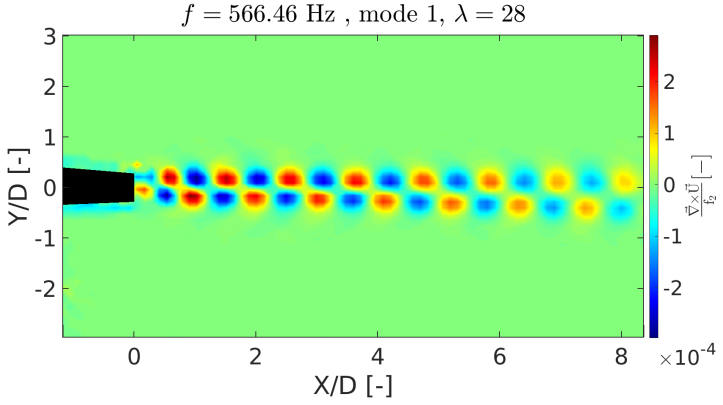

(c) KHVS

Figure 5.18: (x,y) vorticity cartography of three most energetic coherent wake structures identified with SPOD mode 1 at $U_0 = 4.4$ m.s^{-1} ($Re_c = 3.74 \times 10^5$). Activated shunt configuration. (a) is a Karman Vortex shedding mode (KVS), (b) a Separated Shear Layer mode (SSL) and (c) a Karman Harmonic mode (KHVS).

is present, this may be associated with a decay of two-dimensionality of the Karman vortex shedding. The fact of activating the shunt approaches the features of a non-resonant regime in terms of phase correlation.

The reduced order model of the near-wake region obtained by reconstructing the fluctuating vorticity field with POD modes 1 and 2 superposed to the time-averaged vorticity field for the activated shunt configuration is presented in figure 5.16c. The general arrangement of the Karman vortices remains the same as for the no-shunt configuration. The aspect ratio b_s/a_s is reduced from 0.19 to

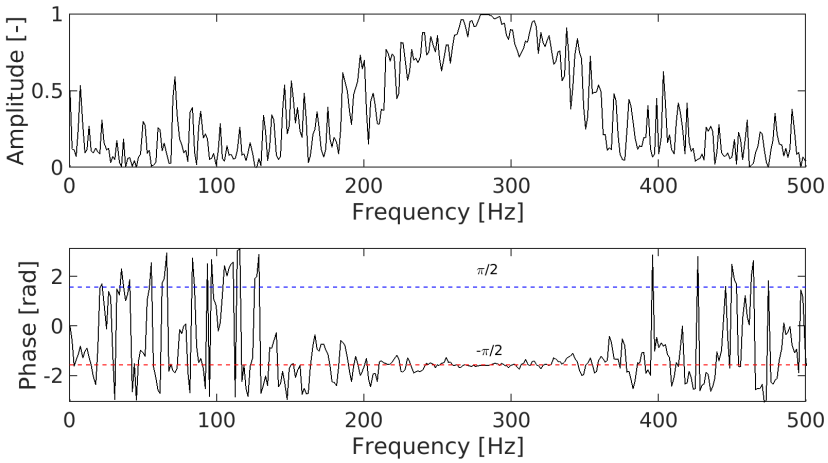

(a) No shunt

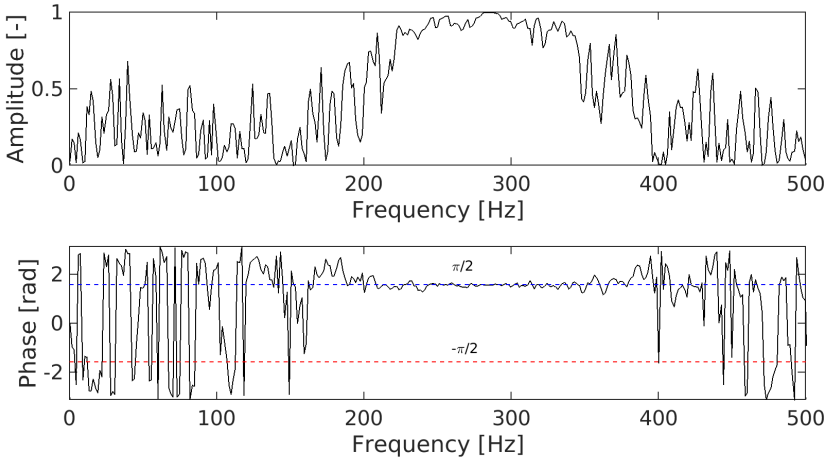

(b) Shunt activated

Figure 5.19: Cross-spectra associated with the POD expansion coefficients $a_1(t)$ and $a_2(t)$ at the lock-in with f_2 regime. (a) non-activated shunt configuration, (b) activated shunt configuration.

0.15 in agreement with a slight decrease in the area of the Karman vortices.

In complement, figures 5.19a and 5.19b present the cross-spectra in amplitude and phase of POD modes 1 and 2 expansion coefficients without and with shunt activation. The range of frequencies where the maximum amplitude of the inter-spectra is reached is larger for the activated shunt configuration than for the non-activated shunt configuration. Interestingly, the phase-lag between POD modes 1 and 2 changes from $-\pi/2$ to $+\pi/2$ when the shunt is activated which implies that there is a phase-lag of π between the KVS proper to each configuration.

The properties of the Karman vortices were investigated by applying the Graftiaux [122] vortex detection algorithm on POD spatial mode Φ_1. Table 5.7 summarizes the size and circulation of the third, fourth and fifth viscous cores behind the trailing edge. The dimensions of the vortices are slightly reduced by the shunt but the permutation of the phase lag from $-\pi/2$ to $+\pi/2$ is illustrated by the inversion of the circulation sign. The magnitude of circulation is also lowered when the shunt is activated which implies that the fluctuating component of the lift force is reduced.

	No shunt	**Activated shunt**
Core location		
Vortex 3	X = 10.6 mm, Y = 0.14 mm	X = 11.3 mm, Y = −0.01 mm
Vortex 4	X = 16.78 mm, Y = −0.10 mm	X = 17.58 mm, Y = −0.08
Vortex 5	X = 23.10 mm, Y = −0.21 mm	X = 24.17 mm, Y = −0.29 mm
Core area		
Vortex 3	14.0 mm^2	13.0 mm^2
Vortex 4	15.6 mm^2	15.0 mm^2
Vortex 5	17.2 mm^2	16.0 mm^2
Core radius		
Vortex 3	2.1 mm	2.0 mm
Vortex 4	2.2 mm	2.2 mm
Vortex 5	2.3 mm	2.3 mm
Core circulation		
Vortex 3	-2.06 $m^2.s^{-1}$	1.88 $m^2.s^{-1}$
Vortex 4	2.02 $m^2.s^{-1}$	-1.92 $m^2.s^{-1}$
Vortex 5	-1.99 $m^2.s^{-1}$	1.79 $m^2.s^{-1}$
Wake aspect ratio		
b_s/a_s	0.19	0.15

Table 5.7: Characteristics of POD mode 1 Karman vortices. Lock-in with f_2 ($U_0 = 4.4\ m.s^{-1}$). Comparison between non-activated and activated shunt configuration.

Conclusion of the chapter

The present chapter has investigated the impact of a vibration mitigation induced by a passive resonant piezoelectric shunt on the fluid structure interaction and the near-wake dynamics of a NACA 66-306 truncated hydrofoil. In a first instance the vibratory response of the hydrofoil was investigated at various free-stream velocities at zero incidence. Different regimes were identified consisting in no-resonance, resonance and lock-in with the first twisting mode f_2, the second bending mode f_3 and a recombination of the first bending mode f_1 and the first twisting mode f_2 ($f_4 = f_1 + f_2$). It appeared that two hydrodynamic excitation sources, representative of Karman Vortex Shedding (KVS) act on the structure and induce high magnitude vibrations at resonance and lock-in. The first excitation source has a Strouhal $St_{D1} = 0.49$ and the second stands for $St_{D2} = 0.34$. The no-resonance regime occurring at $Re_c = 2.55 \times 10^5$ and the lock-in with f_2 occurring at $Re_c = 3.74 \times 10^5$ were investigated for the non-activated and activated-shunt configurations. The no-resonance regime was used as a reference for low vibration magnitude. Through this analysis, it appears that at a non-resonant regime, the global deformation of the hydrofoil is a combination of various types of deflection shapes. This specificity may induce a disorganization of the wake dynamics by reinforcing three-dimensionality in the near-wake but additional PIV recording in the span-wise direction are necessary to confirm this hypothesis. Also, the no-resonance regime is characterized by a broadband frequency content of the Karman vortex shedding. At the lock-in with the first twisting regime, the deformation of the structure mainly consist of a twisting deflection shape which tends to reorganize the near-wake. When the shunt is activated, the vibration magnitude is notably reduced for Reynolds ranging in $[3.5 \times 10^5; 4.25 \times 10^5]$ which demonstrates that the shunt is operational for a certain range of incoming flow velocities. The shunt also induces a smoother transition between different lock-in regimes an a narrower range of Reynolds numbers were resonance occurs.

In a second instance, the hydrodynamic properties of the near-wake generated by the truncated hydrofoil were investigated at the no-resonance and lock-in with f_2 for the non-activated and activated shunt configurations. The near-wake time-averaged properties were analysed and it appeared that the size of the near-wake bubble is significantly reduced during the lock-in regime. Also, the drag is increased and the lift force is reduced at this regime which implies that the overall performance of the hydrofoil is slightly reduced when high magnitude vibrations occur. The shunt increases the size

of the near-wake bubble, the intensity of the lift force and reduces the drag which offers promising opportunities for enhancing the overall performance of lifting surfaces and paves the way for various industrial applications.

The SPOD an POD analysis methods were implement to identify coherent wake structures in the near-wake and characterize the wake dynamics at the different vibration regimes. It appears that Karman vortex shedding (KVS) and its harmonic (KHVS) are the dominant wake patterns which act as structural excitation sources on the structure. At the no-resonance regime, KVS is rather disorganized and characterized by broad-band frequency vortex shedding. This is probably due to three-dimensionality of the near-wake. At the lock-in, the KVS and KHVS is reinforced and presents well-marked narrow-banded frequencies. When the shunt is activated the general organization of the near-wake is not drastically modified but the POD modes 1 and 2, representative of the KVS, are less phase correlated and multi-frequency content is reintroduced. The dimensions of the Karman vortices is also slightly reduced as well as the circulation which tends to decrease the fluctuating component of the lift force.

The study achieved in this chapter has demonstrated that a mitigation by resonant piezoelectric shunt of the flow-induced vibrations, sustained by a truncated hydrofoil, impacts the features of its near-wake. Further investigations with additional experimental or numerical data are necessary to accurately characterize the alteration of the wake properties by the shunt. PIV recordings of the near-wake in the span-wise direction are necessary to analyse the mechanism responsible of the reinforcement of three-dimensionality. Also, a description of the flow upstream of the trailing-edge is necessary to detect a potential influence of the boundary layer transition or separation. Nevertheless, the observations made in this study pave the way for future experimental and CFD investigations and offer interesting opportunities for industrial applications dedicated to wake-flow control and lifting surface performance improvement.

Conclusion and perspectives

Conclusion

In the present thesis, an experimental study of the flow-induced vibrations sustained by marine lifting surfaces was achieved in order to investigate the fluid-structure coupling of elongated bodies and design an efficient vibration mitigation device consisting of a passive resonant piezoelectric shunt. The studied structures consisted of a blunt rectangular flat aluminium plate of chord-to-thickness ratio 16.7 and a truncated NACA 66-306 aluminium hydrofoil of chord-to-thickness ratio 13.9. Various flow velocities, associated with chord-based Reynolds numbers ranging between 2.5×10^5 and 9.5×10^5, were investigated at zero degrees of incidence in the hydrodynamic tunnel of the French Naval Academy Research Institute (IRENav). The vibration velocity of both structures was recorded using laser vibrometry and the near-wake flow field was characterized by Time-Resolved Particle Image Velocimetry (TR-PIV). Post-processing of the data was achieved by statistical analysis, Proper Orthogonal Decomposition (POD) and its spectral variant (SPOD). A passive resonant piezoelectric shunt was connected to a Macro Fiber Composite (MFC) type piezoelectric transducer integrated on the truncated hydrofoil surface in order to mitigate twisting mode vibrations.

For the blunt plate, two different hydrodynamic excitation sources of different Strouhal number were observed. This phenomenology may be attributed to the coexistence of two Karman vortex shedding modes, a chord-to-thickness ratio of 16.7 being at the transition between two regimes of excitation. The primary excitation source is identified as trailing-edge vortex shedding instability (TEVS) and consists in primary Karman vortex shedding of characteristic Strouhal number $St_D = 0.195$. The secondary excitation source of $St_D = 0.227$ is identified as Impinging Shear-Layer instability (ISL) and is associated to a square leading-edge. The analysis of the vibrational response of the blunt plate at various flow velocities has permitted to highlight three distinct vibration regimes consisting of no-

resonance, lock-off resonance and lock-in resonance. Of particular interest is the lock-off resonance regime which occurs when the second Karman mode synchronizes with the twisting mode natural frequency. To our best knowledge, it is the first time that the lock-off resonance regime is observed for high aspect-ratio blunt bodies. It is of particular interest for the design of structures subjected to flow-induced vibrations as it implies the early occurrence of high magnitude vibrations. The observation of these vortex induced vibration mechanisms has permitted to gain new insight about vibrations sustained by elongated blunt bodies and is of great interest for the design of the resonant piezoelectric shunt.

When designing a resonant piezoelectric shunt, the inductor is of prime importance because it allows the tuning of the electrical resonance frequency with the frequency of the structural resonance to mitigate. Two types of inductors were tested and connected to a MFC transducer embedded into the truncated hydrofoil: a copper wired coil and a synthetic inductor. The shunt based on the copper wired coil is well adapted for high vibration magnitudes such as those induced by the flow and resulting in a high voltage level at the electrodes of the piezoelectric transducer. It has demonstrated a vibration mitigation level of 18 dB (equivalent to a reduction ratio of 1/8) of the twisting mode when the hydrofoil is immersed in water at zero flow velocity. It was also tested in the hydrodynamic tunnel under flow excitation when the first twisting mode is locked with the primary Karman vortex shedding frequency. For this configuration, the root mean square value of the vibration velocity signal was reduced by 62%. It is the first time that a twisting mode excited by a water flow is mitigated by a passive resonant piezoelectric shunt. The synthetic inductor shunt is constituted of an electronic circuit based on operational amplifiers (OPA). Its main advantage is its adaptability in terms of variation of the inductance and internal resistance which allows an accurate tuning of the shunt parameters. However, the use of the classical synthetic inductor based on OPAs is restricted to low vibration levels. The synthetic inductor shunt was tested at zero flow velocity and provided a vibration mitigation of 31 dB (equivalent to a reduction ratio of 1/36) in air and of 21 dB (equivalent to a reduction ratio of 1/11) in water. At the end, both types of shunts have demonstrated high vibration mitigation levels and are simple, cost effective and adaptable. In addition to the experimental study, a numerical model of the hydrofoil embedded with MFC and DuraAct transducers was implemented with COMSOL *Multiphysics*. This model is based on finite-element computations. It has offered a valuable design tool to predict the natural frequencies and coupling factors of structures embedded with piezoelectric

transducers. A passive resonant shunt was also simulated in order to predict the frequency response functions depending on different values of resistance and inductance. Numerical and experimental results were compared and appeared to be in accordance which validates the electromechanical model. Using this numerical tool will avoid several expensive experimental iterations and guarantee an optimal set-up of resonant shunts due to the easy variation of the parameters.

In order to test the system in an applicative configuration, the copper wired shunt was connected to the MFC transducer integrated on the truncated hydrofoil surface. Measurements of the vibration velocity, as well as the characterization of the hydrodynamics in the near-wake of the hydrofoil were performed in the hydrodynamic tunnel, under different free-stream velocities . As for the blunt plate, different vibration regimes consisting of no resonance, resonance and lock-in resonance with the first twisting mode and with the second bending mode were identified. Two hydrodynamic excitation sources of Strouhal number $St_{D1} = 0.49$ and $St_{D2} = 0.34$, representative of Karman Vortex Shedding and inducing high magnitude vibrations, were also observed. It appeared that at the no-resonance regime, the global deformation of the hydrofoil is a combination of various types of deflection shapes which may induce a disorganization of the wake dynamics by reinforcing three-dimensionality. For the lock-in regime, the near-wake is reorganized due to the high magnitude twisting deformation. When the shunt is activated, the vibration magnitude is reduced for Reynolds ranging in $[3.5\times10^5; 4.25\times10^5]$ which is larger than the Reynolds range of lock-in resonance with the twisting mode. This demonstrates that the shunt is operational for a relatively wide range of incoming flow velocities. The shunt also induces a smoother transition between different lock-in regimes and a narrower range of Reynolds numbers were resonance occurs. At lock-in, the drag is reduced by the activation of the shunt which offers promising opportunities for enhancing the overall performance of lifting surfaces. In terms of vortex dynamics at lock-in, the Karman modes are less phase correlated and multi-frequency vortex shedding takes place when the shunt is activated, which is a main characteristic of a no-resonance regime. By these observations it appears that the piezoelectric shunt is able to impact the near-wake characteristics which is innovative in the field of wake-flow control. In the end, the investigations conducted through this study have offered new insights about the FIV mechanisms leading to high magnitude vibrations and the resonant piezoelectric shunt has demonstrated its high capability to reduce these vibrations. We believe that the work conducted here will pave the way for various industrial applications aiming at reducing vibrations of lifting surfaces.

Perspectives

The present study demonstrated that a resonant piezoelectric shunt offers significant vibration mitigation capabilities. In order to optimise the mitigation level and gain additional insight about FIV mechanisms, some issues have to be solved and additional experimental data is required.

Integration of piezoelectric transducers in complex structures

Industrial applications will require the integration of piezoelectric transducers among various types of complex structures. Some typical examples are the propeller blades or the curved hydrofoils proper to fast sailing yachts. Integration of the transducers on these structures will require additional studies concerning the positioning, bonding and sealing of the transducers. Also, the manufacturing process will require adaptations in order to build high dimension transducers. The issues of water infiltration and high internal resistance of some of the transducers will also require further investigations and improvements to reach the highest vibration mitigation levels. We believe that piezoelectric transducers fully integrated in composite structures will offer significant benefits because the active layers will be protected from the marine environment. Also, it will avoid the transition between various materials at the surface of the lifting body and prevent the onset of turbulence due to surface roughness.

Optimization of the resonant electrical circuit

It appeared that the limitations of the resonant piezoelectric shunt in terms of vibration mitigation were mainly due to the features of the standard electrical components and of the piezoelectric transducers. Reducing the internal resistance of the circuit will increase the level of vibration mitigation and facilitate the tuning of the shunt. For the synthetic inductor shunt, using operational amplifiers capable of withstanding high voltage levels will allow the use of this type of shunt to reduce high magnitude flow-induced vibrations combined with easy variation of the inductance. Implementing auto-adaptative features to the shunt could also increase the robustness of the system. The synthetic inductor seems compatible with this type of improvement as the inductance could be tuned by an external calculator. Other adaptive shunts based on power electronics may also offer some opportunities for handling high piezoelectric voltage. Finally, the model used to compute the inductance and resistance will be adapted in order to take into account non-linear vibration regimes.

Synchronization between PIV and vibrometry recordings

In this study, vibrometry and PIV recordings were done independently which implies that the phase correlation between the structural response and the hydrodynamic excitations was not evaluable. Achieving synchronized vibrometry and PIV recordings will permit to gain new insight about the fluid-structure coupling mechanisms.

Study of three-dimensionality in the near-wake and of the flow upstream from the trailing-edge

Additional PIV recordings in the span-wise direction are necessary to fully appreciate the three-dimensional properties of the near-wake at the no-resonance regime and the reinforcement of two-dimensionality at the lock-in. This will allow to explain the multi-frequency content of Karman vortex shedding and validate the link between the structural deformation and the properties of the near-wake. Furthermore, an evaluation of the flow upstream from the trailing-edge will offer the opportunity to identify leading-edge separation instabilities and boundary layer separation and transition. These phenomena could interact with the near-wake and influence the vibrational response. Finally, recording the acoustic noise, in addition to the vibration magnitude measurements, could provide a significant assessment of the effect of the shunt on acoustic stealth.

Bibliography

[1] Z. Taylor, E. Palombi, R. Gurka, and G. Kopp, "Features of the turbulent flow around symmetric elongated bluff bodies," *Journal of Fluids and Structures*, vol. 27, pp. 250–265, 02 2011.

[2] A. Deraemaeker, H. Nasser, A. Benjeddou, and A. Preumont, "Mixing rules for the piezoelectric properties of macro fiber composites," *Journal of intelligent material systems and structures*, vol. 20, no. 12, pp. 1475–1482, 2009.

[3] Y. S. Kachanov, "Physical mechanisms of laminar-boundary-layer transition," *Annual review of fluid mechanics*, vol. 26, no. 1, pp. 411–482, 1994.

[4] P. K. Kundu, I. M. Cohen, and D. R. Dowling, *Fluid mechanics*. Academic press, 2015.

[5] F. M. White and J. Majdalani, *Viscous fluid flow*, vol. 3. McGraw-Hill New York, 2006.

[6] J. Gerrard, "The mechanics of the formation region of vortices behind bluff bodies," *Journal of fluid mechanics*, vol. 25, no. 2, pp. 401–413, 1966.

[7] R. D. Blevins, *Flow-induced vibration*. Van Nostrand Reinhold Inc., 1977.

[8] Y. Nakamura, Y. Ohya, and H. Tsuruta, "Experiments on vortex shedding from flat plates with square leading and trailing edges," *Journal of Fluid Mechanics*, vol. 222, pp. 437–447, 1991.

[9] E. Naudascher and D. Rockwell, *Flow-induced vibrations: an engineering guide*. Courier Corporation, 2012.

[10] P. Ausoni, *Turbulent vortex shedding from a blunt trailing edge hydrofoil*. PhD thesis, École Polytechnique Fédérale de Lausanne, 2009.

[11] A. Zobeiri, *Effect of Hydrofoil Trailing Edge Geometry on the Wake Dynamics*. PhD thesis, École Polytechnique Fédérale de Lausanne, 2012.

[12] G. H. Toebes and P. S. Eagleson, "Hydroelastic vibrations of flat plates related to trailing edge geometry," *Journal of Basic Engineering*, vol. 83, pp. 671–678, 12 1961.

[13] E. Ranjith, A. Sunil, and L. Pauly, "Analysis of flow over a circular cylinder fitted with helical strakes," *Procedia Technology*, vol. 24, pp. 452–460, 2016.

[14] J. Ducarne, *Modélisation et optimisation de dispositifs non-linéaires d'amortissement de structures par systèmes piézoélectriques commutés.* PhD thesis, Conservatoire national des arts et metiers-CNAM, 2009.

[15] C. Covaci and A. Gontean, "Piezoelectric energy harvesting solutions: A review," *Sensors*, vol. 20, p. 3512, 06 2020.

[16] J. Briscoe and S. Dunn, "Piezoelectric nanogenerators–a review of nanostructured piezoelectric energy harvesters," *Nano Energy*, vol. 14, pp. 15–29, 2015.

[17] R. Lerch, G. Sessler, and D. Wolf, *Technische Akustik: Grundlagen und Anwendungen.* Springer-Verlag, 2009.

[18] W. K. Wilkie, R. G. Bryant, J. W. High, R. L. Fox, R. F. Hellbaum, A. Jalink Jr, B. D. Little, and P. H. Mirick, "Low-cost piezocomposite actuator for structural control applications," in *Smart structures and materials 2000: industrial and commercial applications of smart structures technologies*, vol. 3991, pp. 323–334, SPIE, 2000.

[19] M. Pohl and M. Rose, "Piezoelectric shunt damping of a circular saw blade with autonomous power supply for noise and vibration reduction," *Journal of Sound and Vibration*, vol. 361, pp. 20–31, 2016.

[20] S. Moheimani and A. Fleming, *Piezoelectric Transducers for Vibration Control and Damping.* Springer, 01 2006.

[21] A. Towne, O. T. Schmidt, and T. Colonius, "Spectral proper orthogonal decomposition and its relationship to dynamic mode decomposition and resolvent analysis," *Journal of Fluid Mechanics*, vol. 847, p. 821–867, 2018.

[22] M. C. Reese, *Vibration and damping of hydrofoils in uniform flow.* PhD thesis, Pennsylvania State University, 2010.

[23] C. Peng, X. Zhao, and G. Liu, "Noise in the sea and its impacts on marine organisms," *International journal of environmental research and public health*, vol. 12, no. 10, pp. 12304–12323, 2015.

[24] A. A. Myrberg Jr, "The effects of man-made noise on the behavior of marine animals," *Environment International*, vol. 16, no. 4-6, pp. 575–586, 1990.

[25] "Directive cadre stratégie pour le milieu marin." dcsmm.milieumarinfrance.fr/.

[26] "Projet life piaquo." lifepiaquo-urn.eu/.

[27] A. Zobeiri, P. Ausoni, F. o. Avellan, and M. Farhat, "Experimental investigation of the vortex shedding in the wake of oblique and blunt trailing edge hydrofoils using piv-pod method," in *Fluids Engineering Division Summer Meeting*, vol. 54518, pp. 149–154, 2010.

[28] A. Zobeiri, P. Ausoni, F. Avellan, and M. Farhat, "How oblique trailing edge of a hydrofoil reduces the vortex-induced vibration," *Journal of Fluids and Structures*, vol. 32, pp. 78–89, 2012.

[29] K. Roussopoulos, "Feedback control of vortex shedding at low reynolds numbers," *Journal of Fluid Mechanics*, vol. 248, pp. 267–296, 1993.

[30] D. Park, D. Ladd, and E. Hendricks, "Feedback control of von kármán vortex shedding behind a circular cylinder at low reynolds numbers," *Physics of fluids*, vol. 6, no. 7, pp. 2390–2405, 1994.

[31] O. Cadot and M. Lebey, "Shear instability inhibition in a cylinder wake by local injection of a viscoelastic fluid," *Physics of Fluids*, vol. 11, no. 2, pp. 494–496, 1999.

[32] J. Cousteix, *Aâerodynamique: Turbulence et Couche Limite*. Cépaduès-editions, 1989.

[33] P. J. Shapiro, "The influence of sound upon laminar boundary layer instability," tech. rep., MASSACHUSETTS INST OF TECH CAMBRIDGE ACOUSTICS AND VIBRATION LAB, 1977.

[34] H. L. Rogler and E. Reshotko, "Disturbances in a boundary layer introduced by a low intensity array of vortices," *SIAM Journal on Applied Mathematics*, vol. 28, no. 2, pp. 431–462, 1975.

[35] M. Nishioka and M. Morkovin, "Boundary-layer receptivity to unsteady pressure gradients: experiments and overview," *Journal of Fluid Mechanics*, vol. 171, pp. 219–261, 1986.

[36] D. Bushnell and M. Malik, "Application of stability theory to laminar flow control—progress and requirements," in *Stability of Time Dependent and Spatially Varying Flows: Proceedings of the Symposium on the Stability of Time Dependent and Spatially Varying Flows Held August 19–23, 1985, at NASA Langley Research Center, Hampton, Virginia*, pp. 1–17, Springer, 1987.

[37] M. Jahanmiri, "Laminar separation bubble: its structure, dynamics and control," tech. rep., Chalmers University of Technology, 2011.

[38] W. Shyy, Y. Lian, J. Tang, D. Viieru, and H. Liu, *Aerodynamics of low Reynolds number flyers*. 2008.

[39] P. W. Bearman, "Vortex shedding from oscillating bluff bodies," *Annual Review of Fluid Mechanics*, vol. 16, no. 1, pp. 195–222, 1984.

[40] S. Balachandar, R. Mittal, and F. Najjar, "Properties of the mean recirculation region in the wakes of two-dimensional bluff bodies," *Journal of Fluid Mechanics*, vol. 351, pp. 167–199, 1997.

[41] M. J. Janocha, G. Yin, and M. C. Ong, "Modal analysis of wake behind stationary and vibrating cylinders," *Journal of Offshore Mechanics and Arctic Engineering*, vol. 143, no. 4, 2021.

[42] C. Norberg, "Flow around a circular cylinder: aspects of fluctuating lift," *Journal of fluids and structures*, vol. 15, no. 3-4, pp. 459–469, 2001.

[43] A. Perry, M. Chong, and T. Lim, "The vortex-shedding process behind two-dimensional bluff bodies," *Journal of Fluid Mechanics*, vol. 116, pp. 77–90, 1982.

[44] T. Von Karman, "Über den mechanismus des widerstandes, den ein bewegter körper in einer flüssigkeit erfährt," *Nachrichten von der Gesellschaft der Wissenschaften zu Göttingen, Mathematisch-Physikalische Klasse*, vol. 1911, pp. 509–517, 1911.

[45] W. K. Blake, "Excitation of plates and hydrofoils by trailing edge flows," *Journal of Vibration, Acoustics, Stress, and Reliability in Design*, vol. 106, pp. 351–363, 07 1984.

[46] R. Parker and M. Welsh, "Effects of sound on flow separation from blunt flat plates," *International Journal of Heat and Fluid Flow*, vol. 4, no. 2, pp. 113–127, 1983.

[47] J. M. Chen and Y.-C. Fang, "Strouhal numbers of inclined flat plates," *Journal of Wind Engineering and Industrial Aerodynamics*, vol. 61, no. 2, pp. 99–112, 1996.

[48] A. Stokes and M. Welsh, "Flow-resonant sound interaction in a duct containing a plate, II: Square leading edge," *Journal of Sound and Vibration*, vol. 104, pp. 55–73, 1986.

[49] L. L. Shi, Y. Z. Liu, and J. Yu, "Piv measurement of separated flow over a blunt plate with different chord-to-thickness ratios," *Journal of Fluids and Structures*, vol. 26, no. 4, pp. 644–657, 2010.

[50] Q. Zhang and Y. Liu, "Influence of incident vortex street on separated flow around a finite blunt plate: PIV measurement and POD analysis," *Journal of fluids and structures*, vol. 55, pp. 463–483, 2015.

[51] E. Naudascher and Y. Wang, "Flow-induced vibrations of prismatic bodies and grids of prisms," *Journal of Fluids and Structures*, vol. 7, no. 4, pp. 341–373, 1993.

[52] R. MILLS, J. SHERIDAN, and K. HOURIGAN, "Particle image velocimetry and visualization of natural and forced flow around rectangular cylinders," *Journal of Fluid Mechanics*, vol. 478, p. 299–323, 2003.

[53] Z. J. Taylor, R. Gurka, and G. A. Kopp, "Effects of leading edge geometry on the vortex shedding frequency of an elongated bluff body at high reynolds numbers," *Journal of Wind Engineering and Industrial Aerodynamics*, vol. 128, pp. 66–75, 2014.

[54] S. K. Chakrabarti, *The theory and practice of hydrodynamics and vibration*, vol. 20. World scientific, 2002.

[55] E. De Langre, *Fluides et solides*. Editions Ecole Polytechnique, 2001.

[56] A. Lelong, *Etude expérimentale du comportement hydroélastique d'une structure flexible pour différents régimes d'écoulement*. PhD thesis, Université de Bretagne Occidentale, 2016.

[57] X. Hu, W. Tao, and Y. Guo, "Fluid-structure interaction simulation of a tree swaying in wind field," *Chin. J. Comput. Mech*, vol. 28, no. 2, pp. 302–308, 2011.

[58] W.-X. Huang and H. J. Sung, "Three-dimensional simulation of a flapping flag in a uniform flow," *Journal of Fluid Mechanics*, vol. 653, pp. 301–336, 2010.

[59] J. M. Moubogha, *Analyse des écoulements autour de structures en mouvement forcé de tangage: application à la propulsion instationnaire.* PhD thesis, Ecole nationale supérieure d'arts et métiers-ENSAM, 2018.

[60] F. Axisa, *Vibrations sous écoulement.* Hermès science publications, 2001.

[61] M. L. Facchinetti, E. De Langre, and F. Biolley, "Coupling of structure and wake oscillators in vortex-induced vibrations," *Journal of Fluids and structures*, vol. 19, no. 2, pp. 123–140, 2004.

[62] M. P. Païdoussis, S. J. Price, and E. De Langre, *Fluid-structure interactions: cross-flow-induced instabilities.* Cambridge University Press, 2010.

[63] S. Kaneko, T. Nakamura, F. Inada, and M. Kato, *Flow-Induced Vibrations: Classifications and Lessons from Practical Experiences: Second Edition.* Elsevier, 2008.

[64] Q. Zhang, S. W. Lee, and P. M. Ligrani, "Effects of surface roughness and freestream turbulence on the wake turbulence structure of a symmetric airfoil," *Physics of fluids*, vol. 16, no. 6, pp. 2044–2053, 2004.

[65] E. Achenbach and E. Heinecke, "On vortex shedding from smooth and rough cylinders in the range of reynolds numbers 6×10^3 to 5×10^6," *Journal of fluid mechanics*, vol. 109, pp. 239–251, 1981.

[66] R. D. Blevins, *Flow induced vibration of bluff structures.* PhD thesis, California Institut of Technology, 1974.

[67] O. M. Griffin and S. E. Ramberg, "The vortex-street wakes of vibrating cylinders," *Journal of Fluid Mechanics*, vol. 66, no. 3, p. 553–576, 1974.

[68] P. K. Stansby, "The locking-on of vortex shedding due to the cross-stream vibration of circular cylinders in uniform and shear flows," *Journal of Fluid Mechanics*, vol. 74, no. 4, p. 641–665, 1976.

[69] R. Parker and M. Welsh, "Effects of sound on flow separation from blunt flat plates," *International Journal of Heat and Fluid Flow*, vol. 4, no. 2, pp. 113–127, 1983.

[70] W. Blake, *Mechanics of Flow-Induced Sound and Vibration: Complex Flow-Structure Interactions*. Academic Press INC, 08 2017.

[71] R. Donaldson, "Hydraulic turbine runner vibration," *Journal of Engineering for Power*, vol. 78, pp. 1141–1147, 01 1956.

[72] G. Heskestad and D. Olberts, "Influence of trailing-edge geometry on hydraulic-turbine-blade vibration resulting from vortex excitation," *Journal of Engineering for Power*, vol. 82, p. 103, 04 1960.

[73] L. Rouleau, *Modélisation vibro-acoustique de structures sandwich munies de matériaux visco-élastiques.* PhD thesis, Conservatoire national des arts et metiers-CNAM, 2013.

[74] S. Krenk and J. Høgsberg, "Tuned mass absorber on a flexible structure," *Journal of Sound and Vibration*, vol. 333, no. 6, pp. 1577–1595, 2014.

[75] E. Maghsoudi Nia, N. A. Wan Abdullah Zawawi, and B. Singh, "Design of a pavement using piezoelectric materials," *Materialwissenschaft und Werkstofftechnik*, vol. 50, pp. 320–328, 03 2019.

[76] B. V. de Almeida and R. Pavanello, "Topology optimization of the thickness profile of bimorph piezoelectric energy harvesting devices," *Journal of Applied and Computational Mechanics*, vol. 5, no. 1, pp. 113–127, 2019.

[77] D. Inman, *Piezoelectric Energy Harvesting*. John Wiley & Sons, 03 2011.

[78] G. Lippmann, "Principe de la conservation de l'électricité, ou second principe de la théorie des phénomènes électriques," *J. Phys. Theor. Appl.*, vol. 10, no. 1, pp. 381–394, 1881.

[79] A. N. S. Institute, *An American National Standard: IEEE Standard on Piezoelectricity Standard*. IEEE, 1988.

[80] A. Safari and E. K. Akdogan, *Piezoelectric and Acoustic Materials for Transducer Applications*. Springer Science & Business Media, 2008.

[81] K. K. Sappati and S. Bhadra, "Piezoelectric polymer and paper substrates: A review," *Sensors (Basel, Switzerland)*, vol. 18, October 2018.

[82] K. Uchino, "Introduction to piezoelectric actuators and transducers," tech. rep., PENNSYLVANIA STATE UNIV UNIVERSITY PARK, 2003.

[83] A. F. Rogers, "A tabulation of the 32 crystal classes 1," *American Mineralogist*, vol. 13, pp. 571–577, 12 1928.

[84] J. Erhart, P. Půlpán, and M. Pustka, *Piezoelectric Ceramic Resonators*. Springer, 01 2017.

[85] S. J. Rupitsch, "Piezoelectric sensors and actuators," *Simulation of Piezoelectric Sensor and Actuator Devices. In: Piezoelectric Sensors and Actuators. Topics in Mining, Metallurgy and Materials Engineering*, pp. 83–126, 2019.

[86] S. Zhang, F. Li, X. Jiang, J. Kim, J. Luo, and X. Geng, "Advantages and challenges of relaxor-pbtio3 ferroelectric crystals for electroacoustic transducers–a review," *Progress in materials science*, vol. 68, pp. 1–66, 2015.

[87] K. S. Ramadan, D. Sameoto, and S. Evoy, "A review of piezoelectric polymers as functional materials for electromechanical transducers," *Smart Materials and Structures*, vol. 23, no. 3, p. 033001, 2014.

[88] P. Ueberschlag, "Pvdf piezoelectric polymer," *Sensor review*, vol. 21, no. 2, pp. 118–126, 2001.

[89] K. Uchino, "Piezoelectric composite materials," in *Advanced Piezoelectric Materials*, pp. 353–382, Elsevier, 2017.

[90] Y. Su, W. Li, X. Cheng, Y. Zhou, S. Yang, X. Zhang, C. Chen, T. Yang, H. Pan, G. Xie, *et al.*, "High-performance piezoelectric composites via β phase programming," *Nature communications*, vol. 13, no. 1, p. 4867, 2022.

[91] C. Richard, D. Guyomar, D. Audigier, and H. Bassaler, "Enhanced semi-passive damping using continuous switching of a piezoelectric device on an inductor," in *Smart structures and materials 2000: damping and isolation*, vol. 3989, pp. 288–299, SPIE, 2000.

[92] N. Hagood and A. von Flotow, "Damping of structural vibrations with piezoelectric materials and passive electrical networks," *Journal of Sound and Vibration*, vol. 146, no. 2, pp. 243–268, 1991.

[93] S. R. Moheimani, "A survey of recent innovations in vibration damping and control using shunted piezoelectric transducers," *IEEE transactions on control systems technology*, vol. 11, no. 4, pp. 482–494, 2003.

[94] D. Niederberger and M. Morari, "An autonomous shunt circuit for vibration damping," *Smart Materials and Structures*, vol. 15, no. 2, p. 359, 2006.

[95] C. H. Park and D. J. Inman, "Enhanced piezoelectric shunt design," *Shock and Vibration*, vol. 10, no. 2, pp. 127–133, 2003.

[96] C. L. Davis and G. A. Lesieutre, "An actively tuned solid-state vibration absorber using capacitive shunting of piezoelectric stiffness," *Journal of Sound Vibration*, vol. 232, pp. 601–617, May 2000.

[97] S. yau Wu, "Piezoelectric shunts with a parallel r-l circuit for structural damping and vibration control," in *Smart Structures and Materials 1996: Passive Damping and Isolation* (C. D. Johnson, ed.), vol. 2720, pp. 259 – 269, International Society for Optics and Photonics, SPIE, 1996.

[98] J. J. Hollkamp, "Multimodal passive vibration suppression with piezoelectric materials and resonant shunts," *Journal of Intelligent Material Systems and Structures*, vol. 5, no. 1, pp. 49–57, 1994.

[99] A. J. Fleming, S. Behrens, and S. O. R. Moheimani, "Reducing the inductance requirements of piezoelectric shunt damping systems," *Smart Materials and Structures*, vol. 12, pp. 57–64, jan 2003.

[100] S. yau Wu, "Method for multiple-mode shunt damping of structural vibration using a single PZT transducer," in *Smart Structures and Materials 1998: Passive Damping and Isolation* (L. P. Davis, ed.), vol. 3327, pp. 159 – 168, International Society for Optics and Photonics, SPIE, 1998.

[101] S. Moheimani, A. Fleming, and S. Behrens, "On the feedback structure of wideband piezoelectric shunt damping systems," *Smart Materials and Structures*, vol. 12, p. 49, 01 2003.

[102] G. Raze, A. Paknejad, G. Zhao, C. Collette, and G. Kerschen, "Multimodal vibration damping using a simplified current blocking shunt circuit," *Journal of Intelligent Material Systems and Structures*, vol. 31, no. 14, pp. 1731–1747, 2020.

[103] W. Clark, "Vibration control with state-switched piezoelectric materials," *Journal of Intelligent Material Systems and Structures - J INTEL MAT SYST STRUCT*, vol. 11, pp. 263–271, 04 2000.

[104] Z. A. Shami, C. Giraud-Audine, and O. Thomas, "A nonlinear piezoelectric shunt absorber with a 2: 1 internal resonance: theory," *Mechanical Systems and Signal Processing*, vol. 170, p. 108768, 2022.

[105] Z. A. Shami, C. Giraud-Audine, and O. Thomas, "A nonlinear piezoelectric shunt absorber with 2: 1 internal resonance: experimental proof of concept," *Smart Materials and Structures*, vol. 31, no. 3, p. 035006, 2022.

[106] L. Pernod, B. Lossouarn, J.-A. Astolfi, and J.-F. Deü, "Vibration damping of marine lifting surfaces with resonant piezoelectric shunts," *Journal of Sound and Vibration*, vol. 496, p. 115921, Mar. 2021.

[107] O. De La Torre, X. Escaler, E. Egusquiza, and M. Farhat, "Experimental mode shape determination of a cantilevered hydrofoil under different flow conditions," *Proceedings of the Institution of Mechanical Engineers, Part C: Journal of Mechanical Engineering Science*, vol. 230, no. 19, pp. 3408–3419, 2016.

[108] C. Willert, S. T. Wereley, and J. Kompenhans, "Particle image velocimetry: a practical guide," 2007.

[109] M. R. Abdulwahab, Y. H. Ali, F. J. Habeeb, A. A. Borhana, A. M. Abdelrhman, and S. M. A. Al-Obaidi, "A review in particle image velocimetry techniques (developments and applications)," *Journal of Advanced Research in Fluid Mechanics and Thermal Sciences*, vol. 65, no. 2, pp. 213–229, 2020.

[110] J. L. Lumley, "The structure of inhomogeneous turbulent flows," *Atmospheric Turbulence and Radio Wave Propagation*, 1967.

[111] J. Weiss, "A tutorial on the proper orthogonal decomposition," in *AIAA aviation 2019 forum*, p. 3333, 2019.

[112] R. Hu and Y. Liu, "Proper orthogonal decomposition of turbulent flow around a finite blunt plate," *Journal of Visualization*, vol. 21, 05 2018.

[113] F. Di Donfrancesco, A. Placzek, and J.-C. Chassaing, "Time domain and time spectral reduced order models for aeroelasticity," in *Second International symposium on Flutter and its Application, 2020*, 2020.

[114] G. Berkooz, P. Holmes, and J. Lumley, "The proper orthogonal decomposition in the analysis of turbulent flows," *Annual Review of Fluid Mechanics*, vol. 25, pp. 539–575, 11 2003.

[115] A. Chatterjee, "An introduction to the proper orthogonal decomposition," *Current Science*, vol. 78, 04 2000.

[116] L. Cordier and M. Bergmann, "Proper Orthogonal Decomposition: an overview," in *Lecture series 2002-04, 2003-03 and 2008-01 on post-processing of experimental and numerical data, Von Karman Institute for Fluid Dynamics, 2008.*, p. 46 pages, VKI, 2008.

[117] P. Holmes, J. L. Lumley, G. Berkooz, and C. W. Rowley, *Turbulence, Coherent Structures, Dynamical Systems and Symmetry*. Cambridge Monographs on Mechanics, Cambridge University Press, 2 ed., 2012.

[118] L. Sirovich, "Turbulence and the dynamics of coherent structures. i - coherent structures. ii - symmetries and transformations. iii - dynamics and scaling," *Quarterly of Applied Mathematics - QUART APPL MATH*, vol. 45, 10 1987.

[119] O. Schmidt and T. Colonius, "Guide to spectral proper orthogonal decomposition," *AIAA Journal*, vol. 58, pp. 1–11, 01 2020.

[120] P. Welch, "The use of fast fourier transform for the estimation of power spectra: A method based on time averaging over short, modified periodograms," *IEEE Transactions on Audio and Electroacoustics*, vol. 15, no. 2, pp. 70–73, 1967.

[121] J. Jeong and F. Hussain, "On the identification of a vortex," *J. Fluid Mech.*, vol. 332, pp. 339–363, 01 1995.

[122] L. Graftieaux, M. Michard, and N. Grosjean, "Combining piv, pod and vortex identification algorithms for the study of unsteady turbulent swirling flows," *Measurement Science and Technology*, vol. 12, p. 1422, 08 2001.

[123] G. Chopra and S. Mittal, "Drag coefficient and formation length at the onset of vortex shedding," *Physics of Fluids*, vol. 31, p. 013601, 01 2019.

[124] P. W. Bearman, "Investigation of the flow behind a two-dimensional model with a blunt trailing edge and fitted with splitter plates," *Journal of Fluid Mechanics*, vol. 21, no. 2, p. 241–255, 1965.

[125] O. M. Griffin, "A note on bluff body vortex formation," *Journal of Fluid Mechanics*, vol. 284, p. 217–224, 1995.

[126] L. S. G. Kovásznay and G. I. Taylor, "Hot-wire investigation of the wake behind cylinders at low reynolds numbers," *Proceedings of the Royal Society of London. Series A. Mathematical and Physical Sciences*, vol. 198, no. 1053, pp. 174–190, 1949.

[127] C. Williamson and R. Govardhan-Ankulkar, "A brief review of recent results in vortex-induced vibrations," *Journal of Wind Engineering and Industrial Aerodynamics*, vol. 96, pp. 713–735, 06 2008.

[128] T. P. Miyanawala and R. K. Jaiman, "Decomposition of wake dynamics in fluid–structure interaction via low-dimensional models," *Journal of Fluid Mechanics*, vol. 867, p. 723–764, 2019.

[129] B. Oudheusden, F. Scarano, N. Van Hinsberg, and D. Watt, "Phase-resolved characterization of vortex shedding in the near wake of a square-section cylinder at incidence," *Experiments in Fluids*, vol. 39, pp. 86–98, 07 2005.

[130] N. J. Cherry, R. Hillier, and M. E. M. P. Latour, "Unsteady measurements in a separated and reattaching flow," *Journal of Fluid Mechanics*, vol. 144, p. 13–46, 1984.

[131] Q. Zhang and Y. Liu, "Separated flow over blunt plates with different chord-to-thickness ratios: Unsteady behaviors and wall-pressure fluctuations," *Experimental Thermal and Fluid Science*, vol. 84, pp. 199–216, 2017.

[132] G. Yin, M. J. Janocha, and M. C. Ong, "Estimation of Hydrodynamic Forces on Cylinders Undergoing Flow-Induced Vibrations Based on Modal Analysis," *Journal of Offshore Mechanics and Arctic Engineering*, vol. 144, 10 2022.

[133] M. Ben Chiekh, M. Michard, M. Guellouz, and J. Béra, "POD analysis of momentumless trailing edge wake using synthetic jet actuation," *Experimental Thermal and Fluid Science*, vol. 46, pp. 89–102, 2013.

[134] D. Mayer, C. Linz, and V. Krajenski, "Synthetic inductor for passive damping of structural vibrations," in *7th ECCOMAS Thematic Conference on Smart Structures and Materials. SMART*, 2015.

[135] O. Thomas, J. Ducarne, and J.-F. Deü, "Performance of piezoelectric shunts for vibration reduction," *Smart Materials and Structures*, vol. 21, no. 1, p. 015008, 2011.

[136]

[137] L. von Wangenheim, "Modification of the classical gic structure and its application to rc-oscillators," *Electronics Letters*, vol. 32, pp. 6 – 8, 02 1996.

[138] A. A. Bent, *Piezoelectric fiber composites for structural actuation.* PhD thesis, Massachusetts Institute of Technology, 1994.

[139] A. A. Bent and N. W. Hagood, "Piezoelectric fiber composites with interdigitated electrodes," *Journal of intelligent material systems and structures*, vol. 8, no. 11, pp. 903–919, 1997.

[140] R. B. Williams, G. Park, D. J. Inman, and W. K. Wilkie, "An overview of composite actuators with piezoceramic fibers," *Proceeding of IMAC XX*, vol. 47, p. 130, 2002.

[141] M. W. Hyer and S. R. White, *Stress analysis of fiber-reinforced composite materials.* DEStech Publications, Inc, 2009.

[142] D. Emad, M. A. Fanni, A. M. Mohamed, and S. Yoshida, "Low-computational-cost technique for modeling macro fiber composite piezoelectric actuators using finite element method," *Materials*, vol. 14, no. 15, p. 4316, 2021.

[143] P. Luzzatto-Fegiz and C. H. Williamson, "Structure and stability of the finite-area von kármán street," *Physics of Fluids*, vol. 24, no. 6, p. 066602, 2012.

[144] J. H. M. Ribeiro and W. R. Wolf, "Identification of coherent structures in the flow past a naca0012 airfoil via proper orthogonal decomposition," *Physics of Fluids*, vol. 29, no. 8, p. 085104, 2017.

[145] P. Saffman and J. Schatzman, "Properties of a vortex street of finite vortices," *SIAM Journal on Scientific and Statistical Computing*, vol. 2, no. 3, pp. 285–295, 1981.

[146] A. Sornborger, C. Sailstad, E. Kaplan, and L. Sirovich, "Spatiotemporal analysis of optical imaging data," *NeuroImage*, vol. 18, pp. 610–21, 04 2003.

[147] L. Sirovich and M. Kirby, "Low-dimensional procedure for the characterization of human faces," *Journal of the Optical Society of America. A, Optics and image science*, vol. 4, pp. 519–24, 04 1987.

[148] K. Afanasiev and M. Hinze, "Adaptive control of a wake flow using proper orthogonal decomposition1," *Lect. Notes Pure Appl. Math.*, vol. 216, 01 2001.

[149] J. H. CITRINITI and W. K. GEORGE, "Reconstruction of the global velocity field in the axisymmetric mixing layer utilizing the proper orthogonal decomposition," *Journal of Fluid Mechanics*, vol. 418, p. 137–166, 2000.

[150] S. Gordeyev and F. THOMAS , "Coherent structure in the turbulent planar jet. part 1. extraction of proper orthogonal decomposition eigenmodes and their self-similarity," *Journal of Fluid Mechanics*, vol. 414, pp. 145 – 194, 07 2000.

[151] J. S. Bendat and A. G. Piersol, *Random data: analysis and measurement procedures*. John Wiley & Sons, 2011.

[152] V. Ingle, S. Kogon, and D. Manolakis, *Statisical and adaptive signal processing*. Artech, 2005.

[153] M. Michard, L. Graftieaux, L. Lollini, and N. Grosjean, "Identification of vortical structures by a non local criterion- application to piv measurements and dns-les results of turbulent rotating flows," in *Symposium on Turbulent Shear Flows, 11 th, Grenoble, France*, pp. 28–25, 1997.

Appendix A

Basics of electrostatics

The theory of piezoelectricity presented further requires some basic knowledge of the electrical specificities of a solid material. The aim of the present section is to remind some general rules of electrostatics proper to a material domain. As the piezoelectric material is not exposed to strong magnetic fields for the present study, our description will only focus on the electric fields. For an in depth description, refer to [14].

A.1 Electrical fields in free space

In a first instance a free space medium is considered. In such a domain, the electric field **E** results from the Coulomb forces generated by electrically laden particles. For example, two A and B particles with a respective charge q_A and q_B, exert on each other a force that is equal to

$$\mathbf{F}_{A\to B} = \frac{1}{4\pi\epsilon_0}\frac{q_A q_B}{r^2}\mathbf{u}_{A\to B} = -\mathbf{F}_{B\to A}, \tag{A.1}$$

with r the distance between the particles, $\mathbf{u}_{A\to B}$ a unit vector and ϵ_0 the electrical permittivity of free space equal to $8.854 \times 10^{12}\ F.m^{-1}$. By generalizing to the whole domain, the electrical field is expressed as

$$\mathbf{F} = q\mathbf{E}, \tag{A.2}$$

with:

$$\mathbf{E} = \frac{q_A}{4\pi\epsilon_0 r^2}\mathbf{u}_{A\to M}. \tag{A.3}$$

Each electrical field generated by a particle has a spherical shape. By summing all the single electrical fields, the total electrical field of a laden particle system is obtained.

A.2 Conductivity of a material

Electrical conductivity σ is related to the presence of free electrons inside a material domain which are able to travel from one atomic orbit to another and induce electrical currents. The ability of the material to generate some currents is directly related to the value of σ. For very low values of σ, the material behaves as an electrical insulator as it does not contain any free electrons. These types of materials are known as dielectrics and piezoelectric materials belong to this category. Higher values of σ imply a high rate of free electrons meaning that the material is conductive.

The displacement of the free electrons occurs when the material is exposed to an electrical field. As a consequence, the electrical current, which is representative of the density of free charges inside the material, gives rise to the local Ohm law, expressed as

$$\mathbf{J} = \sigma.\mathbf{E} \tag{A.4}$$

with $\mathbf{J}$ being the current density.

A.3 Electrical polarization

When an electrical field is applied to a dielectric material, the location of the positive and negative charges is slightly displaced from its equilibrium position due to Coulomb forces. This phenomenon is known as electrical polarization and can affect in a significant way the electrical properties of the material. A polarization field $\mathbf{P}$ is introduced in order to characterize the displacement of positives charges against negative charges and is expressed as :

$$div\ \mathbf{P} = -\rho_p. \tag{A.5}$$

When the polarization is non uniform inside the material a polarization charge density ρ_p of opposite sign of $div\ \mathbf{P}$ is observed.

A.4 Electrical field and displacement inside a material

Differently from the free space domain case, the electrical field $\mathbf{E}$ inside a material domain is generated by:

- The free charges, represented by the free charge density ρ_v.
- The bonded charges, represented by the polarization charge density ρ_p.

As a result the local definition of the Gauss theorem applied to a material domain stands for

$$div\ (\epsilon_0 \mathbf{E}) = \rho_v + \rho_p \iff div\ (\epsilon_0 \mathbf{E} + \mathbf{P}) = \rho_v. \tag{A.6}$$

By defining the displacement field $\mathbf{D}$ as:

$$\mathbf{D} = \epsilon_0 \mathbf{E} + \mathbf{P}. \tag{A.7}$$

The local form of the Gauss theorem becomes:

$$div\ \mathbf{D} = \rho_v. \tag{A.8}$$

By considering a volume Ω with a free charge density equal to ρ_v, the integral form of the Gauss theorem is equal to:

$$\oiint_{\partial\Omega} \mathbf{D}.\mathbf{n} dS = \iiint_{\Omega} \rho_v d\Omega = Q, \tag{A.9}$$

with Q the charge contained in Ω. By considering free and bonded charges, the electrical field $\mathbf{E}$, the polarization field $\mathbf{P}$ and the displacement field $\mathbf{D}$ have been defined. These three fields describe the electrostatic properties of a given material domain and are directly related to the types of charges inside the material.

Appendix B

Additional details about the analysis methods

B.1 Proper Orthogonal Decomposition (POD)

Beyond the historical domain of turbulence, POD has now various fields of applications such as neuronal activity analysis [146], human face recognition [147] and more recently in adaptive control [148]. In the field of fluid mechanics, POD aims to identify large coherent wake structures and also permits the filtering of low energy turbulence. As stated by Weiss [111], its principle is the decomposition of an instantaneous flow variable into a set of deterministic functions that each capture some portion of the total fluctuating kinetic energy in the flow. Hu et [112] explains that the fluctuation is then represented by a linear combination of mutually orthogonal basis functions. As an example, the POD method can be applied to 2 or 3 dimensional flow fields obtained by PIV or by numerical simulation. For a two dimensions and two components (2D-2C) velocity field, the position vector is expressed as $\mathbf{x}$=(x,y), the velocity vector as $\boldsymbol{u}$ = u,v) and t stands for the time. In the case of a statistically stationary flow with a well defined temporal mean ($\overline{u}$ and $\overline{v}$), the fluctuating velocity component $\mathbf{u'}(\boldsymbol{x}$,t) is then decomposed into a sum of deterministic spatial functions $\Phi_k(\boldsymbol{x})$ or POD modes modulated by random time coefficients $a_k(t)$. For a set of N_t fluctuating velocity fields, the expansion is truncated at order N_t:

$$u'(\boldsymbol{x},t) = u(\boldsymbol{x},t) - \overline{u}(\boldsymbol{x}) = \sum_{i=1}^{N} a_i(t)\Phi_i^u(\boldsymbol{x}). \tag{B.1}$$

$$v'(\boldsymbol{x},t) = v(\boldsymbol{x},t) - \overline{v}(\boldsymbol{x}) = \sum_{i=1}^{N} a_i(t)\Phi_i^v(\boldsymbol{x}). \tag{B.2}$$

The time dependence of the expansion coefficient $a_k(t)$ comes from the temporal dependence of the fluctuating velocity field with the POD mode k. A specificity of the method is that each single time coefficient $a_k(t)$ only depends on its associated spatial mode $\Phi_k(\boldsymbol{x})$. This property is due to the fact that the modes are orthonormal, meaning that in an appropriate function space one can write:

$$\iiint_{\boldsymbol{x}} \Phi_{i_1}(\boldsymbol{x})\Phi_{i_2}(\boldsymbol{x})d\boldsymbol{x} = \begin{cases} 1 \text{ if } i_1 = i_2 \\ 0 \text{ if } i_1 \neq i_2 \end{cases} \tag{B.3}$$

Different processes exist to compute the POD method, the following paragraphs will present the direct POD method and the snapshot POD. These methods are very common and extensively used by the fluid mechanics community. For additional theoretical background and mathematical demonstration in the infinite-dimensional space refer to [114, 115, 116, 117].

B.1.1 Direct POD method

Following the description provided by Weiss [111], consider a dataset containing $m = N_t$ longitudinal fluctuating velocity fields $u'(x_i, y_j, t_k)$ of dimension $n = N_x \times N_y$. This dataset can be represented by a $m \times n$ snapshot matrix named $\boldsymbol{U}$:

$$\boldsymbol{U} = \begin{pmatrix} u'(x_1, y_1, t_1) & \cdots & u'(x_{Nx}, y_{Ny}, t_1) \\ u'(x_1, y_1, t_2) & \cdots & u'(x_{Nx}, y_{Ny}, t_2) \\ \vdots & & \vdots \\ u'(x_1, y_1, t_m) & \cdots & u'(x_{Nx}, y_{Ny}, t_m) \end{pmatrix}. \tag{B.4}$$

It is obvious that each row of matrix $\boldsymbol{U}$ represents a snapshot measured at a given time. The next step is the computation of the $n \times n$ covariance matrix $\boldsymbol{C}$ which is equal to:

$$\boldsymbol{C} = \frac{1}{m-1}\boldsymbol{U} = \boldsymbol{U}^T boldsymbol U. \tag{B.5}$$

Then by calculating the eigenvalues λ_i and associated eigenvectors of $\boldsymbol{C}$ and by ordering them from the largest eigenvalue to the smallest, we obtain a $n \times n$ matrix Φ where each column represents an eigenvector:

$$\Phi = \begin{pmatrix} \phi_{11} & \cdots & \phi_{1n} \\ \phi_{21} & \cdots & \phi_{2n} \\ \vdots & & \vdots \\ \phi_{n1} & \cdots & \phi_{nn} \end{pmatrix}. \tag{B.6}$$

Each eigenvector corresponds in fact to a proper orthogonal mode of the dataset. In order to visualise these modes it is possible to convert each column of Φ into a $N_x \times N_y$ matrix which is representative of the spatial mode and which can be used for the identification of coherent wake structures. Furthermore, the snapshot matrix $\boldsymbol{U}$ is projected on each mode of Φ following:

$$\boldsymbol{A} = \boldsymbol{U}\boldsymbol{\Phi}. \tag{B.7}$$

The columns of A are identified as the expansion coefficients for a given mode at each time step. a_{ij} is the projection of u' measured at time i on mode j. Conversely, the snapshot matrix $\boldsymbol{U}$ can be identified as the sum of the contributions from the n modes. Because Φ is orthogonal, it appears that:

$$\boldsymbol{U} \;=\; \boldsymbol{A}\Phi^{-1} \;=\; \boldsymbol{A}\Phi^{T}. \tag{B.8}$$

By rewriting this equation in matrix form, one obtains:

$$\begin{aligned}\begin{pmatrix} u_{11} & \cdots & u_{1n} \\ u_{21} & \cdots & u_{2n} \\ \vdots & & \vdots \\ u_{m1} & \cdots & u_{mn} \end{pmatrix} &= \begin{pmatrix} a_{11} \\ a_{21} \\ \vdots \\ a_{m1} \end{pmatrix} \begin{pmatrix} \phi_{11} & \cdots & \phi_{n1} \end{pmatrix} + ... + \begin{pmatrix} a_{1n} \\ a_{2n} \\ \vdots \\ a_{mn} \end{pmatrix} \begin{pmatrix} \phi_{1n} & \cdots & \phi_{nn} \end{pmatrix} \\ &= \begin{pmatrix} \tilde{u}^1_{11} & \cdots & \tilde{u}^1_{1n} \\ \tilde{u}^1_{21} & \cdots & \tilde{u}^1_{2n} \\ \vdots & & \vdots \\ \tilde{u}^1_{m1} & \cdots & \tilde{u}^1_{mn} \end{pmatrix} + ... + \begin{pmatrix} \tilde{u}^n_{11} & \cdots & \tilde{u}^n_{1n} \\ \tilde{u}^n_{21} & \cdots & \tilde{u}^n_{2n} \\ \vdots & & \vdots \\ \tilde{u}^n_{m1} & \cdots & \tilde{u}^n_{mn} \end{pmatrix}. \end{aligned} \tag{B.9}$$

It appears that the original fluctuating velocity field, or snapshot matrix **u**, has been decomposed into a sum of n contributions associated with n proper orthogonal modes:

$$\boldsymbol{U} \;=\; \sum_{k=1}^{n} \widetilde{\boldsymbol{U}}^{k}. \tag{B.10}$$

This formulation corresponds in fact to the finite-dimensional form of the POD theorem stated by equations B.1 and B.1. The way of computing the POD described here is called the direct POD method. The example is given based on the horizontal fluctuating velocity component but the same way of proceeding could be applied to the vertical fluctuating velocity component v' or even with both component together by including them in the snapshot matrix. The method is also adapted for 3 dimensional dataset, for example those obtained with tomographic PIV or with 3 dimension CFD simulations. Nevertheless, even if this method is intuitive and adapted to datasets with a high temporal resolution, it has the disadvantage of inducing low calculation speed if the spatial resolution is high.

B.1.2 Snapshot method

The snapshot method has been introduced by Sirovich [118] in 1987 and it has the main specificity of speeding up the calculation. It relies on the fact that the original POD equations (B.1 and B.1) is almost symmetric in t and $\boldsymbol{x}$ because mathematically there is no major difference between the temporal variable t and the spatial variable $\boldsymbol{x}$. As a result, the decomposition can involve deterministic temporal modes and random spatial coefficients instead of deterministic spatial modes and random time coefficients which, in simple words, means interchanging t and $\boldsymbol{x}$ in the algorithm. The resulting covariance matrix $\boldsymbol{C}$ has a size $m \times m$ and is expressed by

$$\boldsymbol{C_s} = \frac{1}{m-1}\boldsymbol{U}\boldsymbol{U}^T. \tag{B.11}$$

Many cases using planar or volumetric velocity data have a higher number of spatial measurement points n than the number of snapshots m. This involves that the correlation matrix $\boldsymbol{C}$ has a smaller size. As a result the calculation of the eigenvalues will be faster.

B.1.3 Turbulent kinetic energy

The kinetic turbulent energy (TKE) is a helpful criterion to associate POD modes and real physical phenomena. The TKE is directly related to the eigenvalues, hence the percentage of the TKE of mode i on the total TKE is expressed as the eigenvalue of mode i divided by the sum of all eigenvalues:

$$\%TKE_i = 100 \times \frac{\lambda_i}{\sum_1^n \lambda_i}. \tag{B.12}$$

Associating POD modes with real physical phenomena is much easier when a few number of modes contain a large portion of the TKE. According to the classification of the eigenvalues, the first modes are necessarily the most energetic. As a result, an extensive analysis of the first modes will, in many cases, provide a reliable comprehension of the real flow characteristics. The TKE also offers the opportunity to verify that the POD computation is fully converged (i.e. that the number of snapshots is large enough).

B.1.4 Limitations of the method

When trying to identify coherent structures with the POD method, one should keep in mind that the observed modes are nothing else than mathematical objects representing spatial zones of

correlation. Some of these zones of correlation often appear randomly due to the turbulent nature of most practical flows, which means that these modes are simply a manifestation of the randomness of turbulence [111].

Also part of the flow described by a given POD mode is not necessarily correlated with the part of the flow described by the same POD mode at a later time, or it is not necessary uncorrelated with the part of the flow described by a different mode at a later time. This is due to the fact that POD is only spatially optimal [21]. Therefore space only POD modes do not necessarily represent flow structures that evolve coherently with time. The spatially coherent structures represented by space-only POD are composed of contributions from spatio-temporal coherent structures at many frequencies. Practically, this is manifested as broadband frequency content within the coefficients $a_i(t)$. This highlights the fact that each space-only POD mode typically represents flow phenomena at many different time scales, which muddies their interpretation.

Fluctuations are proper to each variable and these are not necessarily correlated. For example performing a POD analysis on the normal velocity v component could provide a different classification of modes than a computation with the stream-wise velocity component u. This could induce erroneous physical interpretations, for example when computing the vorticity modes based on u and v vector fields independently obtained with POD. A better approach is to perform the POD computation directly on the vorticity variable based on raw u and v fields.

B.2 SPOD algorithm for discrete datasets

B.2.1 General principle

The SPOD algorithm presented here is similar to the one presented by Citriniti et al. [149] and Gordeyev et al. [150] but with an additional simplification introduced by [21] that reduces the computation cost in most cases. Consider the vector $\mathbf{q}_k \in \mathbb{R}^N$ which represents the instantaneous state $\mathbf{q}(\mathbf{x}, t)$ at time t_k on a discrete set of points in the spatial domain Ω:

$$\mathbf{q}_k = \begin{bmatrix} x_1 \\ x_2 \\ \vdots \\ x_N \end{bmatrix}, \tag{B.13}$$

with the length N equal to the number of grid points times the number of flow variables. This vector describes the state of the flow at a particular time k and is often identified as a snapshot. A typical example is the discrete velocity fields provided by the PIV recordings. Although, other variables than velocity can be included in $\boldsymbol{q}_k$ such as temperature, density etc. Snapshots are available for M equally spaced time instances implying that $t_{k+1} = t_k + \delta t$. The entire dataset is then represented by

$$\mathbf{Q} = \begin{bmatrix} \mathbf{q}_1, & \mathbf{q}_2, & \ldots, & \mathbf{q}_M \end{bmatrix} \in \mathbb{R}^{N \times M}. \tag{B.14}$$

A necessary condition to obtain convergent estimates of the cross-spectral density tensor is to average the spectra over multiple realizations of the flow. This is achieved consistently by the Welch's method [120]. In a first instance, the data matrix $\mathbf{Q}$ is divided into a set of smaller, if possible overlapping, blocks:

$$\mathbf{Q}^{(n)} = \begin{bmatrix} \mathbf{q}_1^{(n)}, & \mathbf{q}_2^{(n)}, & \ldots, & \mathbf{q}_{N_f}^{(n)} \end{bmatrix} \in \mathbb{R}^{N \times N_f} \tag{B.15}$$

with N_f the number of snapshots contained in the block and (n) the block number. As an example the k^{th} entry in the n^{th} block is expressed as

$$\mathbf{q}_k^{(n)} = \mathbf{q}_{k+(n-1)(N_f - N_0)} \tag{B.16}$$

with N_0 the number of snapshots by which the blocks overlap and N_b the total number of blocks. With respect to the ergodicity hypothesis each of these blocks are member of an ensemble of realizations of the flow. The next step consists in the computation of the Direct Fourier Transform (DFT) for each block in order to switch from temporal to frequency domain. The frequency form of the data matrix is expressed as:

$$\hat{\mathbf{Q}}^{(n)} = \begin{bmatrix} \hat{\mathbf{q}}_1^{(n)}, & \hat{\mathbf{q}}_2^{(n)}, & \ldots, & \hat{\mathbf{q}}_{N_f}^{(n)} \end{bmatrix} \tag{B.17}$$

with

$$\hat{\mathbf{q}}_k^{(n)} = \frac{1}{\sqrt{N_f}} \sum_{j=1}^{N_f} w_j \mathbf{q}_j^{(n)} e^{-i2\pi(k-1)[(j-1)/N_f]} \tag{B.18}$$

for $k = 1, ..., N_f$ and $n = 1, ..., N_b$ and were w_j corresponds to a scalar weight representing the nodal values of a window function. As a synthesis, the Fourier component at frequency f_k in the n^{th} block corresponds to $\hat{\mathbf{q}}_k^{(n)}$ and the resolved frequencies are:

$$f_k = \begin{cases} \frac{k-1}{N_f \Delta t} & \text{for} \quad k \leq N_f/2 \\ \frac{k-1-N_f}{N_f \Delta t} & \text{for} \quad k > N_f/2 \end{cases} \tag{B.19}$$

A new data matrix is obtained by rearranging the Fourier coefficients at f_k from each block:

$$\hat{\mathbf{Q}}_{f_k} = \sqrt{\kappa}\left[\hat{\mathbf{q}}_k^{(1)} \quad \hat{\mathbf{q}}_k^{(2)}, \quad \ldots, \quad \hat{\mathbf{q}}_k^{(N_b)}\right] \in \mathbb{R}^{N\times N_b} \tag{B.20}$$

with $\kappa = \Delta t/(sN_b)$. The third step consists in estimating the cross-spectral density (CSD) tensor $\mathbf{S}(\mathbf{x},\mathbf{x}',f)$. It is then expressed as

$$\mathbf{S}_{f_k} = \hat{\mathbf{Q}}_{f_k}\hat{\mathbf{Q}}_{f_k}^T. \tag{B.21}$$

It is important to note that the CSD will converge if the number of blocks N_b and the number of snapshots N_f in each block are increased together. By using this estimate, the SPOD eigenvalue problem reduces to an $N \times N$ matrix eigenvalue problem,

$$\mathbf{S}_{f_k}\mathbf{W}\mathbf{\Psi}_{f_k} = \mathbf{\Psi}_{f_k}\mathbf{\Lambda}_{f_k} \tag{B.22}$$

at each frequency. The columns of $\mathbf{\Psi}_{f_k}$ correspond to the approximate SPOD modes classified according to their eigenvalue provided by the diagonal matrix $\mathbf{\Lambda}_{f_k}$. The approximate modes are representative of the properties of the continuous modes and are directly orthogonal: $\mathbf{\Psi}_{f_k}^T\boldsymbol{W}\mathbf{\Psi}_{f_k} = \boldsymbol{I}$. The CSD tensor can then be expanded as:

$$\boldsymbol{S}_{f_k} = \mathbf{\Psi}_{f_k}\mathbf{\Lambda}_{f_k}\mathbf{\Psi}_{f_k}^T. \tag{B.23}$$

By using the expression of $\boldsymbol{S}_{f_k}$ and by applying the eigenvalue decomposition ($\tilde{}$) it is possible to show that the $N_b \times N_b$ eigenvalue problem

$$\hat{\mathbf{\Psi}}_{f_k}^T\boldsymbol{W}\hat{\mathbf{\Psi}}_{f_k}\mathbf{\Theta}_{f_k} = \mathbf{\Theta}_{f_k}\tilde{\mathbf{\Lambda}}_{f_k} \tag{B.24}$$

has the same non-zero eigenvalues as equation B.22. This induces that the eigenvectors corresponding to these non-zero eigenvalues can be exactly recovered as:

$$\tilde{\mathbf{\Psi}}_{f_k} = \hat{\boldsymbol{Q}}_{f_k}\mathbf{\Theta}_{f_k}\tilde{\mathbf{\Lambda}}_{f_k}^{-1/2} \tag{B.25}$$

which provides a significant reduction of the computation costs. A Matlab implementation of the algorithm is available at `https://github.com/SpectralPOD/spod_matlab`. The next section describes the choice of the spectral estimation parameters.

B.2.2 Choice of SPOD spectral estimation parameters

Obtaining reliable results with the SPOD method depends on an accurate estimation of the CSD matrix. The following description provides some general rules to successfully set-up a SPOD analysis.

For additional information, the reader can refer to a signal processing textbook, such as the ones of Bendat and Piersol [151] or Ingle [152]. The rules presented here are inspired from [119]. The main variables proper to SPOD are the data sampling parameters which consist of:

- the sampling time step: Δt which determines the sampling frequency $f_{sampling} = 1/\Delta t$,
- the total number of snapshots: N_t

and the spectral estimations parameters:

- the number of time steps in each data block used to compute the discrete Fourier transform: N_{FFT}.
- the number of snapshots overlapping in each block: N_{ovlp}.

The Nyquist frequency corresponds to the highest resolvable frequency

$$f_{Nyquist} = \frac{f_{sampling}}{2}. \tag{B.26}$$

The period T of each block of data depends on N_{FFT}:

$$T = N_{FFT}\Delta t = \frac{N_{FFT}}{f_s} \tag{B.27}$$

and the frequency resolution of the SPOD is expressed as

$$\Delta f = \frac{1}{T} = \frac{f_{sampling}}{N_{FFT}}. \tag{B.28}$$

Accurate spectral estimation requires that $f_{sampling}$ and Δf are sufficiently large and small, respectively, such that sampling reproduces the true underlying spectrum [119]. If N_{FFT} is large, then there will not be many blocks in the ensemble and the spectrum will not be statistically converged. In order to reduce the uncertainty, the data can be segmented in overlapping blocks which substantially increases the number of blocks [119]. With an overlap of N_{ovlp} snapshots in each block, the total number of blocks N_b is

$$N_b = \left\lfloor \frac{N_t - N_{ovlp}}{N_{FFT} - N_{ovlp}} \right\rfloor, \tag{B.29}$$

where $\lfloor . \rfloor$ indicates the floor operator. According to Welch's original work, the fact of taking 50% overlap ($N_{FFT}/2$) is a commonly accepted best practice. For the present study the SPOD was computed independently for the u, v and vorticity matrices.

B.3 Vortex identification algorithm

B.3.1 Vortex-centre identification algorithm

The vortex identification algorithm has first been introduced by Michard et al. [153]. As presented by figure B.1a, consider a fixed point P surrounded by a two dimensional surface S in the measurement domain and M, an other point located in S. The dimensionless scalar function Γ_1 at P is expressed as

$$\Gamma_1(P) = \frac{1}{S}\int_{M\in S}\frac{(\mathbf{PM}\wedge\mathbf{U}_M)\cdot\boldsymbol{z}}{\|\mathbf{PM}\|\cdot\|\mathbf{U}_M\|}dS = \frac{1}{S}\int_S sin(\theta_M)dS \tag{B.30}$$

where $\boldsymbol{z}$ is the unit vector normal to the measurement plane and θ_M represents the angle between the velocity vector $\mathbf{U}_M$ and the radius vector $\mathbf{PM}$.

When the velocity field is sampled at discrete spatial locations (e.g. the velocity field recorded by PIV) as presented by figure B.1b, S is a rectangular domain of fixed size and geometry centred on P. Accordingly, an approximation of the Γ_1 function is expressed by

$$\Gamma_1(P) = \frac{1}{N}\sum_S\frac{(\mathbf{PM}\wedge\mathbf{U}_M)\cdot\boldsymbol{z}}{\|\mathbf{PM}\|\cdot\|\mathbf{U}_M\|} = \frac{1}{N}\sum_S sin(\theta_M) \tag{B.31}$$

with N the number of points M inside S. Graftiaux et al.[122] have shown that $\|\Gamma_1\|$ is a dimensionless scalar bounded by 1. In the case of an axisymmetric vortex, $\|\Gamma_1\| = 1$ at the position of the vortex center. Hence, the scalar function Γ_1 provides a way to quantify the streamline topology of the flow in the vicinity of P. The rotation direction of the vortex is expressed by the sign of Γ_1. One may think that the value of N influences the position of the vortex centre but experience has shown that

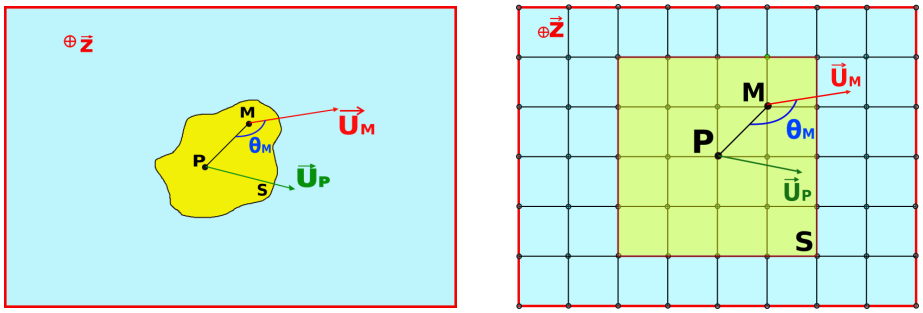

(a) (b)

Figure B.1: Schematic view of vortex detection algorithm in a continuous space (a) and in a discretized space (b).

it weakly affects the maximum location of Γ_1 even if it acts as a spatial filter. In a practical manner, $\|\Gamma_1\|$ reaches values ranging from 0.9 to 1 near the vortex centre, independently of the value of N.

B.3.2 Vortex-core identification algorithm

This methods aims to detect the boundaries of the vortices. It is similar to the vortex centre identification method but takes into account a local convection velocity U_P at P

$$\tilde{\mathbf{U}}_P \;=\; \frac{1}{S}\int_S \mathbf{U}\; dS$$

Accordingly, a dimensionless scalar function Γ_2 at P is expressed as

$$\Gamma_2(P) \;=\; \frac{1}{S}\int_{M\in S} \frac{[\mathbf{PM}\wedge(\mathbf{U}_M-\mathbf{U}_P)]\cdot \boldsymbol{z}}{\|\mathbf{PM}\|\cdot\|\mathbf{U}_M-\mathbf{U}_P\|} dS$$

and is approximated in a discretized space as

$$\Gamma_2(P) \;=\; \frac{1}{N}\sum_S \frac{[\mathbf{PM}\wedge(\mathbf{U}_M-\mathbf{U}_P)]\cdot \boldsymbol{z}}{\|\mathbf{PM}\|\cdot\|\mathbf{U}_M-\mathbf{U}_P\|}$$

Each vortex core is identified as an object of area A and each vortex centre(x, y) has been localized as being the Γ_2 based gravity centre of the vortex core. The circulation Γ of the vortex was deduced by integrating $\boldsymbol{\nabla}\times\mathbf{U}$ over the vortex core area A:

$$\Gamma = \int_A \boldsymbol{\nabla}\times\mathbf{U}\; dS. \tag{B.32}$$

Graftiaux et al. [122] have demonstrated that in the limit of a very small area S (S $\to$ 0) and for a two dimensional incompressible velocity field, Γ_2 is a local function depending only on:

- The rotation rate Ω expressed by the anti-symmetrical part of the velocity gradient ∇u at P.
- The eigenvalue μ of the symmetrical part of the velocity gradient ∇u at P.

Experiments have shown that the local character of the flow may be classified in function of $|\Omega/\mu|$. Table B.1 summarizes the flow specificities and associated $|\Gamma_2|$ values in function of $|\Omega/\mu|$.

$\lvert\Omega/\mu\rvert < 1$	flow locally dominated by strain	$\lvert\Gamma_2\rvert < 2/\pi$
$\lvert\Omega/\mu\rvert = 1$	pure shear	$\lvert\Gamma_2\rvert = 2/\pi$
$\lvert\Omega/\mu\rvert > 1$	flow locally dominated by rotation	$\lvert\Gamma_2\rvert > 2/\pi$

Table B.1: Flow specificities and associated $|\Gamma_2|$ values in function of $|\Omega/\mu|$.